THE UNIVERSITY OF CHICAGO

INTERPLAY BETWEEN CELL PROLIFERATION AND COLLECTIVE BEHAVIOR IN EPITHELIA

A DISSERTATION SUBMITTED TO
THE FACULTY OF THE DIVISION OF THE PHYSICAL SCIENCES
IN CANDIDACY FOR THE DEGREE OF
DOCTOR OF PHILOSOPHY

DEPARTMENT OF PHYSICS

BY
JOHN DEVANY

CHICAGO, ILLINOIS
DECEMBER 2022

To Mom, Dad, and Caroline

It is not really fair to be so critical of [D'Arcy] Thompson; he was far ahead of his time, closer to the truth than most others, and needed constructive criticism, instead of the uncritical adulation he got from those who didn't just ignore him. Both Thompson and his critics should have asked why biological shapes sometimes really do behave as if controlled by oversimplified equations. It isn't because they are made of soap.

Albert K Harris, *The need for a concept of shape homeostasis*

TABLE OF CONTENTS

LIST OF FIGURES

ACKNOWLEDGMENTS

I want to thank many people without which this work would not be possible. First, I'd like to thank my advisors. My PhD advisor Margaret Gardel contributed to all the projects presented here and has been a great mentor. Throughout the years, Margaret has always trusted me to find interesting things to work on and struggling to do this was one of the most important parts of my PhD. I'm really grateful for her constant support and enthusiasm. I'd also like to thank Yamuna Krishnan who let me join her lab for the first year of my PhD where I learned many lab skills. I got interested in biological systems working in Yamuna's lab and got a great foundation for my PhD work. Lastly, I'd like to thank Deborah Fygenson who taught me a lot about research as an undergraduate. Even though I was only an undergraduate, she spent many hours helping me do experiments and interpret data and got me interested in doing a PhD.

Next, I want to thank the collaborators who worked on projects with me throughout my PhD. Their contributions to the work and to guide my thinking about the different problems presented here were critical. Daniel Sussman and Lisa Manning provided expertise in modeling and interpretation of experiments looking at remodeling of epithelial tissues. Takaki Yamamoto also provided simulation results which contributed significantly to the revisions of this project. Bob Harmon got me interested in skin epithelium and taught me a lot. I had a great time helping Bob with his project and extending some of the results. Martin Falk helped with discussing data related to cell proliferation and provided simulations for the project. We had many great discussions which led to interesting breakthroughs. Liam Holt and Arvind Murugan also provided a lot of useful discussion and guidance on this project. Kasturi Chakraborty played a key role in guiding a project which I published during my PhD included in the appendix. Also, I had a chance to collaborate with Anand Saminathan, Akira Imamoto, Ming Han, Vincenzo Vitelli, and Nagarjun Narayanaswamy on other projects which are not discussed here. I enjoyed contributing to these projects,

especially the work building a patch clamping setup with Anand, and the interesting analysis done by Ming. Also, other scientists that I discussed this work with including Thomas Witten, Jan Skotheim, Edwin Munro and many others.

I want to thank all the lab members that I had a chance to interact with in Margaret's lab. In particular, Barbara Hissa worked with me for a few months when I was starting and taught me a lot. Kim Weirich and Nitobe London had a lot of interesting discussions with me about science. Jon Winkelman helped me learn plasmid cloning, Yvonne Beckham for keeping things running in the lab, and Shailaja Seetharaman for many interesting discussions and being a great friend. I'd also like to thank members of Yamuna's lab. Ved Prakash and Kasturi Chakraborty who taught me a lot of skills in the first few months of my PhD. Aneesh Veetil, who taught me a lot about research and has been a good friend.

There are also the many people whose research was important for the development of ideas and experiments. I tried to cite them all, but there are many others who were not properly credited.

Other good friends throughout my PhD, Kevin, Maulik, and Junyi.

Lastly, I want to thank my family for always supporting me both throughout my PhD and everything before that. I wouldn't have become interested in science without my dad teaching me math and science as a kid and my mom always encouraging me to do well in school. I owe most of my success to their hard work and support.

ABSTRACT

Collections of epithelial cells form macroscopic materials that show collective behavior, including deformation, self-organization, and cell turnover. However, the complex cell-cell interactions which drive this collective behavior are not well understood. Therefore, we performed studies which aim to connect molecular pathways regulating the cytoskeleton and cell proliferation to cell-cell interactions and collective cell behavior. By characterizing tissue scale behaviors, we were able to develop and constrain new models which explain the collective behavior of epithelia. We demonstrate that collective motion and self-organization in epithelia is driven in significant part by cell cycle-dependent changes in cell-cell interactions. Conversely, we show that the cell cycle is regulated by collective behavior at the tissue scale through a process called contact inhibition of proliferation. We present a framework for contact inhibition which explains how cell proliferation is regulated by spatial constraints which we then test experimentally. These observations demonstrate that there is feedback between proliferative and collective cell behaviors in the epithelium that may control a transition between tissue morphogenesis and homeostasis. Together, the data we present help elucidate several general phenomena of epithelial tissues observed across diverse tissue types and relevant to understand both normal tissue function and disease.

CHAPTER 1

INTRODUCTION: PHENOMENOLOGICAL MODELS OF COLLECTIVE BEHAVIOR IN EPITHELIA

Living organisms are composed of up to trillions of individual cells, which work collectively to perform a variety of tasks required for an organism's survival. For example, neurons and supporting cells make up the brain and nervous system. Collectively, through cell-cell signaling, these cells perform complex computations to control the behavior of an organism. Epithelia are another example of a complex biological system made from large collections of interacting cells. These cells form a macroscopic material with the primary function of maintaining a selective barrier between an organism and the outside world (Fig.1.1a) ([99], [255], [269], [314]). However, the epithelium is also capable of complex collective behaviors such as generating 3-dimensional deformation, self-organization of cells into spatial domains, and continuous regeneration (Fig. 1.1b). These collective behaviors of the epithelium are important for maintaining biological functions in response to perturbations throughout the lifetime of an organism.

Phenomenological models have been proposed to explain these collective behaviors. Some of these proposed models include: (1) tissue fluidization, where tissues transition from solid-like to liquid-like states to explain tissue deformation, (2) cell sorting, where cell populations separate into spatial domains to explain self-organization, and (3) contact inhibition of proliferation, where cell proliferation responds to cell contact to explain tissue turnover (Fig. 1.1c). These models provide a framework for understanding experimental results and have provided considerable insight into how multicellular tissues function. However, because these models are based on observed phenomenology rather than physical principles, it is a challenge to understand how broadly they apply, and when they sufficiently explain tissue behavior. Despite progress in understanding collective behavior in epithelia, it remains unclear how the interactions between cells give rise to collective behaviors at the tissue scale.

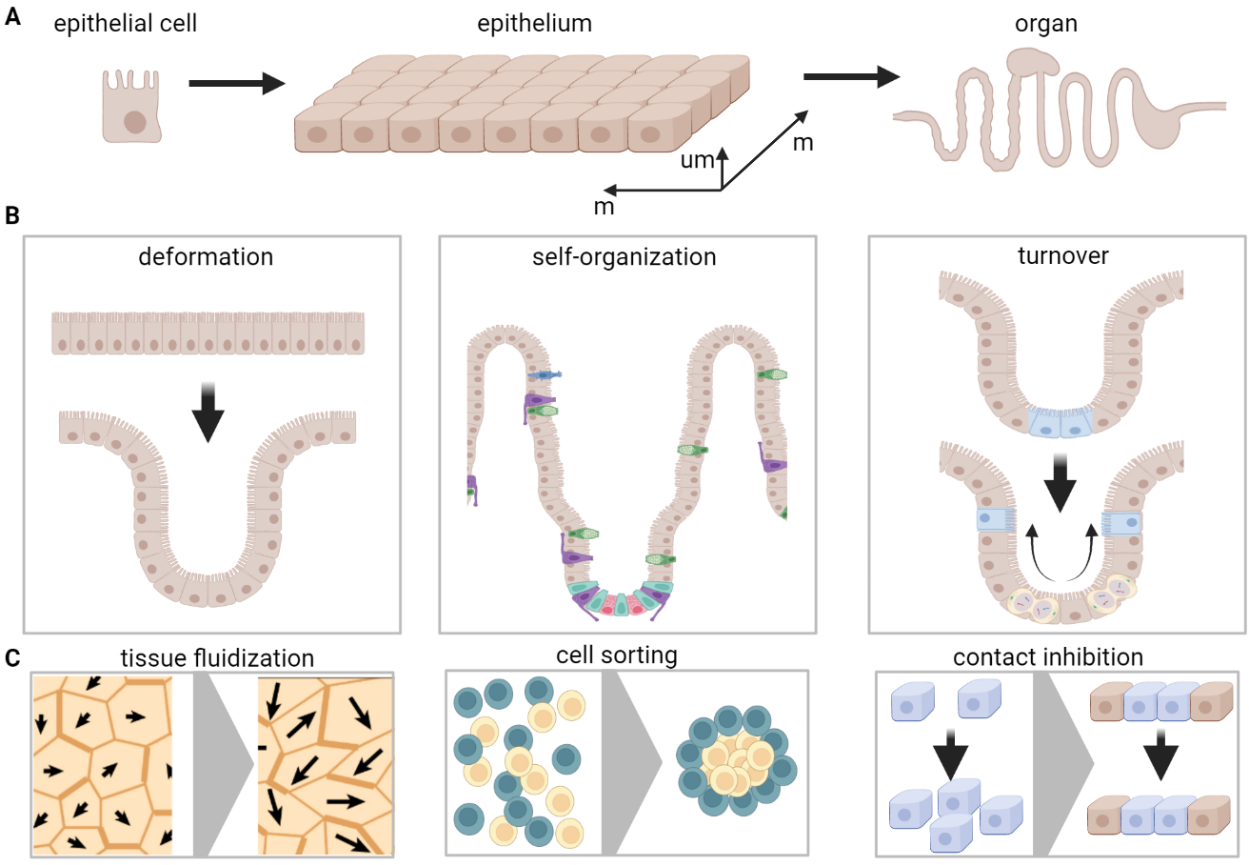

Figure 1.1: Collective behavior in epithelia (a) epithelia are formed from large collections of epithelial cells which form space spanning layers. These layers line the interface between the inside and outside of the body (b) epithelia can perform collective behavior inculding 3D deformation, self-organization and turnover of cells (c) phenomenological models have been used to describe how these collective behaviors occur by tissue fluidization, cell sorting and contact inhibition. Figure prepared with biorender ([1]).

Analogous problems have been studied in the context of nonliving systems which show interesting collective properties. For example, in glass forming materials, collections of molecules can transition from a liquid-like to solid-like state at a specific density ([20]). These collective phenomena, termed phase transitions, occur across diverse non-living systems ([136]). In these cases, a small change in a microscopic parameter of the system (density, fluctuations, affinity) leads to a dramatic in the macroscopic properties (mechanical modulus, conductivity, ordering). It is thought that phase transitions are also important for many biological phenomenon ([128], [212]). Like glass forming materials, epithelia are spatially disordered but show both liquid-like ([93], [188], [247]) and solid-like ([144], [345]) properties under different conditions. Characterization of the mechanical properties of tissues also suggests that rigidity transitions guide large scale deformations within embryonic development ([133], [208], [239], [331]). However, there is not a consensus about the mechanical model which causes this transition ([150], [238], [331]). Explaining changes in tissue mechanics as a phase transition between fluid-like and solid-like regimes is a promising framework to understand the material properties of a broad range of embryos and tissues. However, the underlying details of such a phase transition remains an ongoing area of study which will be discussed below.

Biological systems also have complex signaling networks operating within a single cell and between cells. The principles of complex systems with many interacting agents have been demonstrated in computational models from simple systems like cellular automaton ([207], [343]) to agent-based models of processes like cell migration ([153], [332]). These models demonstrate that simple rules of interaction can give rise to complicated and potentially unexpected macroscopic behavior. While these systems often cannot be understood directly from physical principles, phenomenological models which examine the behaviors of the system can be used to explain how the system works and can be controlled ([198]). In the context of epithelia, phenomenological models have proven useful for elucidating the

principles of epithelial mechanics, self-organization, and proliferation. Here, we outline how such models have been used together with experimental studies to develop our current understanding of the collective properties of epithelia.

1.1 Tissue fluidity tunes the material properties of epithelia

Within the epithelium, individual cells can tune mechanical properties through transcription of genes which regulate the cell cytoskeleton ([91], [170]). The cytoskeleton, in turn, can generate and sense forces in the tissue allowing for complex mechanical feedback and patterning ([105], [240]). One striking example of the regulation of tissue mechanics is in early development, where epithelial-like tissues deform and fold into templates of different adult tissues and organs ([169], [168]). These dynamical tissue motions are specified by genetic patterning and biochemical feedback. Then deformations are driven by mechanical forces and material properties in the epithelium acting downstream of these genetic signals. The overall behavior occurs as a result of physical interactions between cells and can be modeled according to physical principles ([109], [291]). However, methods for modeling embryonic development often rely on continuum models which explain behavior only at the tissue scale. Because tissue motions are determined by dynamic gene expression in single cells, continuum models are not sufficient to model cell scale variation. For example, cells can stochastically differentiate into different cell types, which can have local consequences on the tissue mechanics. Therefore, it remains an important challenge to connect cell scale regulation of the cytoskeleton to the behavior observed at the tissue scale.

In early studies of tissues, embryologists noticed the parallels between the behavior of cells in early embryos and the physics of soap bubbles and foams ([75], [124], [304]). These studies suggested that tissues might be understood using principles borrowed from studying these physical systems. For example, in analogy with foams, it was noted that the structure of epithelial tissues showed a nearly minimized perimeter ([124], [304]). The shapes of soap

bubbles are determined by area minimization by surface tension balanced with the pressure of gas inside that prevents the bubble from collapsing. In a cell, there is a corresponding surface tension-like force exerted by the contracting cytoskeleton at the cell periphery, termed the "cortical tension". The osmotic pressure of the cell generated by its molecular contents are many times greater than the cortical tension, and resist the contraction causing the volume of the cell to be fixed (Fig. 1.2A) ([57], [306]). Aggregates of multiple cells can then be described by considering an additional adhesive force between the cells, which will be described in more detail in the next section (Fig. 1.2B). These cell aggregates can also be constrained by other tissues or extracellular material like eggshells (Fig. 1.2B). Larger collections of soap bubbles make up foams, which can be understood by considering the balance of interfacial tensions ([76]). In tissues, the cell geometry is determined by a force balance at each vertex set by the relative cortical tensions of each interface. The resulting angle between each junction represents the force balance (Fig. 1.2C) ([54], [220]).

Inspired by the modeling of foams, vertex models were developed to explain the behavior of epithelium ([6], [86], [286]). These models consider epithelial monolayers to be a 2D packing of cells with elastic energy associated with the cell area and perimeter to model the osmotic pressure and cortical (surface) tension, respectively (Fig. 1.2D, E). In active versions of the model, there is a self-propulsion term, which captures the active cell motility, and can either be uncorrelated or have defined spatial and temporal correlations (Fig. 1.2E) ([23], [24], [100], [297]). One striking feature of vertex models is that there is a transition between a solid-like and liquid-like state of the tissue when tuning the surface tension past a critical value ([23], [149]). In epithelia, a phase transition between fluid-like and solid-like states was previously hypothesized to be a density dependent transition analogous to a glass transition ([8], [96]). In contrast, vertex models suggest that the transition is density independent and occurs due to changes in cell mechanical properties and active stress generation ([24], [149]). In vertex models, the point at which this phase transition occurs can be observed

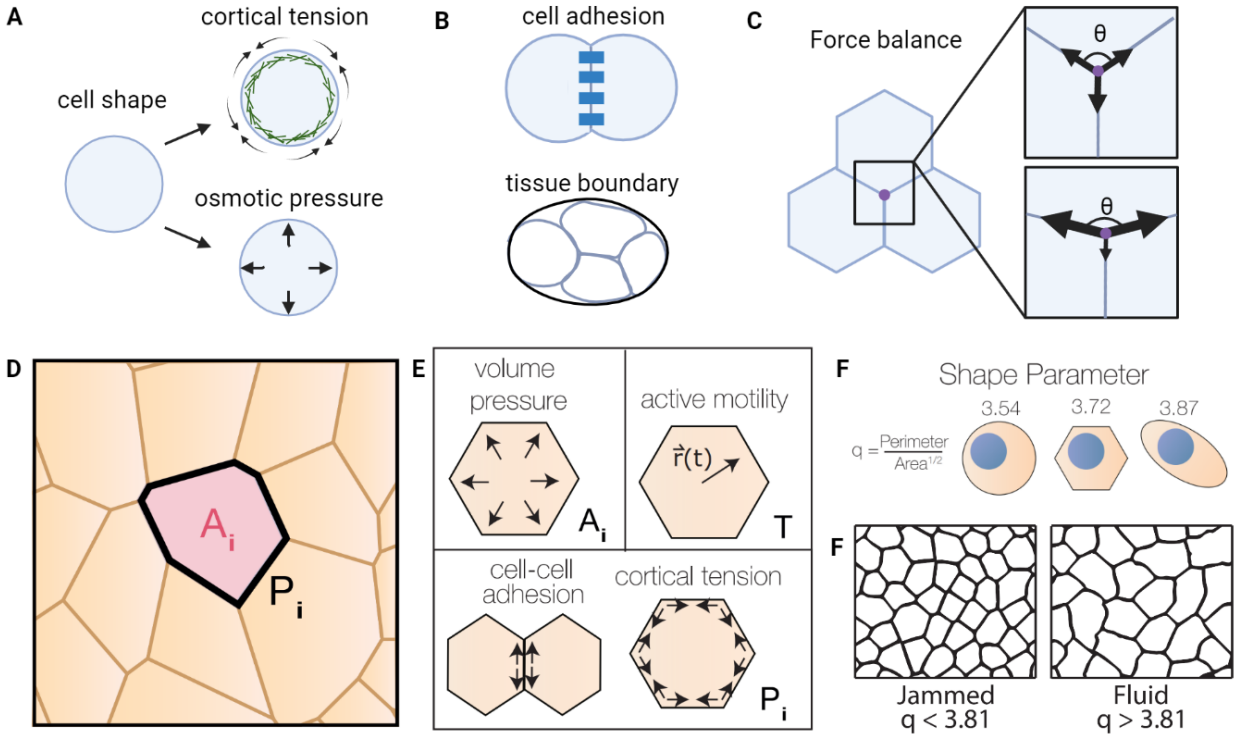

Figure 1.2: Vertex models describe epithelial mechanics (A) cell shape is determined by a combination of cortical tension from the cytoskeleton and osmotic pressure from the macromolecular content of the cell (b) cells also form adhesions which modify the cortical mechanics locally and are bounded by external structures like eggshells (c) at each vertex a force balance determines the angles of the cell interfaces (d) vertex models consider a collection of cells with target area A_i and perimeter P_i (E) the model parameters A_i and P_i capture the effects of volume pressure, adhesion and cortical tension. An additional motility term, T, can also be added (F) cell geometry can be quantified by the shape parameter. When this quantity is less than 3.81 the cell network is rigid and it loses rigidity above this value.

directly from the cell shape across the network. Therefore, suggesting that cell shape can be used to infer the mechanical properties of tissues. As the tension increases and stress decreases, the cell geometry becomes more regular ([356]). The cell shape can be quantified by a dimensionless parameter – the shape parameter - defined as $q = P/\sqrt{A}$ (Fig. 1.2F), and when this parameter becomes lower than a specific value, $q = 3.81$, the network of cell interactions becomes rigid ([24], [356]) (Fig. 1.2G). These models have been used to describe the behavior of cells *in vivo* and *in vitro* by looking at how cell shape and motility are correlated ([111], [133], [189], [224], [231], [331]).

However, there are limitations to the interpretation of experimental data using vertex models. While some tissues do show highly fluid-like behavior with many neighbor exchanges ([59], [208], [214], [239]) there are other tissues where fluctuations are low and neighbor exchanges are rare even when cell shapes suggest a fluid-like state ([8], [346]). Vertex models assume there is no energetic barrier to cellular rearrangement in the fluid-like regime. This has not been tested in detail, and studies of junction contraction have demonstrated that the mechanical behavior of cell junctions may be more complex than assumed by vertex models ([41], [42], [47], [126], [204], [285], [299]). In addition, these simple models provide a prediction of the relative forces on cell junctions ([54], [220]), but compared with experimental measurements there is some discrepancy ([137], [158]). This suggests that modification of vertex models will be required to understand certain tissues. However, despite these potential limitations, a robust correlation between cell shape and motility has been observed across a broad range of epithelia, which is a key prediction of vertex models ([13], [224], [231], [331]).

1.2 Cell sorting drives tissue self-organization

Epithelial tissues perform multiple functions and have developed spatial domains to perform specific tasks, e.g., crypts (proliferation) and villi (absorption) in the intestine, or basal layer (proliferation) and cornified layers (barrier) of the skin (Fig. 1.3a) ([261]). Epithelia

are subject to external forces, cell division, and death on the timescale of hours to days, but robustly maintain these organized domains over the lifetime of an organism, suggesting the presence of mechanisms that maintain tissue organization. This spatial organization of tissues can be disrupted in disease and is often associated with loss of tissue function. For example, tumor formation produces large cell aggregates, which lose both the architecture and function of the tissue they are derived from ([26]). Perturbations to tissue organization in different diseases are unique, yet reproducible across individuals. As a result, images of tissue allow clinicians to distinguish between a number of disorders which disrupt tissue structure ([339]). It is possible that these changes in tissue morphology are also a driver of disease. Normal and cancerous epithelial cells can regain lost tissue function by being cultured under conditions which allow them to reconstitute normal 3d tissue organization ([87], [143]). However, we still lack a complete understanding of how tissue organization is maintained during tissue homeostasis and is disrupted in disease.

In epithelia different cell populations typically have distinct cell geometry, which suggests differences in mechanical properties. For example, in the skin, there is a clear transition from columnar (height $>$ width) to squamous (width $>$ height) cell morphology along the vertical axis, while in the intestine, there are characteristic transitions from negative to positive curvature (Fig. 1.3A). The geometry of epithelial cells is the result of differences in tension and adhesion at different cellular interfaces ([66], [75], [86], [195], [188], [304], [340]). While these differences could be attributed to other cells in the tissue or developmental processes, similar geometric features are found in organoids ([266]), epithelial tissue models, which originate from single epithelial cells and lack other cell types (Fig. 1.3B). In organoid models, it was recently demonstrated that the mechanical properties of these cell populations are different ([355]).

A model of "cell sorting", inspired by the separation of immiscible fluids, like oil and water, has been used to explain the self-organization of epithelial cells into spatial domains

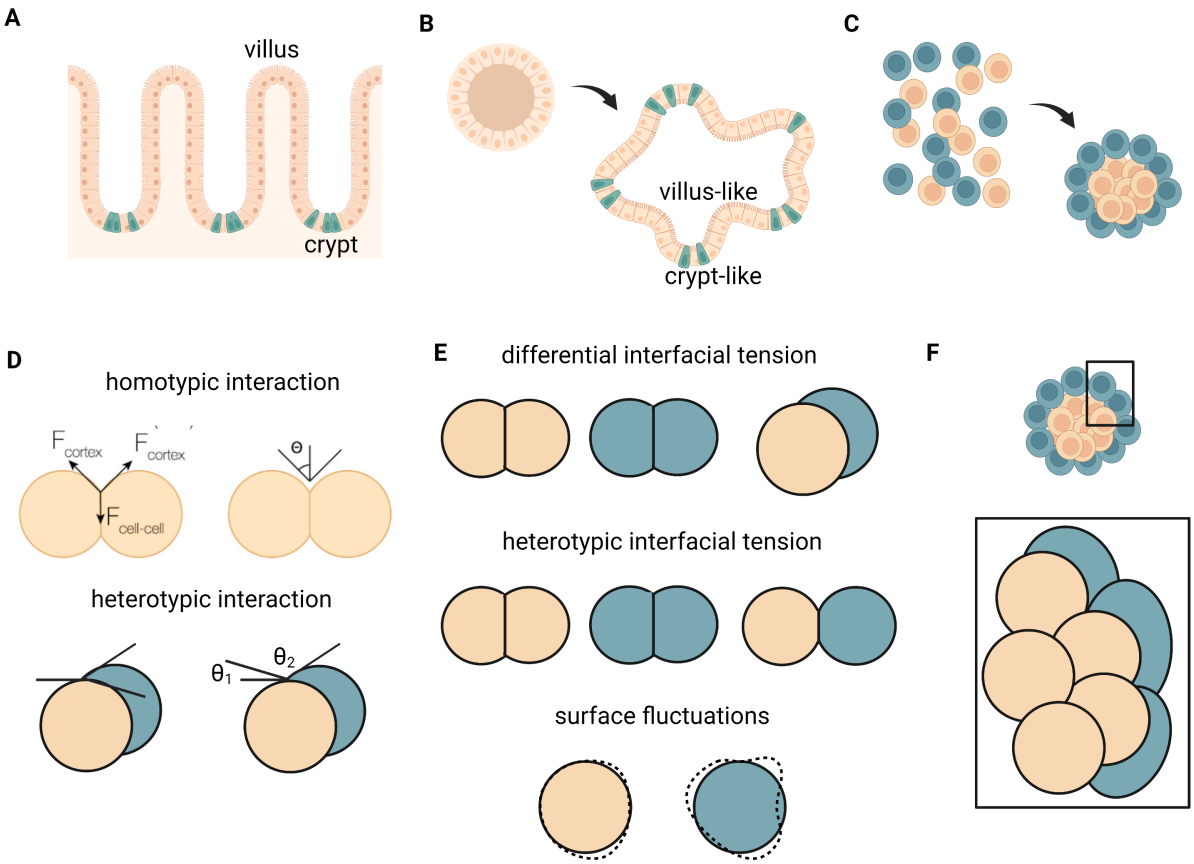

Figure 1.3: Cell sorting connects cell-cell interactions to tissue organization (A) epithelium are organized into spatial domains, for example, in intestine different populations are localized to crypt and villi (B) Organoid tissue models lack many cell types found in tissue, yet they show crypt-like and villus-like domains (C) epithelial cells can be dissociated and will reform into organized aggregates in suspension (D) the geometry of isolated cell pairs can be used to understand the interactions between cells - the contact angle reflects the balance of cortical tensions and can show symmetry in homotypic interactions and asymmetry in heterotypic interactions (E) different mechanisms of asymmetry drive cell sorting, differential interfacial tension is a difference in the cortical tension between populations, heterotypic interfacial tension is an increase in tension at heterotypic interfaces, surface fluctuations are differences in the fluctuations of cortical tension across the cortex of individual cells (F) these different forms of cortical asymmetry cause cells to sort into configurations with populations of cells separated to different domains.

([93], [287], [310], [334]) (Fig. 1.3C). In this model, differences in cell mechanical properties drive segregation of cell populations from a homogeneous mixture of multiple cell types. During development, cell sorting mechanisms can be highly robust. For example, sea urchin and newt embryos can be dissociated and upon reaggregation, retain the ability to develop ([102], [122]). Recently, theoretical and experimental advances in cell sorting have started to provide insight into how cell populations interact during embryogenesis ([17], [40], [146], [161], [168], [312], [341]). Early models of cell sorting implicated differences in the adhesiveness of cells driving their sorting similar to the separation of molecular liquids ([287]). However, cell-cell interactions are considerably more complex than those between molecules, and a passive mechanical model does not account for the active force generating processes of cells ([114]). Later work has recognized that the energy of cell-cell adhesion molecules is small compared with the energetic barriers of cell interaction ([66]), implicating mechanical forces generated at the cell cortex as a key mediator of cell sorting ([195], [188]). These differences in tension at different cellular interfaces is demonstrated by looking at isolated pairs of cells where the contact angle indicates the relative forces (Fig. 1.3D). In different contexts, the interfacial tension that drives cell sorting is regulated at the molecular scale by adhesion signaling pathways including cadherin ([116], [288], [312]), and ephrin signaling ([43], [84], [152], [303]) which may act through actin nucleators to regulate the cortex ([56], [113]). Differences in cytoskeletal gene expression give rise to asymmetry in cell mechanics and influence heterotypic interactions (Fig. 1.3E). Due to this asymmetry, when populations of cells with different mechanics interact, the most energetically favorable configurations have a different population of cells at the inside and outside of the aggregate (Fig. 1.3F). If cells are able to rearrange and explore different configurations over time, the most stable configuration with the cells separated will persist over less stable configurations.

However, some of the basic principles of cell sorting are not well understood due to the difficulty associated with making dynamical measurements of the sorting process ([233]). Dif-

ferent models have been proposed to explain the observed sorting and differences in the cortical tension between cell populations ([66], [195]) as well as increased tension at heterotypic interfaces ([40], [113], [209], [298]) seem to play a role. Recent work has demonstrated that cell surface fluctuations may also be important for cell sorting ([353]) (Fig. 1.3E). Differences in cell size also influence the most stable cell configuration and could potentially promote or inhibit sorting ([148], [156], [250]). Due to limited studies of these effects outside the context of development, it also remains unclear to what extent cell mechanical properties control cellular organization and dynamics in adult epithelia. While there are open questions about the relative roles of these different effects, cell sorting models have still provided considerable insight into how different epithelia self-organize.

1.3 Contact inhibition of proliferation regulates cell growth in a tissue

Within tissues, cells constantly turnover through cell birth and death. In humans, 0.2% of total cell mass turns over each day ([275]). Epithelia show a range of turnover rates, from days in the intestine, to weeks in the skin to over a year in the kidney. Despite constant turnover, epithelial tissues maintain their structure over time through self-organization ([113], [333]), directed cell migration ([162]) and cell differentiation ([203]). However, the effects of cell turnover on cell and tissue physiology are mostly unknown. The capacity to constantly turnover may replace defective cells through a competition for space in the tissue ([36], [157], [202]), but may also contribute to cancer because mutations occur during DNA replication ([308]) or alter the proteome through dilution ([78]).

As cells grow and divide, they need to maintain a similar cell size across generations to maintain cell physiology. There are a range of cell sizes found *in vivo*, but for a given cell type, the cell size is consistent across species and individuals ([205]) . To demonstrate the importance of cell size control, the size of cells has been experimentally perturbed. In this

case, cells which become too large show shifts in the proteome and defects in proteostasis ([51], [167], [218]), demonstrating that size control is important for maintaining cell physiology. Over several decades, knock-out screens have identified many of the key proteins which regulate cell proliferation ([215], [221], [279]). However, understanding the more complex feedback mechanisms underlying cell size control remains challenging. Single-celled organisms proliferate constantly at a high rate which makes it easy to examine the effects of perturbation and develop mathematical models describing growth laws ([34], [274]). In these simple systems, phenomenological models of cell size control were developed to explain the different feedback mechanisms which can maintain cell size ([7]) (Fig. 1.4A). These models provide a basis for classifying the behavior of different systems and looking for molecular mechanisms which explain the feedback ([38], [300], [361], [360]). Similar to most single-celled organisms, single mammalian cells behave like adders, meaning that the mechanism regulating cell division is sensitive to the total amount of growth, δ, that occurs during the cell cycle ([38]). However, in epithelia, cells show G1 sizer behavior, where cells will only transition into the cell cycle if the cell size increases beyond a certain threshold size, a ([348]). A deeper understanding of the underlying mechanisms of cell cycle regulation are still required to reconcile these differences.

However, the turnover of tissues cannot be understood by the same principles as the proliferation of single-celled organisms. One of the key differences is that in multicellular organisms, cell proliferation needs to be coupled to tissue turnover and growth. Cells need to proliferate rapidly during healing or development as tissue grows or slowly during tissue homeostasis to balance cell death. Several mechanisms looking at cell-cell signaling have been proposed to explain the coupling of cell proliferation and cell death in tissues (Fig. 1.4B). Some of these studies focus on the signaling of dying cells triggering the proliferation or survival of neighbors through the release of signaling factors ([35], [178], [316]). Other studies have highlighted how mechanical forces can trigger cell signaling pathways like

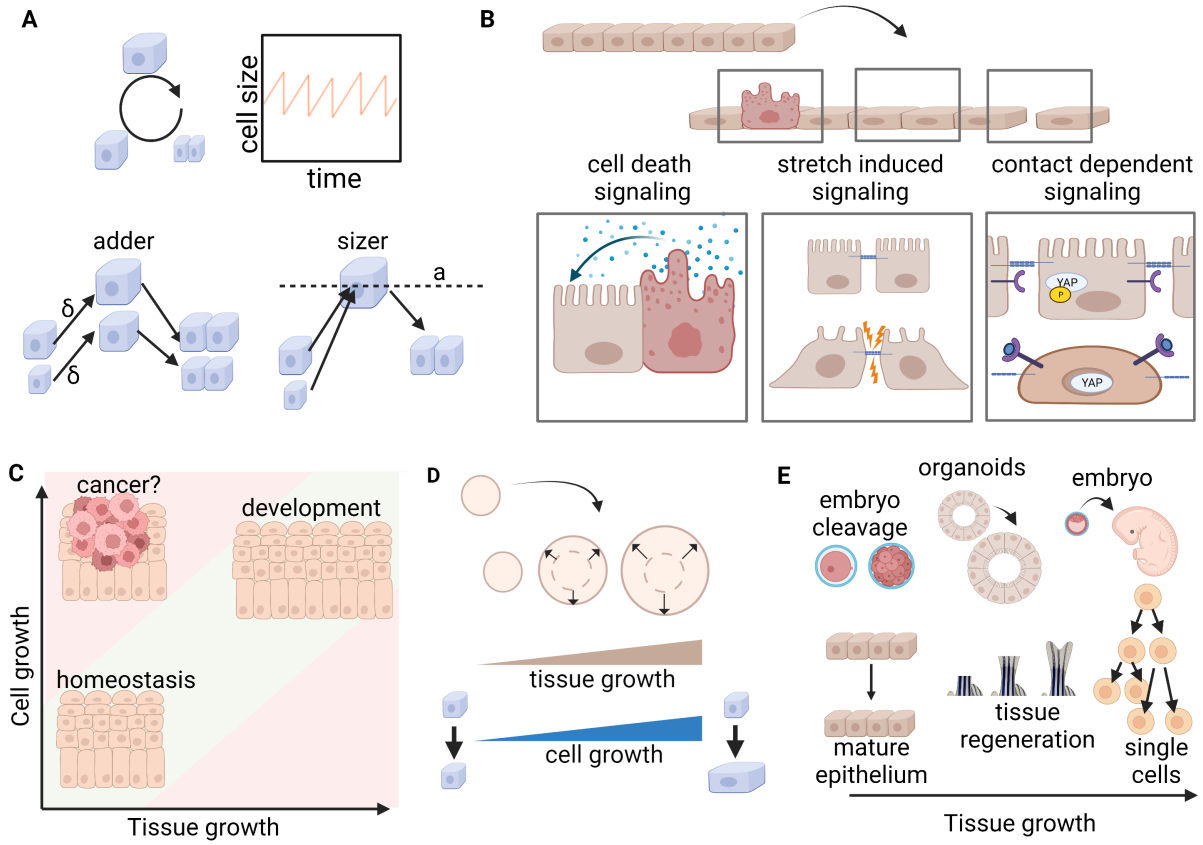

Figure 1.4: Feedback between cell and tissue growth controls cell proliferation (A) single cells have different phenomenological models of cell proliferation. Adders show the same amount of growth each cell cycle while sizers divide at the same size (B) during tissue growth different pathways are stimulated to trigger cell proliferation. Dying cells release growth factors to increase cell proliferation, mechanical forces stimulate cell proliferation, loss of contact stimulates cell proliferation (C) feedback between cell and tissue growth occurs in homeostasis and development but may be lost in tissue diseases like cancer or aging (D) expanding monolayers should reveal the feedback between cell and tissue growth (E) different tissues grow at different rates

Piezo channels or YAP/TAZ signaling to stimulate proliferation during processes like wound healing ([108], [228], [132]). In addition, contact-dependent signaling mechanisms through cadherins contribute to the suppression of cell proliferation in confluent tissue ([147], [196], [201]). Together, these biological mechanisms begin to describe how cell and tissue growth become coupled.

Another framework for understanding this coordination is the phenomenon of contact inhibition of proliferation ([132], [196]). The key idea of contact inhibition is that proliferation is regulated through feedback where cells sense how much space is provided by other processes operating at the tissue scale like cell turnover or tissue growth ([245], [290]) (Fig. 1.4C). Under conditions of tissue homeostasis, growth becomes highly limited and in conditions of tissue growth, cell growth increases as spatial constraints are relieved. Some of this effect is explained by contact-dependent adhesion signaling ([92], [147], [172]), but it is also likely that contact inhibition incorporates mechanical feedback ([129], [228], [280]). Future work may find contact inhibition to be a relevant framework for studying tissue disease. For example, in conditions where cell-cell signaling is perturbed like in cancer, cell growth may exceed tissue growth leading to loss of tissue architecture. While in other conditions where cell growth becomes impaired such as aging or metabolic disorders defects in tissue thickness or healing may be observed as tissue growth outpaces cell growth (Fig. 1.4C).

Feedback between cell and tissue growth has been suggested by previous work looking at tissue growth behavior under perturbation. For example, perturbations which affect local cell growth do not increase proliferation due to feedback ([228]), while perturbations to cell turnover or differentiation produce additional space in the tissues and stimulate cell proliferation ([203]). However, a more detailed test of the feedback between cell and tissue growth is required. For example, in a process like wound healing the expansion of a tissue is driven by migration ([117], [245]). Modifying the cell migration would change tissue growth and the effects on cell growth could be measured. If there is feedback, the corresponding

cell growth should change in quantitative agreement (Fig. 1.4D). It is also possible that tissue growth could be measured across a range of systems and compared with the cell scale behavior (Fig. 1.4E). Then different signaling pathways can be correlated with tissue growth to understand the biological mechanisms which regulate cell growth in epithelial tissue. At the moment, it remains difficult to apply our understanding of contact inhibition to tissues *in vivo* because of the lack of experimental measurements. However, contact inhibition is a promising framework which can potentially be used to understand the proliferative dynamics across a range of tissues in homeostasis, development, and disease.

1.4 Summary

Overall, phenomenological models of collective behavior in epithelia provide a starting point for connecting cell scale properties with tissue behavior. These models assume a highly simplified view of cell mechanics and signaling as a starting point because cell collectives are too complex to model directly from physical principles. For example, vertex models and cell sorting models allow for the complex properties of the actin cytoskeleton to be described by a single parameter, the cell surface tension. Such a simplification is required to understand effects at the tissue scale. For example, when looking at processes in biological systems like embryonic development, 100-1000s of cytoskeletal genes change at the same time, making it difficult to directly implicate a specific gene in changing collective behavior at the tissue scale. When a given gene is identified as critical for this process, it is also difficult to determine if this is the only cause or acts together with other factors. Measuring how a perturbation changes cell surface tension is more feasible and can then be used to explain the collective behavior. Importantly, identifying these relationships provides a starting point for comparing seemingly disparate biological systems to build broader principles of tissue dynamics and function. Cell shape, surface mechanics, or proliferation can be compared across tissues to understand how tissues are similar and unique from one another. For example, in different

stages of morphogenesis cellular flows may be generated with different patterns and driven by different genes, but it is possible that both deformations occur because of similar changes to the cell surface tension. As these models are tested across more tissues and organisms, they may end up providing universal principles which describe how collective cell behaviors occur and become disrupted in disease.

These models also highlight specific properties of a cell in the context of tissue biology and explain how they are maintained. For example, vertex models highlight the importance of cell shape in epithelia and provide a mechanism for the homeostasis of cell shape. Cell shape varies from tissue to tissue but is maintained throughout the lifetime of an organism ([261]). After stretching or tissue damage cells return to their original shape through a remodeling process driven by cell motility, neighbor exchange and proliferation ([66], [77], [101], [123], [299], [346]). Cell shape also has consequences on cell differentiation and signaling ([50], [184], [186], [335]). Vertex models highlight that differences in cell shape correspond to different mechanical states of cells and suggest a mechanism for the homeostasis of cell shape ([115]). Variations in cell shape across a tissue can also give information about the mechanical and proliferative state of different cell population ([75], [77]). Cell shape can also report on tissue scale phenomena like asymmetric strain or growth of a tissue ([197], [331], [346]). As a result, perturbations in cell shape can be a robust marker of disease and potentially be used for the diagnosis of tissue disorders like cancer ([26], [339]). Similarly, cell sorting and contact inhibition provide mechanisms for homeostasis of the organization and density of cells within the epithelium and provide a means for connecting changes in tissue organization and density to disease.

Here we describe experiments which reveal new mechanisms controlling collective cell behavior. We first collect data of the process of epithelial remodeling where the cellular structure of a healing epithelium returns to the original state through cell motion and re-arrangement. We use the framework of vertex models to analyze the different states of the

remodeling epithelium and show a relationship between cell motility and cell division. We propose that fluctuations only occur in dividing cells and that the arrest of cell motility occurs because contact inhibition arrests the cell cycle (Ch2). We go on to use the idea of cell sorting to understand cellular organization in the skin. We show how two different effects, changes in heterotypic surface tension driven by differences in expression levels of the formin Diaphanous 1 and changes in surface tension driven by proliferation can explain how the skin epithelium self organizes into different layers (Ch3). We then study how proliferation is regulated in epithelia by quantifying and experimentally perturbing cell division and growth. We propose and test a new framework for understanding contact inhibition of proliferation as a feedback between tissue growth and cell growth described by a quantity called the "tissue confinement". This new model can potentially describe how cell proliferation is regulated across and variety of epithelium and is a new model for studying the molecular mechanisms that regulate cell growth and division in epithelia (Ch4). Together, these works highlight an unexpected interplay between cell proliferation and collective cell behavior in epithelia.

CHAPTER 2

CELL CYCLE-DEPENDENT ACTIVE STRESS DRIVES EPITHELIA REMODELING

This section is reproduced from the article Cell cycle-dependent active stress drives epithelia remodeling published in PNAS by John Devany, Daniel Sussman, Takaki Yamamoto, M. Lisa Manning, and Margaret L. Gardel ([72]).

The modeling presented in Figures 2.6, 2.7 in this section was done by Daniel Sussman and the modeling in 2.20A, B, E and 2.21 was done by Takaki Yamomoto. Lisa Manning, Daniel Sussman, and Margaret Gardel were also involved in planning the project and writing.

2.1 Abstract

Epithelia have distinct cellular architectures, which are established in development, re-established after wounding, and maintained during tissue homeostasis despite cell turnover and mechanical perturbations. In turn, cell shape also controls tissue function as a regulator of cell differentiation, proliferation, and motility. Here we investigate cell shape changes in a model epithelial monolayer. After the onset of confluence, cells continue to proliferate and change shape over time, eventually leading to a final architecture characterized by arrested motion and more regular cell shapes. Such monolayer remodeling is robust, with qualitatively similar evolution in cell shape and dynamics observed across disparate perturbations. Here we quantify differences in monolayer remodeling guided by the active vertex model to identify underlying order parameters controlling epithelial architecture. When monolayers are formed atop extracellular matrix with varied stiffness, we find the cell density at which motion arrests varies significantly but the cell shape remains constant, consistent with the onset of tissue rigidity. In contrast, pharmacological perturbations can significantly alter the cell shape at which tissue dynamics is arrested, consistent with varied amounts of active

stress within the tissue. Across all experimental conditions the final cell shape is well correlated to the cell proliferation rate, and cell cycle inhibition immediately arrests cell motility. Finally, we demonstrate cell-cycle variation in junctional tension as a source of active stress within the monolayer. Thus, the architecture and mechanics of epithelial tissue can arise from an interplay between cell mechanics and stresses arising from cell cycle dynamics.

2.2 Introduction

Cells in epithelial tissues adopt a variety of distinct morphologies which are defined during development and maintained throughout the lifetime of an organism ([26]). Cellular shape and geometry can be perturbed by stretching or wounding but individual cells within the tissue return to their original shape through increased cellular motility, junctional turnover, neighbor exchange, and proliferation ([346], [123], [299]). In turn, tissue architecture impacts cell fate and tissue physiology ([231], [186]). Cell division has been implicated as a potential mechanism to regulate monolayer topology ([346], [28], [86], [101], [77]). However, tissue architecture can also change as a result of motion, neighbor exchanges, and shape changes of individual cells in the absence of cell division ([66], [208], [90], [168]). One promising physical framework for predicting collective cell behavior are vertex models, which represent confluent epithelial monolayers by a mechanical network of cell-cell junctions ([86], [6], [189], [286], [124]). From these approaches, mechanical descriptions of epithelial tissue dynamics are being developed ([6], [24]), but key questions remain.

For instance, it remains unclear what processes set the length scale over which cells in a tissue can move or migrate. This length scale helps determine developmental outcomes, such as whether convergent extension is effective at generating large-scale changes to the body shape, as well disease outcomes, such as whether cells leave a cancer tumor in invasive streams ([111], [224]). In traditional materials composed of atoms or molecules, particles can freely diffuse when the material is fluid-like, but their motion is arrested in solids,

when surrounding particles inhibit their mobility. In the context of biological tissues, it is tempting to speculate that the arrest of motion in a dense collection of cells occurs as the system becomes jammed, or solid-like, which can arise from changes to either density ([253], [119]) or cell mechanical properties ([356], [23], [149]). However, there is third possible mechanism for arrest of motion: the particles in a fluid-like material could also stop moving if the source of fluctuations becomes very small, despite remaining in a mechanically unstable configuration. Fluctuations in biological tissues are driven by active cellular processes such as cell migration, cytoskeletal contraction, and cell division ([169], [262], [53]). Therefore, the scale of fluctuations in a tissue may be regulated in response to extracellular or intracellular cues to control the degree of tissue remodeling.

In model epithelial tissues, it has been observed that the cells are initially more dynamic – changing neighbors and moving significant distances– and at later times that motion arrests ([231], [8], [96], [13], [187], [245]). Because these changes occur with minimal genetic or biochemical gradients, such epithelial monolayers are an ideal system to study whether cell arrest is governed by an underlying rigidity transition (e.g. collective solidification) caused by changes in density or cell mechanics, or instead by a decrease in active stress fluctuations in a material that remains fluid-like. Particle-based models for tissues predict decreased cell motion arising from reduced interstitial space at increased cell density ([208], [253], [119], [150]). In contrast, vertex models predict that the cell density is not a direct control parameter for cell dynamics ([356]). Instead, vertex models predict that observed steady-state cell shape, tuned by varying passive cell mechanics and active forces, is the control parameter for cell motility ([86], [286], [24], [356], [23]). Cell shape, density and cell adhesion have all been implicated in the arrest of cell motion in epithelial monolayers ([231], [8], [96], [187]). Furthermore, changes to cell density also regulate signaling pathways that could influence single cell mechanics and cell-cell interactions ([196]), and cell divisions also introduce active stress fluctuations which in turn affect cell shape ([356], [262], [74], [193],

[65]). Thus, it remains unclear how cell density, cell mechanics, and active stress fluctuations contribute to the regulation of epithelial monolayer remodeling dynamics.

Here we use epithelial monolayer remodeling as a model system to investigate the biophysical regulation of epithelial architecture and dynamics. After forming a confluent monolayer, cells continue to divide and change shape over time, until reaching a final state characterized by low motility and more regular cell shapes. Such monolayer remodeling is robustly observed, with qualitatively similar evolution in cell shape and dynamics over a large range of experimental conditions. To tease apart the effects of cell density changes from other mechanical perturbations, we study monolayers formed atop extracellular matrix with varied stiffness. This variation in substrate stiffness causes the cell densities to change significantly, but we find relatively little correlation between density with cell motion. In contrast, we find a striking data collapse when cell velocities are plotted as a function of observed cell shape, as predicted by active vertex models. To understand whether observed cell shapes are primarily regulated by active fluctuations or by changes to single-cell mechanical properties, we perturb the monolayer with pharmacological interventions that interfere with cell proliferation and the cytoskeleton. We find that inhibition of the cell cycle immediately arrests cell motion and shape change, suggesting that cell-cycle-dependent active stress contributes significantly to monolayer dynamics and remodeling. Moreover, across all experimental conditions we find that the average cell shape in the homeostatic final state is well correlated with the cell division rate, suggesting that suppressing cell-cycle-based fluctuations leads to an arrest of cell motion that is independent of the underlying cell mechanics. Finally, we show that cell-cycle-dependent changes in junctional tension are an important source of active stress in the tissue, and use simulations to demonstrate the different tissue architectures that can be realized by modeling cell-cycle-dependent changes in edge tensions. Together our results demonstrate that cell geometry and cell cycle dynamics control cell shape remodeling in epithelial monolayers.

2.3 Results

2.3.1 Remodeling of confluent MDCK monolayers to achieve homeostatic architecture

To measure the shape and speed of individual cells in a simple epithelial monolayer we created an MDCK cell line that stably expresses green fluorescent protein localized to the plasma membrane via the transmembrane protein stargazin. We seeded these cells at high density on collagen I gels and imaged multiple fields of view using time-lapse fluorescence microscopy. Initially, the monolayer was not continuous, and there were numerous cell-free voids (Fig. 2.1A). Over time, the cells closed gaps to form a continuous monolayer spanning $\approx$ 15 mm; we designate this as $t = 0$ (Fig. 2.1A). Over the following 12 hours, the cells within the monolayer change shape until a steady-state geometry and density is achieved (Fig. 2.1A, $t = 720$ min). Thus, we use this as a model system to study epithelial tissue homeostasis by which cell shape and density is recovered after injury through wound healing and monolayer remodeling (Fig. 2.1B). While previous work has focused on mechanisms of collective migration in wound healing ([219], [311], [68]), here we focus on the process by which the cells within a confluent monolayer change shape over time.

We use image segmentation to extract cell shape, size, and positions over time (Methods). To quantify cell shape, we use cell vertex locations to reconstruct a polygon with a well-defined perimeter p and area A to calculate the shape parameter (area-normalized perimeter) $q = p/A^{1/2}$; this quantity is bounded from below by objects with a circular shape ($q_{circle} \approx 3.54$) and most cells are observed to have a shape parameter greater than that of a regular hexagon ($q_{hexagon} \approx 3.72$) (Fig. 2.2) ([356], [23]).

We observe cell shape remodeling, along with changes in density and speed, takes place for approximately 12 hours until the system arrests. These dynamics are not sensitive to the details of how time or spatial averaging is performed (Fig. 2.3, 2.4). We also confirmed they

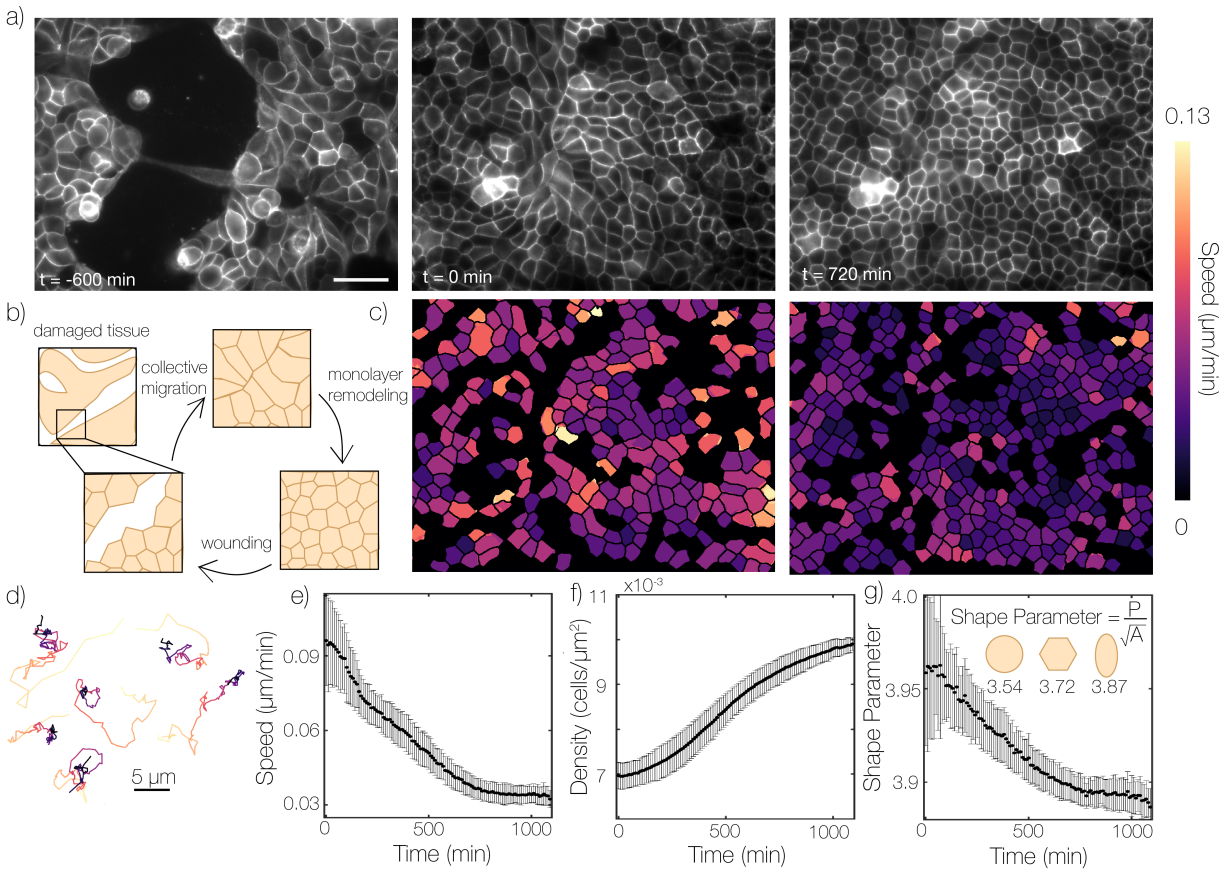

Figure 2.1: Cell shape remodeling leads to homeostatic monolayer architecture. (a) Cells were plated on collagen gel substrates at $t = -1000$ minutes. By $t = -600$ minutes cell have aggregated into large colonies which collectively migrate to fill open space. At t=0 minutes cells have formed a confluent monolayer. Over the next 720 minutes cells become denser and cell morphology becomes increasingly regular. Scale bar is 50 microns. (b) Schematic of the process observed in a). A tissue may be wounded resulting in collective migration followed by monolayer remodeling to the normal epithelial architecture. (c) Heat map of single cell speeds plotted over the segmented cell outlines from images shown in a). Areas in black contain cells which were ignored due to potential segmentation errors. (d) Randomly selected cell trajectories from $t = 0$ to $t = 1100$ minutes, color indicates time. (d-f) Sample averaged values of cell shape, speed and density at each time point across 60 fields of view in the sample depicted in a). Error bars represent standard deviation between fields of view.

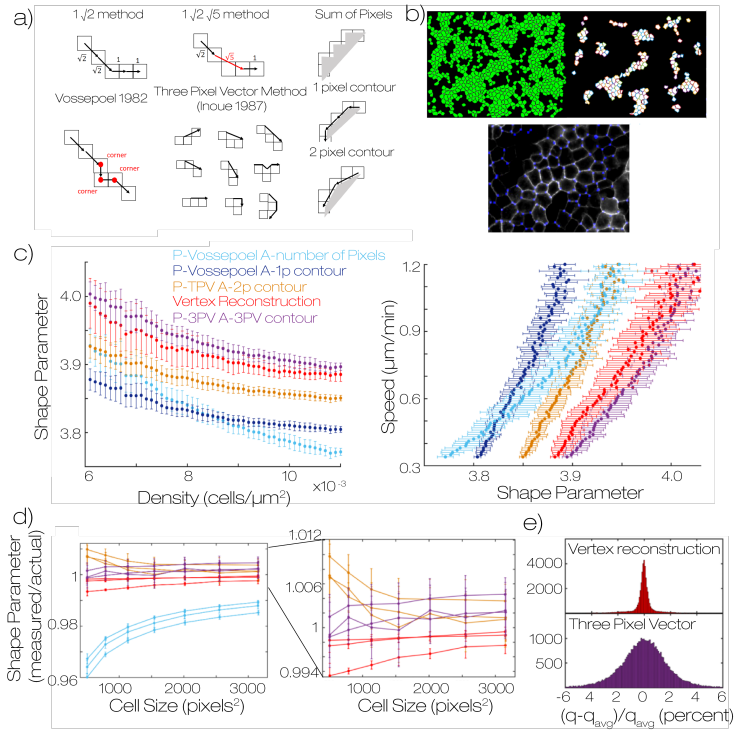

Figure 2.2: Shape metrics are resolution dependent. (a) Schematics describing different popular methods for determination of perimeter and area of a polygon constructed from pixels. Methods depicted include the 1 root 2 method – default in imageJ, and voesspoel – default in Matlab regionprops. We also schematize several methods for determining polygon area. Sum of pixels is default in both imageJ and Matlab (b) An image of cell outlines (green) with marked vertex locations (pink). The cells which do not have a complete set of neighbors are discarded and remaining polygons are constructed from the vertices. We show an overlay of detected vertices on the raw data. (c) For one experimental dataset, WT on 2mg/ml collagen – we plot shape vs density for a variety of shape metrics and Speed vs shape for the same set of metrics. Errorbar represents the standard deviation of 60 fields of view. (d) We segmented simulation data and plot shape/actual shape vs area for this data for a variety of shape metrics for images of different resolution. We observe that some shape metrics show large errors and are highly resolution dependent. We show a zoom in of the top performing metrics. Error bar represents the standard deviation of three replicates (e) We measured shape of fixed cell data and used the two top performing metrics to measure cell shape. The fixed data is a time series of images where there is no cell motion but images show photobleaching and noise variation. We know the shapes are not changing with time, however the measured shape fluctuates due to changes in noise. We measure the distribution of measurements around the mean for the two metrics for each cell. Shapes reconstructed from vertices are much more robust to noise.

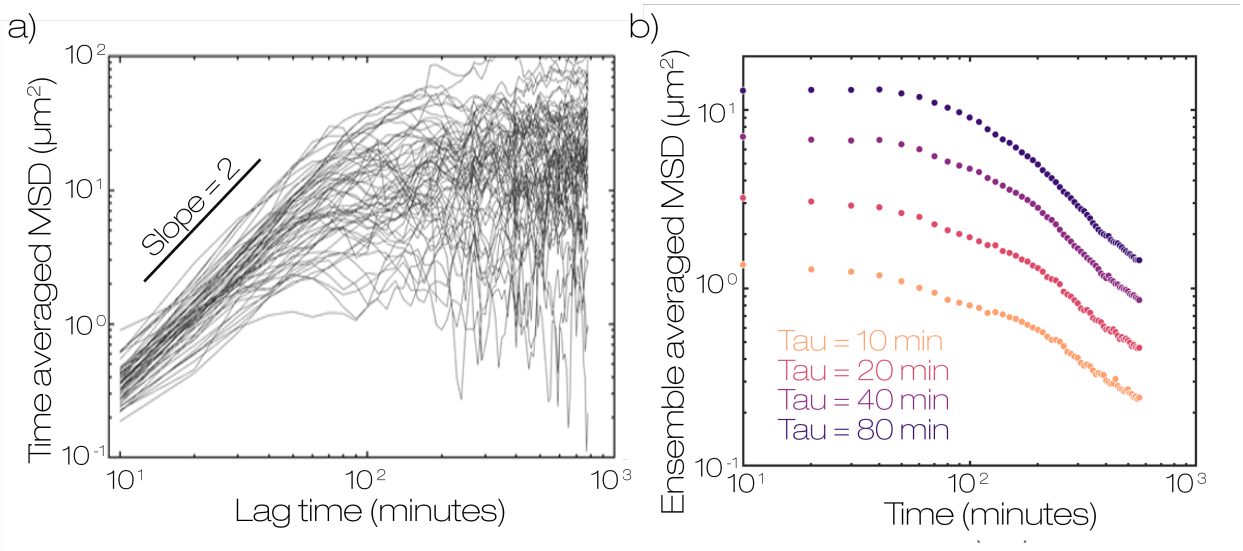

Figure 2.3: Mean square displacements are time-dependent. (a) Time averaged mean squared displacements for individual cells show a plateau at long time scales indicating cells are not freely moving at long times. A small representative subset of 100 cells from one field of view is displayed (b) mean squared displacement for different lag times decay with time indicating that cell motion is reduced at later times. Data is across all cells in 60 fields of view in a single single experiment on a 2mg/ml collagen gel under wild type conditions.

are independent of initial seeding density (Fig. 2.5), consistent with previous data ([96]). Similarly to prior observations ([8], [245]), cell speed decreases (Fig. 2.1C, D, E, 2.3B) as the density increases from cell proliferation (Fig. 2.1F). However, we also observe changes in cell shape over time (Fig. 2.1G). This reduction in shape parameter is correlated with reduced motility in models and experiments where there is no change in density ([231], [24], [13]). Therefore, from these data alone, the order parameters controlling the steady state cell shape and density in epithelial tissues are impossible to discern.

2.3.2 Cell shape and Speed are correlated in active vertex models

To further understand the process of monolayer remodeling, we explore predictions of a thermal Voronoi model ([296], [297]). This model is a variation of standard vertex models which incorporates a simple Brownian noise on each cell to account for active mechanical stress

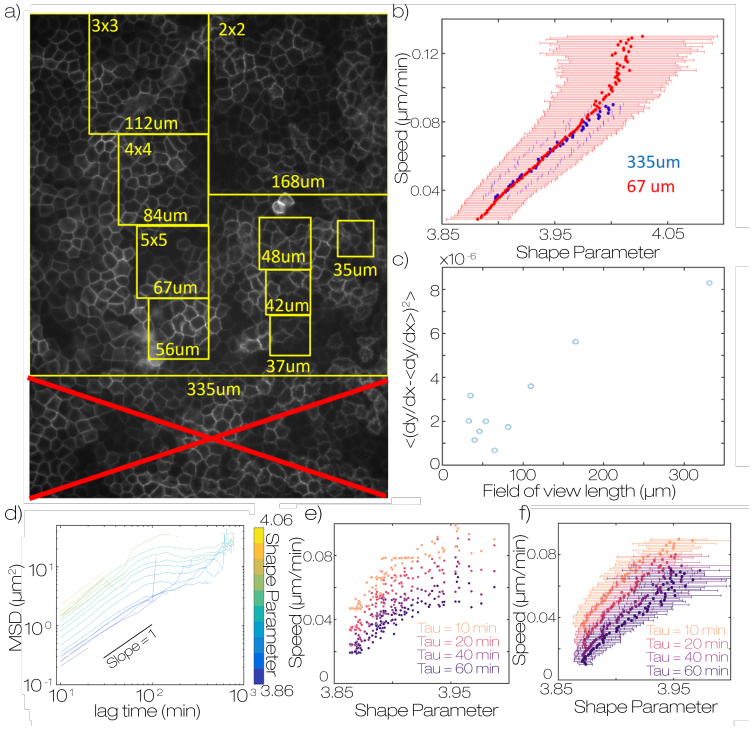

Figure 2.4: Correlation between shape and speed does not depend on the field of view size or time between images. (a) representation of different field of view sizes. For this analysis the field of view was first truncated into a square window 335x335 μm. This field was subdivided into 2x2, 3x3... 10x10 sections and each section was averaged independently as if that was the full field of view. (b) speed vs shape parameter for the full field of view 335x335 μm and a 5x5 truncation 67x67μm. Both field of view sizes show the same final average. All other truncation sizes give the same average values. Errorbars represent the standard deviation of 60 and 1500 fields respectively (c) comparison of the derivative in the linear portion of the curve in b, from $q = 3.93$ to $q = 3.97$. The value is larger for large fields of view because there can be greater heterogeneity within the same field of view. At lower values the linearity plateaus due to noise from averaging fewer cells. This shows that our data is consistent with energy which is defined at the single cell level. At $\approx 100\mu m$ or groups of a couple dozen cells we reach a noise floor. This analysis uses the TPV metric for cell shape to ensure there are enough cells within small fields of view to get a representative average. (d) Mean squared displacement for a dataset on a WT 2mg/ml collagen gel. Curves are binned according to the shape parameter at the initial time of each subtrajectory. Subtrajectories are not overlapping. Lag times are at 10 minute intervals. We observe that for any lag time there is lower displacement for lower shape parameter. (e) Shape parameter vs speed for a single field of view over 12 hours for different lag times. (f) Shape parameter vs speed averaged across all fields of view in the sample. We see that increasing the lag time shifts this curve downward consistent with the motion being diffusive. At longer times the distance traveled only increases by $\sqrt{t}$ as time increases by t leading to lower values of speed. The data appears to reach the noise floor at low shape parameter for larger tau.

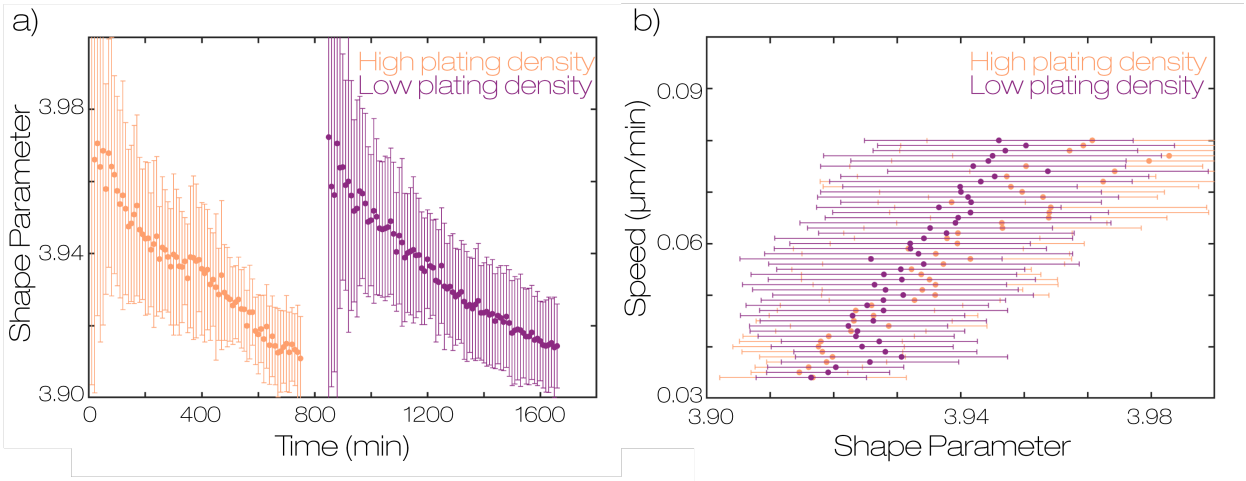

Figure 2.5: Monolayer remodeling does not depend on initial cell seeding density (a) Cell Shape vs time for monolayers seeded at two different densities. Both samples were made at the same time with ≈ 700K cells (high density) and ≈350k cells (low density). The samples were imaged sequentially starting from the time point when the monolayer became confluent across most of the cover slip. (b) Relationship between cell shape and speed for the samples in a).

applied by the cells. This model has two key parameters (Fig. 2.6A): a temperature T that represents via uncorrelated noise the magnitude of active stress fluctuations acting on each cell, and a parameter p_0 that represents the target perimeter of each cell and encodes the mechanical properties of a cell, including cell-cell adhesion and tension in the cortically enriched cytoskeleton. In steady state, these two parameters give rise to a predicted observed shape parameter and cell mobility ([24], [297]). Importantly, in isotropic tissues a shape parameter of approximately 3.8 reflects the onset of rigidity in the vertex model, whereby higher shape parameters reflect a more fluid-like tissue ([24], [356], [23]), although the exact location of the transition point depends on the degree of cell packing disorder ([352], [331]). We expect that the cells tune their active fluctuations and mechanical properties during monolayer remodeling, resulting in potentially time-dependent parameters $T(t)$ and $p_0(t)$ and different "trajectories" through model parameter space (Fig. 2.6B, 2.7A). Along these parameter trajectories we measure the resulting steady-state shape and speed of cells in simulations (Fig. 2.6C, 2.7B), which then can be compared to the experimental measurements.

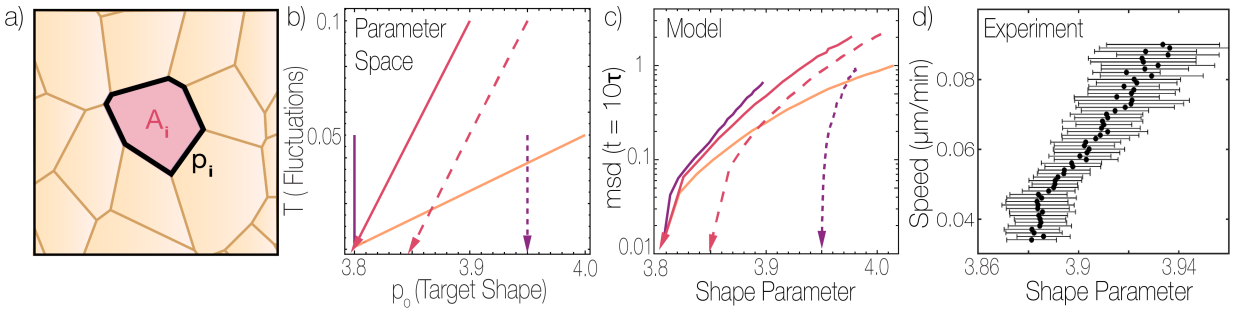

Figure 2.6: Active Vertex models predict a relationship between cell shape and speed during monolayer remodeling. (a) Schematic of the thermal Voronoi model, where each cell has a target geometry specified by a preferred perimeter p_0 and area a_0. Each cell is subject to Brownian noise with amplitude set by the temperature T. (b) Parameters of the thermal Voronoi model were varied along several representative curves. Along these curves a simulated monolayer was equilibrated at each point, after which measurements were made on the monolayer. Solid curves approach $T = 0$ at a value of p_0 where the tissue is weakly rigid, while dashed curves approach $T = 0$ at a value of p_0 where the tissue is floppy. Colors represent trajectories with different slopes. (c) Observed values of speed and cell shape. Line styles correspond to the equivalent parameter space trajectories shown in panel b). MSD is given in units of $\sqrt{CellArea}$ over a time window of 10 natural time units. Data are ensemble averages of 30 simulations each with $N = 1000$ cells. (d) Experimental relationship between cell shape and speed measured for WT dataset on $2mg/ml$ collagen matrix.

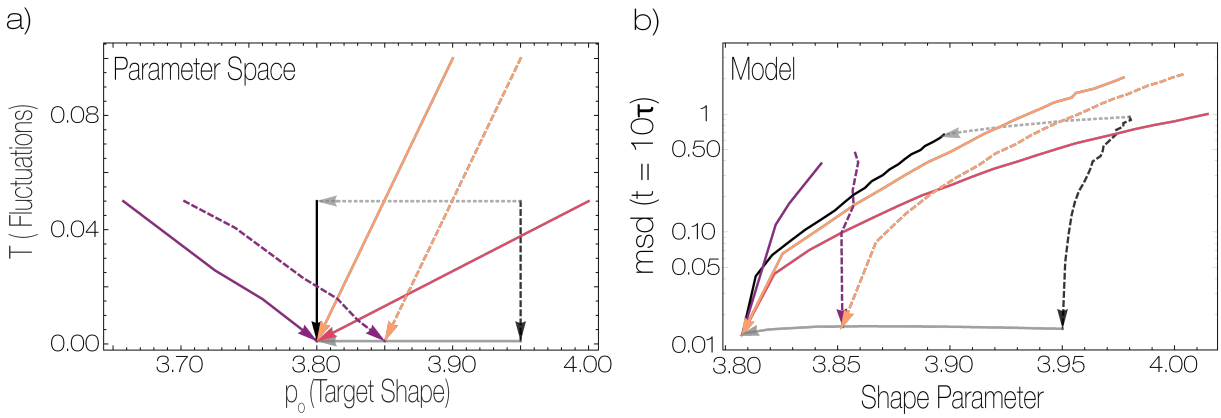

Figure 2.7: Additional modeling of relationship between cell shape and speed in Active Vertex models. (a) Parameters of the thermal Voroni model were varied along several representative curves. Along these curves a simulated monolayer was equilibrated at each point then measurements were made on the monolayer. Solid curves approach zero temperature at a value of p_0 where the tissue is rigid, while dashed curves approach $T = 0$ at a value of p_0 where the tissue is floppy. Colors represent trajectories with different slopes. Dashed lines indicated different values of p_0 approaching $T = 0$. Arrows indicate the order of simulations along a trajectory (c) Observed values of speed (quantified by MSD in a given time window) and shape corresponding to the parameter space trajectories shown in panel b). MSD is given in units of $\sqrt{CellArea}$ over a time window of 10 natural time units.

We find that substantially different trajectories through model parameter space can generate similar curves in a plot of typical cell displacements versus observed cell shape, as shown by all of the solid lines in Fig. 2.6B, C. This is a restatement of the result that, in vertex models, observed cell shape and cell motility are highly correlated ([231], [24]). In our experiments, we observe a similar relationship between shape and speed resembling these model trajectories (Fig. 2.6D), suggesting that vertex models may be able to predict features of remodeling in proliferating epithelial layers. Fig. 2.6B, C also highlights that there is an important exception: the observed shape-motility correlation and convergence breaks down when the temperature (i.e. active stress fluctuation) drops to zero while the cell mechanical stiffness encoded by p_0 is still in the floppy regime, with $p_0 > 3.8$ (See dashed lines in Fig. 2.6B). In this case, the "zero temperature" system stops moving, even though the underlying mechanics of the layer is floppy and weak. Since in the real monolayers active stress is generated by cellular processes, we explore these ideas further by considering how monolayer remodeling is impacted by perturbations to extracellular or intracellular pathways.

2.3.3 Monolayer remodeling is regulated by matrix stiffness and signaling pathways

The stiffness of the extracellular matrix (ECM) can alter cell migration rates through effects on focal adhesion dynamics and cell spreading ([318]). To explore how epithelial tissues are impacted by the physical properties of the ECM, we varied the underlying collagen gel stiffness and density by either increasing the concentration of collagen, or crosslinking gels with glutaraldehyde ([223]). This produced gels with Young's moduli ranging from approximately 200-2000 Pa ([166]). On all gels, qualitatively similar dynamics in cell shape, motion, and density are observed during monolayer remodeling (Fig. 2.8), but there are quantitative differences. For instance, at the onset of confluence when the cell speeds are large ($0.07 \mu m/min$), the cell density is $\approx 50\%$ lower on the stiffer ECM conditions than the

soft ones (Fig. 2.9A, B). These differences remain as the density increases and cell speed decreases during monolayer remodeling (Fig. 2.9A, B). Thus, across different matrix stiffness, the number density at which cell speed reaches its minimal value varies substantially (Fig. 2.9B). This is a strong indication that number density is not directly controlling the arrest of cell motion.

In contrast, the cell shapes robustly and reproducibly change during monolayer remodeling, with the arrest of cell motion occurring at a consistent shape parameter of 3.88 (Fig. 2.9C). Because our collagen gels only span a small range of stiffness, we performed similar experiments on stiffer polyacrylamide gels (16 kPa) and glass and observed similar results, suggesting that this behavior is independent of substrate stiffness across a large range (Fig. 2.10). Therefore, cell shape appears to be a robust parameter to predict dynamics and structure of monolayers formed atop different ECM stiffness, in agreement with vertex model simulations.

As demonstrated in the simulation results in Fig. 2.6B, C, these shape-velocity curves do not by themselves shed light on whether the arrested motion arises predominantly from changes in tissue mechanics or the magnitude of active stresses. An important exception is in regimes where the active fluctuations are driven towards zero while the underlying cell mechanics remains floppy – this scenario results in distinctly different paths through shape-velocity space (dashed lines in Fig. 2.6C).

To access different regimes of tissue mechanics and active stress generation, we performed a screen of pharmacological perturbations to cell signaling by treatments that altered focal adhesion, cell cycle, and Rho GTPase signaling. Across all conditions, we observe qualitatively similar monolayer remodeling dynamics that result in arrested cell motion with a characteristic cell shape and density (Fig. 2.8, 2.11). However, there are substantial quantitative changes that contrast with those found in Fig. 2.9. To illustrate, we consider the impact of fibroblast secreted growth factors by forming monolayers in fibroblast conditioned

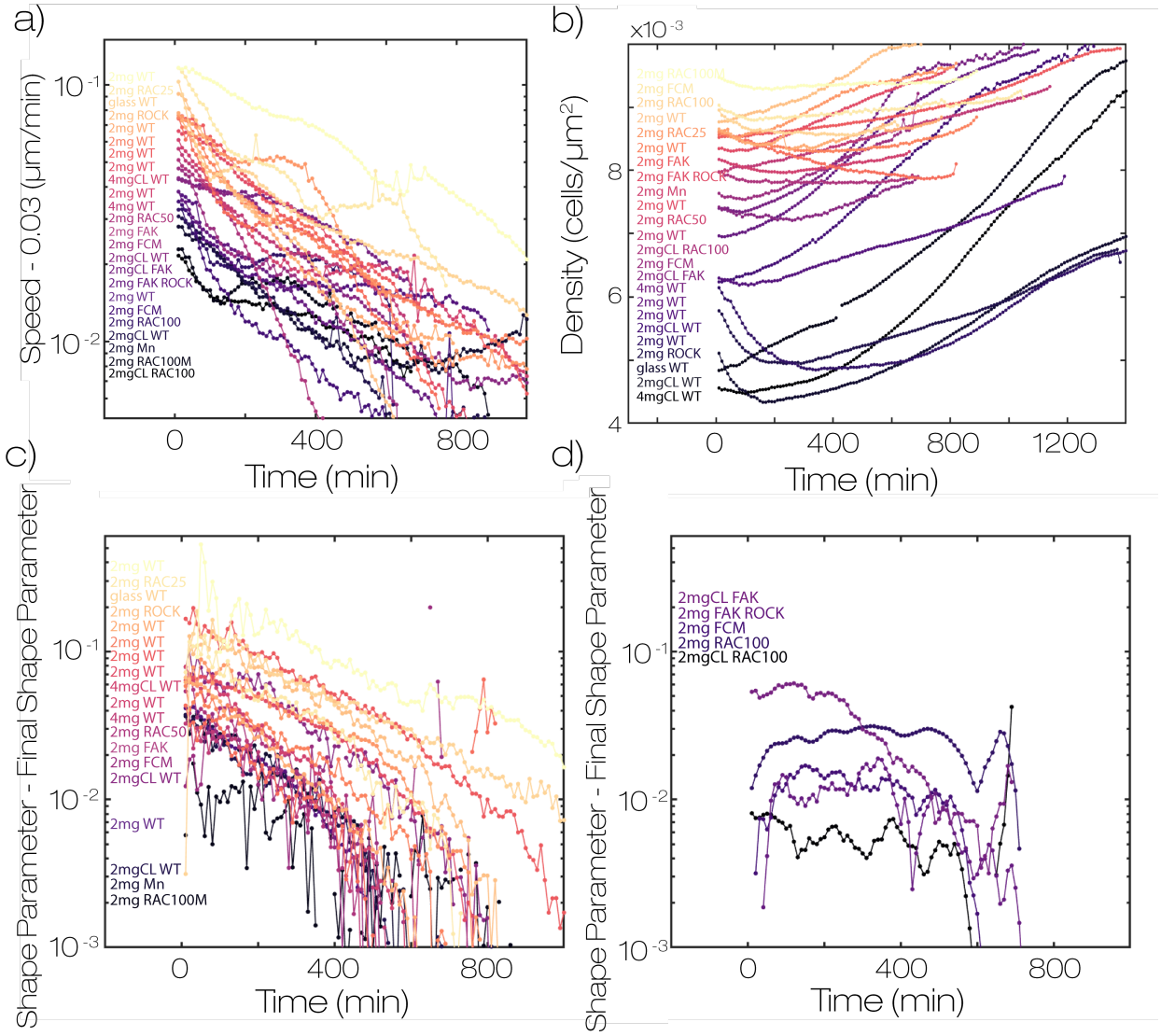

Figure 2.8: Shape, Speed and cell area decrease with time across all conditions (a) plot of speed vs time for all conditions. The final speed for all the time series plateau at 0.03μm/min so this value is subtracted from each time series. Curves are colored in order of speed at time = 0 min. The same color map is used in b, c (b) density vs time for all datasets. The data is colored by initial density and differs in color map from a-c. (c) plot of shape-final shape for all data. Each time series decays to the final shape with similar kinetics. (d) several datasets were too noisy and were moved to a different plot for clarity. These datasets were smoothed temporally with a 10-point window to reduce noise. These data slightly reduce in shape with time however the difference in initial and final shape are comparable to the noise in our measurement. All data points represent the time average of at least 30 fields of view in one sample.

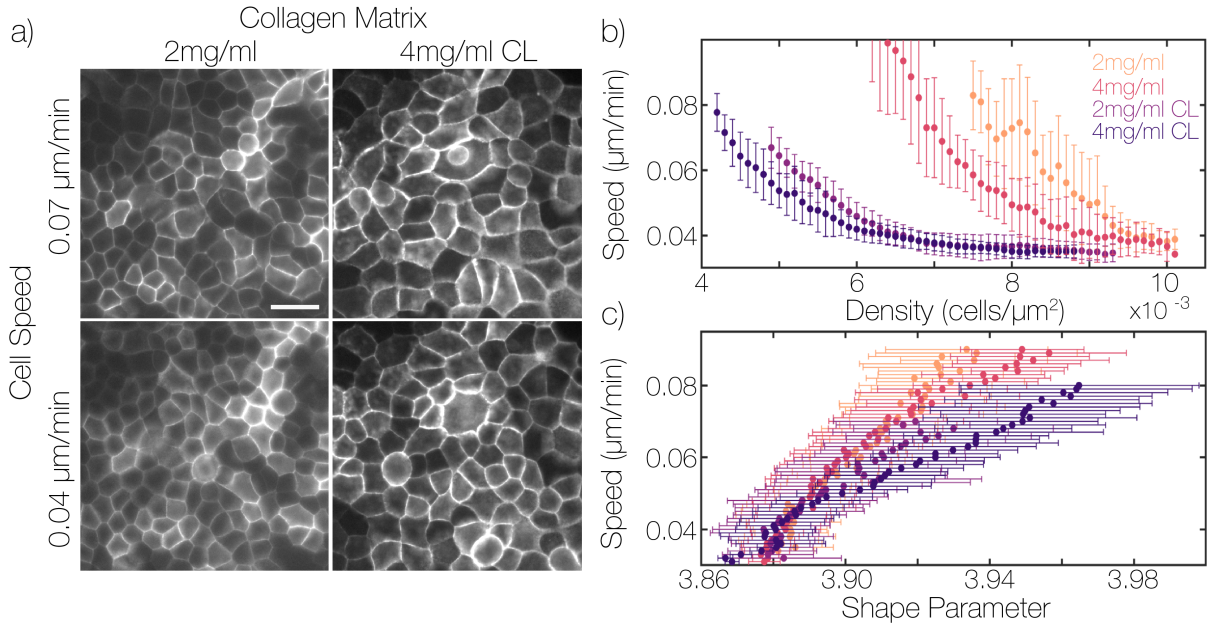

Figure 2.9: Monolayer remodeling is independent of cell density across perturbations to substrate stiffness. (a) Images of monolayers remodeling on substrates with different stiffness near the beginning and end of the experiment. CL is glutaraldehyde crosslinked collagen gel. Scale bar is 25 microns. (b) Correlation between cell speed and cell density for monolayers on substrates of different stiffness. (c) Correlation between cell speed and shape parameter for monolayers on different substrates. Quantities are averaged over a field of view containing at least several hundred cells for each time point, then field of view measurements are binned together by speed in 0.001 increments. Error bars represent standard deviation of each bin.

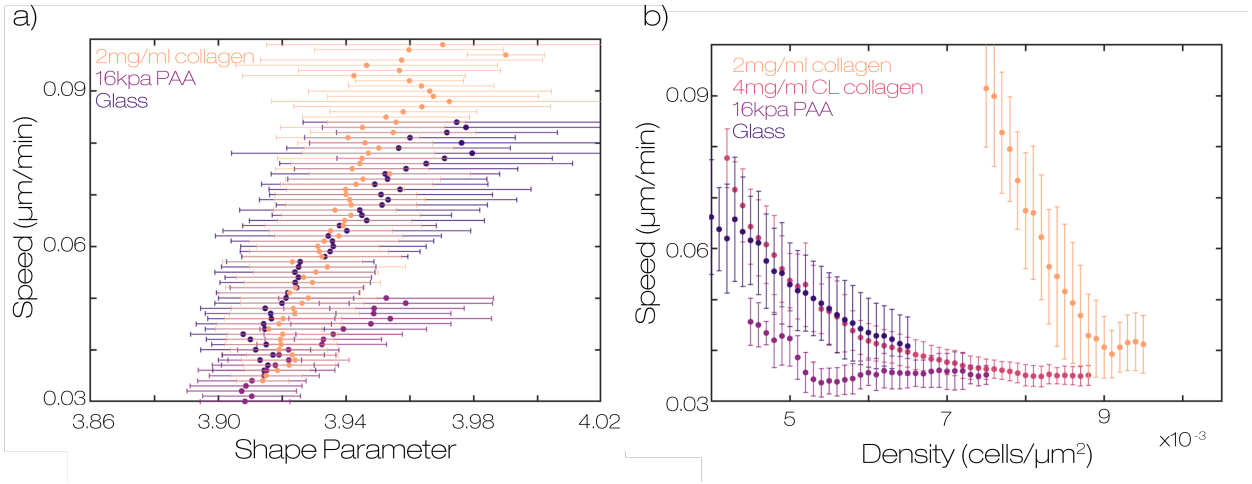

Figure 2.10: Relationship between cell shape and speed is independent of substrate stiffness (a) relationship between shape and speed on division rate matched conditions on collagen, 16KPa polyacrylamide, and Glass (b) relationship between speed and cell density on substrates with different stiffness. Error bars represent binned averages at each speed for at least 30 fields of view over at least 60 time points.

medium (FCM). We observe that the cell shapes in FCM-treated monolayers are more elongated, with a higher shape parameter, throughout the experiment (Fig. 2.12A). At the onset of cell motion arrest, the shape parameter is >3.94 a value much higher than the observed shape in control cells even many hours before arrest (Fig. 2.12B). This results in significantly higher values of shape parameters throughout monolayer remodeling (Fig. 2.12B). Across these perturbations, we consistently observe a correlation between the changes in shape parameter and cell speed but observe significant variations in the final shape parameters that occurs at cell motion arrest (Fig. 2.11, Fig. 2.13).

2.3.4 Cell division rates control cell shape remodeling

The diversity of monolayer architectures observed across all conditions is demonstrated by plotting the final shape parameters and density (Fig. 2.14A). With these perturbations, the steady state architecture varies two-fold in density, with cell shapes ranging from elongated to compact, but with no clear correlation between density and shape (Fig. 2.14A). However,

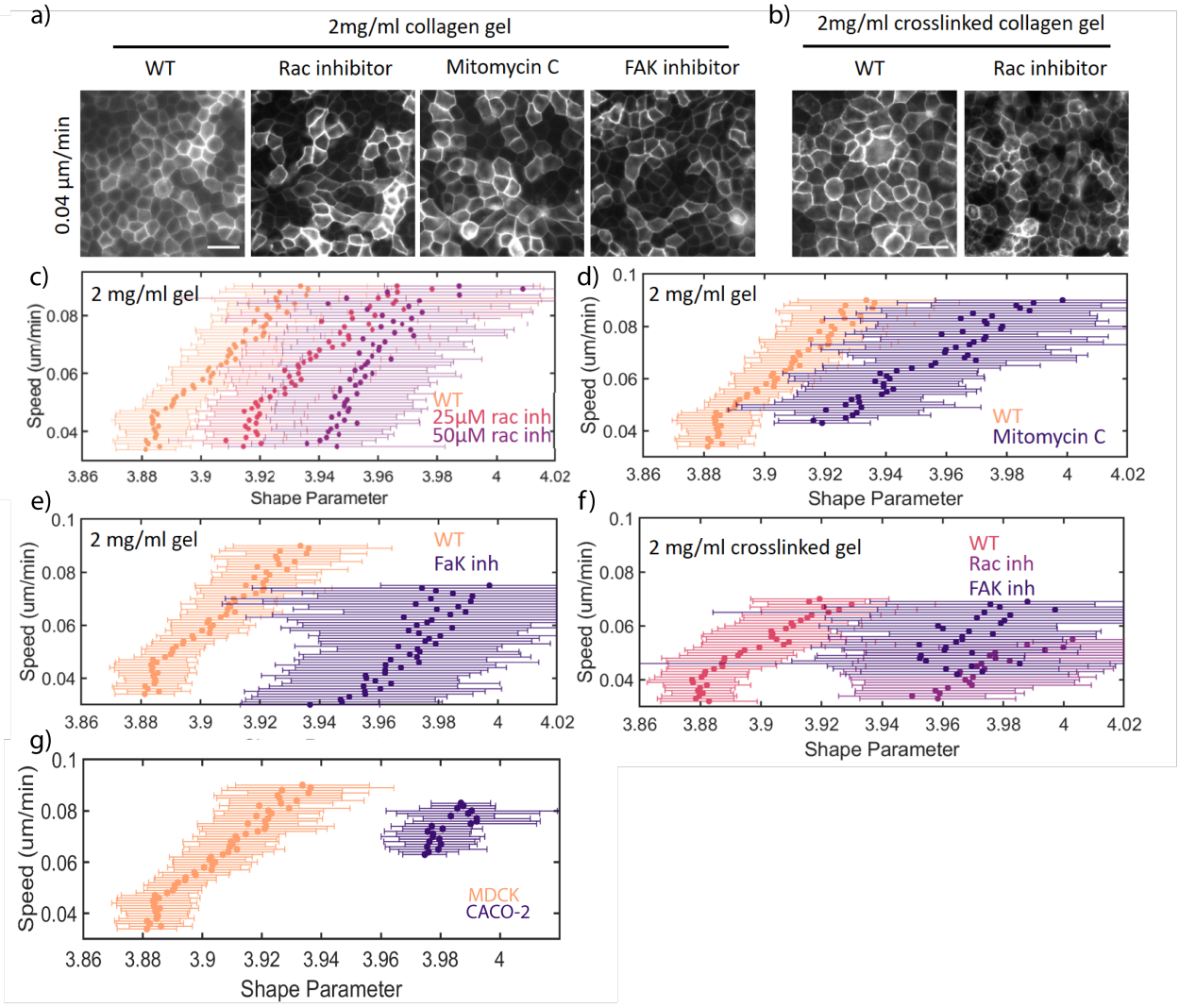

Figure 2.11: Shift in relationship between shape parameter and speed is qualitatively similar across conditions. (a) Representative images for several inhibitor conditions at low average speed. (b) Images on stiff substrates (c-e) Speed vs Shape parameter curves for different inhibitors. Similar shifting behavior is observed across these conditions. (f-g) Similar behavior is also observed on stiff substrates and for CACO-2 epithelial cells. Error bars represent binned averages at each speed for at least 30 fields of view over at least 60 time points.

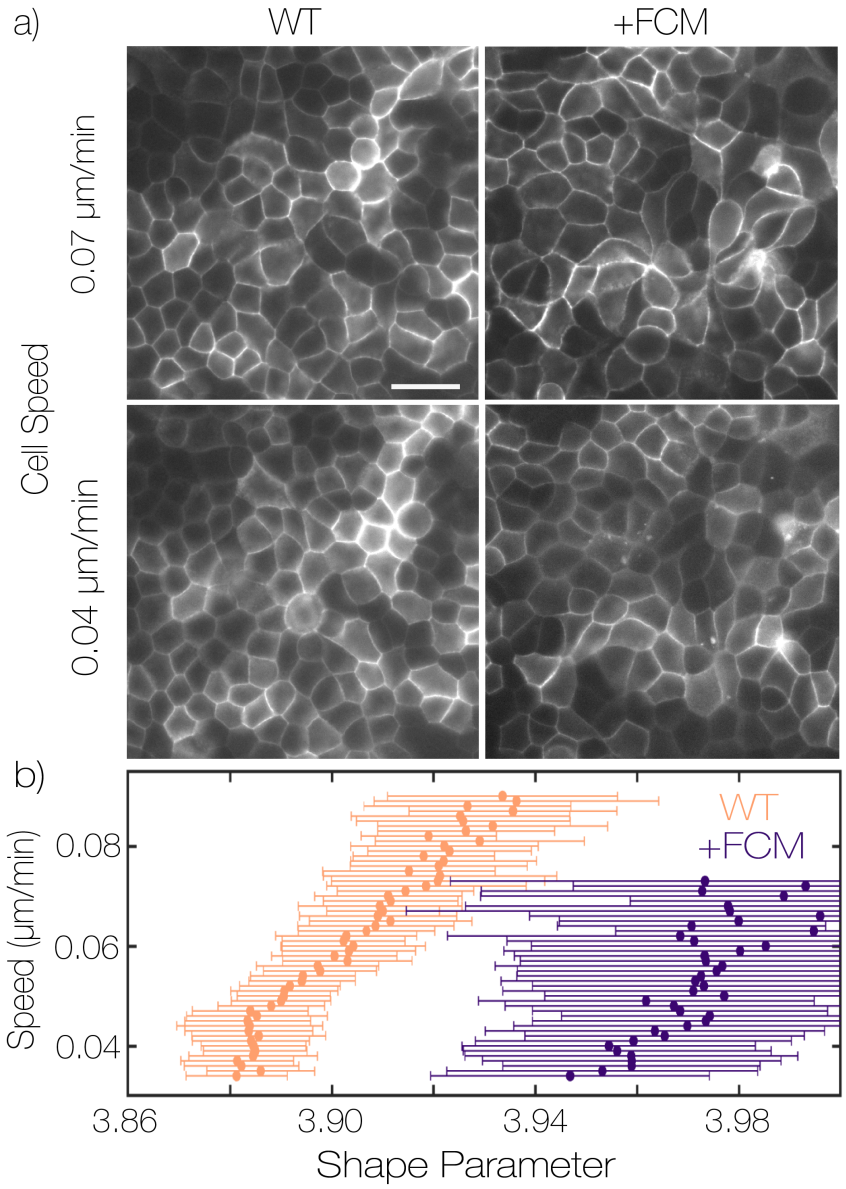

Figure 2.12: Intracellular signaling alters cell shape during monolayer remodeling (a) Images of monolayers at the beginning and end of a remodeling experiment under WT conditions or treated with 1:1 fibroblast conditioned medium to culture medium. Scale bar is 25 microns. (b) Correlation between speed and density for control and FCM treated monolayers. Quantities are averaged over a field of view containing at least several hundred cells for each time point, then field of view measurements are binned together by speed in 0.001 increments. Error bars represent standard deviation of each bin.

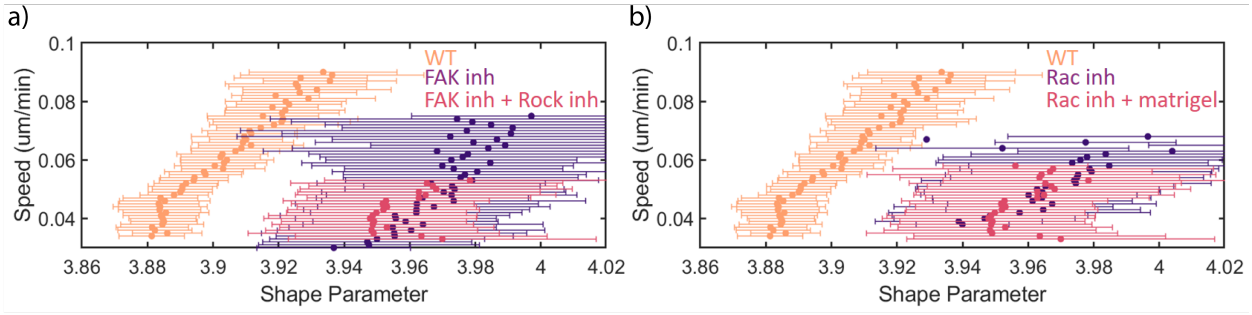

Figure 2.13: Rescue experiments do not restore shape speed correlation. (a) Comparison of shape speed correlation for cells treated with a FAK inhibitor and with the addition of a Rock inhibitor. Rock inhibition has been observed to rescue the polarity of 3D MDCK cultures with FAK knockdown. Rock inhibition has also been observed to restore collective motility in FAK knockdown cells (see discussion). (b) Comparison of shape speed correlation for cells treated with a RAC inhibitor on collagen gels and collagen gels with 1mg/ml matrigel. RAC is required for the assembly of laminin at the basal surface of 3D cultures of MDCK cells. The polarity defect of RAC knockdown cells can be rescued by providing laminin, a component of matrigel, in the substrate (see discussion). Neither experiment significantly restored the correlation between shape and speed. Error bars represent binned averages at each speed for at least 30 fields of view over at least 60 time points.

many perturbations reduced the rate of cell divisions (Fig. 2.8B). Plotting the final cell shape as a function of the cell division rate for all conditions reveals an inverse correlation (Fig. 2.14B). Monolayer remodeling obtained from another common epithelial model, CACO-2 cells, with a much lower cell division rate, can be overlaid on this data (Fig. 2.14B, 2.11G).

To explore how cell division impacts monolayer architecture, we first consider the direct consequences of cell division ([101], [77]). From purely geometric considerations, one would expect a local reduction in cell shape parameter as a result of topology and aspect-ratio changes after a division ([86], [101]). Further, oriented cell divisions can directly change cell shape by producing two daughter cells with lower aspect ratio ([346], [302]). To assess the contribution of division to the overall shape change, we analyzed shape change in individual cells in our segmentation data. We measured the shape changes of a dividing cell and its immediate neighbors before and after division, which we classify into three groups based on their contact relationship with the daughter cells (Fig. 2.14C). Similar to previous findings

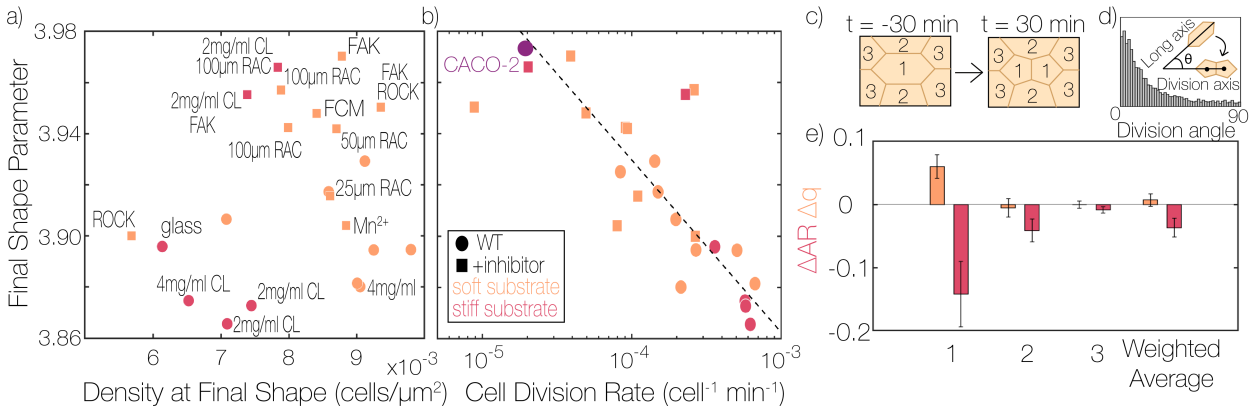

Figure 2.14: Cell shape remodeling is dependent on cell division rate (a) Shape parameter vs. density when the monolayer reaches a speed of 0.04μm/min for all inhibitor conditions tested. (b) Final shape parameter vs. the cell division rate from $t = 200$ min to $t = 600$ min for all conditions in a). Logarithmic fit to data is plotted at dashed line. Each data point in a) and b) are the average of > 10 time points after reaching the final shape from > 30 fields of view from one experiment. (c) Schematic of cell which may experience direct changes in geometry during cell division. 1 is the dividing cell, 2 is a neighbor of both daughter cells, 3 is a neighbor of one daughter cell (d) Histogram of measured angle between the cells interphase long axis and the division plane during WT experiments. ($n = 3137$ cell divisions) (e) Resulting changes in shape and aspect ratio for the dividing cells and neighbors adjacent to one or both cells are plotted. Error bars represent the standard deviation of three WT experiments on 2mg/ml collagen each with at least 1000 cell divisions measured.

([346], [28], [302]) we observe a strong alignment of cell division along the long axis (Fig. 2.14C,D). The division results in a reduction of the aspect ratio of the dividing cell but, on average, modestly increases the shape parameter (Fig. 2.14E, Group "1"). Furthermore, there is minimal change in the aspect ratio or shape parameter for neighboring groups of cells (Fig. 2.14E, Groups "2" and "3"). Considering the weighted average of all groups, the impact of cell division on shape parameter changes is negligible (Fig. 2.14E, "weighted average"). By tracking shape changes occurring in individual cells throughout interphase, we further verified that the direct effects of cell division are small compared to shape changes occurring through changes in cell junction length in non-dividing cells (Fig. 2.15, 2.16). Thus, local distortions and topological changes during cell division alone are insufficient to explain the contribution of cell division rate to monolayer remodeling.

Other sources of active stresses within monolayers include cell motility ([24], [356], [311]) and junctional remodeling ([59], [42]). Compared to other experiments (e.g. wound healing) which show speeds up to 0.7μm/min ([219]), the extent of cell motion in our experiments is low ($< 0.1\mu$m/min). One well-documented type of junctional remodeling that drives cell rearrangements is a T1 transition ([86]), which we observe in the monolayer (Fig. 2.17). However, the overall number of cell rearrangements is quite low. Therefore, we surmise that the dominant source of active stresses driving monolayer remodeling is junction length changes in the absence of neighbor exchanges.

2.3.5 Active stress originates from CDK1-dependent regulation of cell mechanics

Our pharmacological screen included many factors known to impact cell migration, adhesion and force generation, including perturbations to RAC, ROCK, FAK, and Integrin signaling pathways. Surprisingly, these perturbations had little impact on the overall motions within the monolayer Fig. 2.18). However, we did observe a dramatic and immediate decrease

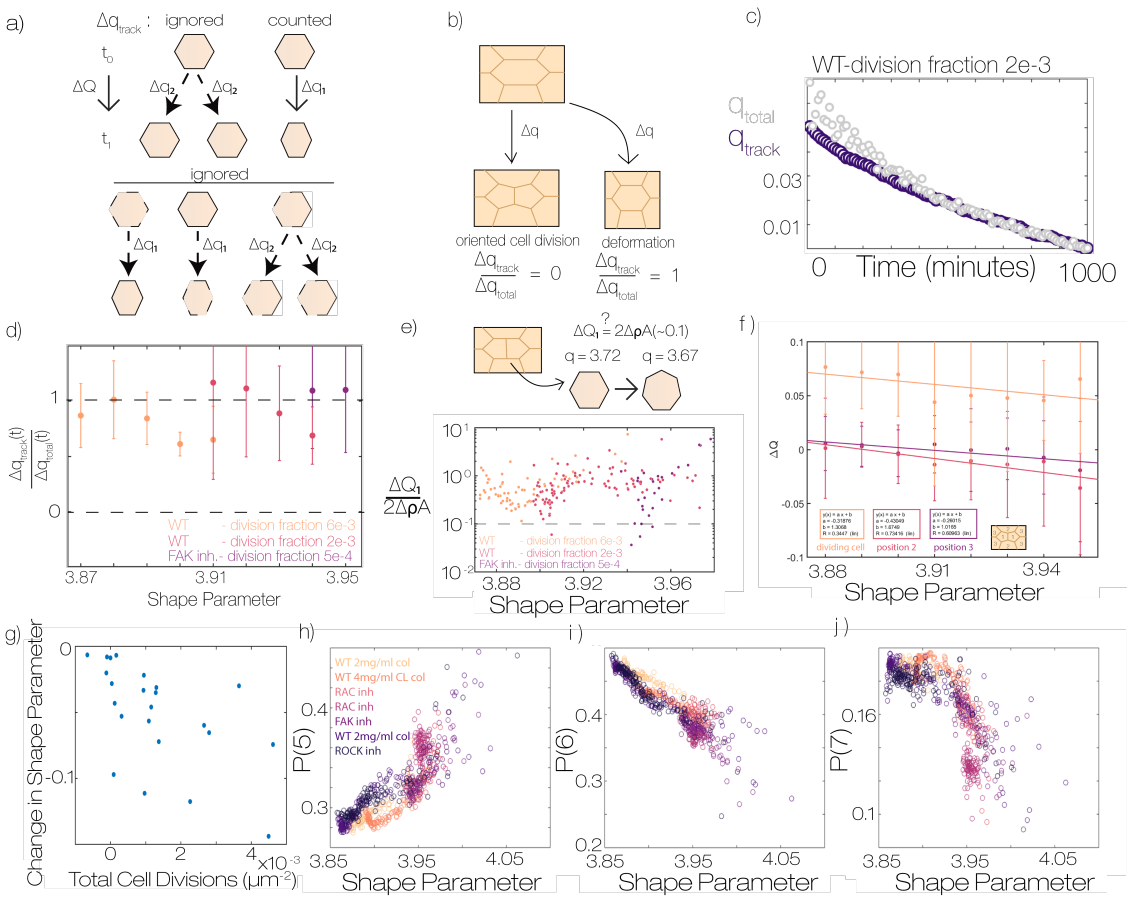

Figure 2.15: Oriented division is insufficient to explain differences in monolayer remodeling (a) Schematic of different modes of shape change – either shape changes during a cell division Q_2 or within a trajectory Q_1. There are additional q_1 type and q_2 type shape changes which are ignored by c_{qq}. (b) schematic of different sources of cell shape change and their relative values of q_{track} (c) for a single condition we plot q_{track} and q_{total} over time. We observe that for most of the experiment these metrics are the same. (d) ratio of q_{track} to q_{total} for three different conditions with variable division fraction noted in the legend. We observe in all cases that the ratio is close to 1 independent of cell shape. Error bars represent standard error of each bin. (e) The q_{track} metric has ignored the gain of neighbors for cells adjacent to division. We show that the value of q_{track} is several fold larger than this effect. Points represent time averaged values for at least 50 fields of view (f) average shape change per cell division from division tracking data as a function of the average cell shape. We observe larger decreases in cell shape when for the mother cell and neighbors when average cell shape parameter is large. Error bars represent standard deviation of divisions in each bin (h) plot of total cell division vs total shape change. If cell divisions cause all shape change, we would expect a strong correlation between these variables. Each point represents a different condition from Fig. 2.14A. (g-h) relationship between shape parameter and the fraction of cells with either 5,6, or 7 neighbors for different conditions. Across these conditions we observe a common relationship between the topology of the monolayer and the shape parameter.

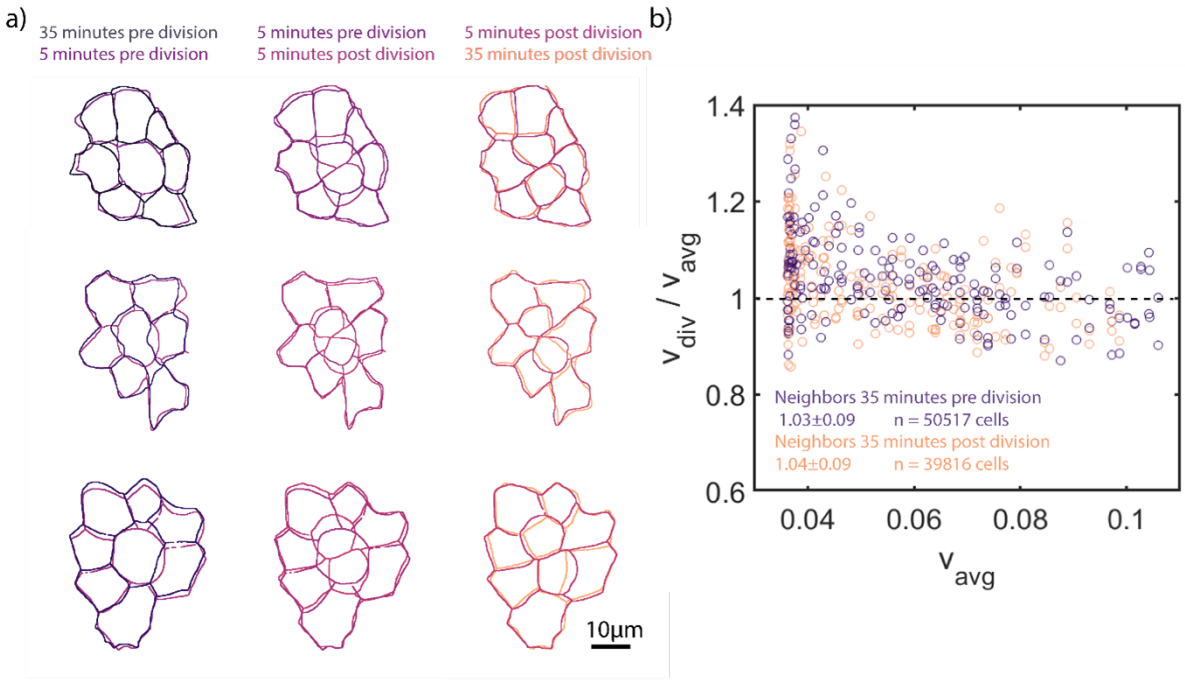

Figure 2.16: Cell divisions do not produce large deformations of the monolayer (a) representative outlines of dividing cells in the monolayer during mitotic rounding, cytokinesis and reintegration of daughter cells into the monolayer. (b) Measurement of neighbor cell speed before and after cell divisions. All cells adjacent to a detected cell division are averaged for a given time point and compared to the average cell speed at that time point. Cell speed is the displacement of cells over a 10 minute lag time.

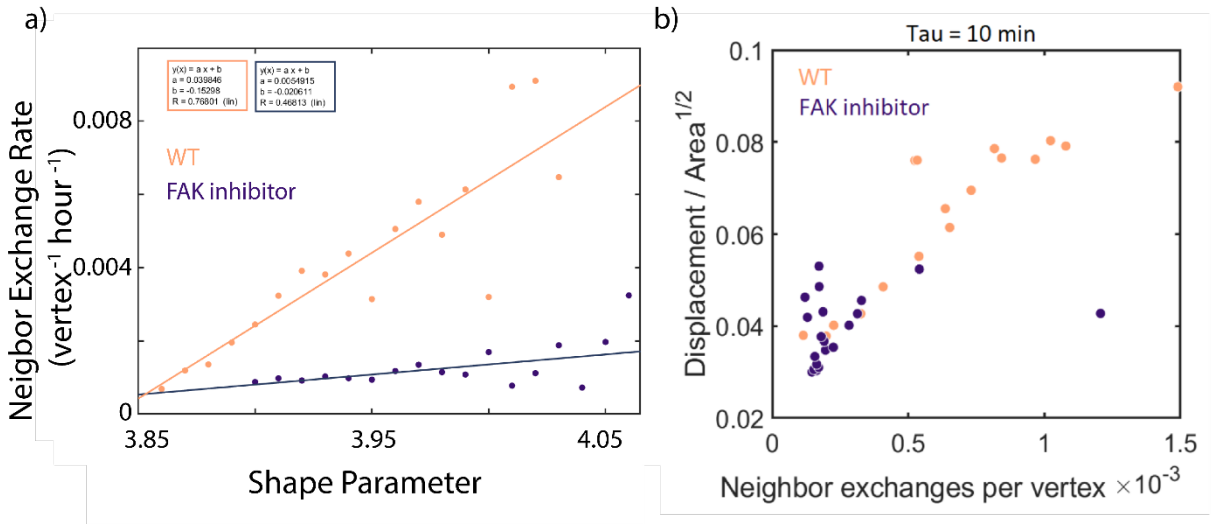

Figure 2.17: Neighbor exchange rates depend on shape and cell division rates (a) Neighbor exchange rate vs shape for WT and FAK inhibited cells on 2mg/ml collagen gels. Neighbor exchanges were counted by identifying 4 fold vertices in the data. A 4-fold vertex represents an unstable configuration in the system and therefore will either resolve in the opposite direction it was formed (successful exchange) or back in the same direction (failed neighbor exchange). Our method does not differentiate the two types of neighbor exchange. Each point is the ratio of four fold to three fold vertices detected at the given average shape parameter across at least 50 fields of view and 80 time points in each condition. (b) relationship between neighbor exchange rates and measured cell speed for data points in a

in cell speed upon perfusion of an inhibitor of cyclin dependent kinase 1 (CDK1), which blocks the cell cycle. After initiating a monolayer remodeling experiment, CDK1 inhibitor-containing media was perfused in at $t = 310$ min. We observed a striking reduction in cell motion within 20 minutes of inhibiting CDK1 (Fig. 2.19A-C). After washing out the inhibitor at $t = 580$ min, there was an immediate recovery of cell motion: remodeling was re-initiated, and the time-evolution of changes in cell shape and speed were similar to those initially observed (Fig. 2.19A-C). To quantitatively compare these curves, we shifted the post-washout shape parameter data by rescaling the time to $(t - 400$ min); this delay time and rescaling is indicated by dashed lines Fig. 2.19C,D. Remarkably, with this rescaling the data evolve in almost quantitative agreement with each other and, moreover, are comparable to the evolution of unperturbed wild type monolayers (Fig. 2.19D). This data is consistent with the hypothesis that CDK1 inhibition dramatically reduces the active stress fluctuations (T, in the model). The enhanced motion observed upon inhibitor removal underscores that tuning cell cycle dynamics may be a means to modulate the active stresses.

As an alternate means to arrest the cell cycle, we used mitomycin C to abrogate DNA replication, and observed a similar arrest of monolayer movement. Interestingly, inhibition of cell division by low doses of nocodazole does not reduce cell motion significantly. Nocodazole allows cells to enter mitosis and initiate mitotic rounding, but prevents further progression of mitosis. This is consistent with our data that cell division, per say, is not the primary source of stress in the monolayer (Fig. 2.16). Instead, these stresses arise in the interphase portion of the cell cycle. Together with our characterizations of cell shape changes, we surmise these may come from cell cycle dependent effects on cell mechanics ([135], [323]).

To test this, we examined the geometry of cell-cell contacts formed by suspended cell-doublets. As demonstrated previously ([195]), this contact angle θ can be related to the balance between tension of the cell-cell interface ($F_{cell-cell}$) and cortex (F_{cortex}) (Fig. 2.19E). We first measured the contact angle under both WT and CDK1 inhibitor treatment and no-

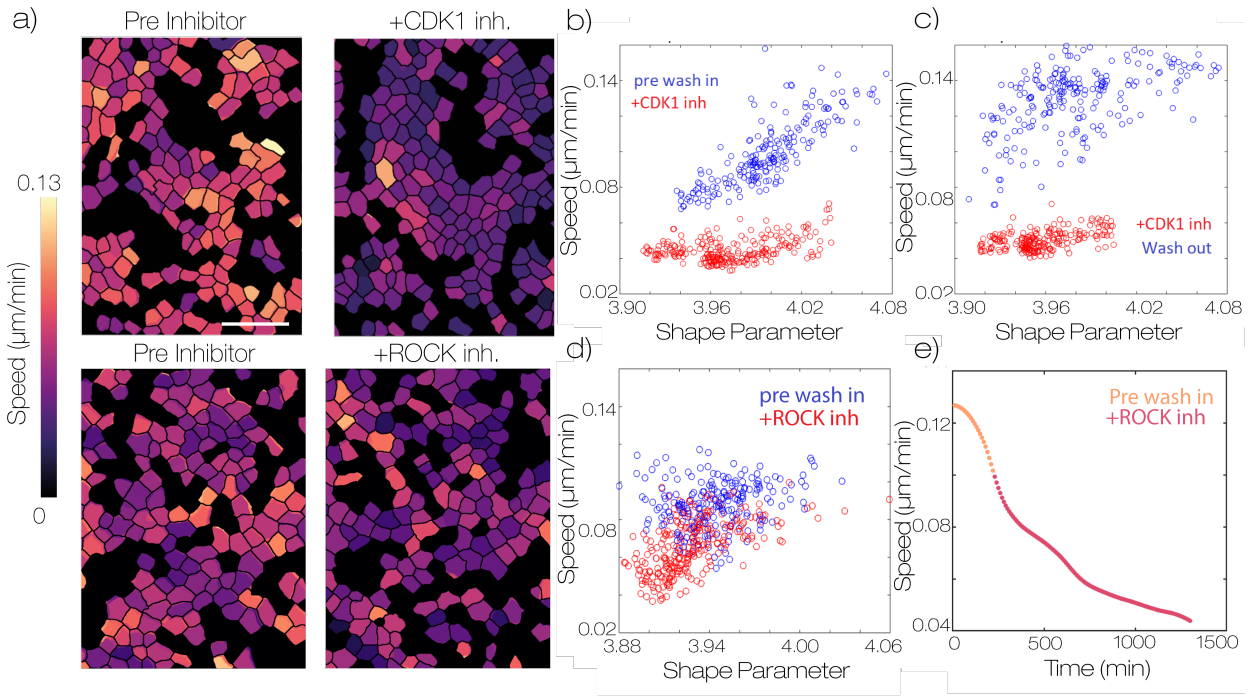

Figure 2.18: Inhibition of ROCK does not lead to large reduction in cell motility (a) representative maps of cell speed before and after adding inhibitors of CDK1 (5μM RO-3306) and ROCK (20 μM y27632). Scale bar is 50 microns (b) measurements of cell shape vs speed for each field of view 100 minutes before and after adding the CDK1 inhibitor (c) measurements of cell shape vs speed for each field of view 100 minutes before and after washing out the CDK1 inhibitor (d) measurements of cell shape vs speed for each field of view 100 minutes before and after adding the ROCK inhibitor (e) plot of average cell speed vs time for samples treated with ROCK inhibitor.

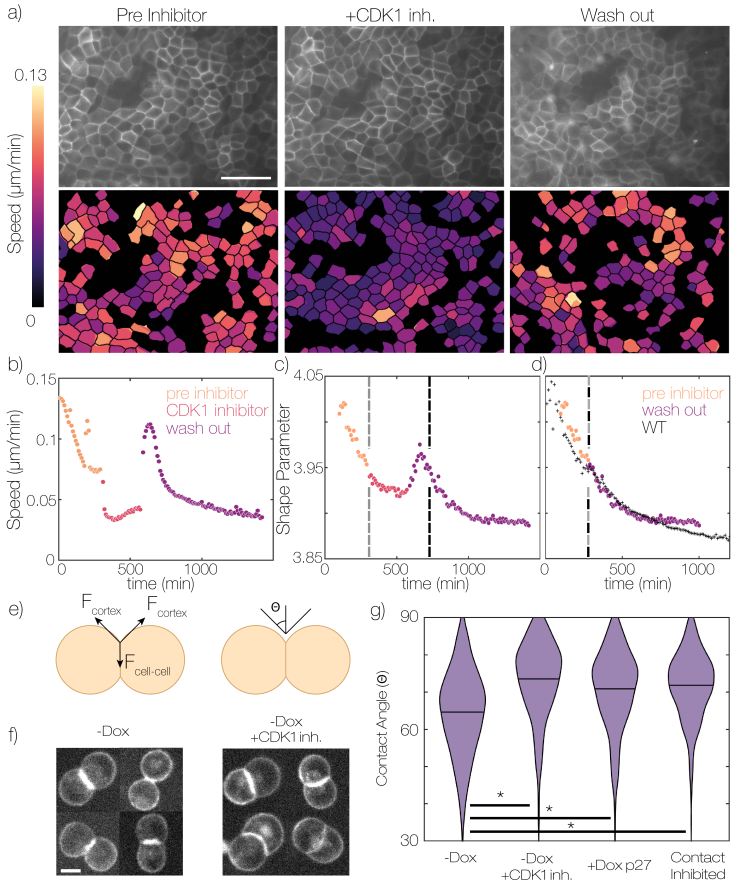

Figure 2.19: Cell division is a source of active stress required for monolayer remodeling. (a) Representative field of view of monolayer during CDK1 inhibitor wash in experiment. Below each image heat maps of cell speed for successfully segmented cells are displayed. Pre inhibitor is 30 minutes before adding the inhibitor. Inhibitor is 30 minutes after adding the inhibitor. Wash out is 120 minutes after washing out the inhibitor. Scale bar is 50 microns. (b) Average cell speed vs time during CDK1 inhibitor wash in experiment. (c) Average cell shape vs time during CDK1 inhibitor wash in experiments. (d) Time shifted shape vs time curves comparing WT and CDK1 inhibitor wash in data. CDK1 inhibitor wash in data points represent the time average of 12 fields of view in one sample. WT data represents the average of 3 independent experiments each with $>$ 20 fields of view. CDK1 inhibitor is 5μM RO-3306. (e) Schematic of cell contact angle measurements. Force balance at the contact gives rise to a contact angle θ. (f) representative images of MDCK cell doublets in suspension, in the presence and absence of CDK1 inhibitor 5μM RO-3306. Scale bar is 10 μm. (g) Measurement of MDCK tet-p27 cell contact angles under different conditions. -Dox – cells without doxycycline, +CDK1 inh. – 5μM Ro-3306, -Dox p27 – 200ng/ml doxycycline, Contact inhibited – Cells cultured to high density before re-suspension, no doxycycline added. -Dox $n = 512$, -Dox +CDK1 inh. $n = 480$, +Dox p27 $n = 394$, Contact inhibited $n = 565$. Data come from at 3 experimental replicates. $*p < 0.001$.

ticed a significant increase in the cell contact angles when CDK1 was inhibited (Fig. 2.19G). To explore whether increased tension at cell-cell contacts is observed by other means of cell cycle arrest, we overexpressed p27kip , a protein which binds and inactivates cyclin-dependent kinases, to arrest the cell cycle that is expressed during contact inhibition ([48]). To isolate CDK-dependent effects, we used a variant of the protein which lacks a c-terminal domain known to interact with RhoA ([244], [21]). Cell pairs over-expressing p27kip also had increased contact angles, compared to WT conditions. Finally, we measured contact angles of cells obtained from dense contact-inhibited cultures similar to the conditions at the end of monolayer remodeling experiments, and observed an increase in contact angle (Fig. 2.19G). Thus, all of this data demonstrates a cell cycle-dependence of the force balance at the cell-cell interface relative to the cortex. Together with effects of CDK1 inhibition on monolayer remodeling (Fig. 2.19A-D), these data strongly suggest that cell-cycle dependencies in junctional tension are a primary source of active stress that drives monolayer remodeling.

2.3.6 Cell cycle arrest leads to low fluctuation arrest of motility in the monolayer

To capture cell-cycle-dependent junctional tension in the vertex model, we built upon previous work that considered the consequences of system-wide fluctuations in interfacial tension ([351]). Here, we simulate systems where only a subset of edges, which we term "active edges", generate fluctuating interfacial tension with a characteristic persistence time scale, τ (Fig. 2.20A) ([351]). At the beginning of these simulations all edges are active, and the fraction of active edges, ϕ , is reduced from 1 to 0 over the course of a simulation. This emulates the effect of varying the fraction of cell-cycle-arrested cells in the monolayer (Fig. 2.20A). Concretely, we randomly select an active edge every τ^R natural time units and permanently eliminate the fluctuation of the edge. We observe that as ϕ decreases the average cell speed diminishes (Fig. 7b). Notably, this parametric plot of speed vs. active edges is nearly inde-

pendent of the tissue-stiffness parameter p_0 (Fig. 2.20B). To compare this to experiments, we used the pip degron Fluorescent Ubiquitin Cell Cycle Indicator (pip-FUCCI) system to directly monitor cell cycle progression during epithelial remodeling ([107]). Similar to previous results we see that the fraction of cells in later stages of the cell cycle (S, G2) decreases with time as the cells experience contact inhibition of proliferation (Fig. 2.20C) ([48], [290]). When the cell speed is plotted as a function of the fraction of cells which are early in the cell cycle or exited from the cell cycle (G1/G0), we see that an increasing fraction of such cells correlates with a decrease in overall cell motility (Fig. 2.20D), similar to the simulation results.

To place this simulation data within a broader framework for cell arrest, we plot the speed versus cell shape for $p_0 = 3.7 - 4.0$. As expected from the homogeneously fluctuation Voronoi model results (Fig. 2.6), as the fraction of active edges decreases, the speed decreases and the shape parameter approaches p_0 (Fig. 2.21). Along these curves cell motion arrests at a shape parameter approximately equal to the target shape index p_0, with very little dependence on τ^R . Moreover, the qualitative shapes of these curves over a range of p_0 show little sensitivity to the value of p_0 and resemble the experimental data (Fig. 2.20E). We conclude that at later times in experiments, the cell cycle arrests due to contact inhibition. This leads to a reduction of active stress and the monolayer motility arrests in a "low fluctuation" regime (Fig. 2.20F). This transition to a low fluctuation regime contrasts with the fluid-solid jamming transition ([231], [24], [8]). In contrast to the presently proposed scenario, in a jamming transition cell motion would arrest even as large fluctuations in active stresses persist (Fig. 2.20F). These different scenarios present two distinct paths for controlling cell shape and movement in epithelial tissue.

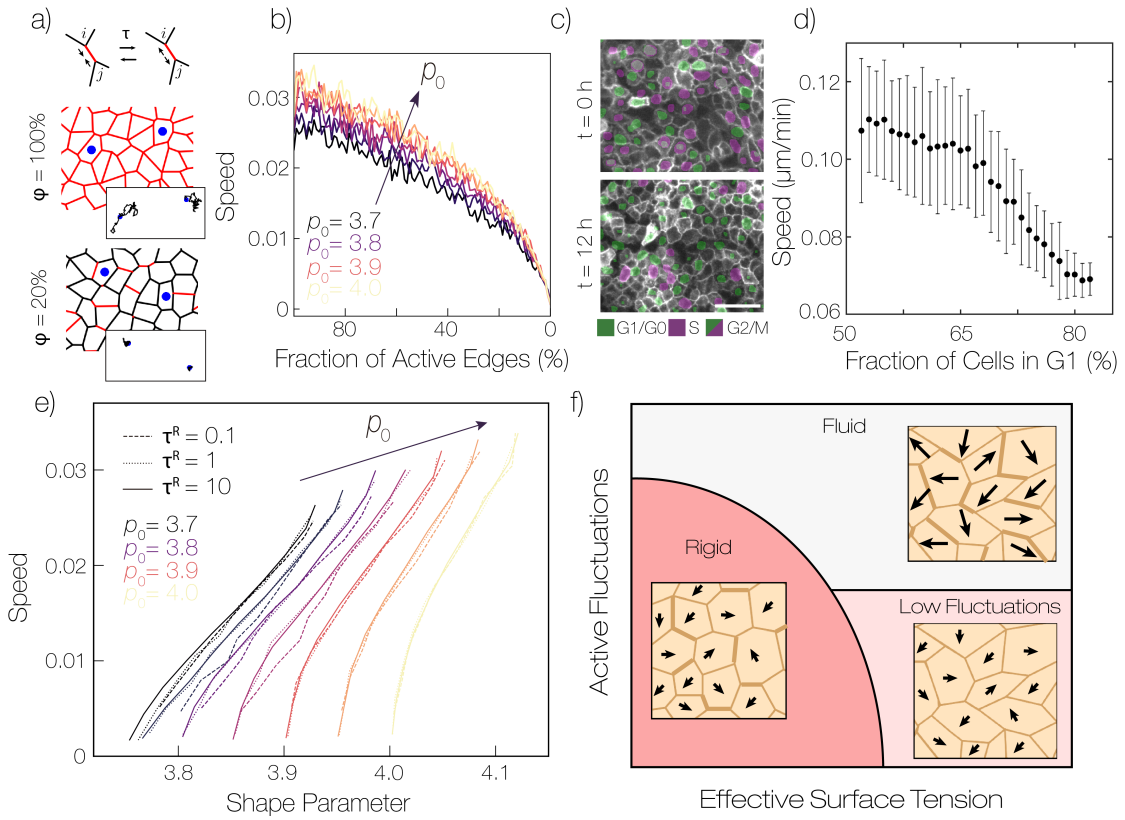

Figure 2.20: Active Edges as a Source of Stress in Epithelial Tissue (a) Schematic of vertex model with junction tension fluctuations. A fluctuating additional tension is applied between junctions i and j. The fluctuations can be either contractile or extensile, and have a characteristic persistence time τ^R See the methods for values of all simulation parameters used). Snapshots of cellular configuration at $\phi = 100\%$ and 20% are also shown, respectively ($\tau^R = 1$). (b) Plot of cell speed vs the fraction of active edges in simulated vertex models with fluctuating edge tension ($\tau^R = 1$). Different curves represent different values of the target shape parameter p_0 . (c) Images of MDCK monolayers with cell cycle information extracted from pip-FUCCI biosensor. Images from the individual biosensor channels are segmented and overlaid in pseudocolors green (PIP-Venus) and purple (Geminin-mCherry). Presence of only green indicates G1/G0 phase, only purple indicates S phase, and both makers indicates G2/M phase. (d) plot of cell speed against fraction of cells in G1/G0 phase of the cell cycle. Error bars represent standard deviation between 30 fields of view. (e) Plot of cell speed vs shape parameter from simulations. Curves represent different values of τ^R (dashed, dotted lines) and the target shape parameter p_0 (color scale). (f) Schematic phase diagram of epithelial arrest, where edge thickness represents the magnitude of tension on an edge and arrows represent cell displacements.. In addition to fluid and jammed phases which occur at different cell shapes, monolayers can arrest at high average cell shape parameter, indicating a low fluctuation regime. In this low fluctuation regime, the magnitudes of active fluctuations are too small to produce large cell displacements and frequent neighbor rearrangements.

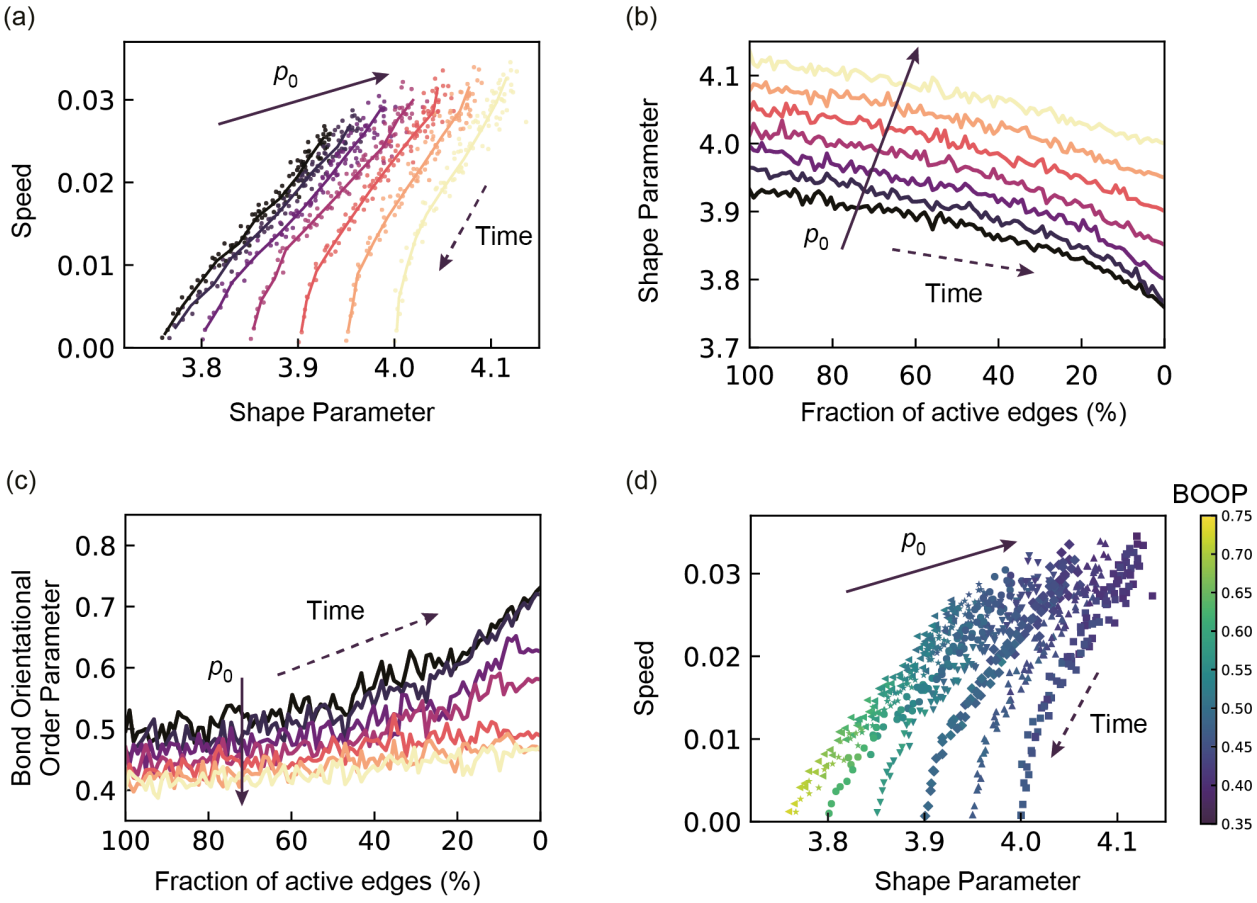

Figure 2.21: Time-evolution of the average cellular speed, the average shape parameter and the bond orientational order parameter (BOOP) for different shape indices, p_0, with $\tau^R = 1$ (a) The average cellular speed is plotted against the average shape parameter. The curves are obtained by smoothing the data points. (b) The average shape parameter is plotted against the fraction of active edges. (c) The BOOP is plotted against the fraction of active edges. (d) The average cellular speed is plotted against the average shape parameter with the color mapping the value of the BOOP. The color is mapped as shown in the color bar. In (a-c),$p_0 = [3.70, 3.75, 3.80, 3.85, 3.90, 3.95, 4.0]$ from dark color to light color. In (d), the data for each p_0 is respectively represented by left-pointing triangle (3.70), star (3,75), filled circle (3.80), down-pointing triangle (3.85), diamond (3.90), up-pointing triangle (3.95) and square (4.00) symbols. In (a-d), the direction of time is indicated by dashed arrows.

2.4 Discussion

The mechanisms that regulate epithelial architecture are central to understanding tissue morphogenesis in development, maintenance, and disease. While cell proliferation results in direct changes in topology ([101], [77]), this does not account for the shape remodeling we observe. In recent years, the development of mechanical models of tissue as active soft materials has provided predictive power to relate local cell mobility and shape. The vertex model predicts that cell motion arrests as cell shapes approach a value that is a sharp rigidity transition, independent of cell density ([24], [23]). Our data of epithelial remodeling atop matrices with varied stiffness are largely consistent with this model. As the remodeling proceeds, there is 2-fold variation in the monolayer density, but all data collapse on to a "universal" curve of the cell speed as a function of shape parameter. Moreover, the shape parameter at the onset of arrest is 3.88, which is within the range of transition points predicted by vertex models ([331]). Several previous studied have illustrated the potential of a jamming framework for understanding motion arrest in epithelia ([231], [208], [96], [13], [187]). However, to the best of our knowledge our data is the first to systematically challenge model epithelia with perturbations to demonstrate the robustness of the speed-shape parameter correlation. Importantly, our data strongly supports the utility of cell shape, rather than density, as an order parameter to assert the arrest of cell movement and local epithelial tissue mechanics.

Our data from perturbed systems, however, does not show arrested cell motion at a shape at the predicted jamming transition. Across myriad of pharmacological stimulations and perturbations to signaling pathways, cell motion is arrested even at larger shape parameters and over a wide range of densities. After observing that CDK inhibition immediately arrests the monolayer, we explored the possibility of reducing fluctuations in the monolayer as cells arrest the cell cycle via contact inhibition. In these simulations the monolayer can be arrested at various cell shapes as the fluctuations are reduced. In these conditions arrest occurs at

cell shape approximately equal to the model target shape parameter p_0; observing changes in the shape-speed curves corresponds to changing the underlying mechanical properties of the cells. By exploring predictions of the vertex model simulations, a likely possibility is that the effects of these perturbations on active stress are also coupled to changes in the preferred cell shape. However, it may be that additional active-stress-dependent effects on junction remodeling are not captured by our vertex model.

In the fluid regime, the standard vertex model rapidly equilibrates at low temperatures and, at $T = 0$, the final observed and target shape are the same. In such models, perturbations that affect the final shape of cells result in tissues with vastly different mechanical responses. Specifically, these models predict that tissues that arrest due to jamming with target cell shape parameters close to or below 3.8 would be stiffer and less sensitive to small mechanical perturbations than those that arrest due to a decrease in active stress while remaining floppy, with target cell shape parameters significantly above 3.8. Thus, while previous work attributed the arrest of epithelial monolayers to a rigidity transition dependent on density ([8], [245]) or mechanics ([231], [23], [13]) our work suggests that arrest can also occur because of a reduction in active stress. Mechanical measurements of epithelia will be required to probe the energy landscape in detail and understand the differences between these scenarios.

In addition, standard vertex models may be too simple to capture the mechanical response in the limit of small active stresses. Recent experiments suggest the existence of dynamic energy barriers, which may prevent equilibration over experimental time scales, arising from junctional stability ([299], [47]) and/or remodeling ([41]). In this scenario small but finite fluctuations would not be sufficient to cross those dynamic energy barriers, and so the tissue "freezes" into a metastable state. Thus, a reduction of active stresses could quench the tissue into an arrested state of lower, but non-zero, rigidity. Further work is needed to explore how energetic barriers in remodeling can be exploited for control over tissue mechanics.

The epithelial remodeling we observe is primarily driven by individual junctional length changes, with little contribution from neighbor exchanges or cell division. The limited number of neighbor exchanges observed distinguishes this remodeling from the highly fluid-like behavior observed in other scenarios ([59], [214]). We find that cell-cycle regulation is the primary source of active stress driving monolayer remodeling. The wide variation in observed shapes across perturbations can be understood by considering their impact on cell proliferation rate. Perturbations that decrease proliferation rate result in motion arrest at higher shape parameters. Moreover, CDK1 inhibition immediately abrogates movement and further epithelial remodeling. While previous data has implicated the importance of mitotic rounding as a source of stress ([74], [239], [249]) we do not observe large local distortions (Fig. 2.16). Therefore, we have demonstrated a role for an active stress generated during interphase or potentially through non cell autonomous behaviors. Cell cycle dependent processes which impact cell adhesion ([135]), junction tension and cortical mechanics ([323], [56]) all could give rise to the active stress generation during interphase. Disentangling these effects will be an interesting avenue for future research on cell shape remodeling in epithelia.

Cell proliferation rates can vary widely across different tissues, e.g., the intestine can be entirely replaced on the timescale of days to weeks while the skin may turnover on the timescale of months ([125]). Moreover, epithelial turnover can be upregulated in response to external stimuli and tissue damage ([178], [108], [241]). Regulation of cell division rates under these different circumstances may be a way for the epithelium to tune fluidity and facilitate repair. The extent to which cell turnover rate is used to regulate epithelial fluidity and architecture *in vivo* will be an interesting line of future research. Numerous recent studies have identified a role for cell division in driving morphogenetic processes ([90], [239], [263], [103]). Our data suggests a mechanism for the increased fluidity observed in highly proliferative tissues through an increase in active stress generation. Measurements of cell shape and motility in these different contexts are required to determine if they are similarly

driven by cell cycle-dependent active stress and to discover new mechanisms driving epithelial organization. Further understanding of the interplay between cell cycle, tissue mechanics and cell shape remodeling may lead to a more comprehensive understanding of tissue function in development, homeostasis and disease.

2.5 Materials and methods

MDCK cells were cultured under standard conditions in DMEM with 10% FBS at 37C and 5% CO_2. Cell monolayers were prepared on by seeding approximately 6×10^5 MDCK cells on a $500mm^2$ collagen gel substrate overnight. Collagen gels were prepared by polymerizing a neutral collagen solution on silane-glutaraldehye modified glass substrates for 1 hour. Cells were imaged by widefield fluorescence microscopy using standard filter sets. We imaged many locations in the monolayer and verified that they show qualitatively similar behavior (Fig. 2.22) Image segmentation, cell tracking and cell division detection were done using custom MATLAB code based on previous methods ([63], [12]) . By tracking fixed monolayers we found that the tracking errors are small compared to cell motions (Fig. 2.23). We also found that stage drift is sufficiently small to be corrected for drift by subtracting the mean displacement. Simulations of the thermal Voronoi model were performed as described in previous publications ([296], [297]). A detailed description of all methods can be found in the supplementary information.

Reagents

PND1186, Nocodazole, y27632, NSC23766, Mitomycin C, Human Transferrin, (3- Aminopropyl)trimethoxysilane were purchased from Sigma-Aldrich (Saint Louis, MO), Glutaraldehyde purchased from Electron Microscopy Sciences (Hatfield, PA), BD Collagen I, rat tail was purchased from BD Biosciences (San Jose, CA). 1X PBS, 1X DMEM, Fetal Bovine Serum, l-glutamine, Penicillin-Streptomycin, Trypsin EDTA were purchased from Corning Inc. (Tewksbury, MA), TBS, MnCl, NaOH were purchased from Fisher Scientific (Hampton,

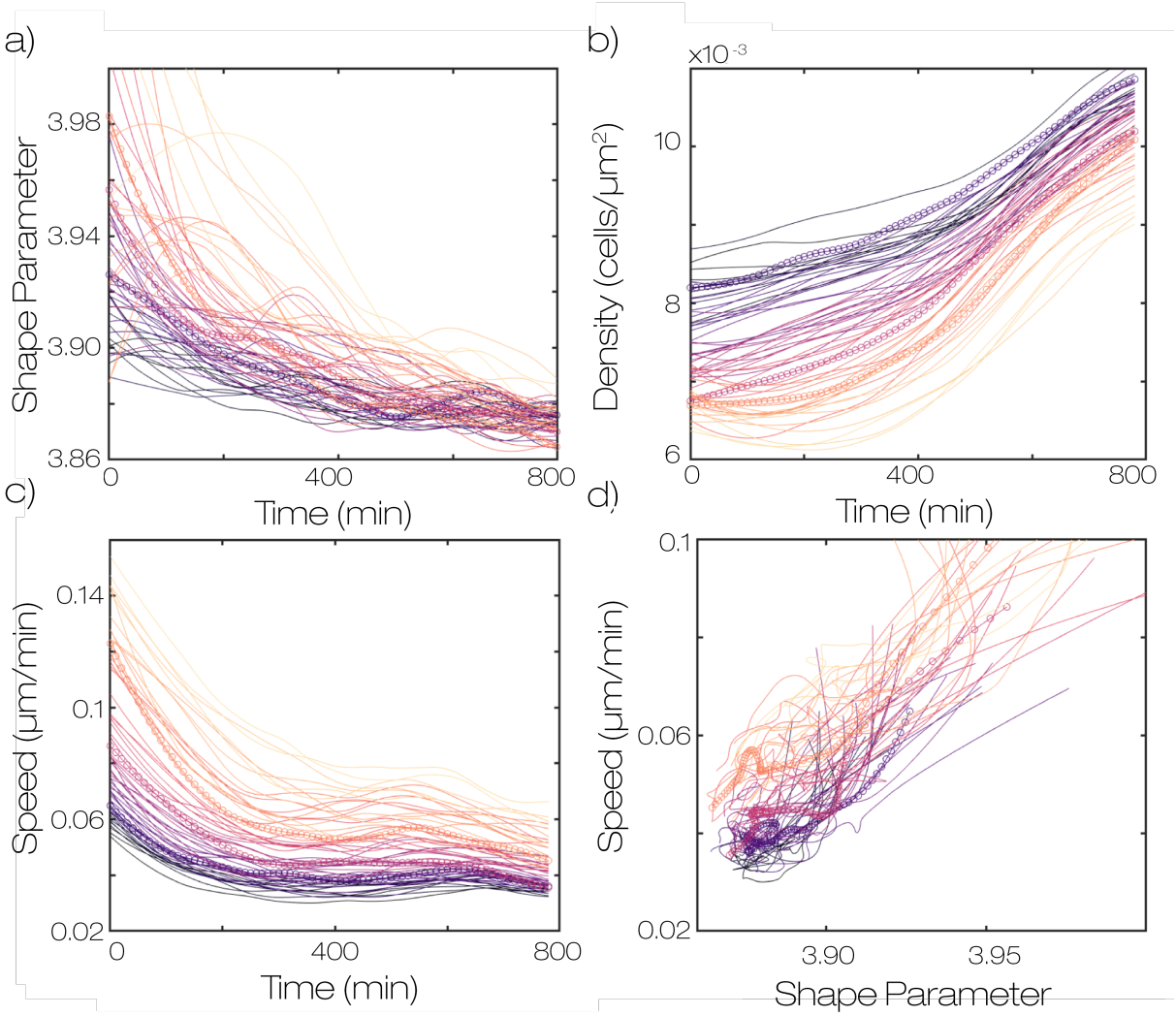

Figure 2.22: Different fields of view across the sample are qualitatively similar to the mean. (a) values of shape parameter for each field of view over time (b) density against time for the same set of fields of view. (c) speed vs time for the same set of fields of view (d) shape vs speed for the same set of fields of view. Time points are taken every 10 minutes. Data is colored according to the initial speed in the field of view. Colors are consistent across all panels. We see that the datasets which have larger initial speed also have larger initial shape and lower initial density.

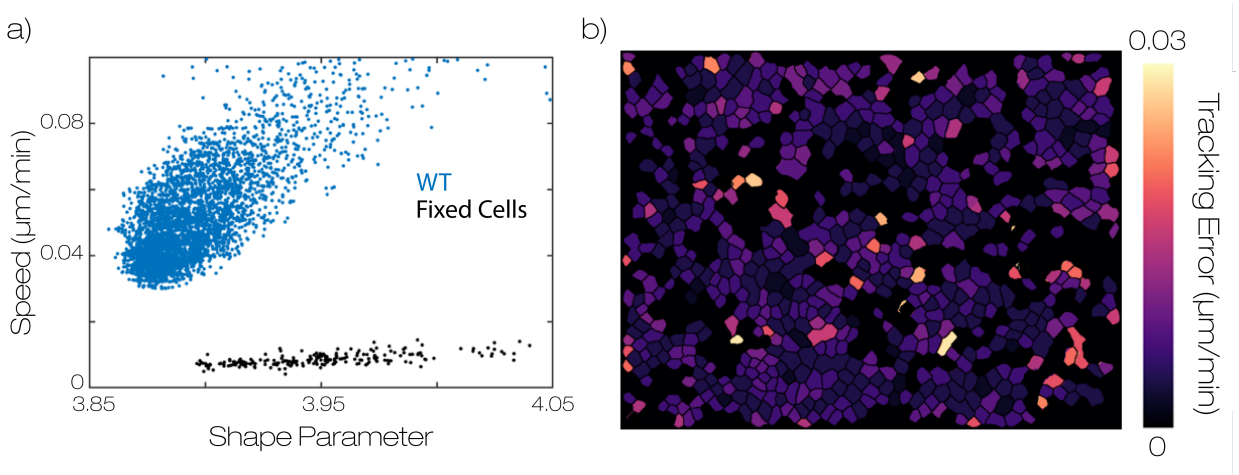

Figure 2.23: Characterization of lower bound for noise floor (a) relationship between shape and speed in WT data on a 2mg/ml collagen gel and under the same conditions but fixed in 4% PFA for 10 minutes before imaging. We observe an estimated noise floor with minor shape dependence and average value well below the speeds measured in the experiment. The noise floor may be larger due to larger fluctuations in protein levels and cell heights in live samples. Points represent the average cell shape and speed at a single field of view and time point (b) heat map of perceived displacements in fixed data. Measurement error is fairly homogeneous and very few single cells tracking errors comparable to experimental displacements.

NH), Ro-3306 was purchased from Cayman Chemical (Ann Arbor,MI)

Cell culture

Madin-Darby Canine Kidney (MDCK) cells and Mouse Embryonic Fibroblasts (MEFs) were cultured in high-glucose DMEM supplemented with 10% FBS, 2mM L-glutamine, 100 U/mL penicillin, and 100 μg/mL streptomycin at 37C and 5% CO2. Caco-2 cells were cultured in high-glucose DMEM supplemented with 10% FBS, 2mM L-glutamine, 100 U/mL penicillin, and 100 μg/mL streptomycin and Human Transferin at 37C and 5% CO2. Cells were passaged using 0.25% trypsin EDTA every 2-3 days. Cells were checked for mycoplasma by Hoechst staining.

Stargazin-GFP MDCK cells we produced by transient transfection of WT MDCK cells with a PiggyBac-stargazin-GFP construct followed by selection by puromycin and subcloning. A clone with high expression of the marker and similar morphology to WT MDCK cells was selected for experiments. Stargazin-GFP was a gift from Michael Glotzer. Stargazin-halotag Caco-2 and MDCK cells were produced by lentiviral infection of WT CACO-2 and MDCK cells by a WPT-Stargazin-halotag construct packaged in 293T cells by a second generation lentiviral system with rev8.2 and VSVG. Viral supernatant was collected at 24, 48 and 72 hours then concentrated $\approx$30x using Amicon Ultra-15 Centrifugal Filter Unit (100kDa). Cells were treated with virus and 8μg/ml polybrene overnight. Positive cells were isolated using a cell sorter. PIP-FUCCI MDCK cells were produced by lentiviral infection with virus packaged the same way. Cells were then selected using 800 μg/ml G418. pLenti-PGK-Neo-PIP-FUCCI was a gift from Jean Cook (Addgene plasmid 118616 ; $http://n2t.net/addgene:118616; RRID:Addgene-118616$). Tet P27 1-176 cells were produced using the Lenti-X Tet-On 3G (Takara Bio). Human Snaptag-P27 1- 176 was subcloned into the Tre3g vector. Cells were infected with lentivirus for both the Tet-on 3g and Tre3g snaptag-p27 1-176 plasmids then selected using 2 μg/ml puromycin and 800 μg/ml G418

AminoSilane Glutaraldehyde modification of glass coverslips

Glass coverslips were modified as previously described to couple collagen gels to the surface of the glass ([365]). Coverslips were first cleaned by sonication in 70% and 100% ethanol solutions then dried with compressed air. We placed coverslips in a staining rack and submerged the rack in a solution of 2% (3-Aminopropyl)trimethoxysilane (APTMS) 93% propanol and 5% DI water for 10 minutes at room temperature while stirring. Staining racks were removed and washed in DI water 5 times then placed in a 37C incubator for 6 hours to allow the water to dry and aminosilane layer to cure. The staining racks were then submerged in 1% glutaraldehyde in DI water for 30 minutes while stirring. Then the samples were washed 3 times for 10 minutes in distilled water, air dried and stored at room temperature. Activated coverslips were used within 2 months of preparation.

Collagen gel preparation

10x PBS, milli-q filtered water, a 5mg/ml collagen stock and 1N NaOH were mixed to generate a polymerization mix with 1xPBS and 2 or 4 mg/ml collagen at neutral pH. To visualize 3 collagen gel thickness we produced a fluorescently labeled collagen stock by mixing collagen with alexa647-NHS ester in 0.02M acetic acid overnight. We added fluorescently labeled collagen at a 20:1 ratio to unlabeled collagen in the polymerization mix. 70uL of the polymerization mix was added on to a 25mm round modified coverslip and quickly spread to coat the surface using a pipette tip. Samples were transferred to a humidified incubator at 37C to polymerize for 1 hour. After polymerization gels were washed 3 times in 1x PBS and it was verified that gels were still intact and adhered to the glass by a tissue culture microscope.

Glutaraldehyde crosslinked gels were prepared as above and crosslinked as previously described (Lang et al., 2015). Directly after polymerization and washing gels were incubated in 1xPBS containing 0.2% glutaraldehyde for 30 minutes. Gels were then washed quickly 3 times in 1xTBS, washed in 1x TBS at 1 hour intervals 5 times and left in 1x TBS overnight

to quench excess crosslinking groups on the gel. The gels were then washed in 1x PBS three times. All gels were used within 2 days of polymerization

Monolayer preparation

Monolayers were formed on collagen I gel to study monolayers under more physiologically relevant conditions than typical glass, plastic or hydrogel surfaces ([25], [81], [282], [328], [358]). Cells were seeded onto collagen gels at high density (≈600,000 cells on $500mm^2$ surface) such that cells coated ≈ 70% of the gel surface at seeding. The sample was returned to the incubator overnight (8-12 hours) before the experiment. For inhibitor treated conditions the inhibitor was added 10-20 minutes after the cells were seeded on the gel to allow cells to attach before adding fluid volume. Before mounting samples, the monolayer was viewed under a tissue culture microscope and continuously covered a region 10-15 mm across. Samples were washed 3 times with 1x PBS and quickly mounted into a sealed round chamber with 1.5mL of culture media and with equal concentration of inhibitor to at seeding. Before taking each time lapse the collagen gel was verified by fluorescence microscopy to be homogeneous and 150-250 μm thick. The monolayer was confirmed to extend at least several hundred microns in each direction outside selected fields of view. By only observing cells more than a few hundred microns from a free edge we avoid the increased migration speed and correlation from cytoskeletal assemblies specific to wound healing ([219], [311]).

Fluorescence microscopy

Cells were imaged on an inverted epi-fluorescence microscope (Nikon TI-E, Nikon, Tokyo, Japan) with a 20x plan flour multi-immersion objective. Glycerol was used as an immersion medium to more closely match the index of refraction of the collagen gel. Images were acquired at 10 minute intervals in GFP, 642 and transmitted light channels using standard filter sets (Ex 490/30, Em 525/30, Ex 640/30, DAPI/FITC/TRITC/cy5 cube) (Chroma Technology, Bellows Falls, VT). Samples were mounted on the microscope in a humidified stage top incubator maintained at 37C 5% CO2. Images were acquired on either a Photo-

metrics Coolsnap HQv2 CCD camera (Photometrics, Tucson, AZ) or Andor Zyla 4.2 CMOS camera (Andor Technology, Belfast, UK).

Image Segmentation

Images were segmented using custom MATLAB code. The main algorithm performs initial segmentation using the Phase Stretch Transform algorithm developed by the Asghari and Jalali ([12]). Phase stretch images were thresholded and skeletonized to obtain cell outlines. Broken edges in the skeleton were repaired using a modified implementation of edgelink developed by Peter Kovesi ("Peter's Functions for Computer Vision," n.d.). After edge-linking the remaining unclosed portions of the path were removed. The interior of each cell is checked for high intensity features which typically indicate under-segmentation. Any region containing a high intensity region within the boundary are discarded. The above algorithm has 4 parameters describing the PST parameter set and the interior threshold. Parameters were first optimized by hand. We then randomly generated 1000 parameter sets around these values. We generated a rough ground truth segmentation by averaging over 4 several parameter sets which we verified to segment the images well. The 1000 parameter sets were checked against this ground truth to choose a final parameter set. This parameter set was used to segment all images analyzed in this paper. Examples of the segmented outlines overlaid on the fluorescence images are found in the original manuscript.

Cell tracking

Cell tracking was performed using established particle tracking methods ([63]). Cell centers were determined by taking the centroid of each region in the cell outlines generated as described above in Image Segmentation. The particle trajectories were compiled from these position measurements using SimpleTracker, a MATLAB function developed by Jean-Yves Tinevez ([305]). For each image in a given time series the average displacement was determined and was subtracted from the cell positions to account for stage drift between each frame. We determined a lower bound on the tracking error by tracking image series of

fixed cells (Fig. 2.23)

For each movie the cell position, shape, magnitude of displacement at a 10-minute interval, and cell area were determined for each individual cell over all time points. The average magnitude of displacement was calculated for each field of view at each time point to obtain a cell speed. The inverse of the average area was calculated to determine cell density in each frame. We computed displacements squared at all subsequent images in the time series and averaged across the dataset to produce a mean squared displacement curve (Fig. 2.4D). Cell positions, velocities and shapes obtained from the tracking were used to compute all correlation functions described in the following sections.

Measurement of Cell Shape

We benchmarked a variety of algorithms for determining perimeter and area and found many give rise to large systematic errors. We have chosen to report the shape of a polygon reconstructed from identified cell vertex locations which we found to be the most accurate and robust metric (Fig. 2.2, supplemental discussion). Shape parameter was computed for each cell based on the perimeter and area of a polygon constructed from cell vertex locations. The vertex locations parameterize the vertex model and therefore also allow for direct comparison with the model. Reconstructing a polygon from vertices also removes resolution dependent ambiguity in perimeter measurement (Coastline Paradox)

Vertex locations were found by locating branch points in the segmentation mask generated as described in Image Segmentation using the built in Matlab bwmorph function. Cells which do not have a complete set of segmented neighbors also do not have a complete set of vertices and therefore were discarded. We measured average cell shape for the full set of cells and cells remaining after discarding edge cells and found only a small difference in the average. We believe this difference comes from a small segmentation bias for cells whose outline is not correctly constrained by the neighbor. Therefore, the interior cell shapes are likely slightly more accurate. The shape parameter $q = perimeter/\sqrt{area}$ was measured by computing

perimeter and area for the reconstructed polygon. The shape parameter is related to the another popular shape metric – $circularity = 4\pi * area/perimeter^2 = 4\pi/q^2$. Final cell shape was determined for each experiment by averaging the shape parameter for all fields of view measured to have a speed below 0.04μm/min. This final shape value is within a few percent of the value obtained by fitting the shape vs time curves to an exponential decay

Simulation methods

We perform numerical simulations of monodisperse thermal Voronoi models, as described in ([296]). Briefly, we begin by writing down a dimensionless form for the standard vertex model energy, $E = \sum_{i=1}^{N}[k_A(a_i - a_0)^2 + (p_i - p_0)^2]$. This simple expression assigns an energy to the cells in a confluent monolayer in terms of their preferred geometry. The energy depends on the area a_i and perimeter p_i of each of the N cells (indexed by i), which are determined by a Voronoi tessellation of the cell positions. The unit of length in the simulations are defined such that the average cell area is unity, and we also set both the preferred area $a_0 = 1$ and the stiffness parameter $k_A = 1$. The preferred value for the cell perimeter, p_0 then constitutes the remaining control parameter which sets the target state of the monolayer.

We then use the cellGPU package to simulate overdamped Brownian dynamics of the model at different temperatures, T. The curves in Fig. 2.6C were created by performing an ensemble average over approximately 30 independent systems of $N = 1000$ cells at each (p_0 ,T) point in parameter space along the lines indicated in (Fig. 2.6B). Each system was initialized in a high-temperature configuration and then allowed to equilibrate at the target temperature for a large multiple of the system's characteristic relaxation time, as estimated from the data in Ref. (Sussman et al., 2018); after this equilibration period the observed average shape parameter of the cells and mean-squared displacement at several typical time lags was evaluated.

Numerical simulations of the vertex model with fluctuating junctional tension are performed as previously described ([351]). The dimensionless energy of the vertex model is writ-

ten as a function of the vertex coordinates a Here α and N denote the label of each cell and the total number of cells, a_α and p_α are the area and perimeter of cell α. The preferred area and perimeter are denoted as p_0 and a_0, respectively. k_α is the stiffness parameter. In the non-dimensionalized form, we choose the length scale to satisfy the average cell area $< a_\alpha >= 1$. The edge length between the vertices i and j is denoted as l_{ij} and the fluctuating line tension is introduced by $\Delta\lambda_{ij}(t)$ dynamics of $\Delta\lambda_{ij}(t)$ is described by an Ornstein-Uhlenbeck process satisfying $< \Delta\lambda_{ij}(t) >= 0$ and $< \Delta\lambda_{ij}(t_1)\Delta\lambda_{kl}(t_2) >= \delta_{ik}\delta_{jl}\sigma^2 e^{-|t_1-t_2|/\tau}$. The vertex dynamics is described by the time-evolution equation $\eta(dr_l/dt) = \partial\epsilon(r_l)/\partial r_l$. In this paper, we choose the $\sigma = 0.2, \tau = 1, k_\alpha = 1, a_0 = 1, \eta = 1$ and we run simulations with 340 cells in a square simulation domain with periodic boundary conditions. As we for our Voronoi model simulations, we initialize the cellular configuration under a high-temperature condition ($\sigma = 0.35, \tau = 1$), and thermalize with the target parameters. After the thermalization, we begin setting the tension $\Delta\lambda_{ij}(t)$ of edges to zero permanently by randomly selecting a target edge every constant time interval τ^R

Preparation of Fibroblast conditioned Medium

Fibroblast conditioned medium was prepared as described previously ([210]). We cultured a 10 cm dish of MEF cells to confluence. Cells were washed and 20 mL of fresh medium was added to the cells. 48 hours later the media was collected and centrifuged to remove any cells. Conditioned media was aliquoted and frozen at -20C then used within 1 month of preparation. The conditioned medium was mixed 50:50 with fresh culture medium and added to MDCK cells 15 minutes after plating. We tested that fibroblast conditioned medium caused cell scattering of small colonies on collagen coated glass substrates as previously described ([289]).

Cell division tracking

We found that our cell tracking consistently does not follow cell trajectories through a cell division because the distance threshold of trajectory linking is significantly larger than a cell

radius. We exploit this to identify cell divisions and to measure shape change independent of cell division (Fig. 2.14d, 2.15). We identified cell divisions by identifying pairs of cells which appear in adjacent to each other in a frame after both cells were not present in the previous frame. We further filter out cells which are not of similar size to one another. We confirmed by inspection that this gives us a subset set of cells which have divided in the previous frame with few false positives. We then find the mother cell by looking several frames back for a cell near the centroid of the pair of daughter cells. We identify neighbors adjacent to both or one of the daughter cells and track each of these cells back in the trajectory to compare cell shapes before and after the division. We then average across all cell divisions in the dataset to produce the final values (Fig. 2.14E)

Calculation of mean squared displacements

Particle trajectories were compiled as described in the Particle Tracking section of the methods. We took each trajectory and decomposed it into non-overlapping sub trajectories starting from the initial time point with length ranging from $\tau = 10$ minutes to the full trajectory length. The average displacement squared for each sub trajectory was computed and averaged across the dataset (Fig. 2.4D). To compute the time averaged mean squared displacement averaging was done for all sub-trajectories of a single particle and each cell with a full trajectory is plotted (Fig. 2.3A). To plot mean squared displacement against time we averaged for a given value of τ and t across the dataset (Fig. 2.3B).

Three Pixel vector method of measuring perimeter and area

The three pixel vector method was implemented as previously described ([131]). Briefly, the different ways of linking pixels are divided into 4 classes and 13 subclasses. Each subclass has a defined length giving a 1x13 vector. For each class there is a linking correction depending on the difference of the direction of the current and subsequent vector which is specified by a 4(classes)x16(directions) matrix. To determine the areas enclosed by each vector we sketched the set of 13 available classes of linking and computed the

area of edge pixels and pixels outside the polygon for each case. We obtained the values [2,3,2,2,2,2,3/2,1,11/4,3,2,3/2,2]. We then inferred area corrections for each class from their respective perimeter corrections linking as follows : [0,0,0,0,1/2-2,1-1/2,2-2,0,2,2,2,2,1,1,1,1]; [0,0,1/2-2,1/2-2,2- 5,0,0,2,2,2,1,1,1,1,0,0]; [0,-1,-1,2-2,0,0,0,0,2,1,1,1,1,0,0,0]; [0,0,0,1/2-2,2-2*1/2,2-2,0,2,2,2,2,1,1,1,1,0]. We compute the perimeter as described by Inoue et al. and using the same rules and values specified above plus the area of the interior pixels calculate the area of the polygon.

Field of View analysis

The shape vs speed for different size fields of view were computed by segmenting each field of view into a set of sub fields. To simplify this process first the field of view was truncated into a square to make sub division possible in such a way that the same set of cells are always measured. Then the field was subdivided into 1, 2x2, 3x3... 10x10 regions. We computed the average speed and shape in each sub-region, then binned the results of all regions according to average speed in the region. To characterize noise in the correlation we computed the average deviation of the derivative in a linear region of the curve for shape parameters ranging from 3.93 to 3.97.

Measurement of neighbor exchange rate

To measure a neighbor exchange rate, we detected 4 fold vertices and computed the ratio of 4 fold to 3 fold vertices per unit time. Such 4 fold vertices are not stable in the system and thus result in either a successful or attempted neighbor exchange. Our method does not detect the difference between successful neighbor exchanges and attempts which resolve in the original direction. A 4 cell vertex after formation was observed to resolve in either direction within at most 10 frames. Therefore, we iterated through each set of outlines and detected all 4 cell vertices. We discarded detections which happened within 10 pixels and 10 frames of a detected event to avoid double counting due to time delay between formation and resolution. This set of candidate events contained many false positives where the outline

appeared to have a four-fold vertex but upon inspection of the raw data we observed a short 3 cell vertex. To remove these false positives, we manually sorted through the 4 cell vertex candidates and selected out real events

Cell doublet preparation and measurements

Cell doublets were produced by treating cells with trypsin until detachment from cell culture dishes. Around 15,000 cells were transferred to a PDMS well which was pretreated with 1% Pluronic f127 for 1 hour then washed 3 times with 1X PBS. Cells were incubated in the wells at 37C and 5% CO2 for 4 hours in the presence of inhibitors or doxycycline (100ng/ml) and halotag and snaptag ligands (1μM) then imaged at room temperature for less than 30 minutes. For the "Contact inhibited" condition cells were plated at nearly 100% confluence and grown for 3 days prior to detachment while other conditions were cultured under normal cell culture conditions. Cells were imaged by mounting PDMS wells on coverglass and using imaging methods described above. The contact angle was measured between isolated pairs of cells manually using imageJ.

FUCCI measurements

Cells were imaged in GFP and RFP channels similar to above methods. Images of FUCCI markers and cell boundaries were segmented using Phase Stretch Transform in Matlab. Each cell was identified using the cell boundaries and was determined to be GFP or RFP positive by measuring the intensity contained within the segmented images of each nuclear marker. The percent of cells in G1 was determined by taking the ratio of cells identified as only GFP positive to the cells identified as GFP positive, RFP positive and positive for both markers.

2.6 Additional discussions

Shape Metric Benchmarking - Common Shape Metrics are resolution Dependent

In the initial analysis we noticed an unexpected density dependence of cell shape which had a different magnitude depending on which metric we used for measuring shape. We therefore

decided to benchmark methods of measuring object shapes in digital images. Measuring the shape of polygonal objects projected onto a pixel grid is nontrivial because segmented edges are limited to single pixels while the actual object edge is a subpixel feature. Data is recoded on a 6.45μm/pixel camera at 20x magnification giving 0.3225 μm/pixel final resolution for a cell radius of $\approx$15μm. Therefore, the edge of a cell contains few enough pixels that choice of shape metric is important. The simplest method to determine a length in an image made of pixels is to count the number of pixels along the perimeter. A more sophisticated method count pixels at 0, 90,180,270 degree angles (even) as a distance 1 and diagonal (odd) pixel connections as $\sqrt{2}$. This method is used to determine perimeter in the popular image processing software imageJ. This method overestimates the length where even and odd edges meet. Another method developed by Vossepoel uses a correction factor for pixels which change from odd to even with parameter values fit from simulated images of lines. This is used in the built in perimeter determination in regionprops in Matlab. This correction factor is not always accurate for small polygons. The corner correction can also be made by estimating that these connection have length $\sqrt{5}$ although this method does not correctly capture the length of some corner corrections. The Three Pixel Vector method developed by Inoue and Kimura explicitly implements all possible corner corrections ([131]). Object areas also can be measured in several ways. The most common method is to add up all the pixels in the polygon which the default method used in ImageJ and Matlab. This method overestimates the area of the polygon as it encloses area outside of the corrected perimeter contours described above. Instead the area can be measured by constructing the contours described above and finding the enclosed area.

To measure shape we implemented several of the methods described above. We also implemented an additional method which is specific to our dataset, where the objects can be defined by simple polygons constrained by the cell vertices. To measure this polygon shape we measure vertex locations estimated to the nearest pixel and reconstruct the polygon by

connecting the vertices by straight lines. The vertex locations were determined by locating branch points in the cell outlines. One drawback of this method is that segmented cells which do not have a complete set of neighbors lack a complete set of vertices and must be discarded. For every cell with a complete set of neighbors, the vertices belonging to each cell were determined. The perimeter and area of a polygon defined by a set of vertex locations can be computed directly without lines being interpolated on to a grid of pixels. A representative image of the vertex locations on the membrane GFP image are displayed (Fig. 2.2B).

We compared the relationship between cell shape and density which reveals the presence of resolution dependent artifacts at increased density (Fig. 2.2C). We observe a larger density dependence for more simple methods of perimeter and area determination which are known to produce large resolution dependent errors. The methods from three pixel vector closely match the vertex reconstruction – we infer that these are the two most accurate methods. We confirmed these findings by generating simulation images from the thermal voronoi model with known shape parameter and measuring the cell shapes (Fig. 2.2D). This confirms that TPV and vertex reconstruction typically have less than 1% error. Finally, we segmented images of fixed cells (Fig. 2.2E) and measured the cell shape over a trajectory. This shape should be constant because there is no motion in the images only small changes in signal to noise and small stage drifts. We compared the measured values across each trajectory to the mean and observe larger fluctuations in the TPV method (Fig. 2.2E). This indicates that small differences in the segmentation boundaries can lead to relatively large errors in the final value of shape parameter. Therefore, the vertex reconstruction appears to be more robust to small changes in the signal. Although the vertex reconstruction requires discarding cells with an incomplete set of neighbors, for our 335x445 μm field of view and signal to noise the number of measurements (100-400 cells) is still large enough to provide a reliable average.

Cell Motility decreases with time

We observed that dynamics in the MDCK monolayers evolve with time. To confirm that individual cells show similar motile behavior we plot the time averaged mean squared displacement (TAMSD) (Fig. 2.3A). We observe qualitatively similar behavior for all cells in the monolayer. At short time scales the motion is nearly ballistic, however at later lag times the TAMSD plateaus for each cell. This indicates that at longer time scales most cells are confined by the neighboring cells and as a result do not end up traveling more than a few microns – only a fraction of a cell diameter. We also look at the time evolution of this motion by plotting the mean squared displacement as a function of time (Fig. 2.3B). We observe that for different lag times the mean squared displacement decreases. This shows that at later time points even for short time scales the diffusion is slower

Correlation between shape and speed is not dependent on field of view size or lag time

From our vertex model, we expect that shape parameter is useful for describing dynamics in the system. In the model, passive and active forces are defined at the level of single cells and therefore we expect that behaviors are mainly dictated by a cell and its nearest neighbors. The relationship between shape and speed should not be dependent on how the system is measured, meaning that the size of the field of view or lag time is somewhat arbitrary. We first test the relationship between the correlation we observe and the field of view size. We subdivide the field of view into at 335μm square, 2x2 168μm squares, ... 10x10 35μm squares (Fig. 2.4A). These squares contain the same data but if the properties of the system were not uniform, the smaller partitions may show different behaviors. If the forces are defined at the cellular scale, as we expect from the model, this partitioning should not change the relationship between shape and speed. We observe that across all partitions the same final relationship is recovered (Fig. 2.4B). However, we see that there is less noise in the correlation curve when partitioning into smaller regions. Because the correlation curve is not linear and the field of view is not uniform, as we average over a larger area the

average shape does not capture local shape variation which results in regions much faster or slower than the average. We plot the fluctuations in the correlation curve with respect to the average to describe this effect (Fig. 2.4C). As we reduce the size of the region we see the curve becomes more smooth until we reach a noise floor at $\approx 100\mu$m. We anticipate that if we had lower noise of cell displacements and a full segmentation these fluctuations would continue to decrease to the scale of a few interacting cells.

We also wanted to ensure that this correlation is not dependent on the lag time within a range of timescales. We plot the mean squared displacement as a function of the shape parameter at the beginning of each trajectory (Fig. 2.4D). We see that for each lag time there is still a relationship between shape and speed. We plot the relationship between shape and speed for one field of view at different lag times and see similar behavior (Fig. 2.4E). The relationship shifts down because the motion is diffusive so as lag time is increased by a factor of two displacement increase by a factor of $\sqrt{2}$. We also see the same trend for the ensemble averaged correlations (Fig. 2.4F)

Cytoskeletal rescue experiments do not restore relationship between shape and speed

Across inhibitors tested we examined the relationship of shape and speed. A subset of these conditions is plotted (Fig. 2.11). In general, we see that the relative relationship between shape and speed for a given condition is similar however the absolute values are all shifted in the inhibitor cases. One potential concern in these experiments is that cytoskeletal polarization may be perturbed ([3], [37], [222], [243], [359]). Changes in cytoskeletal organization may affect how well the system is described by vertex models which assume the monolayer mechanics are dominated by cortical actin at the cell-cell junctions. We wanted to examine if these defects are related to changes in cell polarity observed for many of these inhibitors. We attempted rescue experiments based on published rescues of RAC and FAK knockdown experiments. It has been observed that RAC promotes apical basal polarity

through its role in assembling laminin into the basement membrane ([222]). We seeded cells on a collagen gel with 1mg/ml matrigel to see if the inclusion of exogenous laminin in the matrix via the matrigel would rescue the relationship between shape and speed (Fig. 2.13B). We observe the same relationship between shape and speed in the presence of matrigel. We also attempted inhibiting both FAK and ROCK at the same time. ROCK inhibition rescues wound healing in FAK knockdown cells and restores apical basal polarity ([37], [49]). We observe similar behavior in conditions with both inhibitors (Fig. 2.13A)

Neighbor exchanges rates are low

We measured the rate of neighbor exchanges for one wild type and one inhibitor dataset (Fig. 2.17A). We were not able to reliable measure neighbor exchange rates with automated analysis so we only made this measurement for these two datasets. These neighbor exchange rates range from 1-10 per hour per 1000 cells which seems low compared to observations from some phases of development where neighbor exchanges are important for tissue flow ([27]). We observe that neighbor exchange rates are shape dependent and lower in the inhibitor treated conditions at all shape parameters. This suggests that the rate of neighbor exchange also depends on the cell division fraction, or active stress in the system. We relate these neighbor exchange rates to observed velocity and observe a correlation (Fig. 2.17B).

A metric q_{track} can be related to different modes of shape change

We wanted to confirm that the relationship between final shape and cell divisions was not simply the consequence of oriented cell division. We exploit the fact that q_{track}, the difference in cell shape between subsequent time steps ($q_{track} =< q(t+1) - q(t) >$), measures certain forms of cell shape change while ignoring others. For a given time step we directly observe, by tracking, a subset of the shape change which occurs. We denote the two types of cell shape change, division based (Q2) and deformation based (Q_1 / q_{track}). The observed subset selectively ignores cell divisions, because division results in large enough displacements that the trajectory is broken in our tracking algorithm. q_{track} also ignore a subset of shape

changes where the cell is not segmented in the initial or subsequent frame which are of either type (Fig. 2.15A). Importantly, only type 1 shape changes are observed in q_{track}. Therefore, as long as there is not a difference between the behavior of cells which are not segmented we can obtain the average value of a Q1 shape change for a give frame. We can also determine the total shape change by measuring shape in each frame over all cells. We show that the ratio of these two, multiplied by a small correction factor ($\approx 1\%$), gives a relationship for the relative value of non-division based shape change (Fig. 2.15B, C). If this value were on average 0 we could explain the correlation in Figure 2.15D by oriented cell division. We 11 observe values much larger than zero for this metric demonstrating there is an additional mechanism driven by cell divisions. Our calculation ignores the addition of a neighbor to cells adjacent to the dividing cell. We confirm that the shape change by q_{track} is several times larger than the shape change which would result from the gain of an additional neighbor (Fig. 2.15E). We observe that this metric is nearly 1 across all average shape parameters for three datasets with very different division rates (Fig. 2.15E). We show that for one condition q_{track} is similar to the total shape change except at early time points (Fig. 2.15F). We also observe that the direct shape change before and after cell division is shape dependent in this dataset consistent with the deviations in q_{track} we observe at high shape parameter (Fig. 2.15G). For a derivation of q_{track} see the original manuscript

q_{track} values are consistent with junction length changes as the main source of shape change

We measured shape change along cellular trajectories $\Delta q_{track} =< q(t+1) - q(t) >$ which we show measures deformation based changes and ignores oriented division effects (Fig. 2.15B,C). We then compare this to the total shape change between time points $\Delta q_{total}(t) = q(t+1) - q(t)$ to measure the relative contribution of junction length changes and oriented division (Fig. 2.15E). We observe a slight discrepancy between these two metrics at early times in the experiment. At these time points cell aspect ratios may be large enough for

oriented division to cause a net decrease in cell shape (Fig. 2.15D). However, we observe at later time points the q_{track} metric which ignores oriented division effects is sufficient to capture nearly all shape change in the monolayer. Across conditions with different division fraction junction length change consistently explains a majority of shape change in the monolayer (Fig. 2.15E). Therefore, the relationship in Figure 5d implies that in monolayers with higher division fraction there is additional cell shape remodeling which occurs as a result of differences in cell mechanical properties or active stress caused by cell division

CHAPTER 3

DIA1 AND CELL CYCLE DEPENDENT MECHANICS DRIVE EPITHELIAL STRATIFICATION

This section is partially reproduced from the article Dia1 coordinates differentiation and cell sorting in a stratified epithelium published in JCB by Robert M Harmon, John Devany, Margaret L Gardel ([113]).

Much of the work presented in this chapter was performed by Robert Harmon including preparation of epidermal organoids, staining of organoids, preparation of knockdown cells, and design and implementation of the assay for cell stratification with Dia1 KD and WT cells. The text is adapted from the paper above, which was mainly written by Robert Harmon.

I performed data analysis in the first and third figures, the contact angle measurements, and extended the results to look at how contact angles and cell sorting depend on cell proliferation.

3.1 Abstract

Epithelia have multiple spatial domains which perform specific tasks, e.g., crypts and villi in the intestine. This spatial organization can be disrupted in disease and is often associated with loss of tissue function. There are key differences between these compartments, some are highly proliferative, while others contain mainly non-proliferative cells. Cells also express different actin regulatory proteins in each compartment, driving changes in cell mechanics and interactions. Cells drastically change their proliferation rate and transcription of cytoskeletal proteins when they differentiate and move between these compartments, however, it remains unclear how these differences affect epithelial organization. Here we focus on the skin as a model system which can build these compartments starting from a single layer of stem cells. We heterogeneously express the actin nucleator Diaphanous 1 (dia1) or cell cycle

inhibitors during the formation of skin organoids to measure how perturbing proliferation or actin nucleation can change the organization of cells in the skin. We show that cells which become arrested in the cell cycle or which lack dia1 expression, resembling differentiated cells, are more likely to exit the stem cell layer. By measuring the contacts between cell-cell interfaces, we show that cell mechanics and adhesion are altered depending on cell cycle and dia1 expression states. Together, our results show that proliferation and dia1 dependent changes in cortical mechanics are an important driver of cell organization in the skin.

3.2 Introduction

Throughout adulthood, epithelia turn over yet retain distinctive architectures. Such tissues often encompass subdomains distinguished by unique cellular morphology and behavior. The mechanisms, however, by which these domains arise and persist remain a puzzle. Exemplifying the problem, keratinocytes establish stratified structures at the skin surface characterized by layers with distinct morphologies ([186], [284]). A basal layer of proliferative columnar cells pack atop the collagenous dermis and give rise to overlying layers with flattened squamous morphology. As cells stratify and change shape, a differentiation program ensures that suprabasal cells repress proliferative behavior and express factors required for producing an effective barrier to water loss, pathogens, and mechanical insult ([18]).

Of note, basal cell shape affects the capacity to coordinate stratification with differentiation ([29], [206]). Reduced cell spread area, concomitant with basal layer packing, also triggers serum-response factor (SRF), Yes-associated protein (YAP) and NOTCH responses which drive differentiation ([60], [309]). Coordination of cell movement with differentiation in these models, however, is contingent upon establishing a densely packed basal layer. The question arises as to how the skin and other stratified epithelia shunt proliferation into packing the basal layer rather than distributing cells homogenously throughout the tissue thickness. To compartmentalize tissues, cells sort out based on differential intercellular adhesion

and actomyosin contractility ([83], [195], [188]). The segregation of like cells based on these properties guides prominent developmental processes like gastrulation but is also thought to aid in maintaining compartments at homeostasis ([160]). In epidermal tissues, genetic studies indicate that cadherin and integrin-based adhesion ensure proper basal layer formation ([30], [248], [307], [321]). Similarly, classic *in vitro* studies indicate that when mixed in a cell aggregate, undifferentiated keratinocytes separate from differentiated neighbors to form compartments ([333]). Recent studies highlight the differences in basal and suprabasal layer stiffness ([89]), pointing to mechanics as a likely determinant of this separation.

How actin regulatory proteins, through their effects on cell–cell adhesion and cortical mechanics, enforce compartmentalization of the basal layer is not well understood. Whereas earlier studies implicate depolymerizing agents like cofilin in epidermal function ([185]), the role of actin nucleators requires further attention. Disruption of the branched actin nucleator, Arp2/3, or its activator, the WAVE complex, perturbs epidermal function with varying effects on the structure ([58], [317], [364]). Unbranched actin filaments produced by the formin family anchor adhesions and participate in physiological adaptations to mechanical stretch within the epidermis ([10], [154]). Endogenous miRNA restricts expression of the canonical formin, Dia1, to the basal layer of human epidermis and tongue ([293], [294]). Though diabetic ulceration and certain carcinomas yield aberrant expression patterns ([46], [293], [294], [337], [350], [354]), the normal physiological function of Dia1 in the basal layer remains unclear. One hypothesis is that differential Dia1 expression translates into differential adhesion effects amenable to packing and producing a properly shaped basal compartment.

In addition, different compartments of the epithelium have differences in proliferation. Cell differentiation which drives the change in localization of cells to different epithelial compartments, coincides with a permanent arrest of the cell cycle ([39]). Recent work has also showed cell cycle-dependent changes in cell-cell interactions, which could potentially drive cell sorting independent of gene expression ([72]). It is possible that the difference in

proliferation between the compartments also acts to maintain this separation by regulating the generation of cortical tension or active mechanical stress.

In addressing this hypothesis, we found that Dia1 depletion in a model epidermis disrupted basal layer morphology. These changes in Dia1 expression coincided with differentiation and proliferation defects throughout the model tissues. *In vitro* assays also supported the hypothesis that Dia1 expression and cell proliferation discrepancies can guide cell compartmentalization. We show in a model of stratification that both depletion of Dia1 and inhibition of the cell cycle drive cells to stratify more quickly than WT cells. We go on to show that these perturbations affect cell-cell interactions by looking at isolated doublets of cells lacking Dia1 or under cell cycle inhibition. Our results provide the first indication that formin expression and proliferation gradients, through effects on cell sorting, enforce the maintenance of distinct morphological zones within complex tissues.

3.3 Results

3.3.1 Dia1 controls basal layer morphology and packing

Involvement of Dia1 in immune function and the sensitivity of skin to immunological influence steered us toward the *in vitro* approach of a well-characterized, organotypic culture model ([5], [180], [235]). To mimic the *in vivo* juxtaposition of epidermal epithelia to its supporting connective tissue, three-dimensional cultures are produced by plating keratinocytes, like the HaCaT line, upon fibroblast-doped collagen ([271]). Although they mature slower than primary cell counterparts ([271]), HaCaT cultures developed at an air–liquid interface construct a stratified tissue with architecture and expression profiles mimicking those of normal tissues ([155], [294]). Immunostaining of tissue sections produced from 10-day-old, paraffin-embedded control (CTL) cultures indicated that Dia1 expression, as well as the shape and orientation of nuclei, changed with respect to position in the stratified tissues.

Dia1 concentrated in the basal layer, approximated as keratinocytes lying within 10 μm of the underlying collagen (dashed line, Fig. 3.1A).

Basal layer keratinocytes produced a mean linear density of 13 cells per 100 μm (Fig. 3.1B, C). Within the basal layer, nuclei are elongated, with an average aspect ratio of 2.5 (Fig. 3.1B, C), and are oriented such that the long axis is nearly perpendicular to the basal surface, with the average angle between these axes being 25° (Fig. 3.1E). Both the nuclear shape and orientation change in a stereotypical fashion toward the apical surface. As their relative position increases, the nuclei are less elongated but maintain their orientation (Fig. 3.1A–E). In the most suprabasal layers, the aspect ratio and orientation increases such that the long axes are parallel to the basal interface (Fig. 3.1A–E).

To explore the role of Dia1 on the architecture of stratified tissues, we used CRISPR and shRNA to reduce Dia1 expression (Fig. 3.2). Both techniques diminished Dia1 expression, with shRNA yielding knockdown efficiencies of $65 - 80\%$ and CRISPR edits causing near total abrogation of Dia1 protein levels. Next generation sequencing identified two frameshift variants with premature stop codons, accounting for $\approx 85\%$ of the genomic sequencing signal (Fig. 3.2). Tissue depleted of Dia1 by CRISPR (Dia1KD) stratified but produced a basal layer that was 20% less dense than CTL cells and lacked the stereotypical columnar morphology (Fig. 3.1A, C). Within the basal layer, the nuclei of Dia1KD cells were less elongated and randomly oriented, at times lying parallel to the underlying collagen (Fig. 3.1A, D, E). The nuclear shape remained constant in the suprabasal layers and showed a similar trend toward becoming parallel to the basal interface at high relative positions (Fig. 3.1E).

3.3.2 Dia1 expression supports normal epidermal organization

Since morphology dictates the success with which basal cells differentiate ([60], [309]), we next tested whether the aberrant morphology caused by Dia1 depletion impacted epidermal

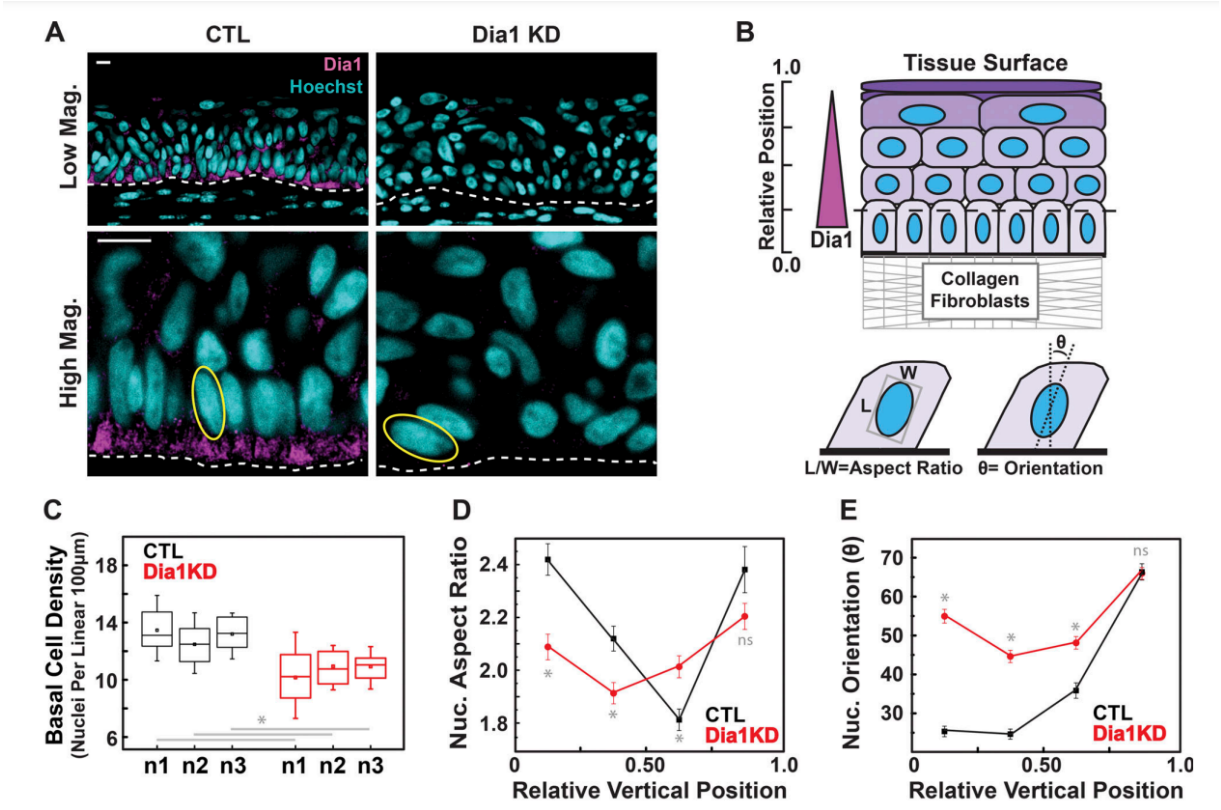

Figure 3.1: Dia1 supports basal layer packing in stratified tissue. (A) Immunohistochemical staining of Dia1 in cross sections obtained from paraffin-embedded cultures, fixed 10 days after lifting to an air–liquid interface. Scale bars = 10 μm. Example of fit ellipses used for subsequent measurements indicated in yellow. Dotted line separates keratinocytes from the underlying collagen and fibroblasts. (B) Schematic illustrating measurements taken from tissue cross sections and presented in C–E. (C) Linear density of basal nuclei, 20–27 images analyzed per sample. (D) Aspect ratio of nuclei as a proxy for cell shape throughout tissue thickness. (E) Orientation of nuclei throughout the tissue thickness with respect to the keratinocyte–collagen border. For D and E, plotted points represent the mean ± SEM of data derived from 85 to 235 nuclei lying within bins bounded by x-axis ticks for a single sample set.

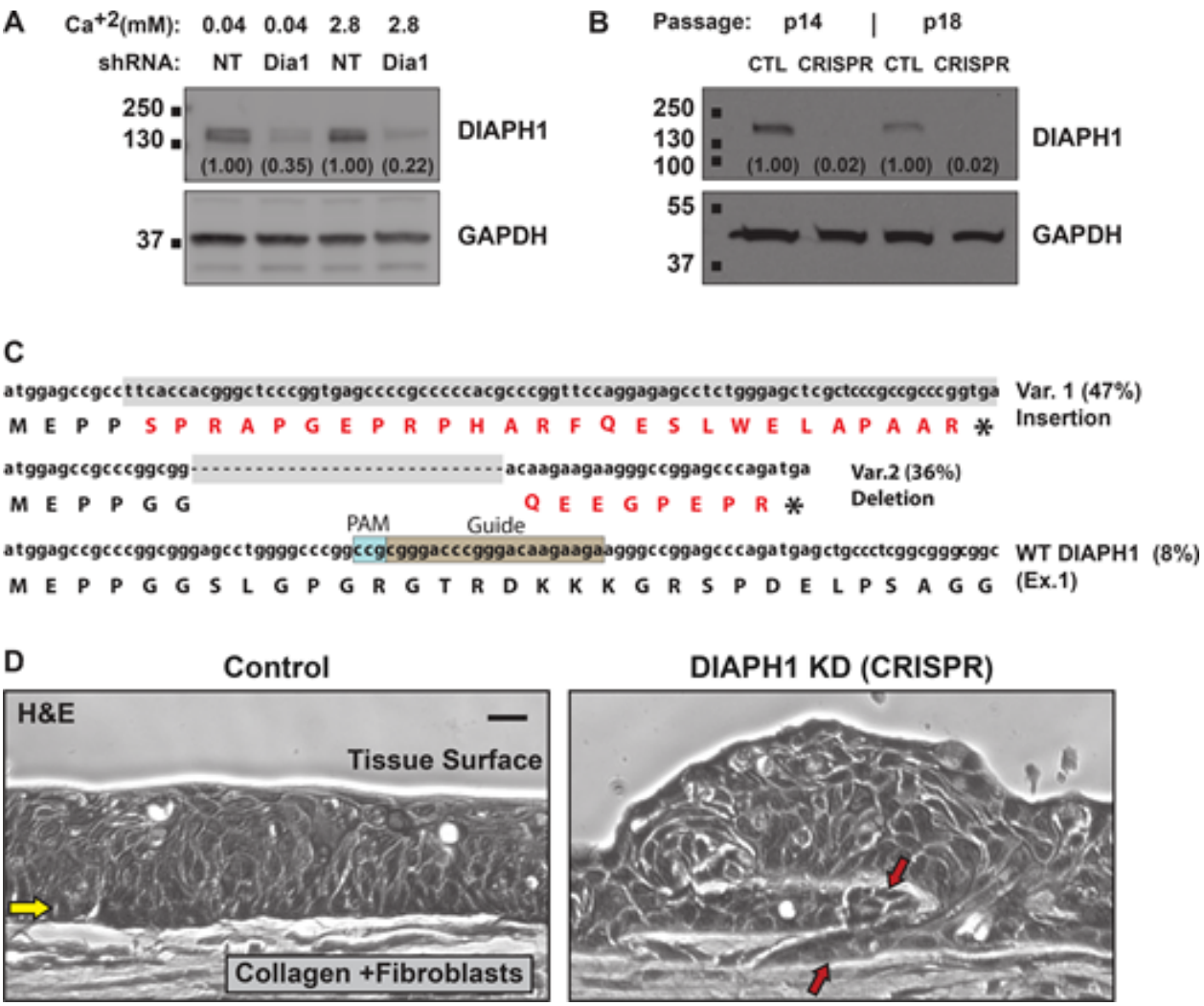

Figure 3.2: Disruption of DIAPH1 gene expression and example of ingressions found in DIAPH1-deficient cultures. (A) Western blot analysis of HaCaT cells transduced with non-targeting (NT) and DIAPH1-directed (Dia1) shRNA via lentivirus, cultured in low or high calcium media for 20 h. Relative abundance indicated with respect to control samples. Black squares = molecular weight markers at indicated weight (in kilodaltons). (B) Western blot analysis of control cells (CTL) and those carrying a disrupted DIAPH1 locus (CRISPR) at two different passages. Relative abundance to controls is indicated. (C) NGS analysis of genomic DNA flanking CRISPR-editing site and variant frequency. (D) Example of DIAPH1-deficient tissue growth into the underlying collagen substrate. Hematoxylin and eosin stain of cross sectioned, paraffin-embedded tissue fixed 10 days after raising to an air–liquid interface. Scale bar = 20 μm. Yellow arrow indicates basal keratinocyte layer. Red arrows indicate distinct ingressions.

differentiation. To address this possibility, sections of organotypic cultures were immunohistochemically stained for the differentiation marker, keratin-10 (KRT10). As in normal tissue, CTL cells produced a three-dimensional culture in which KRT10 localized specifically to suprabasal layers (Fig. 3.3A, B). Dia1KD cells, conversely, produced tissues that stratified but contained lesions of KRT10-negative cells (Fig. 3.3A, B). Organotypic cultures derived from shRNA-treated cells (shCTL and shDia1) corroborated these results (Fig. 3.2). Spatially segregated proliferation is an important attribute of differentiation in stratified tissues, and its loss is linked to pathologies ranging from barrier disruption to viral oncogenesis ([211], [258]). Staining for the proliferation marker, proliferating cell nuclear antigen (PCNA), allowed for visualization of where proliferative cells reside in the stratified layers. Control tissues demonstrated proper restriction of proliferative cells to the basal layer (Fig. 3.3C, D). Dia1-depletion led to the extension of PCNA positive cells throughout the tissue thickness (Fig. 3.3C, D). Further, the percentage of PCNA positive nuclei was 18% in the Dia1KD cells, reflecting a sixfold overall increase from that of control tissues (2.9%). This is reminiscent of hyperproliferative phenotypes associated with stratified tissue disorders such as psoriasis and esophageal disease ([127], [329]). This experiment also demonstrates that the pattern of cell proliferation is disrupted at the same time which may further affect the tissue organization.

3.3.3 Dia1 expression and cell proliferation control cell stratification

To explore the formation of stratified tissue, we used live cell imaging to monitor the onset of suprabasal layer production in cultures of GFP-H2B marked cells plated atop fluorescently labeled collagen (Fig. 3.4A). CTL-H2B initially formed monolayers (Fig. 3.4A). At 24 h, basal layer density in CTL-H2B cultures increased by twofold, accompanied by the onset of a suprabasal layer (Fig. 3.4A). Over the next 75 h, the basal layer density remained constant, whereas the number of suprabasal cells continued to increase (Fig. 3.4A). We then wished

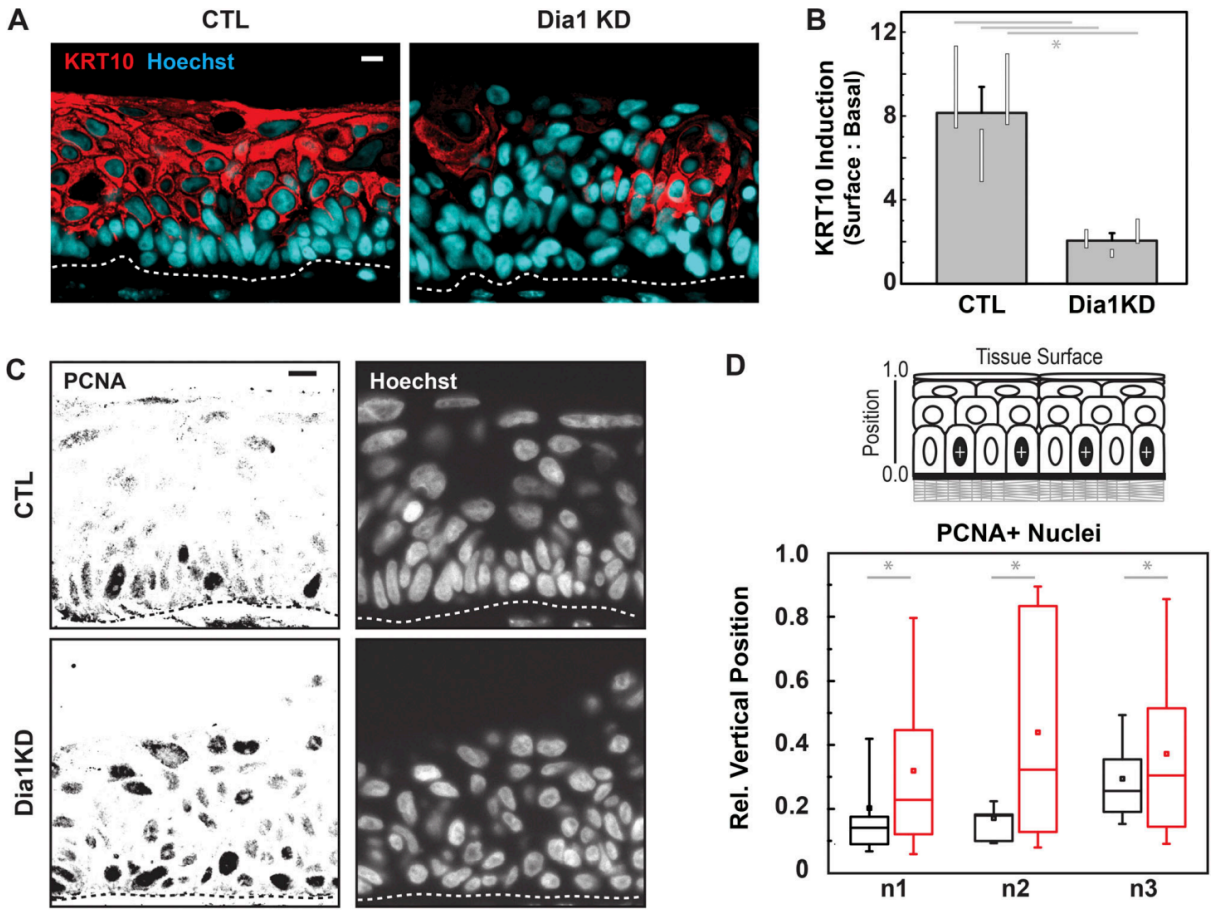

Figure 3.3: Dia1 supports epidermal differentiation. (A) Keratin-10 (KRT10) staining of cross sectioned, paraffin-embedded 3D cultures. (B) Induction of KRT10 expressed as the ratio of cytoplasmic KRT10 signals obtained from cells at the tissue surface and basal layer in a given field. Results represent three independent experiments. To compare CTL and Dia1KD cultures, 15 vs. 20, 20 vs. 20, and 27 vs. 26 fields were analyzed in n1, n2, and n3, respectively. Column graph indicates mean of the three experiments ± SEM. White boxes represent 25–75 percentile range of samples from each experiment. Each individual experiment was subjected to a two-tailed, independent Student's t-test. (C) PCNA staining of paraffin sections. (D) Distribution of PCNA+ cells with respect to vertical position in the epidermis. $PCNA+ = 1.5$ fold greater signal than control, suprabasal nuclei for three independent experiments. 755 vs. 989, 281 vs. 335, and 859 vs. 862 nuclei were analyzed for CTL and Dia1KD cultures in n1, n2, and n3, respectively.

to explore whether stratification would preferentially occur in cells lacking Dia1 expression in mixed cultures of Dia1KD and CTL cells. We produced mixed cultures containing even portions of Dia1KD cells expressing the fluorescent protein Scarlet, marking the cytoplasm, with CTL-H2B cells. After 4 days of growth on collagen gels, confocal imaging was used to assess the spatial relationship between Dia1KD-Scarlet and CTL-H2B cells (Fig. 3.4B). We assessed the lateral positioning of the cells by imaging orthogonal sections of three independent trials (Fig. 3.4B). In control cultures at similar time points, we would expect all cells to have suprabasal partners at this timepoint (Fig. 3.4A). However, we found that 25–35% of control cells lacked suprabasal partners (Fig. 3.4B). For those that did have a suprabasal partner, we found that 30–41% of CTL-H2B cells had acquired Dia1KD-Scarlet cells as suprabasal neighbors, whereas 11–17% of CTL-H2B cells had assumed a suprabasal position overlying a Dia1KD-Scarlet cell (Fig. 3.4B). In 13–25% of cases, CTL-H2B cells wedged between two layers of Dia1KD-Scarlet cells (Fig. 3.4B). These data indicated that Dia1KD-Scarlet cells preferentially localize to the suprabasal compartment when challenged by CTL-H2B cells.

We then looked at perturbations to cell proliferation by expressing p27, a protein which binds cyclin/CDK complexes to arrest the cell cycle ([279]). We performed a similar assay but in this case mixed WT cells with cells overexpressing the cell cycle inhibitor p27. We then quantified the distance of cells from the minimal nucleus height in the field of view (Fig. 3.4C). This allowed us to assess if the populations of proliferative and non-proliferative cells would show different localization within the tissue. We first looked at cells expressing Keratin 10 (K10) – a marker of keratinocyte differentiation. We see cells expressing K10 are localized to a greater height than cells that lack K10 expression (Fig. 3.4D). This matches expectations that differentiating cells would also be stratifying. We then look within the K10- undifferentiated cells at the relative cell heights and see that the cells which express the cell cycle inhibitor p27 are located at a larger height (Fig. 3.4E). This shows that

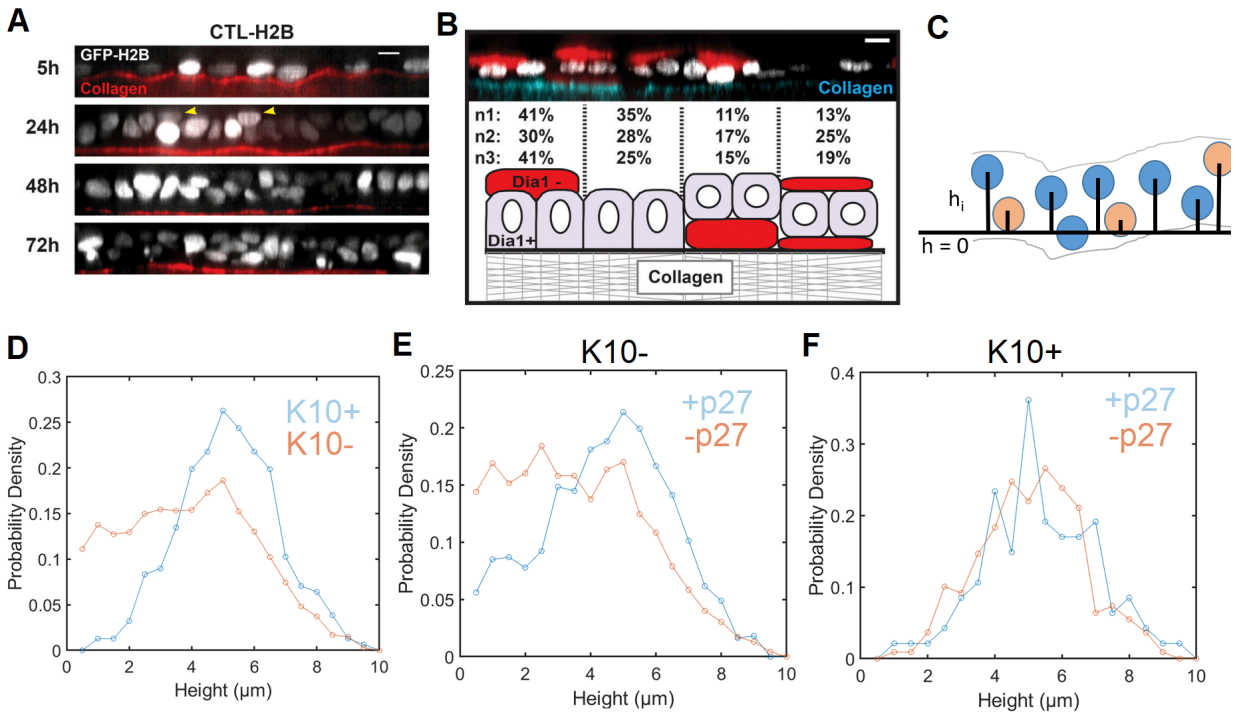

Figure 3.4: (A) Orthogonal slices, averaged across 5 μm thicknesses, of live, GFP-H2B marked cells, plated upon labeled collagen gels for the indicated times. Yellow arrowheads = suprabasal cells.(B) Orthogonal slice along CTL-H2B nuclei bordering a Dia1KD-Scarlet region marked by yellow in D. Frequencies of illustrated spatial relationships between CTL-H2B and Dia1KD-Scarlet cells at boundary regions. Values represent frequencies of three independent experiments, each encompassing 100–400 CTL nuclei. (C) to quantify statification we determined the cell height relative to the lowest nuclei found in a given section (D) Quanitification of the height of K10+ and K10- cells in the stratification assay (E) quantification of the hieght of K10- p27+ and K10- p27- cells in stratification assay (F) quantification of the height of K10+ p27+ and K10+ p27+ cells. Data are from one experiment quantifying $>$ 500 cells across 20 fields of view. Qualitatively similar results for p27 dependence were observed in one other experiment which did not have K10 staining.

independent of differentiation, cells which are not able to progress through the cell cycle are more likely to stratify. When we look at the population of cells which are K10 positive, we see that expression of the cell cycle inhibitor has no effect as both populations show a height consistent with stratification (Fig. 3.4F). Together these results show that the cell cycle state affects localization of cells in a stratified epithelium independent of differentiation.

3.3.4 Differential Dia1 expression and proliferation affects cell organization by altering cell-cell interactions

The observed effects on stratification implicated Dia1 expression and cell proliferative state in modifying cell adhesion and/or cortical mechanics. To query this, we measured the contact angles formed between cell doublets in suspension. This configuration removes all contributions made by adhesion to collagen. In this configuration, the balance of forces at the cell-cell interface and cell-medium interface determines the contact angle ([195]) (Fig. 3.5A). Doublets formed between CTL-H2B and Dia1-rescue cells produced similar contact angles to those produced by Dia1KD-H2B/Dia1KD-Scarlet doublets (Fig. 3.5B, C). However, heterotypic mixtures of CTL-H2B/Dia1KD-Scarlet or Dia1KD-H2B/Dia1-rescue, intriguingly, produced significantly lower contact angles when compared to homotypic interactions. Thus, in contexts where both Dia1-positive and Dia1-negative cells are present, heterotypic junctions fail to develop as robustly as homotypic interactions. This observation, and prior literature ([40]), led us to hypothesize that heterotypic interactions might elicit the separation of Dia1-positive and Dia1-negative cells into distinct compartments.

We then looked at the effects of cell proliferation on cortical mechanics. We measured the contact angles of WT cells (-dox) and compared this with different treatments that inhibit the cell cycle, either overexpression of p27 (+dox p27), addition of a CDK1 inhibitor (5μM RO3306) or culture for 72h in dense contact inhibited cultures (Fig. 3.5D). We observe that across all these conditions the contact angles are increased, consistent with an observation

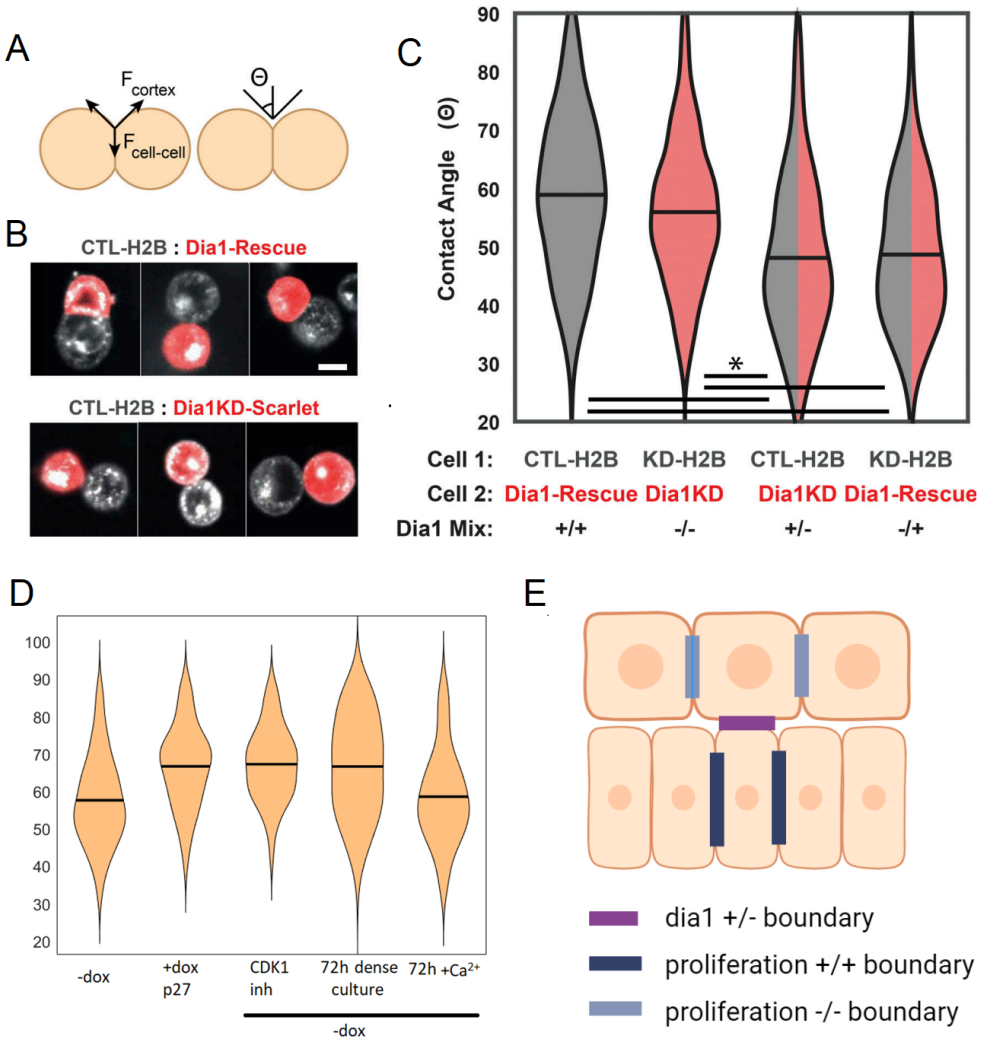

Figure 3.5: Dia1 expression and proliferative state affect cell-cell interactions (A) Diagram of suspended cell doublets indicating how the balance between forces at adhesive ($F_{cell-cell}$) and nonadhesive (F_{cortex}) portions of the cortex impact contact angles (θ). (B) Examples of doublets formed between two Dia1-expressing cells (CTL-H2B and Dia1-rescue) versus those formed between Dia1 expressors and nonexpressors (CTL-H2B and Dia1KD-Scarlet, respectively). (C) Contact angle quantitation of doublets formed between the indicated cell types. Violin plots indicate the median (line) derived from cell doublets pooled from three independent experiments. n = 338, 347, 340, and 322 doublets from left to right. Note, the indicated significant differences ($*$) were also present within each underlying experiment and each condition contained $\approx$ 100 doublets within individual experiments. Two-tailed, independent Student's t-test results are indicated, where $P < 0.05(*)$. Scale bar: 5 μm (D) Contact angle quantitation of doublets formed between the indicated cell types. Violin plots indicate the mean from $>$ 100 doublets in each condition from 1 experiment. Increased contact angle in +dox p27 and CDK1 inhibitor conditions compared to -dox were also observed in 2 other experiments (E) Schematic showing the different interfaces in the skin where the tested interactions are found.

made in MDCK cell culture ([72]). We also cultured cells for 72 hours in high calcium conditions to see whether any of the observed effects could be explained by induction of differentiation. Under these conditions, we expect a mixed population of differentiated and undifferentiated cells, but we observed no change in the contact angle from WT conditions. Therefore, we see that both proliferative state and Dia1 expression affect homotypic and heterotypic contacts, respectively (Fig. 3.5E). These changes in the cell-cell interactions can explain the differences in stratification behavior we observed in our model tissues (Fig. 3.4).

3.4 Discussion

In summary, we have demonstrated that differential formin expression aids in defining the morphology and packing of basal layer epidermal keratinocytes with downstream impacts on differentiation. The study broaches new ground in offering evidence that specific formin expression profiles can guide cell positioning through modulating cell–cell interactions. In addition to the implications for other formins and tissues that must channel stem cell proliferation into defined architectures, the present study offers a unique perspective regarding the basic process of cell sorting. One implication of our work is that the adhesion kinetics associated with a formin become particularly meaningful in tissues populated by cells with heterogeneous formin expression profiles. Viewing formin expression gradients as determinants of tissue domain architecture represents a novel perspective. Extending this possibility to the entire formin family opens a potentially fruitful avenue for exploration of morphology maintenance in all regenerative epithelia. Toward expanding upon the present work, future studies will begin tackling the potential contribution of Dia1-deficiency to *in vivo* wound healing assays, potentially in the context of skin lesions associated with myelodysplastic diseases ([141], [173]).

We also demonstrate a potential role for differences in cell proliferation in guiding cell sorting into different compartments. This effect may have broad implications as differences in

proliferation between epithelial cell populations is a widespread phenomenon found in many epithelial tissues. There are also dramatic changes in cell proliferation during wound healing and development which could affect how cell populations interact. Moreover, in disease states like cancer, there is an increase in proliferation, loss of proliferation gradients, and a concurrent loss of tissue architecture. Our work suggests that changes in the proliferative state of cells could lead to loss of tissue organization. We also observed a loss in differentiation in Dia1 knockdown, this phenotype also changes the proliferative state of the cells in the stratified layers. Normally stratified cells arrest proliferation. It is possible that the increased proliferation of these dia knockdown cells also contributes to the loss of tissue organization. These findings may also be relevant to understanding senescent cells in the skin. Senescence is an aging-related disorder of cells which leads them to become non-proliferative while remaining undifferentiated. These cells occupy space in the stem cell niche and disrupt tissue homeostasis ([14]). Coupling between cell proliferation and sorting is a potential mechanism for senescent cells to be cleared from the tissue to maintain tissue function. Together, our data show the key factors which drive self-organization of cells within the skin, which gives a more detailed understanding of how epithelial cells organize in tissue homeostasis and disease.

3.5 Materials and methods

Cell culture and reagents

The HaCaT line of immortalized keratinocytes was provided by Yu-Ying He (University of Chicago) and was originally developed by the laboratory of Norbert Fusenig (Schoop et al., 1999). HaCaTs were maintained in low calcium DMEM prepared from calcium-free DMEM powder (09800; US Biological), spiked with 40 μM $CaCl_2$, penicillin-streptomycin, L-glutamine, and 10% fetal bovine serum depleted of calcium by Chelex-100 (Sigma-Aldrich) treatment. For calcium-induced differentiation experiments, calcium concentration was

raised to 2.8 mM for the indicated time span. ROCK-inhibitor (Y-27632; Cayman Chemical) was used at 10 μM. RO3306 was purchased from Cayman chemical and used at 5 μM.

Antibodies and subcloning

The following antibodies were used in this study. Mouse anti-Keratin-10 (MS-611-P0; Thermo Fisher Scientific) and mouse anti-PCNA (AB29; Abcam) were used at 1:100 for immunohistochemistry. Rabbit anti-Dia1 (20624-1-AP; ProteinTech and ab129167; Abcam) was used at 1:1,000 for Western blotting and 1:100 for immunohistochemistry. Rabbit anti-GAPDH (G9545; Sigma-Aldrich) was used at 1:2,000 for Western blotting. Rabbit phospho-myosin light chain (S19; 3671; Cell Signaling) was used at 1:100 for immunostaining and 1:1,000 for Western blotting. Mouse anti-E-cadherin (ab1416; Abcam), and rabbit anti-vinculin (v4139; Sigma-Aldrich) were used at 1:100 for immunostaining.

To generate tagged mDia1 constructs, SnapGene software (from GSL Biotech; available at snapgene.com) was used to develop InFusion cloning (Takara) reactions for disabling the miRNA cassette and replacing the GFP in pGIPZ with mScarlet. The mScarlet insert was purchased from IDT as a gene block. Full-length mDia1 (NM-007858), was cloned into pGIPZ-scarlet via PCR amplification (Forward primer:
$5' - GGACTCAGATCTCGAATGGAGCCGTCCGGC - 3'$ and reverse primer:
$5' - TCTAGGATCCCTCGATTAGCTTGCACGGCCAACC - 3'$) and the InFusion cloning system (Takara).

Experiments utilizing coverslip-supported collagen gels and 3D organotypic cultures

For experiments conducted on collagen gels, 75 μl of 3.6 mg/ml rat tail collagen I (354236; Corning) was spread upon activated 25 mm diameter coverslips. Activated coverslips were prepared by sequential incubation with 3-aminopropyltrimethoxysilane and glutaraldehyde as described in Aratyn-Schaus et al. ([11]) . Gel polymerization was induced by exposure to ammonium hydroxide vapor for 4 min, followed by neutralization in PBS (pH 7.4). An

8 mm (inner diameter) glass cloning ring was placed upon the center of the gel which was, subsequently, incubated overnight at 37°C in culture media prior to receiving cells. Labeling of collagen was accomplished by spiking the mixture, 1:50, with AlexaFluor-647-conjugated collagen prepared with a protein labeling kit (A20186; Thermo Fisher Scientific). Unless otherwise noted, 1.75×10^5 cells were plated per cloning ring.

Production of 3D organotypic cultures was based on protocols described by Simpson et al. ([283]) with the following modifications. Collagen I solutions (ALX-522-435-0100; Enzo) of 1.5 ml (final concentration 4 mg/ml) containing J2 fibroblasts at 4.0×10^5 cells/ml were cast in 3 μm pore filter inserts (657630; Greiner) set in deep 6-well plates (355467; BD). Fibroblasts were allowed to condition the collagen plug overnight prior to 1.0×10^6 keratinocytes being added per collagen plug. After 2 days of submerged culture, keratinocytes were brought into contact with air by removing media from the upper chamber and allowed to stratify for the indicated duration.

Both organotypic and keratinocyte cultures grown on coverslip-supported collagen gels were carried out in E-media, based on a 3:1 DMEM:F12 media mixture supplemented with following reagents from Sigma-Aldrich: 180 μM adenine, 5 μg/ml insulin, 5 μg/ml transferrin, 5 μg/ml T3, 0.4 ng/ml hydrocortisone, 10 ng/ml cholera toxin, 4 mM L-glutamine (Sigma-Aldrich), and 10 μg/ml gentamicin/0.25 μg/ml amphotericin B described by Simpson et al. ([283]), containing 5% fetal bovine serum. For the 2 days prior to raising to an air–liquid interface, E-media is spiked with 5 ng/ml EGF (Chemicon).

Lentiviral transduction and CRISPR editing

A pGIPZ construct carrying shRNA targeting nucleotides 1528–1546 (GGATTAATTGATCAAATGA) of the human DIAPH1 mRNA (NM-005219.4) was purchased from Dharmacon (Cat V2LHS-43611). The Dia1 shRNA had been previously described by Bovellan et al. (2014). pGIPZ constructs were co-transfected with pHR1-8.2-deltaR and a VSV-G pseudotyping plasmid (gifts from M. Rosner) into 293T cells for lentivi-

ral particle production via a second-generation system as described by Zufferey et al. ([367]). After concentrating virus using Amicon Ultra-15 30 kD centrifugal filters, HaCaTs were incubated 6 h with concentrated virus in the presence of 4 μg/ml polybrene. shRNA expressing cells were then selected for by incubation with puromycin. pGIPZ lentiviral transduction was also utilized for introducing Scarlet-tagged protein. GFP-H2B lentivirus were produced, similarly, but with a pLKO.1-based vector (gift from Elaine Fuchs; Addgene plasmid 25999; http://n2t.net/addgene:25999; RRID: Addgene-25999). GFP-H2B transduced cells were sorted by the University of Chicago Cytometry and Antibody Technology Core. P27 cells were prepared by lentiviral infection with the lenti-x tet-on 3g system, cells were infected with an ef1a-tet-on 3g lentivirus and selected with G418, then with a tre3g-snap-p27-1-176 lentivirus and selected with puromycin.

Before conducting CRISPR editing, parental HaCaT cells were subcloned and tested to ensure that the chosen clone produced differentiated, 3D cultures. Alt-R CRISPR-Cas9 crRNA targeting DIAPH1 exon1
(5'-UCUUCUUGUCCCGGGUCCCGGUUUUAGAGCUAUGCU-3')
and Alt-R CRISPR-Cas9 tracrRNA ATTO-550 acquired from IDT were complexed with Cas9 enzyme (GeneArt) and transfected into a suitable HaCaT clone using Lipofectamine CRISPRMAX (Thermo Fisher Scientific) as per IDT instructions. Through flow cytometry, successfully transfected cells were identified and deposited as single cells into separate wells and allowed to expand. Successful disruption of the DIAPH1 locus in individual clones was determined by Western blot and editing at the genomic level was assessed by the CRISPR amplicon sequencing service provided by the Massachusetts General Hospital CCIB DNA Core. Specifically, a qPCR amplified portion of the DIAPH1 exon1 genomic sequence (Forward primer: 5'-CAGCGTGAACCGGGACATGGA-3' and reverse primer: 5'-GACCGAGCGAAACGAGGAAGG-3') was sent for sequencing.

Western blotting

Cell lysates were collected in Laemmli buffer and sheared with 22- and 25-gauge needles before carrying out amido black protein assays. Western blots were conducted by running equivalent amounts of protein on $4-20\%$ Tris-Glycine SDS/polyacrylamide gradient gels (Lonza) after reduction with 2-mercaptoethanol and heating to 95°C for 5 min. Protein was transferred to nitrocellulose, overnight at 4°C in standard Tris-Glycine buffer containing 20% methanol without SDS at 30 V. Blots were blocked for 1 h in a 5% milk/0.05% Tween-20/TBS (pH 7.8) solution. Primary antibody incubation occurred overnight at 4°C in blocking buffer followed by washing with TBS/Tween and a 1 h incubation of HRP-conjugated secondary antibody at room temperature. After a final series of TBS/Tween washes, blots were developed using chemiluminescence reagent (Pierce) and film (CL-Xposure; Thermo Fisher Scientific) development. Blots for assessing shRNA-based knockdowns were done similarly; however, a LiCor Odyssey system was used to image fluorescent secondary antibodies and LiCor proprietary blocking buffers and washing instructions were used.

Immunohistochemistry, phalloidin and nuclei staining

Three-dimensional organotypic cultures were fixed in 10% formaldehyde for 3 days then transferred to 70% ethanol. The University of Chicago Human Tissue Resource Center paraffin-embedded, sectioned and provided hematoxylin/eosin stained slides of the skin cultures shown in Fig. 3.1A and Fig. 3.2D. This center also provided banked, paraffin-embedded sections of human skin and tongue samples. For immunohistochemistry, 5 μm sections were de-paraffinized by baking at 55C for 1 h followed by sequential bathing in xylene and ethanol. Antigen-retrieval was conducted by holding the sections in a pH 6.0 citrate solution at 95°C for 10 min. Sections were then blocked in a 2% BSA/TBS solution and incubated with primary antibodies overnight followed by washing and incubation with secondary antibodies for 1 h. After a final series of TBS washes, sections were mounted in gelvatol.

Cell doublet preparation and measurements

To produce cell doublets, cell line pairs were cocultured together at subconfluent density

for 1 day, then treated with trypsin until detachment from cell culture dishes. Cells were stained with CellMask Deep Red Plasma membrane Stain (Thermo Fisher Scientific) for 10 min, then resuspended in culture medium. Around 15,000 cells in 200 μl of medium were transferred to a PDMS well, which was pretreated with 1% Pluronic f127 for 1 h then washed three times with 1X PBS. Cells were incubated in the wells at 37°C and 5% CO2 for 4 h, then imaged at room temperature for less than 30 min. Cells were imaged by mounting PDMS wells on coverglass and using imaging methods described below. The contact angle was manually measured between isolated pairs of cells using ImageJ.

Microscopy and live cell imaging

Confocal microscopy of fixed and live samples was conducted on an inverted microscope (Ti-E; Nikon) with a confocal scan head (CSUX; Yokogawa Electric Corporation) and laser-merge module housing 491-, 561-, and 642-nm laser lines (Spectral Applied Research), a stage controller (Prior), and a cooled CCD (HQ2-Roper Scientific) or CMOS (Zyla-Andor) camera. Images were acquired using 20 × 0.75 NA Plan Fluor multi-immersion, 40 × 1.15 NA Plan Apochromat water immersion extra-long working distance and 60 × 1.2 NA Plan Apochromat water immersion objectives (all from Nikon). This set up enabled capture of GFP, mScarlet, AlexaFluor 488/561/642, and SPY650 fluorophores throughout the study. Metamorph software was used for image acquisition. Live-cell imaging utilized a stage incubator for temperature, humidity, and CO2 control (Chamlide TC and FC-5N; Quorum Technologies). The stage adapter, stage cover, and objective were maintained at 37°C, whereas humidified 5% CO2 air was maintained at 50C at its source to prevent condensation within its tubing. Unless otherwise noted, serial z-sections were done at 0.25-μm steps for fixed samples and 0.5-μm steps for live samples. For live, lateral membrane growth studies, cells were preincubated with 50 nM siR-actin (Cytoskeleton) for 1 h prior to trypsinization and immediate transfer to an imaging chamber. A 50 nM siR-actin concentration was maintained in the imaging media.

Image analysis and processing

ImageJ and MatLab were used for image analysis. To make basal nuclei more visible in images of living H2B-labeled 3D cultures the following filtering technique was applied to average projections of the planes spanning 10 μm up from the lowest in focus nuclear signal. The original image was modified by applying a sigma = 40 pixel median filter. The original image was then divided by the transformed image to remove uneven background signal. For studies concerning positional relationships, H2B-labeled cells were considered to have a suprabasal neighbor if Scarlet signal from a neighbor occluded the nuclear signal by $> 50\%$. For studies utilizing only H2B-labeled cells, cells were considered suprabasal if their H2B signal occluded $> 50\%$ of an underlying H2B signal or could be seen to overlie 2 or more H2B-labeled nuclei. Collagen deformation below forming junctions was taken to be the distance between the line connecting the lowest observed collagen positions between two adjacent cells and the highest position marked at forming junctions.

Statistics

Where indicated, independent two-sample Student's t-tests were utilized to calculate statistical significance with P values < 0.05 indicative of a significant difference being detected between means. Data distribution was assumed to be normal, but this was not formally tested. In cases where the sample size was small ($n < 7$), a nonparametric two-tailed Mann–Whitney U test was performed.

CHAPTER 4

TISSUE CONFINEMENT REGULATES CELL GROWTH AND SIZE IN EPITHELIA

This section is reproduced from the article Tissue confinement regulates cell growth and size in epithelia published in biorxiv by John Devany, Martin J Falk, Liam J Holt, Arvind Murugan, Margaret L Gardel ([71])

Modeling presented in this chapter was done by Martin Falk. Martin Falk, Arvind Murugan, Liam holt, and Margaret Gardel helped with planning experimenets and editing/writing.

4.1 Abstract

Cell proliferation is a central process in tissue development, homeostasis and disease. Yet how proliferation is regulated in the tissue context remains poorly understood. Here, we introduce a quantitative framework to elucidate how tissue growth dynamics regulate cell proliferation. We show that tissue growth causes confinement that suppresses cell growth; however, this confinement does not directly affect the cell cycle. This leads to uncoupling between rates of cell growth and division in epithelia and, thereby, reduces cell size. Division becomes arrested at a minimal cell size, which is consistent across diverse epithelia *in vivo*. Here, the nucleus approaches a volume limit set by the compacted genome. The loss of Cyclin D1-dependent cell size regulation results in an abnormally high nuclear-to-cytoplasmic volume ratio and DNA damage. Overall, we demonstrate how epithelial proliferation is regulated by the interplay between tissue confinement and cell size regulation.

4.2 Introduction

Regulation of cell proliferation is a central question for understanding tissue development, growth and homeostasis ([215], [221]). In contrast to the exponential proliferation of isolated

cells ([34],[274]), multicellular tissue requires tight coupling between cell proliferation and tissue growth ([132]). One proposed mechanism for regulating proliferation in epithelia is the so-called process of "contact inhibition of proliferation" (henceforth referred to as contact inhibition) where cell proliferation becomes highly restricted due to spatial constraints imposed by the tissue ([132], [196]). The disruption of contact inhibition results in cell overgrowth and altered tissue architecture ([92], [147], [172]). Therefore, contact inhibition is thought to play a key role in maintaining tissue homeostasis and preventing tumor formation ([132], [201]). However, because contact inhibition is regulated through multiple signaling pathways and largely unknown parameters, we currently lack a framework for understanding the process across diverse tissues. This is evident from the literature where contact inhibition is described as dependent on cell density ([129]), adhesion signaling ([147], [196]) and mechanical stress ([132], [228]). As these variables are difficult to manipulate independently, it remains unclear how tissue geometry and growth dynamics impacts size and growth of constituent cells.

The regulation of size and growth of isolated mammalian cells is, by contrast, well understood ([38], [300], [361], [360]). Single cells go through cycles of coupled growth and division and have stable cell size due to feedback between cell growth and division. However, there appear to be different feedback mechanisms acting in different contexts. For example, single cells mainly sense the total amount of cell growth throughout the cell cycle to regulate the length of cell cycle phases ([38], [300]). In contrast, mouse epidermal tissue shows feedback via a cell size checkpoint preventing small cells from entering S phase ([348]). Due to limited data *in vivo* it remains unclear if this is a consequence of tissue specific behavior in the skin or could reflect a difference in regulation between single cells and epithelial tissue. Several lines of evidence suggest the latter is true. For instance, the cell cycle duration can be on the scale of weeks or months *in vivo* ([275]), challenging established dilution-based mechanisms of cell cycle regulation ([361], [360]). Further, prior work has shown a possible switch to

size-dependent regulation of the cell cycle in cell culture models of epithelial tissue ([246], [245]). However, we lack a systematic study that explores how tissue-scale growth dynamics impact regulation of cell size and growth in epithelia.

To understand how cell proliferation is regulated in epithelium, we first performed a meta-analysis of cell size data and found that epithelial cell sizes are remarkably consistent and highly context dependent. The cell size in epithelial tissue *in vivo* is always smaller than single cells in culture. However, we could recapitulate the *in vivo* cell size using a cell culture model of epithelial tissue formation, indicating that tissue-scale phenomena impact cell size regulation. To quantitatively explore this, we employed model epithelial tissues with varied growth rates. We then introduce a general framework to quantify how tissue-scale growth dynamics constrain cell growth, providing a measure of "tissue confinement". We show that increasing tissue confinement reduces cell growth and YAP/TAZ signaling but does not impact the cell cycle duration directly. Instead, cell cycle duration is regulated by cell size. There is a sharp cell cycle arrest at a cell volume of $\approx$1000 μm3 , consistent with cell size found *in vivo*. In both epithelial and single cell contexts, cell size regulation is well described by a "G1 sizer model" with a tunable growth rate. In epithelia cyclin D1 protein levels are strongly cell size-dependent and overexpression of cyclin D1 reduces the minimal cell size. This suggests that the levels of cyclin D1 controls size-dependent cell cycle arrest. We see that abnormally small cells display DNA damage as these cells approach a size limit set by the volume occupied by the fully compacted genome. This suggests that, in addition to mediating cell cycle arrest during contact inhibition, cell size regulation pathways are critical for maintaining epithelial homeostasis. Overall, we demonstrate the general mechanisms of cell growth and division regulation in epithelia which provides new insight into proliferative processes in tissue development, homeostasis, and disease.

4.3 Results

4.3.1 Epithelial cell size is context dependent

To screen for varied cell size regulation in epithelial tissue, we systematically compared cell volume from different tissues *in vivo* and cell culture models (Table S1). We compiled these data from available sources including histology sections from the human protein atlas (Fig. 4.1A) ([315]), 3D segmentation data from Allen Cell Institute (Fig. 4.1A) (3D cell viewer - Allen Cell Explorer.) and published cell volume measurements ([38], [80], [82], [104], [110], [139], [174], [199], [213], [227], [232], [237], [273], [322], [357], [362]). When cell volume measurements were not available, we estimated cell volume by identifying cells perpendicular to the tissue slice and then measuring their length and width. We confirmed that this provides an accurate estimation of volume from benchmarking against full 3D imaging (Fig. 4.2, 4.3). Across 15 tissue types in the human protein atlas, we find the volume of epithelial cells is surprisingly consistent, with a narrow distribution of 630±180 μm^3 (Fig. 4.1B, circles). By comparison, the volume across 12 types of isolated epithelial or epithelial-like cells is consistently measured to be severalfold larger, with a volume of 2330±650 μm^3 (Fig. 4.1B, squares) ([38], [110], [174], [232], [237], [322],[362]). Interestingly, the volumes of epithelial cells cultured in 3D more closely matched those *in vivo*, with a mean of 1020±520 μm^3 (Fig. 4.1B, diamonds) ([80], [82], [104], [139], [199], [213], [273]). These data suggest that epithelial cell volume is strongly influenced by the tissue environment.

To test this hypothesis, we utilized several different epithelial cell lines (Madin-Darby canine kidney (MDCK), Caco-2 and HaCaT) to measure the cell volume in either subconfluent colonies (SC) or mature epithelium (ME). Controlling cell plating density allowed for the formation of subconfluent colonies each comprised of 50-1000 cells or a nearly confluent monolayer on collagen gels (see Methods). After the initial plating of monolayers, cell dynamics drive changes in their density, shape and speed over the next 1-2 days ([72]); we define

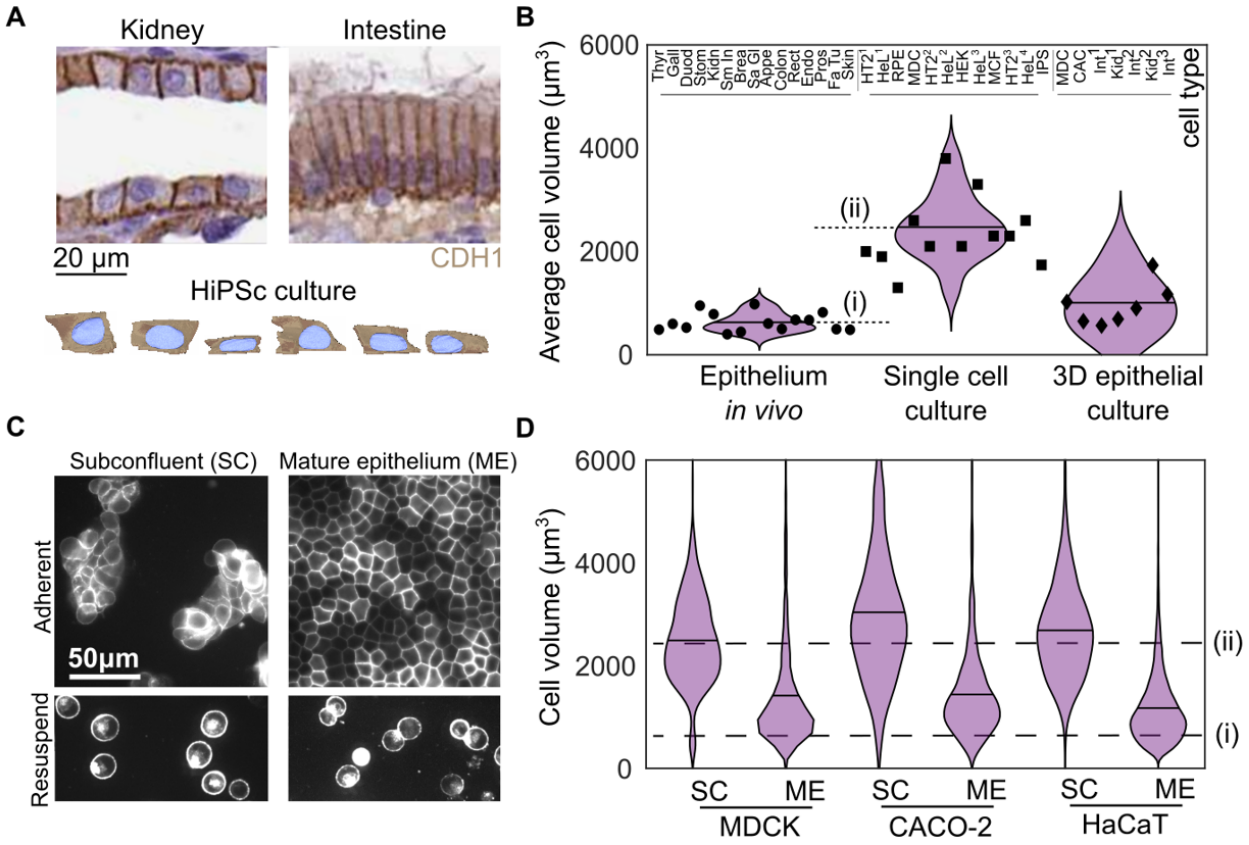

Figure 4.1: Epithelial cell size is consistent across tissues but context dependent (A) Histology sections published by the Human Protein atlas showing E-cadherin (CDH1) staining kidney and Intestine (Duodenum) tissue (image credit: Human Protein Atlas) and human induced pluripotent stem cell (HiPSc) segmentation data from Allen Cell Institute (Available from allencell.org/3d-cell-viewer). (B) Cell volume from 15 tissues *in vivo* (circles), 12 published measurements from cell lines cultured as single cells (squares) and 7 measurements from 3D epithelial cell cultures (diamonds). Each data point is the average cell size from >50 cells for a given cell type. Measurement details available in Table S1. Dashed lines show the average cell volumes from epithelium *in vivo* (i) and in single cell culture (ii) (C) (Top) Images of MDCK cells with fluorescently labeled cell membranes (stargazin-gfp) in subconfluent colonies (SC) and mature epithelium (ME). (bottom) Cells under each condition are also shown after being treated with trypsin for 10 minutes and resuspended. (D) Cell volume in SC and ME for MDCK, CACO-2 and HaCaT cell lines. Dashed lines show the average cell volumes from epithelium *in vivo* (i) and in single cell culture (ii) from B ($N = cells(experiments), N_{MDCK-SC} = 5884(4), N_{MDCK-ME} = 13513(5), N_{CACO2-SC} = 732(1), N_{CACO2-ME} = 2735(2), N_{HaCaT-SC} = 9248(2), N_{HaCaT-ME} = 13451(2)$).

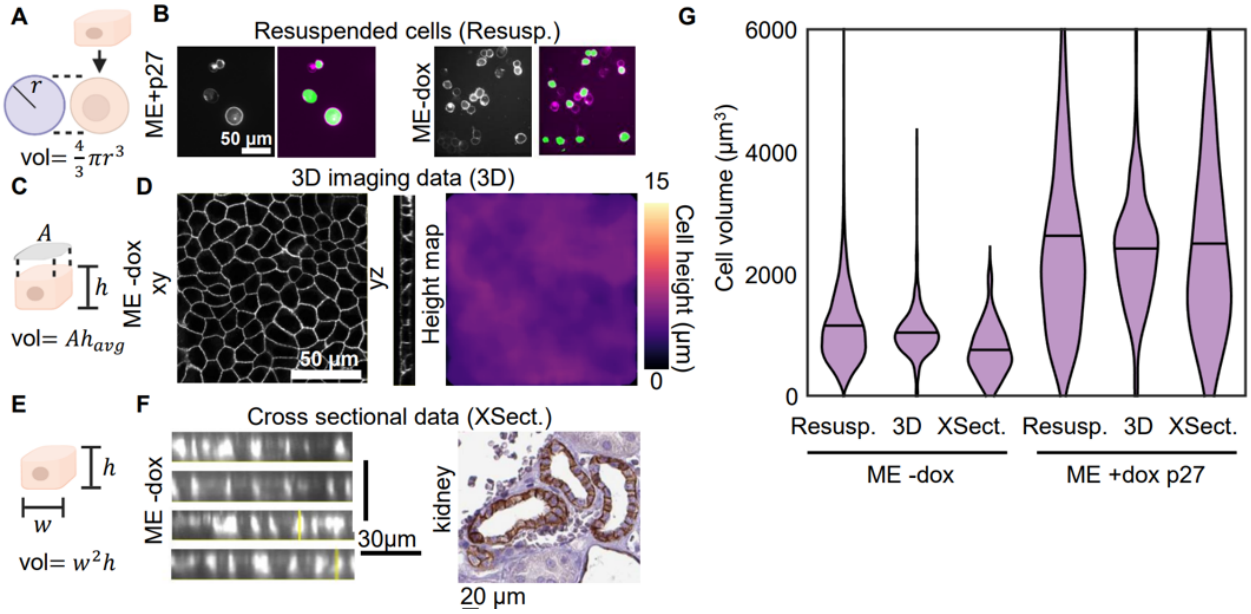

Figure 4.2: Different volume measurement methods give consistent results. We used several methods to estimate the cell volume across different experiments. While the measurement in 3D is the most accurate method of measuring the cell volume it is not feasible in all experiments. We verified that our other methods of approximation in resuspension and cross section yield the same results as full 3D imaging. (A) Schematic of cell volume measurement in resuspension (Resusp.). The resuspended cell is nearly spherical, and a measurement of the radius is used to determine the cell volume (B) Labeled membranes of resuspendend MDCK cells and corresponding cell segmentation. (C) Schematic of cell volume measurements in 3D – a height map is constructed by measuring the intensity profile at each pixel to identify the top and bottom membrane. The average cell height is multiplied by the cell cross sectional area to obtain the volume (D) 3D z-stack of labeled MDCK cell membranes in XY and YZ views. A height map measured from membranes in the image is displayed and used to measure volume from 2D segmented cell area. (E) schematic cell volume measurements in cross section (XSect.) – cells perpendicular to the imaging plane are identified and the length and width of the cell area measured to estimate the cell volume (F) images of MDCK cell membranes in cross sectional and kidney histology from Human Protein Atlas (image credit: Human Protein Atlas) stained for E-cadherin (CDH1) show cross sectional views of human kidney cells (G) quantification of cell volume using each method for MDCK tet-on P27 cells in ME-dox and ME+dox conditions. ($N_{R-} = 12641(5), N_{3D-} = 1405(2), N_{Xsect-} = 78(1), N_{R+} = 1136(3), N_{3D+} =, 324(2) N_{Xsect+} = 59(1)$).

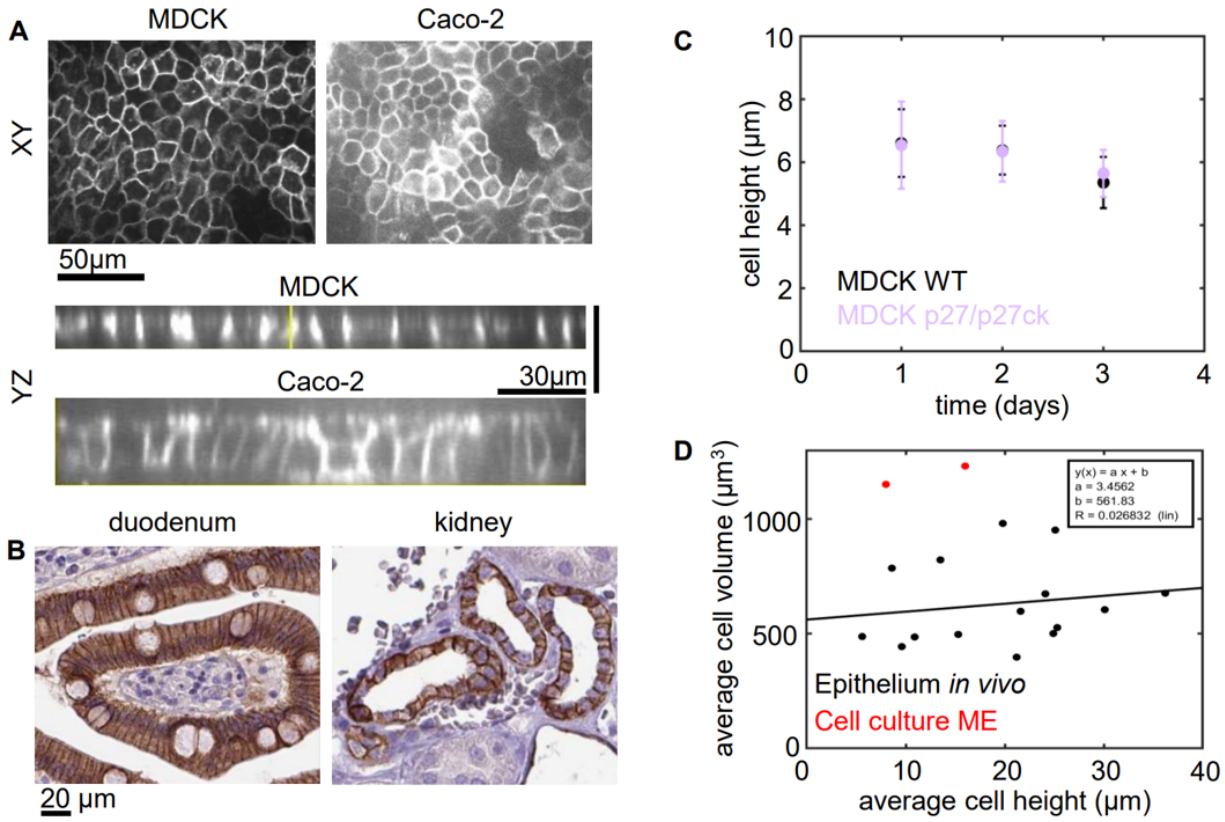

Figure 4.3: Cell height is consistent for a given cell type but varies between tissues. Across our dataset we observed a large variation in cell height. We verified that across experiments and different time points with the same cell line the height remains nearly consistent. We also show that the difference in volume between different cell types is not a consequence of differences in height. (A) MDCK and Caco-2 cell membranes showing XY and YZ views of monolayers. (B) Histology section images from Human Protein Atlas (image credit: Human Protein Atlas) of Duodenum and Kidney tissue stained for E-cadherin (CDH1). (C) Cell height of MDCK monolayers across different time points. Data are from 3D segmentation. Error bar shows standard deviation of 20 different fields of view containing >100 cells from 1 experiment each. P27/p27ck are monolayers made from a mixture of Tet-On p27 and Tet-On p27ck cells with doxycycline added at t=0. (D) Plot of cell height vs volume measured in cross section across 15 different tissues *in vivo* analyzed in Fig. 4.1B and two cell lines cultured as ME *in vitro* (MDCK and CACO-2). Black line shows linear fit to *in vivo* data. Variations in cell height do not explain the variation in cell volume.

a mature epithelium as the time at which these properties stop changing in time (see Methods). Cell sizes were visualized with a fluorescently tagged membrane protein (stargazin-gfp (CACNG2-gfp) or stargazin-halotag) (Fig. 4.1C). To facilitate measurement of cell volume, cells were trypsinized, resuspended and then imaged (Fig. 4.1C, Fig. 4.2, see Methods). When in sub-confluent colonies, the cell volume of all three epithelial cell types is ≈ 2800 μm^3 (Fig. 4.1D, SC), consistent with the mean value of single cells in Fig. 4.1B (Fig. 4.1D, dashed line (ii)). Further, we found that ME culture conditions reduced the cell volume by 60% to plateau at ≈ 1000 μm^3 (Fig. 4.4), a size consistent with *in vivo* data reported in Fig. 4.1B (Fig. 4.1D, dashed line (i),). We performed the same experiment on two cell lines which do not form coherent colonies, retinal pigment epithelial cells (RPE-1) and Mouse embryonic fibroblasts (MEF) and did not see size reduction (Fig. 4.5). This suggests this context-dependency of cell size may be specific to epithelium. Together, these data suggest that contact inhibition qualitatively changes cell size regulation across diverse epithelia.

4.3.2 Cell size reduction involves an uncoupling of growth and the cell cycle

To query how cell growth and division rates change during the transition from subconfluent colonies to mature epithelium, live cell imaging was used to monitor changes in cell size and number. The data was aligned such that t=0 h denotes the onset of confluence (OC). For all earlier times, cells are in subconfluent colonies. By $t > 12$ h the cell movement has ceased, and density is constant; we denote this as a mature epithelium (Fig. 4.6A). We first consider cell division and growth rates for $t << 0h$ (SC), $t \approx 0h$ (OC) and $t >> 0h$ (ME). Cell division rate, obtained by cell counting measurements, was completely arrested in the ME but only suppressed by $\approx 40\%$ at OC, as compared to SC (Fig. 4.6B, black bars). By contrast, the cell growth, obtained by quantifying the rate of protein dilution using pulse chase labeling (see Methods), was suppressed almost entirely at OC (Fig. 4.6B, purple bars). These data indicate suppression of cell growth and cycle are not tightly coupled during the

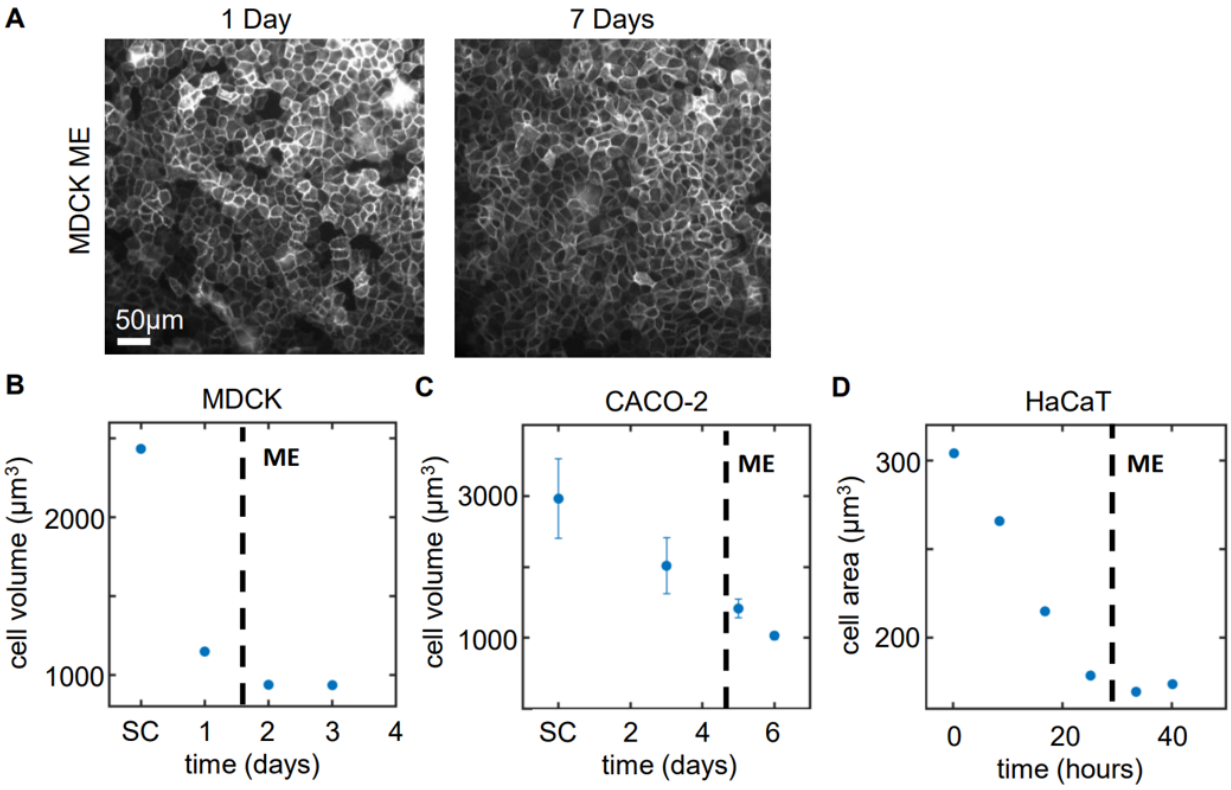

Figure 4.4: Cell volume reaches a plateau in mature epithelium (ME). We wanted to confirm that in the mature epithelium there are no changes in cell volume. We performed volume measurements across different time points for each cell line and define what time points we consider the system to reach ME by for each cell line. Due to differences in division rates this varies but all cell lines show a decreasing size over time leading to a plateau. (A) MDCK cells with labeled membranes in monolayers imaged at ME+1 day and ME+7 days (B) Measurements of MDCK cell volume at different time points in. Data are from 3D segmentation of $>$ 200 cells at each time point from $>$ 10 fields of view in 1 experiment (C) CACO-2 cell volume measured in resuspension at different time points. Error bar shows standard deviation from 2 experimental replicates. (D) Measurement of HaCaT cell area at different time points. Each point is the average area from n=50 cells from 3 different fields of view in a single time lapse experiment. In all experiments t=0 is the onset of confluence experiments and the point of ME is indicated with a dashed line.

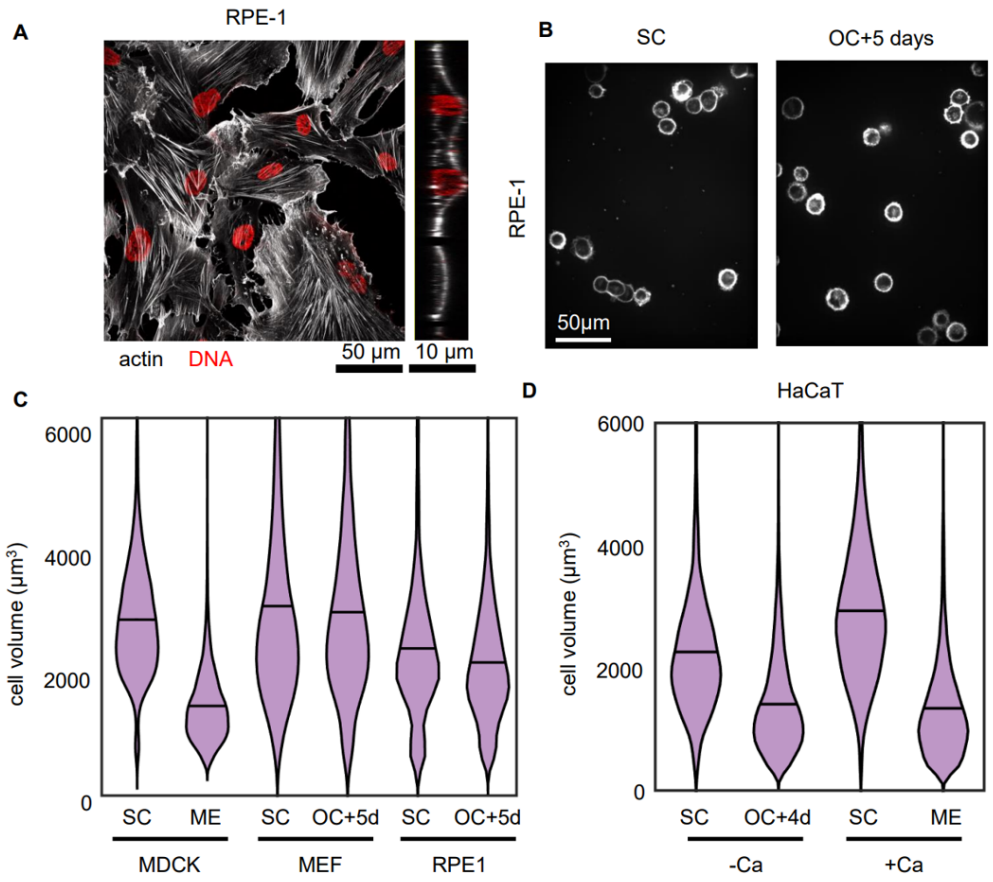

Figure 4.5: Cell volume does not change during contact inhibition of non-epithelial cells. We wanted to determine if the uncoupling of cell growth and division also extends to other cell types which would not form epithelium *in vivo*. We tested two cell lines with fibroblast-like morphology and found that these do not show cell size changes. HaCaT cells are routinely cultured in the absence of calcium which inhibits junction maturation and differentiation, but this did not inhibit cell size reduction in HaCaT cell under confinement. Future work is required to understand this difference in behavior for epithelial and non-epithelial cells. (A) staining for actin and DNA in retinal pigment epithelial (RPE-1) cells. Cells do not form coherent colonies or show epithelial morphology (B) RPE-1 cells in suspension labeled with CellMask Deep Red from 5 day old cultures plated at low density to remain SC all 5 days or high density to reach OC at day 0. (C) Volume measured in resuspension of MDCK, RPE-1 and mouse embryonic fibroblast (MEF) cells SC and ME-like culture conditions. SC – subconfluent, ME- mature epithelium at day 4, OC+5d- 5 days after the onset of confluence N = cells (exp) ($N_{MDCK-SC} = 4940(3), N_{MDCK-ME} = 12641(5), N_{MEF-SC} = 1459(1), N_{MEF-OC5} = 1352(1), N_{RPE-SC} = 906(2), N_{RPE-OC5} = 3429(2)$) (D) Volume measured in resuspension of HaCaT cells in SC and ME cultures with and without calcium. -Ca – 40uM calcium, +Ca – 1.8mM calcium ($N_{SC-Ca} = 3642(2), N_{OC4-Ca} = 23996(2), N_{SC+Ca} = 9248(2), N_{ME+Ca} = 13451(2)$).

transition from subconfluent to confluent tissue. Instead, cell growth is suppressed acutely at OC whereas cell cycle progression is only impacted in later stages (Fig. 4.6C). In single cells, cell growth and division are coupled to maintain a constant size ([361]). A division rate exceeding the growth rate would, instead, be expected to result in cell size reduction.

To test this hypothesis, we measured the cell size between $t = 0$ and 18 h during the transition from OC to ME. Over this time, the cell height remained constant, such that changes in cell area were accurate indicators of cell volume (Fig. 4.3C). The average cell area from a population of ≈ 1000 cells decreases by $\approx 50\%$ from OC ($t = 0$ h) to ME (Fig. 4.6D). To determine the mechanism driving changes in cell volume we performed single cell tracking. Cells that divided near the beginning of the experiment ($t = 0$ h) were identified and tracked through the experiment. Individual cell trajectories revealed that the cell size reduction occurred by successive cell division events in the absence of cell growth (Fig. 4.6E, F). Indeed, across a large population of mother-daughter cell pairs, the cell size of a daughter cell 8 hr ($\approx 1/2$ cell cycle time, τ) post cell division remained approximately half that of the mother cell size (Fig. 4.6G). This indicates minimal cell growth during the cell cycle. This is in stark contrast with subconfluent cells, where a cell grows at a constant rate and doubles in size prior to division into two daughter cells ([38]). For single cells, we would expect the cell to grow by $\approx 50\%$ at 8 hours post division, resulting in a slope of $\approx 3/4$ (Fig. 4.6G, dashed line)

To demonstrate that cell division is necessary for cell size to decrease, experiments similar to those in Fig. 4.6A were performed with a Tet-On p27 MDCK cell line to artificially arrest the cell cycle in the presence of doxycycline ([279]). In the absence of dox (-dox), the volume decreases in ME compared to SC, similar to our previous experiments (Fig. 4.6H, I). Addition of doxycycline at OC prevented cell volume decrease in ME (ME +dox p27), and the volume of these cells remained similar to that of SC (Fig. 4.6H, I). Induction of a mutant p27 which does not arrest the cell cycle (+dox p27ck) ([324]) had no effect on cell size in ME

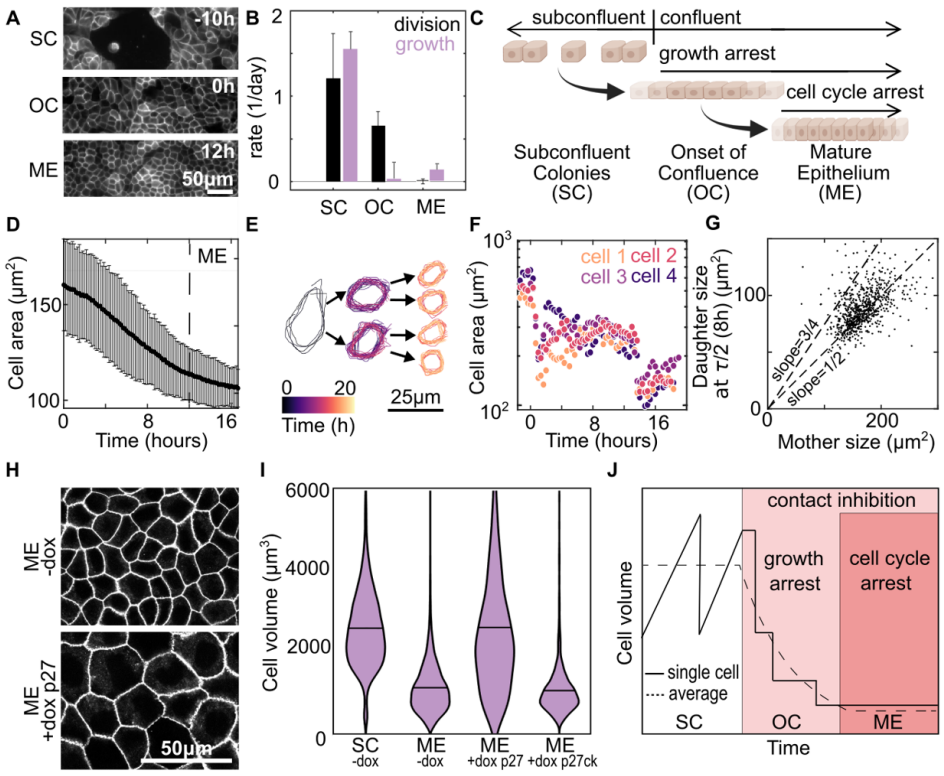

Figure 4.6: Uncoupling of division and growth at the onset of confluence leads to cell size reduction (A) Images of MDCK cell membranes at time points during the transition from subconfluent colonies (SC) ($t = -10h$) to mature epithelium (ME) ($t = 12h$). The data are aligned such that onset of confluency (OC) occurs at $t = 0h$. (B) Average rates of cell division (black) and growth (purple) at SC, OC and ME. For growth data protein dilution is measured by CellTrace, $n = 10$ fields of view with > 100 cells from 1 experiment; Error bars are S.E.M. of the fields of view. For division rate, the change in cell number, determined by a cell counter, are averaged from 3 experiments. Error bars are S.D. of experiments (C) Schematic summarizing result that, at the onset of confluence, there is a temporal decoupling of growth and cell cycle arrest. (D) Average cell area over time, $t = 0$ is OC. Error bars are S.D. of 30 fields of view each containing > 500 cells; Time at which ME forms indicated by dashed line. (E) Outline of a representative cell, and subsequent daughter cells, over the experiment. (F) Areas of 4 representative cells over the course of the experiment. Traces are shifted in time so that the first cell division occurs at time 0 for all cells. (G) Area of daughter cell halfway through the cell cycle versus the area of mother cell ($N = 758$ cells from 1 experiment. Linear fit $slope = 0.52$) (H) Images of cell membrane at $t = ME{+}3$ days in monolayers formed from Tet-On P27 cells. ME were formed under control conditions (-dox) or with the cell cycle inhibited (+dox p27) by the addition of doxycycline at $t = 0h$ (I) Cell volumes in SC and ME with Tet-On p27 or Tet-On p27ck (non-cell cycle inhibiting control) in control conditions (-dox) or in ME with doxycycline added at $t = 0hr$. SC and ME -dox data also displayed in Fig. 4.1D ($N_{SC} = 5884(4) N_{ME} = 13513(5) N_{ME+p27} = 1606(3) N_{ME+p27ck} = 1930(3)$). (J) schematic of the mechanism of cell volume regulation during the transition from SC to ME.

(Fig. 4.6I). Together, these data demonstrate that temporal uncoupling of cell growth and cell cycle result the cell size reduction during formation of mature epithelial tissue. At the onset of confluence, cell growth is highly suppressed and cell volume reduces by division in absence of cell growth (Fig. 4.6J). Then at later times the cell cycle also becomes arrested, and cells reach a final cell size which is comparable to epithelium *in vivo*. We next sought to understand regulation of cell growth and cycle in the epithelium.

4.3.3 Tissue confinement regulates cell growth

These data motivate the need to introduce a quantitative framework to relate the tissue and cell growth rates. We first consider the growth of a multi-cellular tissue with initial area A_0 and time-dependent area, $A(t)$ Then, consider this tissue broken up into individual cells to represent the proliferation dynamics of this tissue in the absence of spatial constraints (Fig. 4.7A). The collection of single cells grows in total size exponentially, such that the total time-dependent area is described by $A_U(t) \approx 2^{t/\tau}$, where τ is the average cell cycle time. The deviation of the tissue growth from this hypothetical maximum exponential rate quantifies the constraints tissue growth places on cell growth. For a certain tissue area, A', if the ratio of the tissue growth rate to the unconfined growth rate: $\frac{\frac{dA}{dT}|_{A'}}{\frac{dA_U}{dT}|_{A'}}$ is less than 1, then the tissue growth dynamics constrain cell proliferation. We then define the tissue confinement $C(A') = 1 - \frac{\frac{dA}{dT}|_{A'}}{\frac{dA_U}{dT}|_{A'}}$ such that there is no confinement effect ($C = 0$) when single cells and tissues have identical growth dynamics and $C = 1$ when tissue growth rate is zero.

We explored this framework using model tissues comprised of large, circular colonies of MDCK cells, chosen for their well-characterized growth dynamics and the facility of controlling their size ([117], [245]). Circular colonies of variable size A_0 from $\approx 1 - 7\ mm^2$ were formed by seeding the cells in a Polydimethylsiloxane (PDMS) stencil atop a glass coverslip (Fig. 4.7B,C). The stencil was then released to allow for colony expansion for $\Delta t = 48$ hours (Fig. 4.7D). Importantly, the colony expansion is determined by radial migration speed v of

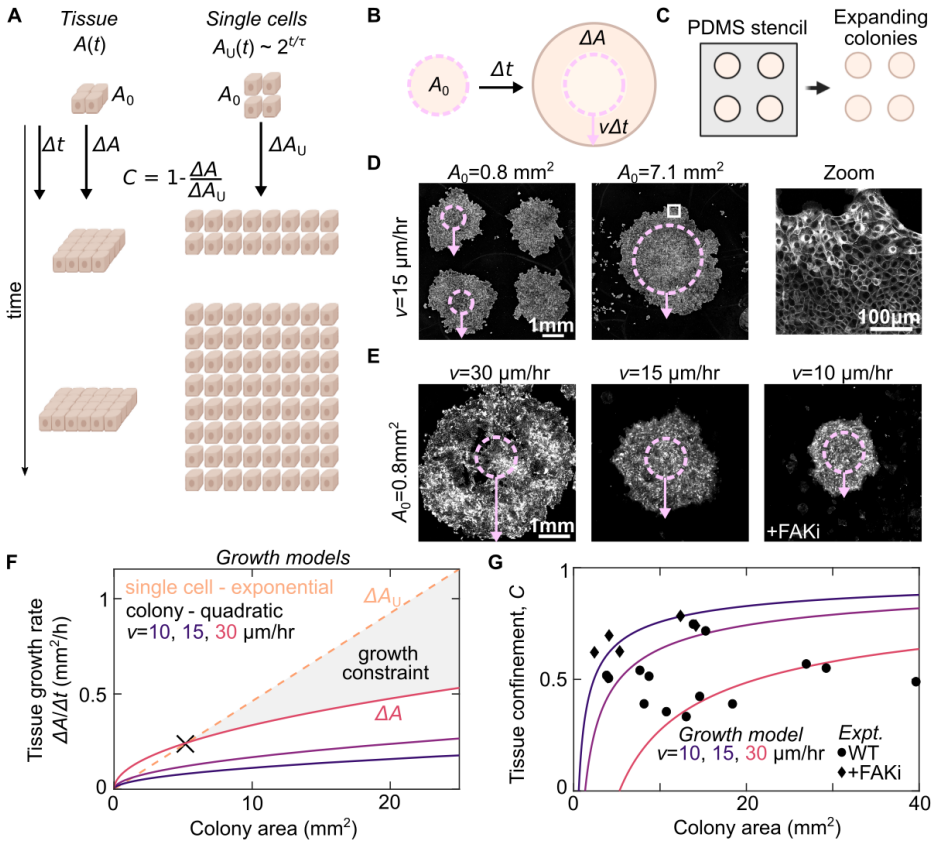

Figure 4.7: Tissue confinement quantifies how tissue-scale growth dynamics constrain cell growth (A) We consider the growth dynamics of a portion of multicellular tissue with time-dependent size $A(t)$ with that of comprised of isolated cells of equal initial size, A_0. The population of individual cells grows exponentially $A_u(t) \approx 2^{t/\tau}$. The confinement, C, is measured by comparing the relative growth rates. (B) Schematic of expanding colony system. Cell colony of initial size A_0 expands at a constant radial velocity v such that, for a given time interval Δt, the radius increases by $v\Delta t$ (C) Cells are initially seeded into a PDMS well of defined size A_0 then this well is removed to initiate colony expansion (D) Cell Mask Deep Red staining in expanding MDCK colonies with two different initial sizes at $\Delta t = 48$ hours after removing the barrier. Overlay shows the initial size A_0 (dashed circle) and expansion $v\Delta t$ (arrow). Zoom-in shows part of larger monolayer (white box). (E) CellTrace Far Red staining of expanding MDCK colonies with variation in expansion rate from variation in WT dynamics and under FAK inhibition (500nM PND-1186) Images are scaled differently for clarity and intensity is not comparable in these images. (F) Quadratic growth models of colonies as a function of tissue area and expansion rate compared with a model of the exponential rate for single cells growing at the experimentally measured proliferation rate 15 hours. (F) plot of the tissue confinement parameter, defined in the main text, calculated from comparing the model of colony growth rate to the model of single cell growth rate. Curves show tissue confinement as a function of tissue area and expansion rate. Black points show confinement measurements from the experimentally determined area growth rate of expanding colonies at $\Delta t = 48$ hours (see methods).

cells at the periphery to increase the colony radius by $v\Delta t$ (Fig. 4.7B, arrow). Consistent with previous studies, the radial expansion rate was independent of colony size (Fig. 4.7D, Fig. 4.8). This results in a growth rate that scales quadratically with colony area (see Methods). For a given colony area, variation in v provides additional control over colony growth rate (Fig. 4.7E). Under control conditions, v varied between experiments from 15-30 μm/hr (Fig. 4.8). This tissue growth rate was not impacted when inhibiting cell division but was reduced by inhibiting cell migration by a focal adhesion kinase inhibitor (FAKi) (Fig. 4.8). Thus, variations in both the initial colony size and expansion velocity provide a wide range of tissue growth rates.

We generated model curves of the expected colony growth rates for the ranges of areas and edge velocities observed experimentally (Fig. 4.7F, solid lines). These rates were then compared to that expected for exponential growth of single cells, using the experimentally measured doubling time of 15 h (Fig. 4.7F, dashed line). For small areas, exponential growth is smaller than the growth rate of the expanding colony (Fig. 4.7F); here tissue-scale growth dynamics do not constrain cell proliferation. This is the behavior for SC. By contrast, for large areas, expanding colony growth rates become substantially lower than the exponential growth of single cells (e.g. Fig. 4.7F, gray shaded region). Here, tissue growth dynamics constrain cell proliferation. The colony area when exponential growth and quadratic growth rates are equal demarks the transition between these two regimes and, here, $C = 0$ (Fig. 4.7F, black X). For each given growth model, the confinement C is plotted as a function of colony area (Fig. 4.7G, lines). Confinement was determined from experimental data with varying A_0 and v (Fig. 4.7G, points). These experimental conditions then provide a means to systematically explore cell behavior in varied C from < 0.25 to ≈ 0.8. Thus, our tissue confinement framework provides a quantitative method to assess how tissue-scale growth dynamics are expected to constrain growth of single cells.

To test the utility of this framework, we explored cell growth and signaling in tissues

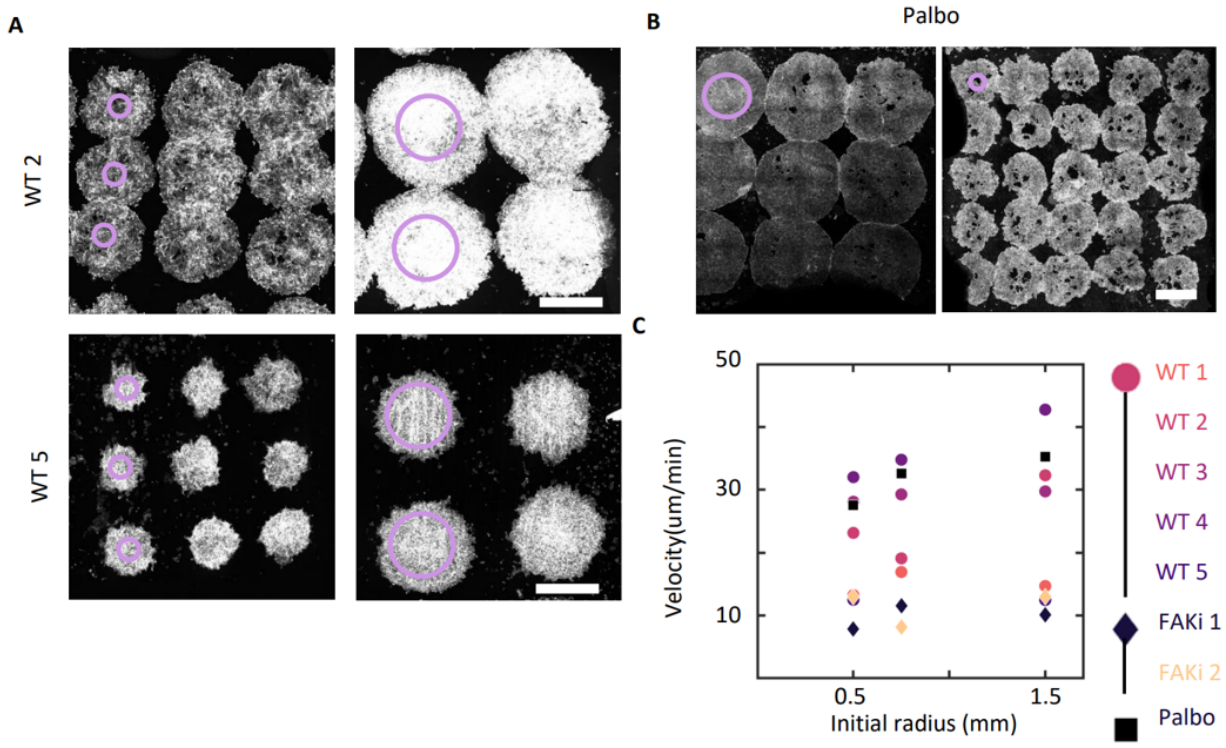

Figure 4.8: Colony expansion rate varies between experiments and is not cell division dependent. Between different expanding monolayers we observed different migration velocities. We characterized the variation in speed across all experiments. We also tested that the expansion of colonies is not driven by cell division by inhibiting the cell cycle with Palbociclib (A) Expanding colonies labeled with CellTrace Far Red with initial radius 0.5mm and 1.5mm in two different experimental replicates. Migration velocity is consistent within the same experiment but varies between experiments (B) Expanding colonies labeled with CellMask Deep Red treated with 1μM Palbociclib to block cell division. Migration rate is $\approx 30\mu$m/hr equal to the highest rate observed in control conditions. (C) Colony expansion speeds in each experiment for different initial sizes. Expansion occurs for 48 hours and the difference between initial and final radii is used to calculate the velocity. +FAKi is 500nM PND1186. Palbo is 1μM Palbociclib.

with varied levels of confinement. To query cell growth, we labeled the cells at t=0 with CellTrace, a fluorescent dye which reports on biomass production by its dilution (i.e. more growth leads to lower cell intensity) (see Methods). The total growth is determined from the CellTrace images by the ratio of intensity $\frac{I(t=0)}{I(t=\Delta t)} - 1 = \frac{Vol(t=\Delta t)}{Vol(t=0)} - 1 = \Delta Vol$. Since the growth rate of confluent monolayers is close to zero (Fig. 4.6B), the intensity of the confluent monolayer $I_C \approx I(t = 0)$, can be used as the standard to compare to the intensity I of expanding colonies (Fig. 4.9A, $C = 1$). This allows for determination of the growth rate by $I_C/I - 1$. For $\Delta t = 48$ hours, subconflucent cells show significant 10-fold CellTrace dilution consistent with the cells doubling every 15h (Fig. 4.9A, $C = 0$). We then used expanding colonies with varied A_0 to explore intermediate levels of confinement from 0.2 to 0.8. In smaller colonies with $C = 0.2$, cell growth is already suppressed to $< 50\%$ that of sub-confluent conditions. By $C = 0.6$, growth is restricted to $< 10\%$ that of the subconfluent cells and is suppressed to nearly zero by C=0.8 (Fig. 4.9A). Changes in growth can also be modulated by changing the edge velocity. In our experiments, we observed that differences in migration rate significantly impact the cell growth, as predicted by our modeling (Fig. 4.9C). In all conditions, the intensity is remarkably uniform across the tissue suggesting that the growth regulation mechanism is a tissue-scale phenomenon.

To query cell growth signaling under confinement, we also performed immunostaining against YAP. YAP is a transcription factor implicated in regulating cell proliferation during contact inhibition ([9], [196], [363]). When YAP is active, it is localized to the nucleus; when inactive, YAP is localized to the cytoplasm. We see in the conditions with lower confinement, a greater faction of YAP is localized to the nucleus, whereas around $C = 0.5$ it becomes more localized to the cytoplasm (Fig. 4.9B). This suggests that YAP activity is regulated in response to changes in tissue confinement (Fig. 4.9B). Taking together, all our experimental data from colonies with varying size and edge velocity (Fig. 4.7G) reveal a systematic decrease in cell growth and YAP signaling as a function of confinement (Fig.

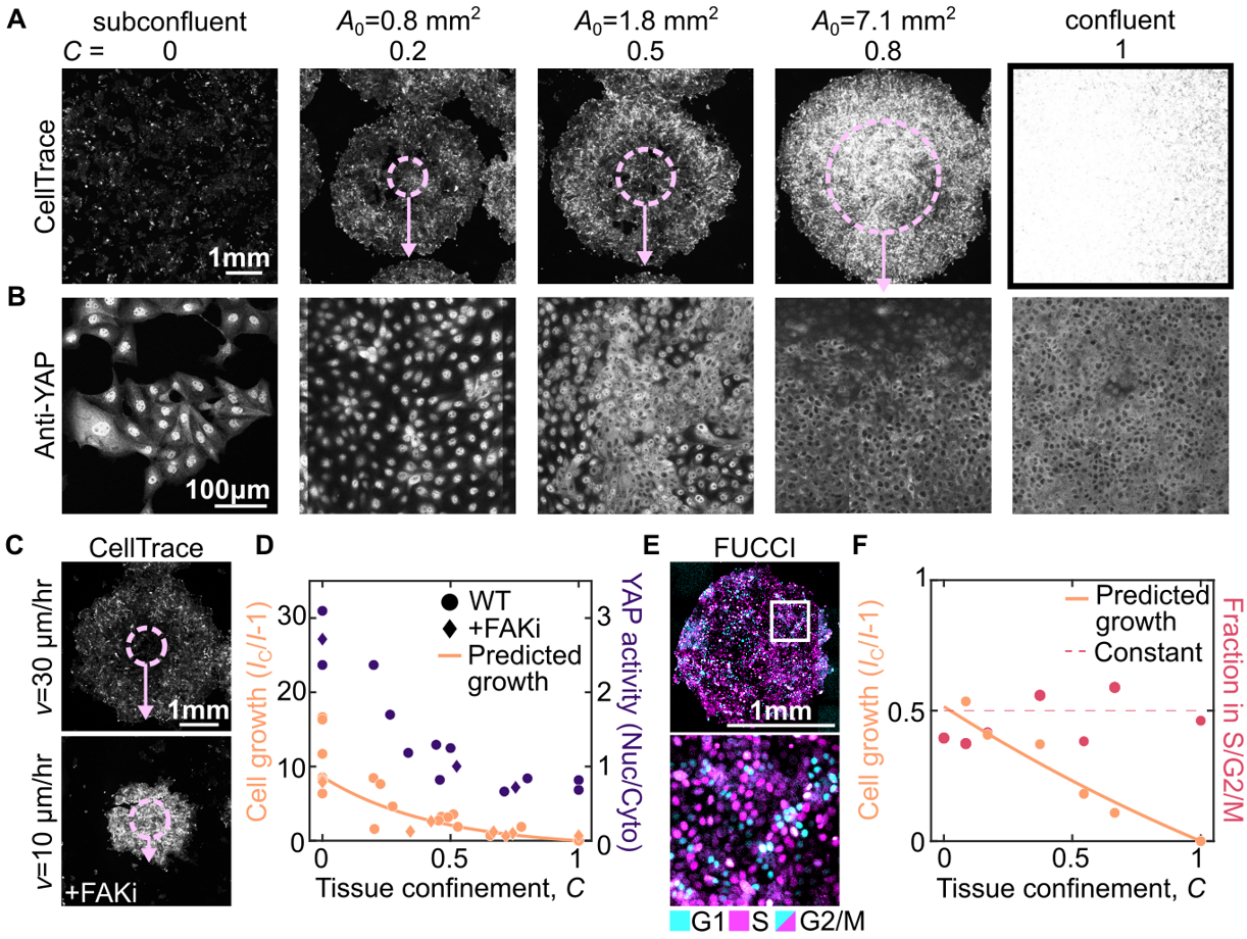

Figure 4.9: Tissue confinement determines cell growth rate and signaling (A-B) Images of Cell Trace (A) and YAP (B) at $\Delta t = 48h$ in expanding colonies with initial size, A_0, varying from 0.8-7.1mm^2, subconfluent colonies and confluent conditions. In (A), overlay shows initial colony size A_0 (dashed circle) and expansion $v\Delta t$ (arrow). Note different scale bars in (A) and (B). (C) CellTrace images of expanding monolayers with $A0 = 0.8mm$ at Δt = 48h in the presence and absence of 500nM PND1186 (+FAKi) to illustrate the effect of changes in $v\Delta t$. (D) Quantification of cell growth and YAP signaling at varying tissue confinements with $\Delta t = 48h$ across multiple experiments. Each data point is an average of multiple colonies from one experiment (see Methods). YAP activity is determined by the nuclear to cytoplasmic ratio of anti-YAP intensity, quantified for $>$ 150 cells in each experiment. Growth is plotted against the time averaged confinement and YAP activity is plotted against the final confinement. Data are from 6 independent experiments (Cell growth) and 3 independent experiments (YAP activity) (E) MDCK FUCCI cells in expanding colony with $A_0 = 1.8mm^2$ and $\Delta t = 12h$. (F) quantification of cell growth and fraction of cells in the S/G2/M cell cycle states as a function of the average tissue confinement. Each data point is quantified from >3 colonies in a single experiment with $A_0 = 0.8mm^2, 1.8mm^2$, or $7.1mm^2$ and $\Delta t = 12h$. Data are from 2 independent experiments.

4.9D, points). Moreover, the predicted growth from the definition of tissue confinement is consistent with the experimental data (Fig. 4.9D, line). All of these data demonstrate the rapid suppression of cell growth at low levels of confinement

At the onset of confluence, the cell division rate remains similar to subconfluent cells despite the increased confinement (Fig. 4.6B); this suggests that tissue confinement may not immediately affect the cell cycle. To query the cell cycle, we performed the expanding colony experiments with MDCK cells expressing the pip-degron fluorescent ubiquitination cell cycle indicator (FUCCI MDCK) (Grant et al., 2018) to measure the fraction of cells in S/G2/M in model tissues with varying levels of confinement. We restrict our analysis to short expansion times ($\Delta t = 12h$) before cells have reached the ME state and arrested the cell cycle. In contrast to cell growth (Fig. 4.9F, peach data), there cell cycle is insensitive to tissue confinement (Fig. 4.9F, red). Instead, the fraction of cells in S/G2/M is constant (Fig. 4.9F, dashed line). This data reveals the qualitatively different impact of confinement on cell cycle and growth. Thus, the transient uncoupling between cell cycle and growth observed in Fig. 4.6B is consistent with a rapid increase in confinement at the onset of confluence.

4.3.4 A G1 sizer arrests the cell cycle in confined epithelium

We next explored how the cell cycle arrests in monolayers at the later stages of contact inhibition. After confinement reduces the growth rate, cell size decreases through successive cell division until the cell cycle becomes arrested (Fig. 4.6J). Previous work has shown that cell cycle regulation in isolated mammalian cells is cell size independent ([38]) whereas it can be size-dependent for in *in vivo* epithelium ([348]). To examine if cell division is regulated by cell size in our data, we measured how the cell division rate varied as a function of cell size by tracking individual division events. We estimate volumes from the cell area multiplied by the typical cell height of 6.5 ± 1.5 μm (Fig. 4.3, mean$\pm$S.D.). Above a volume of 1200 μm3 , the cell division rate is independent of size (Fig. 4.10A). However, the division rate

sharply decreases for smaller volumes. This trend is observed across a range of experimental conditions and two epithelial cell types, indicating it is a robust feature of cell size regulation in confluent epithelial tissue (Fig. 4.11). We then used FUCCI MDCK cells to look more closely at the cell cycle regulation for large and small cells. From the FUCCI data, we obtained the S/G2/M duration by tracking single cell trajectories and saw that the duration of the S/G2/M phases is ≈ 10 hours and independent of cell size (Fig. 4.10B). In the same data, the duration of the entire cell cycle was estimated by measuring the fraction of cells in each cell cycle phase (see Methods). We see that the cell cycle duration rapidly increases for smaller cells (Fig. 4.10B, purple data). The division rate in Fig. 4.10A can also be used to estimate cell cycle duration and shows a similar trend (Fig. 4.10B, dashed line). Together, these data indicate an increased duration of the G1 phase for smaller cells. This is consistent with previous results that size regulation occurs at the G1-S transition ([38], [215], [348])

Motivated by this data, we developed a simple "G1 sizer" model of size-dependent exit from G1 (Fig. 4.10C) ([118], [348]). In the model, we simulate an ensemble of cells that grow at a constant rate, have two cell cycle phases G1 and S/G2/M, and divide into two daughter cells with half the mother volume. We added additional features based on experimental observations: (1) There is a sharp volume threshold of the G1-S transition rate and below this minimal size a, the transition rate is zero, (2) cells have an S/G2/M duration of $\tau = 10$ hours independent of cell volume, and (3) a variable cell growth rate G that is normalized to vary from 0 for no growth to 1 for growth in the unconfined condition. Due to rule (2) the minimum cell cycle time is τ hours and cells will grow by a minimum of $G\tau$ before each division. When $G\tau >> a$, cells are large compared to a and the G1-S transition proceeds quickly. In this regime, the cell cycle regulation is size independent (timer-like) with a time τ between cell divisions (Fig. 4.10D, $G = 1$, Fig. 4.12). However, when the growth rate is suppressed such that $G\tau << a$, additional time is required to relieve the size constraint of the G1-S transition (1) (Fig. 4.10D, $G = 0.05$, Fig. 4.12). In this regime, the cell cycle

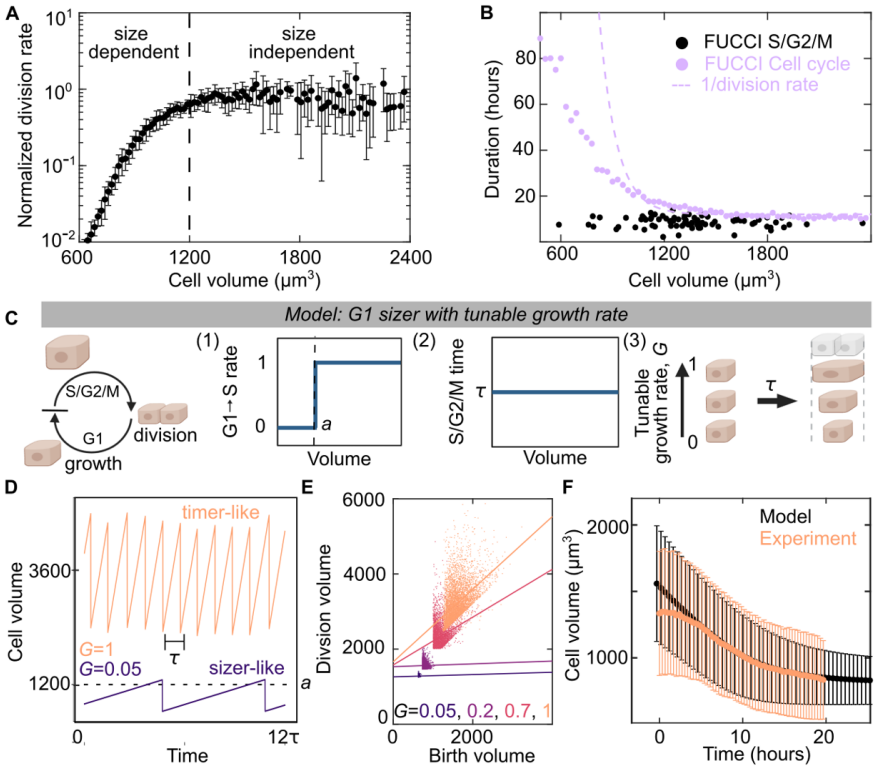

Figure 4.10: A G1 sizer arrests the cell cycle (A) Normalized cell division rate as a function of cell volume in MDCK monolayers. Volume is calculated from cell areas multiplied by the average experimental height (see Methods). Data are averaged from 4 experimental replicates with $>$ 500 division events, error bar is standard deviation of experimental replicates (B) Duration of cell cycle (violet) and S/G2/M (black) for MDCK cells as a function of cell size. Dotted violet line is a fit to the data in A to extract the cell cycle duration. S/G2/M time are from $N = 82$ trajectories for cell cycle. Cell cycle time data (violet points) are population averaged FUCCI measurements from 50 fields of view containing $>$ 100 cells from 1 experiment (see Methods) (C) Schematic of G1 sizer model – cells are simulated to grow at a constant rate, transition between cell cycle states and divide. (1) Cells transition rapidly from G1 to S only when above a critical volume a, (2) cells have a set S/G2/M duration equal to time τ that is independent of size, (3) cells have a variable growth rate, G, independent of the cell cycle (D) G1 Sizer models results of cell volume as function of time for two growth rates ($G = 1$ and $G = 0.05$) (E) G1 Sizer model results of cell volume at division as a function of birth volume for $G = 0.05, 2, 0.7 and 1$. Dotted lines show a linear fit to the data ($slope = 0, 0, 0.4, 1$). Each condition contains 400 simulation trajectories. (F) Cell volume as a function of time for experimental data from Fig. 4.6D (peach) and for G1 sizer model results (black). The onset of confluence occurs at t=0 for experiments. For simulations, this is models with a growth rate quench from 1 to 0 at $t = -10h$. Data is mean cell volume, error bars are the standard deviation. Each time point in the experiment is the average of $>$ 10000 cells from 30 fields of view. Each simulation time point is an average of $>$ 15000 cells from 35 simulations.

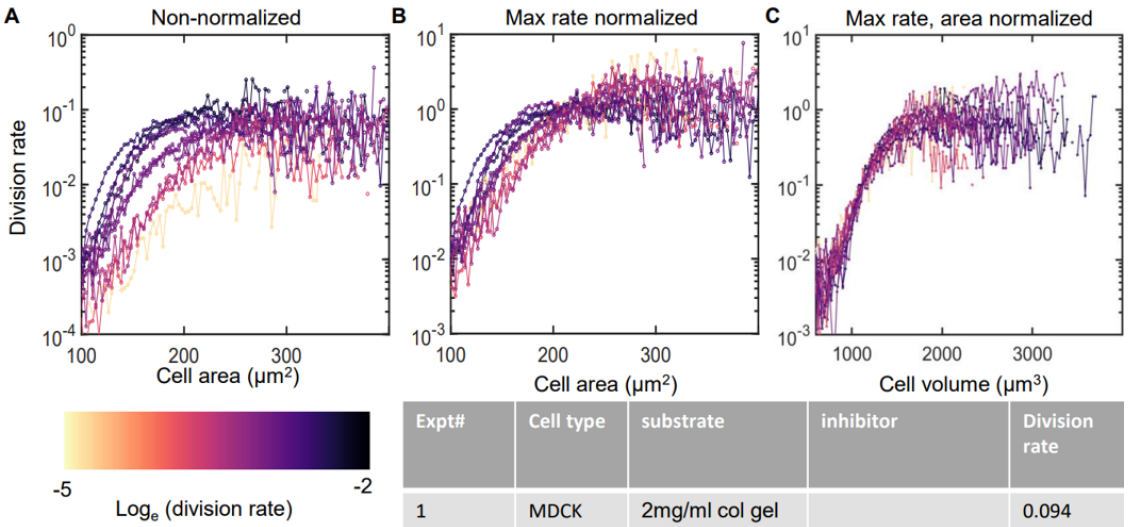

Expt#	Cell type	substrate	inhibitor	Division rate
1	MDCK	2mg/ml col gel		0.094
2	MDCK	2mg/ml col gel		0.088
3	MDCK	2mg/ml col gel		0.046
4	MDCK	2mg/ml col gel		0.067
5	MDCK	2mg/ml cross linked col gel		0.078
6	MDCK	4mg/ml cross linked col gel		0.047
7	MDCK	Glass		0.033
8	MDCK	2mg/ml col gel	25μM rac inh.	0.048
9	MDCK	2mg/ml col gel	50μM rac inh.	0.030
10	MDCK	2mg/ml col gel	500nM FAK inh.	0.022
11	MDCK	2mg/ml col gel	3um Mn^{2+}	0.046
12	CACO-2	2mg/ml col gel		0.008

Figure 4.11: Cell division rate shows a similar size dependence across a range of experimental conditions. We reanalyzed a previously published dataset to see how cell division rates vary with cell size in epithelium. A subset of the data is presented in Fig. 4.10A but complete set of data analyzed is presented in this Figure. We see a consistent relationship between division rate and area despite differences in the overall division rate across experiments. (A-C) Plots of division rates against cell size across 12 timelapse imaging experiments that are previously published by Devany et. al. 2021. Plots show data from 4 replicates of MDCK cells on 2mg/ml collagen gels, data with variation in substrate stiffness, with inhibitors of RAC1 (NSC 23766) and FAK (PND1106), and with CACO-2 cells. See table for full experimental details. Data are plotted non-normalized in A, normalized by the maximum rate in B, and normalized by both maximum rate and the area is normalized so the rate 0.1 is at a volume of 1200 μm3. Curves are colored according to the maximum division rate. Each division rate curve is generated from tracking >300 division events from each experiment over a timelapse imaging series of at least 16 hours (see Methods).

regulation is highly size-dependent (sizer-like).

Plotting the cell size at division as a function of cell size at birth for a range of growth rates shows that the model transitions smoothly from size-dependent to size-independent behavior as a function of growth rate (Fig. 4.10E, Fig. 4.13). Size-dependent cells divide at the same size and show no correlation between birth size and division size (Fig. 4.10E, dashed lines for $G = 0.05, 0.2$). This contrasts with size independent cells which show a correlation between birth size and division size (Fig. 4.10E, dashed lines for $G = 0.7, 1$) ([7], [38], [348], [360]). These different regulation mechanisms also occur in distinct cell size ranges consistent with previous work showing that large, rapidly growing, single cells are size independent ([38]) and small, slowly growing cells, *in vivo* are size-dependent ([348]).

Having developed an understanding of the model at constant or near-constant growth rates, we tested if the model could also predict the cell size distributions found in the experiments of monolayer formation and maturation in Fig. 4.6B. We simulate monolayer formation in our model by a rapid quench of cell growth rate from 1 to 0 at $t = 0$ and measure the cell size distribution over time (Fig. 4.10F). The simulation results (Fig. 4.10F, black) are consistent with those of the experiment (Fig. 4.10F, peach). This suggests that the G1 sizer model together with an understanding of how confinement impacts cell growth (Fig. 4.9F) is sufficient to explain transitions in size of isolated cells to those in epithelial tissue.

4.3.5 Size-dependent Cyclin D degradation leads to cell cycle arrest

To investigate molecular mechanisms of size control, we took advantage of our Tet-inducible cell lines to manipulate cell size in confluent monolayers. We prepared monolayers at the onset of confluence with Tet-On p27 and Tet-On p27ck cells. At $t = 0$ we added doxycycline (+dox) to induce expression. After 5 days, both monolayers are in a cell cycle and growth arrested ME state, but the +dox p27ck cells are 40% the size of +dox p27 cells (Fig.

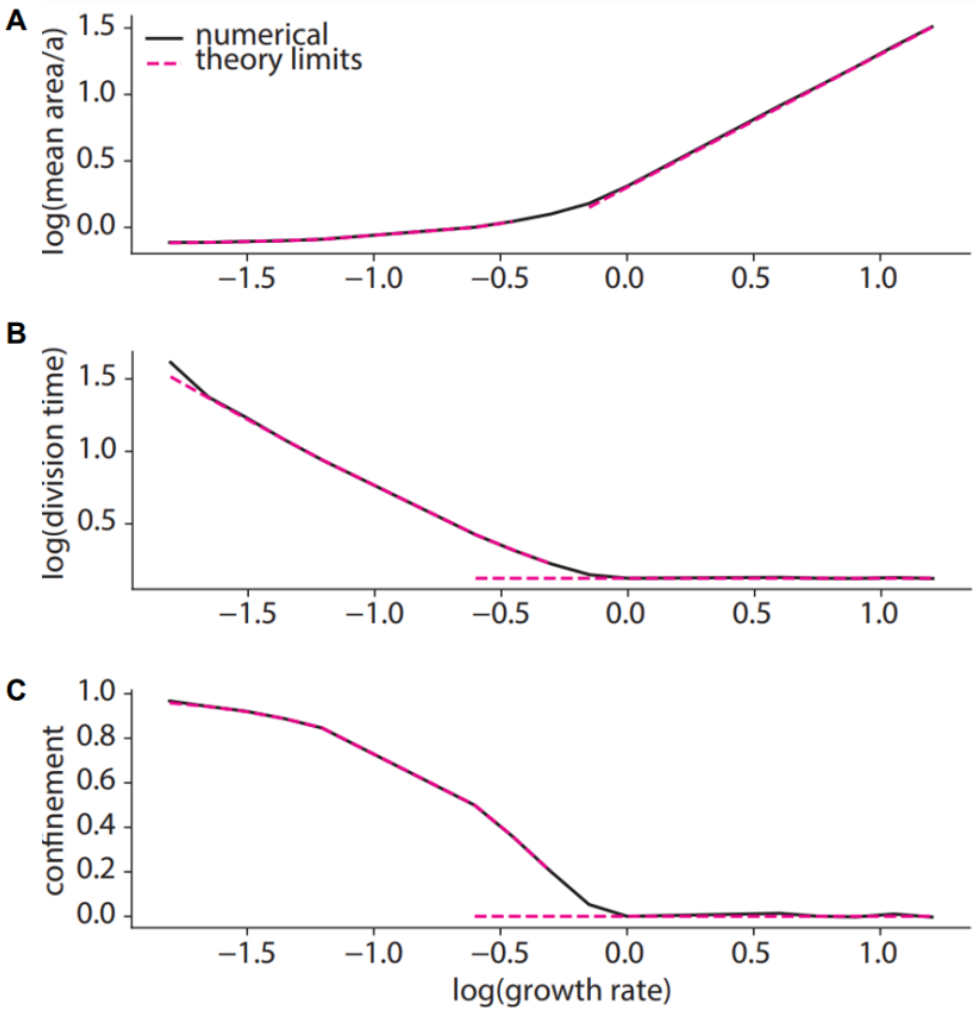

Figure 4.12: G1-sizer control generates timer and sizer behaviors depending on growth rate. We numerically simulate single-cell trajectories (see Methods) as a function of growth rate. We compare our numerical results to analytical expressions (see Methods) derived in the fast- and slow-growth limits of the model. (A) Numerical simulation of mean non-dimensional cell size (black) reveals two distinct regimes: a sizer regime where cell size is only weakly dependent on growth, and a timer regime where size is linear with growth. This agrees well with theoretical expectations in the limits of fast and slow growth (pink). (B) Numerical simulation of mean division time (black) reveals two distinct regimes: a sizer regime where division time diverges with decreasing growth, and a timer regime where division time is independent of growth. This agrees well with theoretical expectations in the limits of fast and slow growth (pink). (C) Numerical simulations (black) reveal a confinement transition when cells switch from sizer to timer behavior: confinement is non-zero for slow-growth sizers, and zero for fast-growth timers. This agrees well with theoretical expectations in the limits of fast and slow growth (pink).

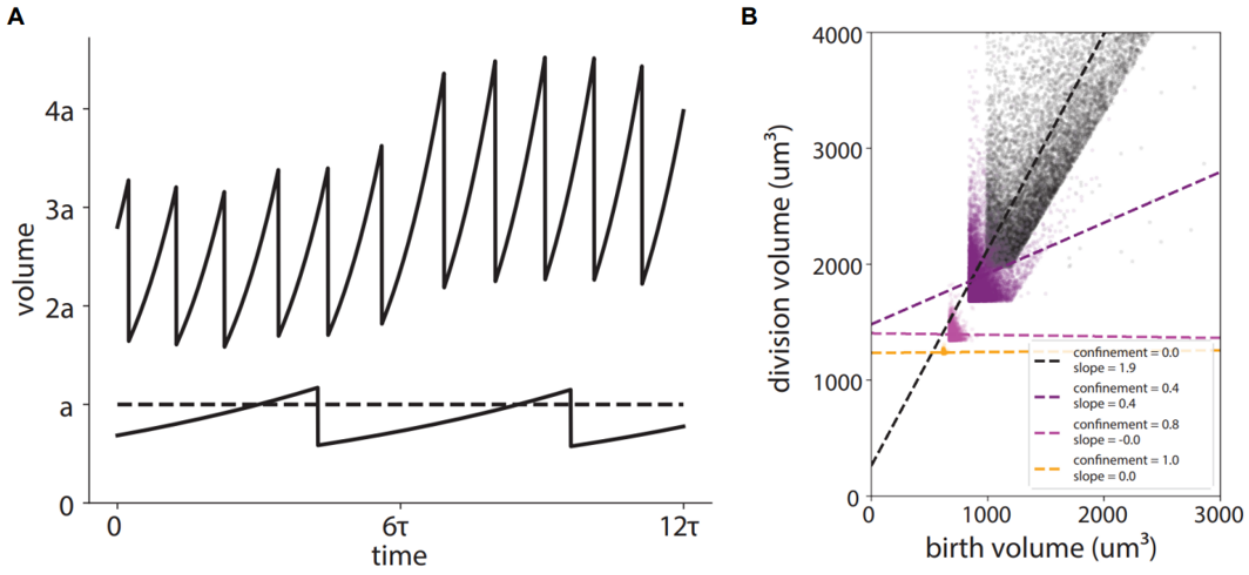

Figure 4.13: A G1-sizer with single-cell exponential growth shows a transition between timer and sizer behavior. To verify that the transition between timer and sizer behavior in our model is not an artifact of linear cell growth, we simulate a model with exponential growth, where cell size a_i increases by an amount $a_i G\ dt$ at each time step. (A) Numerical simulation of cells with $G = .74$ (upper solid line) and $G = .14$ (lower solid line) reveals qualitatively distinct timer and sizer behaviors as a function of growth relative to the G1-exit size cutoff (dashed line). The $G = .74$ trajectory displays the increasing variance of cell size characteristic of timer control with exponential single-cell growth. (B) Plotting numerically simulated cell birth sizes vs division sizes reveals a transition from timer to sizer behavior as a function of confinement. The slope of the linear best fit lines (dotted) to the data goes from timer-like (≈ 2) to sizer-like (≈ 0) as confinement increases. Growth rates $G = 0.5, 0.33, 0.11, 0.025$ going from small to large confinement.

4.6I; Fig. 4.14A). RNA sequencing revealed almost no differences in the steady-state transcriptome of these samples (Fig. 4.14B). However, close examination revealed several weak signatures (Fig. 4.15) including a slight downregulation of cyclin D1, 2, 3 in the smaller contact inhibited cells (Fig. 4.14B, inset). The G1/S transition has a steep dependence on cyclin D concentration ([85]) so it is possible that small changes in cyclin D concentration are sufficient to arrest the cell cycle. Furthermore, cyclin D is strongly post transcriptionally regulated by degradation ([4]). To check if this difference in RNA abundance leads to changes in protein levels, we looked at cyclin D1 (cyD1) protein levels via immunofluorescence in ME formed with Tet-On p27 cells (+dox p27) and co-cultures including Tet-On p27ck cells (+dox p27/p27ck). Since p27 is known to interact with cyclin D, we tested that its overexpression did not change the cyclin D1 levels by inducing p27 after ME formation (Delay +dox p27). Interestingly, we found significant difference in cyclin D1 abundance, with nearly undetectable levels in cells with a nuclear area $< 100\mu m^2$ (Fig. 4.14 C; Fig. 4.16). We observed that the intensity of CyD1 drops rapidly with decreasing cell size, measured by the nuclear area (Fig. 4.14D). The same trend was seen for all monolayer preparations, suggesting that the cyclin D1 level is regulated by a size-dependent pathway. This suggests that in addition to transcriptional changes in cyclin D, additional size-dependent post transcriptional regulation occurs, possibly as reported in other contexts ([4], [191]).

To test if decreased cyclin D levels are required to arrest the cell cycle, we overexpressed cyclin D1 in contact inhibited cells. We used Tet-On Cyclin D1-GFP (CyD) or Tet-On Cyclin D1 T286A T288A-GFP (CyDAA, a degradation resistant mutant) cells and induced the expression of additional cyclin D1 at OC. We then looked at the cell size 3 days later, after it had reached a plateau. We observe that overexpression of either CyD or CyDAA leads to decrease in minimal cell size in ME, compared to control (-dox) (Fig. 4.14E,F). Therefore, restoring Cyclin D1 in small cells is sufficient to initiate the cell cycle. This suggests that the depletion of cyclin D is necessary for size-dependent arrest of the cell cycle.

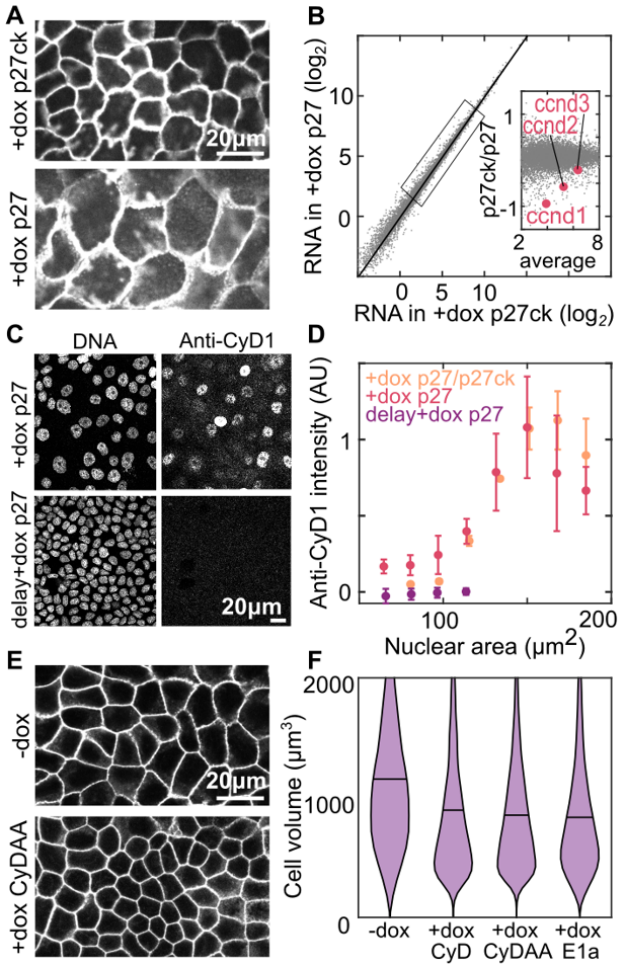

Figure 4.14: Low cyclin D causes cell cycle arrest in small cells (A) Cell membranes of Tet-On p27 and Tet-On p27ck MDCK cells in ME+4 days; dox added at $t = 0h$. (B) RNA sequencing data from monolayers prepared in A. Data are averaged transcripts per million from 3 experimental replicates. Inset: zoom in of genes in indicated box, cyclin D genes expression levels are highlighted in red. (C) DNA staining and anti-Cyclin D1(CyD1) immunofluorescence staining in MDCK monolayers at ME+3 days. Dox is added at either t=0 (+dox p27) or at t=ME+2 days (delay +dox p27). (D) Quantification of anti-CyD1 intensity from immunostaining data as a function of nuclear area. Intensity is normalized in each experiment to a maximum value of 1. P27/p27ck are monolayers with a mixture of Tet-On p27 and Tet-On p27ck cells. ($N_{+dox} = 4564(3)$, $N_{Delay+dox} = 7515(2)$, $N_{p27/p27ck} = 11080(4)$) (E) Labeled cell membranes in Tet-On Cyclin D1 T286A T288A (CyDAA) MDCK monolayers at ME+3 days without dox (-dox) or with dox added at t=0 (+dox CyDAA). (F) Cell volume measured in resuspended Tet-On Cyclin D1, Tet-On Cyclin D T286A T288A, and Tet-On 12sE1a cells at ME+3 days without dox (-dox) or with dox added at t=0 (+dox CyD, +dox CyDAA, +dox E1a). ($N_{-dox} = 13513(5)$, $N_{CyD} = 7240(2)$, $N_{CydAA} = 9092(3)$, $N_{E1a} = 6457(4)$).

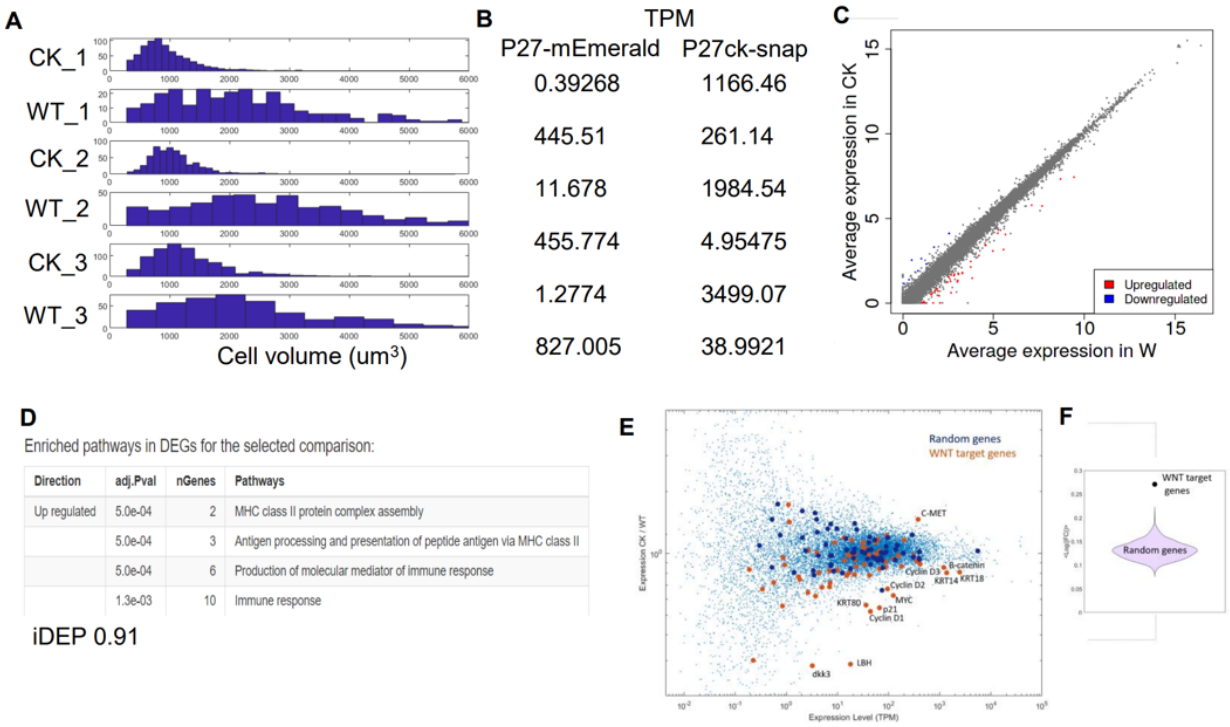

Figure 4.15: RNA expression is similar between large and small cells but shows weak immune and WNT signature. We performed RNA sequencing on monolayers with different cell size determined by inhibiting cell division. The data is presented in Fig.6B. This figure includes additional analysis performed on the data which identified some weak transcriptional signatures that we do not interpret to explain the size dependent cell cycle arrest (A) Distributions of cell volumes measured in suspension from each RNA seq experiment (CK – Tet-On Snaptag-p27ck cells +dox, WT – Tet-On GFP-p27 cell +dox). Dox was added at t=0 and RNA was collected 5 days later at ME+4 days. 3 samples were made for each experiment and 2 were pooled for RNA extraction and sequencing while the other sample was used to measure the volume distribution (B) expression level of GFP-p27 and Snaptag-p27ck found in each of the samples. Each data set is one experimental replicate with 2 technical replicates. (C) Plot of RNA expression from Fig. 6b with genes which are significantly upregulated or downregulated ($P < 0.05$) highlighted. Data are averaged from 3 experimental replicates each with 2 technical replicates (D) Pathway enrichment analysis of genes from RNA sequencing data showing all pathways with significant upregulation or downregulation. Analysis performed using iDEP 0.91 (see Methods) (E) plot showing the ratio of gene expression vs the average expression. 65 WNT target genes from The WNT Homepage are plotted in orange while a random set of 65 genes is shown in blue (F) violin plot of average fold change in 1000 sets of 65 random genes compared to the average fold change of WNT target genes in E.

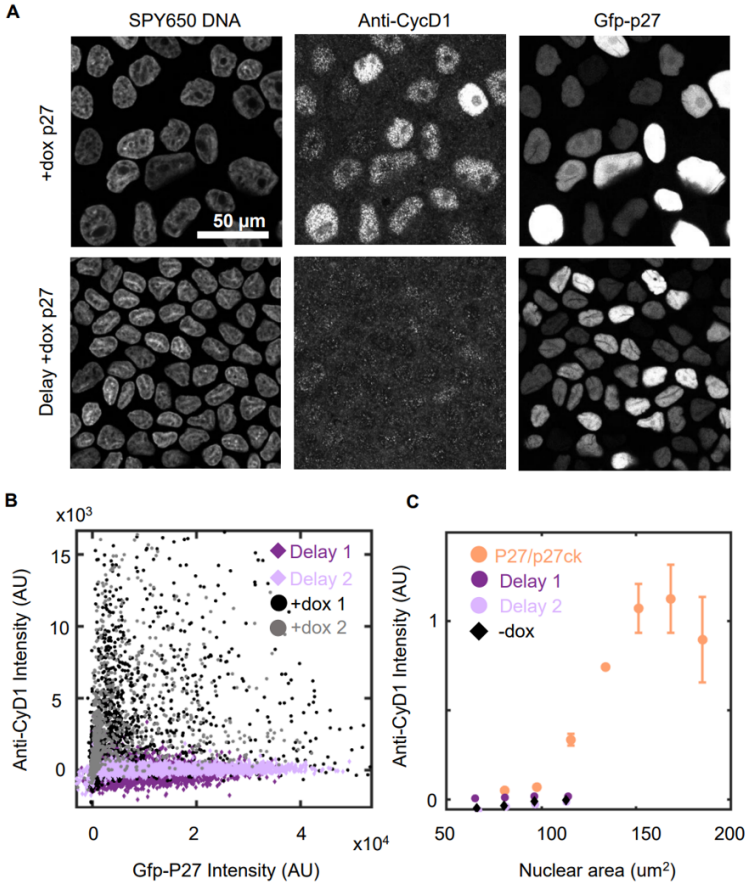

Figure 4.16: Cyclin D1 level is independent of p27 expression. Due to a direct binding interaction between p27 and Cyclin D we were concerned that overexpression of p27 may alter the levels of Cyclin D1 found in normal cells. We performed controls where we manipulate cell size independent of p27 levels and show that there is no resulting effect on expression levels of Cyclin D1 (A) MDCK Tet-On GFP-p27 monolayers labeled with spy650 DNA, anti-cyclin D1 and GFP-p27 under conditions where doxycycline is added at day 0 (+dox p27) or at day 2 (Delay +dox p27) (B) plot of anti-Cyclin D1 nuclear intensity vs GFP-p27 nuclear intensity in +dox P27 or delay +dox P27 conditions (C) Plot of anti-Cyclin D1 nuclear intensity in p27/p27ck coculture, delay +dox p27 and -dox condition. Delay+dox p27 and -dox show similar behavior suggesting that p27 expression does not affect the relationship between Cyclin D1 levels and cell size ($N_{+dox1} = 1820(1)$, $N_{+dox2} = 1112(1)$, $N_{Delay1} = 3479(1)$, $N_{Delay2} = 4036(1)$, $N_{-dox} = 4155(1)$, $N_{p27/p27ck} = 11080(4)$).

We also overexpressed the viral oncoprotein E1a which is known to bind and inactivate Rb pocket proteins and activate the G1/S transition ([338]). Cells that overexpressed E1a also showed decreased size, suggesting that cyclin D depletion arrests the cell cycle by inhibiting the G1/S transition (Fig. 4.14F).

4.3.6 Cell cycle arrest occurs near cell size minimum set by the genome size

We next wanted to understand why the cell cycle normally arrests at a volume of $\approx 1000\mu m^3$. A possible constraint on cell size comes from the volume occupied by the genome. As the cell size decreases, the nucleus gets smaller and chromatin gets more compact ([322]). A simple estimate suggests low chromatin concentrations $\approx 5\%$ by volume in an average subconfluent mammalian cell ($Vol_{nuc} \approx \frac{1}{3} Vol_{cell} \approx 800\mu m^3$ vs $Vol_{genome} \approx 40\mu m^3$) ([205]). However, the concentration would increase several fold as cell size reduces and the total chromatin per cell remains constant. Previous measurements of chromosome size by TEM and AFM have shown that the volume of a full set of chromosomes are approximately $50 - 100\mu m^3$ ([94], [120]) and 50% chromatin by volume ([226]), thus, setting a lower limit on cell size. When we stained both the DNA and cell membrane, we observed that the abnormally small Tet-On CyDAA cells appear to have an unusually large nucleus relative to the cell size (Fig. 4.17A). This was surprising given that there is typically a tight scaling relationship between cell size and nuclear size ([322]). Comparing the cell volume against the nuclear volume for epithelium prepared under our previously described conditions, we observe this scaling relationship except in the Tet-On CyDAA cells in the presence of doxycycline (Fig. 4.17B, peach). Instead, we observe that the ratio of nuclear to cell size is rapidly increasing as cell size decreases below $1000\mu m^3$ (Fig. 4.17C) and approaches the regions where DNA compaction exceeds the chromosomal values or where nuclear size would exceed cell size (Fig. 4.17B, gray, Fig. 4.17C gray). We hypothesized that increasing chromatin concentration could disrupt normal chromatin function, leading to DNA damage. In abnormally small

cells we observed phospho-H2A.X foci indicating locations of DNA damage (Fig. 4.17D, E). This suggests that normal cells arrest near a cell size minimum but outside the range where DNA damage occurs frequently. DNA damage is known to arrest the cell cycle through Rb/Cyclin D independent mechanisms ([277]) preventing further size reduction. Therefore, in epithelia, proliferative homeostasis is maintained by an interplay between cell growth in proportion to tissue constraints and cell size-dependent G1/S regulation which arrests cell size near a minimum (Fig. 4.17F).

4.4 Discussion

While growth and division are coupled in single cells, we observe their regulation is uncoupled in epithelial tissue. The tissue growth dynamics regulate cell growth whereas cell division is regulated solely by cell size. Differences in these two rates drive changes in cell size depending on the tissue environment. In single cells, the environment places no constraint on cell growth leading to high growth rates and large cell size. In contrast, in mature epithelia, tissue growth rates are low and reduce cell size to a minimum. In this regime, cell size regulation is critical for maintaining cell homeostasis and preventing DNA damage. The consistency in cell size distributions across diverse epithelial cell types (Fig. 4.1B) suggest that our models should be broadly applicable to understand contact inhibition and cell size regulation across diverse biological systems.

Canonically, growth factor signaling is thought to be the main pathway to control and coordinate proliferation ([178], [270]). We identify an independent role for tissue confinement in controlling cell growth. While we exploited model tissues with a particular type of growth dynamics driven by edge migration, these ideas can be easily extended to arbitrary systems so long as the tissue growth dynamics can be readily characterized (Fig. 4.18). Tissue growth is driven by diverse processes, including migration, tissue buckling or mechanical stretch and occurs in response to cell turnover ([62], [109]), all of which would reduce tissue confine-

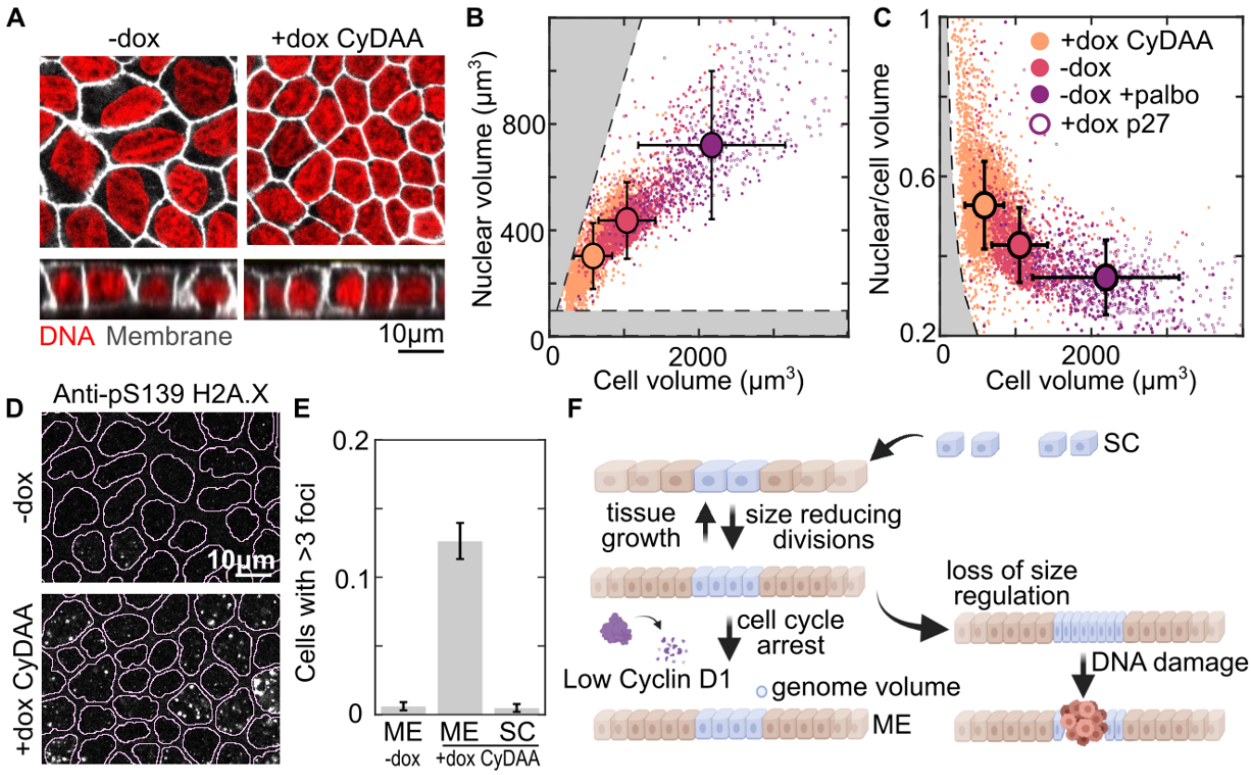

Figure 4.17: Cells arrest near a minimum size set by genome volume (a) Nuclear (red) and membrane (white) staining of Tet-On Cyclin D1 T286A T288A MDCK cell monolayers at ME+3 days without dox (-dox) or with dox added at t=0 (+dox CyDAA) (B-C) Plots comparing nuclear volume and cell volume measured from 3D imaging in conditions from A (-dox, +dox CyDAA) or in cell cycle inhibited conditions (-dox +palbo) or Tet-On p27 cells (+dox p27). +palbo is 1μM Palbociclib. B shows the correlation between the cell and nuclear volumes while C show the ratio of these volumes. Gray regions indicate when nuclear volume is larger than cell volume (B-top left) or when chromatin density is larger than chromosomes (B-bottom, C-left). Error bars show standard deviation of data($N_{-dox} = 1405(2)$, $N_{+doxCyDAA} = 4207(2)$, $N_{-dox+Palbo} = 390(1)$, $N_{+doxp27} = 324(1)$) (D) Monolayers in the same conditions as A immunostained for pS139 H2A.X (yH2A.X). Lines overlayed on images show nuclear segmentation from DNA staining. (E) Quantification of pS139 H2A.X foci from conditions in D. Bar is the mean fraction of cells with >3 foci between 3 experimental replicates. Error bar is standard deviation of different experiments ($N_{ME-dox} = 5813(3)$, $N_{ME+doxCydAA} = 9127(3)$, $N_{SC+doxCydAA} = 2470(3)$) (F) schematic summarizing cell size regulation in epithelium.

ment. Previous work has implied that cell growth and YAP/TAZ signaling in epithelium are regulated by mechanical stress ([132], [228], [245], [280], [290]). Our framework provides a means to isolate the roles of physical constraints on cell growth regulation. Importantly, confinement is a geometric quantity readily determined from timelapse microscopy. Our data show that confinement is a strong predictor of YAP/TAZ activity, demonstrating the utility of our model to study the mechanisms underlying epithelial growth control. However, future work is needed to determine the relationships between tissue confinement, growth and mechano-transduction.

Our observation of a transition between size-dependent and independent behaviors in epithelia may explain prior observations of size regulation in mammalian cells ([38], [349], [348]). In our computational model we find that a size-dependent G1/S transition gives rise to both sizer-like and timer-like behaviors of cell size regulation at low and high growth rates, respectively (Fig. 4.10E). In future work, such a cell cycle model may be extended to other cell types or non-mammalian systems which show uncoupling between growth and division like Chlamydomonas or cyanobacteria ([177], [179]). Furthermore, the molecular mechanisms of G1 sizer regulation have remained elusive ([349], [348], [366]). By experimentally manipulating cell size, we showed that cyclin D1 regulation underlies G1 sizer behavior in epithelium. Cyclin D1 is strongly post transcriptionally regulated by degradation ([4]), suggesting that upstream kinase localization or activity may function in the size sensing pathway. Our observations may lead to future work to connect cyclin D1 regulation directly to cell size sensing.

Finally, below the minimal size set by cyclin D1 regulation, significant DNA damage occurs suggesting an important role of size regulation in maintaining cell homeostasis. Cancers which are driven by mutations in genes implicated in cell size regulation, such as small cell cancer, may show similar DNA damage leading to additional mutations. Alongside recent work which shows that very large cells become nonfunctional ([51], [167], [218]), the lower

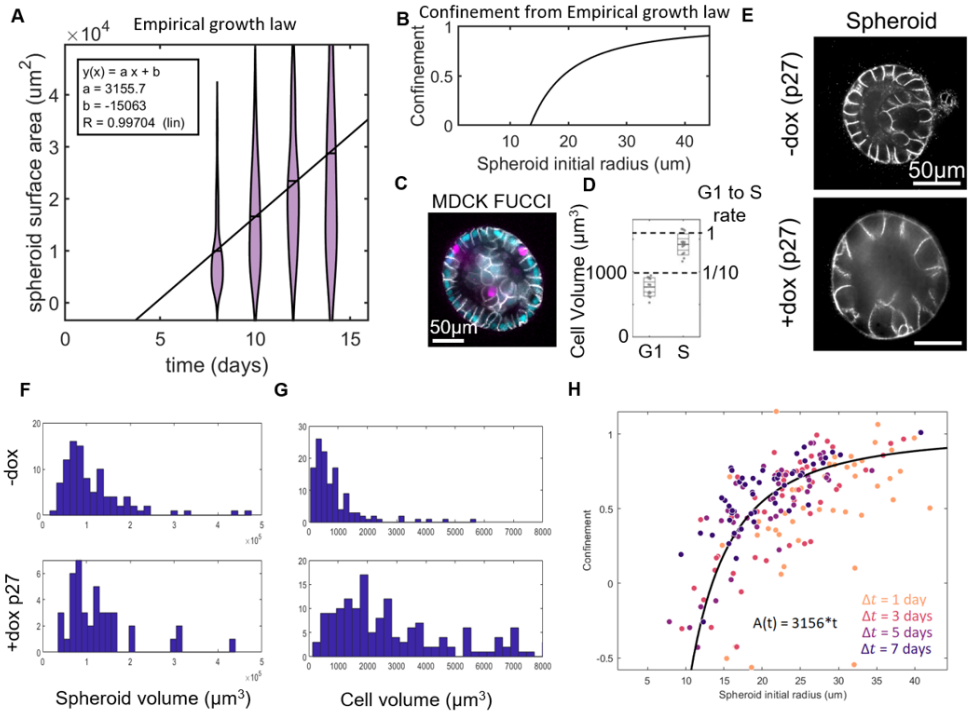

Figure 4.18: Epithelial spheroids are amenable to confinement analysis and show high confinement We measured the growth rate of MDCK spheroids and of cells within spheroids to demonstrate another application of our confinement framework. In this context the spheroid expansion is not driven by migration as it is in the expanding monolayers and the growth law is not known. By measuring the behavior of spheroids, we find an empirical growth law and use this to predict the confinement. This confinement agrees with an independent growth measurements on single cells. (A) Distribution of epithelial spheroid size measured at different time points. Linear fit show the surface area of the spheroid increases with time (B) Confinement as a function of size calculated using the linear growth of spheroid area empirically determined from A (C) Epithelial spheroid of MDCK FUCCI cells with labeled cell membranes (D) Quantification of cell volume of randomly selected cells in G1 and S phase in MDCK spheroids at day 8 ($N = 13$ cells from 1 experiment in each condition). Dotted lines show volumes where the division rate reaches is maximal or 1/10 the maximum from Fig. 5A (E) Representative images of spheroids formed with Tet-On p27 MDCK cells without dox (-dox) or with dox added at $t = 5$ days. Spheroids were imaged at $t = 10$ days (F) spheroid volumes in -dox and +dox p27 conditions. Data are from > 40 spheroids each in 1 experiment (G) distribution of cell areas in -dox and +dox p27 conditions. Data are from > 100 cells each in 1 experiment (F) Measured confinement for individual spheroids from the cell growth averaged across a spheroid measured from changes in cell size under p27 induction compared with the growth model shown in B (see Methods). Cell size in each spheroid is measured after Δt in the presence of dox and compared with the expected size in -dox conditions $\approx 1000 \mu m^3$. The difference in cell size divided by Δt gives the cell growth rate which is compared to the single cell rate of MDCK to give the confinement.

bound set by the genome size establishes a range of cell sizes for viable diploid mammalian cells from $\approx 200-10000\mu m^3$, similar to the range observed across different cell types ([205]). Overall, our understanding of the proliferative behaviors in epithelium provides a new basis for studying development, homeostasis, and disease in complex epithelial tissues across diverse biological contexts.

4.5 Materials and methods

Reagents

PND1184 and (3- Aminopropyl)trimethoxysilane were purchased from Sigma-Aldrich (Saint Louis, MO). Cell trace purchased from Invitrogen (Waltham, MA). Glutaraldehyde purchased from Electron Microscopy Sciences (Hatfield, PA), BD Collagen I, rat tail was purchased from BD Biosciences (San Jose, CA). 1X PBS, 1X DMEM, Fetal Bovine Serum (DMEM), l-glutamine, Penicillin, Streptomycin, Trypsin EDTA were purchased from Corning Inc. (Tewksbury, MA), TBS, MnCl, NaOH were purchased from Fisher Scientific (Hampton, NH), Palbociclib was purchased from Cayman Chemical (Ann Arbor,MI). Anti-cyclin D1 ((E3P5S) XP® Rabbit mAb 55506), Phospho-Histone H2A.X (Ser139) (20E3) Rabbit mAb 9718 were purchased from Cell Signaling Technologies (Danvers, MA). Anti YAP purchased from Santa Cruz Biotechnology (Dallas, TX). Infusion and Lenti-X™ Tet-On® 3G Inducible Expression System purchased from Takara Bio (San Jose, CA). Janelia Fluor 646 halotag ligand, Janelia Fluor 549 halotag ligand and Fugene HD purchased from Promega (Madison, WI).

Cell culture and lines

All cells were maintained at 37C and 5% CO2. Cells were passaged using 0.25% trypsin EDTA every 2-3 days. Cells were checked for mycoplasma by Hoechst staining. MDCK, CACO-2 and MEF cells were cultured in dulbecos modified eagle medium (DMEM) high glucose supplemented with 2mM L-glutamine and 10% FBS. HaCaT cells were maintained

in low calcium high glucose DMEM prepared from calcium-free DMEM powder (09800; US Biological) supplemented with 40 μM calcium-chloride, 2 mM L-glutamine and 10% calcium depleted FBS using Chelex-100 (Sigma-Aldrich). RPE-1 cells were maintained in 1:1 high glucose DMEM:F12k supplemented with 2mM glutamine and 10% FBS. Tet inducible gene expression was done with 200ng/μl doxycycline in all indicated experiments (+dox)

HaCaT cells were provided by Yu-Ying He (University of Chicago). Caco-2 cells (HTB-37) and HEK293T cells (CRL-3216) were acquired from ATTC. MDCK cells were provided by James Nelson. RPE-1 cells were provided by Wallace Marshall. MEFs were provided by Mary Beckerle. Stargazin-halotag Caco-2 and MDCK cells were produced by lentiviral infection of CACO-2 and MDCK cells by a WPT-Stargazin-halotag construct packaged in 293T cells by a second generation lentiviral system with pHR1-8.2-deltaR and a VSV-G pseudotyping plasmid (gifts from M. Rosner). Viral supernatant was collected at 24, 48 and 72 hours after transfection then concentrated ≈30x using Amicon Ultra-15 Centrifugal Filter Unit (100kDa) or concentrated ≈30x by peg precipitation ([190]). Cells ($\approx 50,000$ cells a in 6cm diameter dish) were treated overnight with 300μl of concentrated virus in 2ml of media supplemented with 8μg/ml polybrene. Positive cells were isolated using a cell sorter. FUCCI MDCK cells were produced by lentiviral infection with virus of pLenti-PGK-Neo-PIP-FUCCI packaged and infected the same way. Cells were then selected using 800 μg/ml G418. pLenti-PGK-Neo-PIP-FUCCI was a gift from Jean Cook (Addgene plasmid 118616 ; http://n2t.net/addgene:118616 ; RRID:Addgene-118616). Tet mEmerald-P27 1-176, snaptag-P27ck 1-176, Cyclin D1-mEmerald, Cyclin D1 T286A T288A-mEmerald, mKate-T2a-12sE1a cells were produced using the Lenti-X Tet-On 3G system (Takara Bio). DNA above were subcloned into the Tre3g vector. Lentiviral particles were packaged in 293T cells transfected with pHR1-8.2-deltaR and a VSV- G. Cells were infected with lentivirus with both the EF1a-Tet-on-3g and Tre3g plasmids above using the infection protocol above then selected using 2 μg/ml puromycin and 800 μg/ml G418. Plasmids used in this study

will be available on addgene.

Epithelial monolayer cultures

For all experiments unless indicated otherwise, monolayers were formed on 2mg/ml collagen I gels ($\approx$ 200μm thick) formed on top of a coverglass substrate (see Collagen gel substrate preparation section for more detail). For monolayer samples to reach the OC state after $\approx$ 12 hours and ME at $\approx$36 hours cells were seeded onto collagen gels at high density ($\approx 80,000 cells/cm^2$). For SC samples a low density of cells ($\approx 8,000 cells/cm^2$) were plated on the same substrates and cells were measured before reaching OC. Cells were added on top of the gel in a volume of 100-200μl and allowed to adhere for 5-10 minutes before adding 1.5ml to the culture dish containing the coverslip and gel. Culture media was changed once each day.

Expanding colony assay

Expanding colonies were prepared using published methods ([117]). 4.4 grams of 10:1 PDMS (Silgard 184) was cast in a 10cm petri dish and cured at 70C overnight. A piece of PDMS $\approx$20x20 mm was cut out then a set of holes was cut into the PDMS using a leather hole punch of 1mm,1.5mm or 3mm (Nuhank 0795787181775). The PDMS was washed in 70% ethanol for 5 minutes repeated 3 times then milli-Q water 3 times and allowed to dry. Cover slips were coated with collagen 1 by incubating them on a drop of 0.2mg/ml collagen in 0.02M acetic acid for 1 hour. Coverslips were washed with 1xPBS 3 times then with MQ water 3 times and allowed to dry completely. Dry PMDS and coverslips were stuck together ensuring that no air bubbles remain between the surfaces. Cells were seeded in the well ($2000 cells/mm^2$) and allowed to adhere for 5-10 minutes before adding 2ml of media to the petri dish. Colonies were left overnight then the PDMS was removed to allow colonies to expand. The initial colony size under these conditions was measured and used for subsequent analysis. Each experiment included a subconfluent and confluent sample as exponential and non-growing controls to ensure that results could be compared across

experiments. After the desired time delay samples were either fixed and imaged or fixed, permeabilized, immunostained and imaged according to methods below.

Cell Trace labeling

Cells were labeled using cell trace according to the manufacturer's protocol. Cells were resuspended in PBS (10^6 cells in 1 ml) and cell trace was added at 1μM for 15 minutes at 37C. Then cells were pelleted and resuspended in media and either directly used for experiments or cultured under normal conditions for 1 day before use.

Immunostaining

For halotag labeling, 30nM halotag JF 646 or 549 solution was added for 1 hour before fixation. Just before fixation cells were washed once in 1xPBS. Cells were fixed in 4% PFA in 1xPBS for 15 minutes at room temperature. Cells were blocked and permeablized in 1xTBS, 0.3% triton-X 100, 2%BSA solution for 1 hour. Antibody solutions were prepared in 1xTBS 0.3% triton-X 100 2% BSA using 1:400 anti-Cyclin D1, 1:100 anti-YAP, 1:400 anti-Phospho-Histone H2A.X. Samples were incubated in primary antibody overnight at 4C. Samples were washed 3 times in 1xPBS then incubated in 1xTBS 0.3% triton-X 100 2% BSA and secondary antibody for 1 hour. In conditions with DNA staining 1x SPY650 DNA was added during the secondary staining step according to the manufacturer's protocol at 1x concentration. Samples were washed 3 times for 5 minutes in 1xPBS then mounted on a slide in prolong gold antifade mounting media – non curing (Invitrogen), sealed and imaged.

Fluorescence microscopy

For time lapse imaging cells were imaged on an inverted epi-fluorescence microscope (Nikon TI-E, Nikon, Tokyo, Japan) with a 20x plan flour multi-immersion objective. images were acquired at 10-minute intervals in GFP, 642 and transmitted light channels using standard filter sets (Ex 490/30, Em 525/30, Ex 640/30,
DAPI/FITC/TRITC/cy5 cube) (Chroma Technology, Bellows Falls, VT). For halotag labeling, 30nM halotag JF 646 or 549 solution was added for 1 hour before imaging. Samples were

mounted on the microscope in a humidified stage top incubator maintained at 37C and 5% CO2. Images were acquired on either a Photometrics Coolsnap HQv2 CCD camera (Photometrics, Tucson, AZ) or Andor Zyla 4.2 CMOS camera (Andor Technology, Belfast, UK). Cell volume measurement samples in resuspension were imaged on an inverted spinning disk confocal microscope (Nikon TI-E) with laser lines at 491, 561 and 642 and suitable emission filters (Chroma Technology). Images were acquired using a 40x plan fluor oil immersion objective (NA 1.3) and Andor Zyla 4.2 CMOS camera (Andor Technology, Belfast, UK). Images were acquired at room temperature within 1 hour of cell resuspension. All other imaging was done using a point scanning confocal microscope (Ziess Airyscan LS980) with laser lines at 491,561,642 and an adjustable emission filter suitable for fluorophores that were imaged. Cell trace images were acquired using a 5x air objective (NA 0.16), YAP images were acquired using a 20x air objective (NA 0.8), Immunostaining images were acquired using a 40x oil immersion objective (NA 1.3).

RNA Sequencing

Cells were treated with 1um Palbociclib for 16 hours then replated to make 3 monolayers from each condition. All monolayers were cultured together in a 10cm petri dish with 10ml of media containing 100ng/μl doxycycline. Media was replaced each day for 5 days. Then 2 monolayers from each condition were lysed, pooled and total RNA was collected using a NucleoSpin RNA kit (740955; Macherey-Nagel). 1 monolayer from each condition was labeled with JF 646 halotag and imaged, then cells were resuspended for volume measurements as described above. Volume distributions corresponding to each RNA seq experiment are available in Fig. 4.15. RNA samples were submitted to the University of Chicago Genomics Facility. The sequencing facility performed QC measurements on RNA (RIN from 9.4-10), libraries were prepared using Oligo-dT mRNA directional primers, and sequenced using Illumina NovaSeq 6000 with $\approx 60M$ PE reads/sample. Alignments were made to the canine genome (Canis-lupus-familiaris.CanFam3.1) by psudeoalignment using Kallisto 0.46.1 ([32]).

between 62.2 and 69.2% of reads were mapped with two technical replicates per experiment a total of $N_{p27_1} = 28049196$, $N_{p27_2} = 28117815$, $N_{p27_3} = 28012202$, $N_{p27ck_1} = 28212157$, $N_{p27ck_2} = 27961694$, $N_{p27ck_3} = 27964407$ reads. Data were then processed using iDEP 0.91([97]) to measure differential gene experssion ("Wnt Target genes | The Wnt Homepage," n.d.).

AminoSilane Glutaraldehyde modification of glass coverslips

Glass coverslips were modified as previously described ([365]). Coverslips were first cleaned by sonication in 70% and 100% ethanol solutions then dried with compressed air. We placed coverslips in a staining rack and submerged the rack in a solution of 2% (3-Aminopropyl)trimethoxysilane (APTMS) 93% propanol and 5% DI water for 10 minutes at room temperature while stirring. Staining racks were removed and washed in DI water 5 times then placed in a 37C incubator for 6-12 hours to allow the water to dry and amino-silane layer to cure. The staining racks were then submerged in 1% glutaraldehyde in DI water for 30 minutes while stirring. The coverglass was washed 3 times for 10 minutes in distilled water, air dried and stored at room temperature. Activated coverslips were stored under vacuum and used within 6 months of preparation.

Collagen gel preparation

10x PBS, milli-Q water, a 5mg/ml collagen stock and 1N NaOH were mixed to generate a polymerization mix with 1xPBS and 2 mg/ml collagen at pH $\approx$ 7. 70uL of the polymerization mix was added on to a 22x22mm coverslip modified with aminosilane according to the protocol above and quickly spread to coat the surface using a pipette tip. Samples were transferred to a humidified incubator at 37C to polymerize for 20 minutes. After polymerization gels were washed 3 times in 1x PBS and it was verified that gels were still intact and adhered to the glass by a tissue culture microscope

Cell Volume Measurements

Resuspended: Cells were plated as monolayers for indicated times. Just before making

volume measurements the cells were resuspended by adding 0.25% trypsin EDTA solution to the cells. Resuspending cells from ME conditions required partial physical disruption of the monolayer using a pipette tip. Cells were resuspended in 35ul of media containing 30nM JF646 and incubated for 5-15 minutes before adding to the sample prepared by sticking a coverslip to a glass slide using double stick tape. Cells were imaged immediately with spinning disk confocal microscopy. We verified that samples showed no changes in cell volume measured over time up to 1 hour and performed all measurements within this time window. Cells were imaged at the middle plane so that the radius of the cell could be measured. The cross-sectional area was used to estimate the radius which was used to calculate the volume of the cell. It was verified that this provided a comparable measurement to 3D segmentation of cells in the monolayer (Fig.4.2).

3D Images: Monolayers were stained using JF 549 halotag ligand and imaged using an airyscan LSM 980. Z- stacks spanning the height of the cell were imaged. The height of the monolayer was determined at each point by identifying maxima of the intensity corresponding to labeling at the top and bottom membrane of the cell. The membrane label averaged across the middle 5 planes of the cell was used to determine the area of the cell in the XY plane and this value is multiplied with the average cell height contained within this region to give the cell volume. A similar process was repeated with nuclei images to measure the nuclear volume

Cross-sectional Images: 3D images were acquired above and displayed as projections in the YZ plane. Images were opened in imageJ and the width and height of individual cells was measured from these cross sectional images. The same method was applied to histology sections where cells oriented perpendicular to the tissue section were first identified then the width and height of these cells was measured. The volume was estimated by the width squared times the height of each individual cell. These measurements are compared with 3D images for MDCK cells (Fig. 4.2)

Image Segmentation

Images of cell membranes were segmented using custom MATLAB code. The main algorithm performs initial segmentation using the Phase Stretch Transform algorithm developed by the Asghari and Jalali ([12]). Phase stretch images were thresholded and skeletonized to obtain cell outlines. Broken edges in the skeleton were repaired using a modified implementation of edgelink developed by Peter Kovesi ("Peter's Functions for Computer Vision," n.d.). Segmentation code can be made available upon request or from github/gardelLab.

Cell tracking

Cell tracking was performed using established particle tracking methods ([63]). Cell centers were determined by taking the centroid of each segmented cell area generated as described above in Segmentation. The particle trajectories were compiled from these position measurements using SimpleTracker, a MATLAB function developed by Jean-Yves Tinevez ([305]).

FUCCI Analysis

Cells were imaged in GFP and RFP channels similar to above methods using timelapse imaging. Images of FUCCI markers and cell boundaries were segmented using Phase Stretch Transform in Matlab as described above. Each cell was identified using the cell boundaries and was determined to be GFP or RFP positive by measuring the intensity contained within the segmented images of each nuclear marker. The percent of cells in G1 was determined by taking the ratio of cells identified as only GFP positive to the cells identified as GFP positive, RFP positive and positive for both markers. To determine duration of S/G2/M phase the cell cycle state was measured along the cell trajectory and points where the cell switched from G1 to S and then back to G1 were identified. Then the time between these events was measured to give the duration. To determine the full cell cycle duration the fraction of cells in S and G2/M phase was measured and along with the S/G2/M phase duration was used to estimate the cell cycle duration by CC duration = S phase duration/S phase fraction (i.e.

if 10% of cells are in S/G2/M which lasts 10 hours, cells spend 9 times longer on average in G1 and the duration of the cell cycle is likely 100 hours)

Division rate measurement

We identified cell divisions by finding pairs of cells which appear adjacent to each other in a frame after both cells were not present in the previous frame. We further filter out cells which are not of similar size to one another. We confirmed by inspection that this gives us a subset set of cells which have divided in the previous frame with few false positives. We then find the mother cell by looking several frames back for a cell near the centroid of the pair of daughter cells. We compare the number of cells of a given size which are detected to divide compared to the total number of cells of that size to get a probability of division. This process is repeated for the entire time series with a total number of division events typically > 500. The division rate is determined by the change in cell density over time to compute the overall rates

Quantification of H2ax staining

Foci were segmented using a phase stretch transform-based method and an intensity threshold. The cell nuclei were segmented using methods above and the number of foci in each nucleus was quantified

Growth Models

Growth curves were generated from growth models of exponentially proliferating cells with doubling time τ ($A(t) = 2^{t/\tau}, \frac{dA(t)}{dt} = \frac{log(2)}{\tau} 2^{t/\tau} = A(t)\frac{log(2)}{\tau}$) and of a circle with an expanding radius r ($r(t) = vt, A(t) = \pi v^2 t^2, \frac{dA(t)}{dt} = 2\pi v^2 t = 2v\sqrt{\pi A}$). Confinement curves are calculated from the ratio of these rates as defined in the main text.

G1-Sizer Model

Our phenomenological model of cell size control is a "G1 Sizer", which posits that exit from G1 is controlled by a size-dependent function. Based on the sharp drop-off in the G1 exit rate seen in the log-plot of experimental data in Fig. 4.10A, we assume that the rate is

a constant $k >> 1$ above a critical size a and 0 below that size. Following G1-exit, division proceeds in time τ .

As discussed in the main text, this model has two regimes: one of slow growth ($G\tau << a$), and one of fast growth ($G\tau >> a$) Switching to non-dimensional units where $a = 1$ and $\tau = 1$, we can derive results for time-averaged single-cell quantities, including average area, average time between divisions, and confinement. This can be done for both the fast- and slow-growth limits. In the following expressions, $< >$ indicates an average over time for a single cell.

In the fast-growth limit with growth rate G, cells never interact with the size-threshold , and hence have a constant division time set by the mean length of G1 plus the length of S/G2/M. This means a confinement of 0, and an average size s proportional to G. To summarize:

$< s >= 1.5(1 + 1/k)G; < t_{div} > (1 + 1/k); C = 0$

In the slow-growth limit with growth rate G , cells are almost exclusively below the size-threshold, and hence have division time set by the mean length of G1, plus the length of S/G2/M, plus the time it takes to grow up to the size threshold. Solving for the division time yields the following expressions:

$< s >= 0.75(1 + G(1 + 1/k)); < t_{div} > \frac{1}{2}(1 + 1/k + 1/G); C = 1 - \frac{1+1/k}{\frac{1}{2}(1+1/k+1/G)}$

These expressions are verified against numerical results (Fig. 4.12).

Numerical Simulation of G1-Sizer Model

In order to further understand the implications of the phenomenological G1-sizer model in a tissue context, we implemented a stochastic agent-based simulation of growing cell monolayers. In this simulation, each cell carries an index i, as well as two quantities a_i and p_i, representing the size and cell cycle phase respectively. Time and size are in non-dimensional units during the simulation and are converted to dimensional units for analysis after the simulation. We do this by associating 1 unit of simulation time to be the length

of a typical S phase (10 hours), and 1 unit of simulation size to be the volume at which it is seen experimentally that cells transition from a size-dependent to a size-independent division rate ($1250\mu m^3$). We run our simulations with constant timesteps dt of .005. In the specific use case of Fig. 5E, we verified that the results obtained with a timestep of .0005 were not quantitatively different from those generated at $dt = .005$.

At every step in the simulation, growth of cells is advanced by changing each a_i by an amount $G * dt$, where G is the growth rate of the cell. G is in principle a function of the parameters of the cell itself, such as a_i and p_i, as well as global parameters such as the total number of cells N and the total area of cells A. We observed similar results in a model with exponential single-cell growth (Fig. 4.13)

Division of cells is regulated by a size-dependent probability of entrance into S-phase. If a cell exceeds an area of 1, it enters S at a rate of 3, at which point its phase variable p_i is set to a value of $1/dt$. At every step in the simulation, the phase variable p_i decreases by 1, and once pi reaches 0, the cell's S/G2/M phase is completed. Therefore, following stochastic initiation, each cell experiences S/G2/M phase as being a deterministic time of 1. We choose a G1 entrance rate of 3 so that the average total time of the cell-cycle in the size-independent regime is matched between simulation and experiment. At the point that a cell exits M, the cell's size a_i is reduced by a factor of 2, and an additional new cell is created with size $a_i/2$. These two elements – size-dependent S entrance, and growth of cells – constitute the core of how we advance single-cell trajectories through time. We explore the implications of this framework in two categories of simulations – ensemble simulations, and single-cell simulations. In single-cell simulations, we track the trajectory of only one cell, following only one daughter cell after division. In ensemble simulations, we track a whole population of cells, and the growth rate can therefore depend on quantities like N, the total number of cells in the population.

In Fig. 4.10D, we show example single-cell trajectories with two different constant growth

rates G . To exhibit timer-like behavior, we simulated cells with a growth rate $g = 1.6$. To demonstrate sizer-like behavior, we simulated cells with a growth rate $G = 0.1$. In this particular set of simulations, the S entrance rate was set to 10, to more clearly demonstrate the differences between the two growth regimes. Cells are initialized with a size uniformly drawn from 1 to 2, and a phase pi that is either 50% uniformly distributed between 0 and $1/d$t, or 50% $p_i = -1$. Trajectories are simulated for 50 units of simulation time, though only a small fraction is shown of those trajectories

In Fig. 4.10E, we use single-cell simulations to look at the relation between cell size immediately post-division versus immediately pre-division in the subsequent round as a function of growth rate. We did this for 4 growth rates $G = 1.0$, 0.7, 0.2, and 0.05. Each growth rate was simulated with 400 simulation replicates, each run for 40 units of simulation time. We initialize each simulation with $p_i = -1$, and a random size uniformly distributed between 1 and 2, and allow cells to grow with $G = 1$ for 10 units of simulation time before switching to the simulation specific growth rate. After another 10 units of simulation time, we begin recording the size of a cell immediately post-division, and immediately pre-division. Confinement values are estimated as $1 - \frac{divisions.observed}{divisions.expected}$

In Fig. 4.10F, we show results from an ensemble simulation of cells. Ensembles are initialized from 4 cells with sizes uniformly drawn from 1 to 2, and then normalized such that they have total area 8. Cell phases are either 20% uniformly distributed between 0 and $1/dt$, or 80% $p_i = -1$. We first allow the cells to expand in an unconstrained way, i.e. we grow each cell in our simulation with a growth rate G, which is drawn for each cell and each time point from a uniform distribution with support between .9 and 1.1. When the ensemble of cells collectively exceeds a critical total size, we quench all their growth rates to 0, and therefore only division occurs from beyond that time point, which we set to be $t = 0$. We perform these simulations for three different critical total sizes 500, 1200, and 4700, with 20, 10, and 5 simulation replicates respectively. After the critical size is reached, we can track

the ensemble distribution of areas as a function of time, which we do for 4 units of simulation time, corresponding to 48 hours of real time. We did not notice any significant differences in the distributions as a function of the total size at which we quench the growth rate

CHAPTER 5

DISCUSSION

5.1 Summary and Future Directions

In these studies, we have demonstrated an interplay between cell proliferation and collective cell behavior in epithelia. We find that when cell proliferation rates are high, cells show increased mechanical fluctuations (Ch2) and differences in cortical mechanics (Ch3). Conversely, we show that proliferation depends on the collective behavior of epithelial cells because of a relationship between spatial constraints and cell growth (Ch4). Cell proliferation could be an important factor distinguishing active and quiescent tissue states such as wound healing and homeostasis (Fig. 5.1). Our results suggest that when proliferation is triggered cell-cell interactions change to facilitate tissue behaviors required for development or repair. Coupling proliferation and tissue mechanics creates a positive feedback mechanism where both division and collective behavior become active and reinforce one another. Due to the complexity of cell-cell interactions and biological systems, more work is required to test and build on these ideas. I hope that these findings will lead to further development of new modified vertex models which can account for the complexity of cell-cell junctions, an exploration of how proliferation affects cell-cell interactions and sorting across additional epithelial tissues, and an understanding of contact inhibition *in vivo* across different epithelial tissues.

5.1.1 Cell cycle dependent active stress in epithelia

We performed an exploration of cell shape remodeling in epithelia to understand what mechanisms regulate cell shape (Ch2). Understanding how cells change their shape is a key question in developmental systems. For example, convergent extension of tissues require cell shape changes and rearrangements for tissue elongation ([27], [327]). While proliferation has been

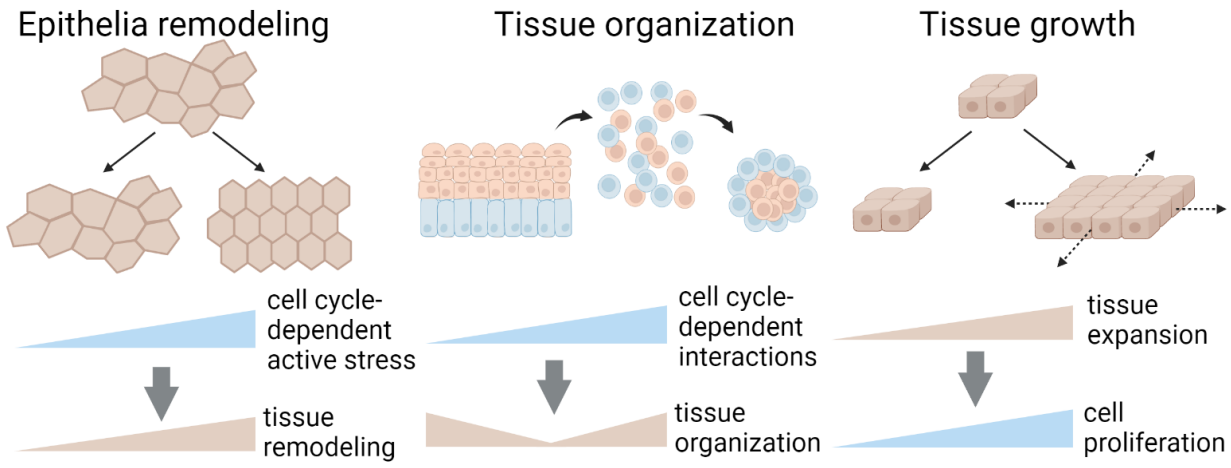

Figure 5.1: Epithelium show an interplay between cell proliferation and collective cell behavior. In studies of epithelia remodeling we observe that cell proliferation leads to active stress which drives changes in cell morphology at the tissue scale. In studies of tissue organization we see that differences in proliferation drive tissue self-organization. In studies of tissue growth we see that tissue expansion driven by collective cell migration is required for cell growth and division.

demonstrated to directly affect cell shape ([77], [101]), a significant fraction of the shape change we observed came from changes in junction length in nondividing cells. *In vivo*, most of the cell shape changes and rearrangements occur on a time scale that is faster than the division cycle. Our work suggests that cell cycle-dependent fluctuations could be important in these contexts. In agreement with this, there is also evidence of cell cycle dependent processes driving tissue flow *in vivo* ([90], [239], [238] [263]). In these experiments blocking the cell cycle with inhibitors immediately arrests the flow, similar to our experiments on epithelia remodeling. More work is required to understand if common mechanisms are responsible for cell cycle-dependent tissue flow. For example, future work could uncover the molecular mechanisms underlying cell cycle-dependent changes in cell mechanics between different tissues and see if there is a common pathway. The *in vitro* approach we used may be the simplest way to determine the molecular mechanisms and then these mechanisms could be tested in developmental systems.

Importantly, our work also builds on prior work developing vertex models of epithelial

tissue ([6], [23], [24], [356]). We used vertex models as a framework for interpreting data from monolayer remodeling experiments. These models predicted a relationship between cell shape and mechanics, which we searched for experimentally. The initial expectation from the model was that under a range of conditions we would observe an arrest of cell motion at the same shape parameter ($q = 3.81$). Instead, we observed certain perturbations which leave this relationship unchanged (differences in substrate). Whereas, other perturbations could change the relationship between shape and speed. We showed that across many conditions this was caused by perturbations to the cell cycle. By perturbing the cell cycle directly, we saw that the cell cycle is responsible for driving active mechanical fluctuations in the epithelium. Therefore, cell dynamics depend on active cell cycle-dependent fluctuations independent of rigidity. We then modified our model so that a fraction of cells are exerting active tension, representing the fraction of dividing cells. We showed with this model that when decreasing the fraction of active cells we see a reduction in the cell motility, in agreement with our experiments.

However, there are still difficulties interpreting the data from our experiments because active fluctuations were small and cells did not rearrange readily at the time scales accessible in experiments. Mechanical measurements on cell monolayers are required to test when changes in cell motility result from changes in active stress or from a rigidity transition. Such measurements have been made in some cases in developing systems, but it remains challenging to make simultaneous measurements of cell shapes and tissue mechanics across different conditions ([239], [208]). Our results suggest that to account for low motility in states which are predicted to be fluid-like, new models which incorporate shape-independent barriers to cell remodeling are needed. This is most notable in our experiment where we wash in a CDK1 inhibitor. This arrested the motion and shape remodeling immediately. Vertex models would suggest that a sudden quench in active stress would cause cell shapes to become more regular but we observe that instead cell shapes remain the same. If there

are shape-independent barriers to junction length changes, this would explain how the cells could arrest in a metastable state when active stress is reduced instead of remodeling to a more regular cell shape. It is possible that a model with these additional energy barriers would apply broadly for different regimes of active stress. For example, when looking at low motility tissues like the epithelial monolayers we studied, shape-independent barriers are important, but in highly motile developmental systems the shape-dependent barriers are more important for controlling the collective cell behavior.

Our work suggests an interesting connection between the cell cycle and the generation of active mechanical stress. This hypothesis has been recently explored in other work looking at how key cell cycle proteins regulate the cytoskeleton ([106], [135], [249], [254]). However, the molecular mechanisms are not completely understood. Notably, these studies focused on focal adhesions but have not examined adherens junctions which are more relevant to epithelial remodeling. One of the main candidates are kinases which are central to regulation of the cell cycle, the cyclin dependent kinases (CDKs). While CDKs have been heavily studied in cell cycle regulation, other non-cell cycle functions have been recently discovered. For example, CDK1 has been shown to phosphorylate adhesion proteins to alter adhesion size and turnover ([135], [106]). It is possible that CDK1 or other CDKs also phosphorylate proteins at the adherens junction to modify cell-cell interactions. Another possibility is that division associated cytoskeletal proteins are also active in interphase. For example, the centralspindlin complex, which drives cell rounding during mitosis, has also been observed at interphase adherens junctions where it activates ECT2, a Rho guanine nucleotide exchange factor (RhoGEF) ([254]) It is possible that centralspindlin expression or activation is higher in cells which are going through or recently went through the cell cycle and this may explain the increased active stress. There is also evidence of increased contractility during S phase compared with other cell cycle phases supporting a role for cell cycle proteins regulating the cytoskeleton ([323]). Further work looking at the localization and activity of cell cycle

proteins at the cortex are required to understand the origins of cell cycle dependent active stress. If these molecular mechanisms were known, they could be examined *in vivo* to find out their role during embryonic development.

5.1.2 Cell proliferation drives cell sorting

Another important consequence of cell cycle-dependent cell-cell interactions is on the self-organization of cells in epithelia. We performed experiments to explore the mechanism by which self-organization occurs in the skin. As cells differentiate they change gene expression and inhibit proliferation. Therefore, we looked at the effects of both gene expression of the formin Dia1 and proliferation. We made model skin tissues using organoid methods to test how these perturbations affect the development of skin. Blocking Dia1 expression or proliferation causes cells to preferentially move toward the upper layers. This suggested that both play a role in tissue organization. Building on prior work looking at cell sorting, we use a measurement of contact angles to assess the cell-cell interaction ([195]). In both cases we observed significant changes in contact angles. Therefore, suggesting that cell sorting mechanisms control self-organization of skin.

The correlation between cell sorting and proliferation that we observed may suggest a broad principle of tissue self-organization. While it remains untested, there is a possibility that this dependence of cell-cell interactions on proliferation is observed broadly and could explain the spatial segregation of dividing and non-dividing cells observed across numerous epithelial tissues *in vivo*. However, there are still outstanding questions regarding cell sorting and the dependence on the cell cycle. We looked at the contact angles in 2 different contexts, but the measurement must be made in additional systems to show if this extends beyond the skin epithelium. At the same time, we did not examine the underlying mechanisms driving this change in contact angle. High throughput methods like single-cell RNA sequencing or proteomics could be used to look at how cell cycle perturbations lead to changes in the cell-

cell interaction. A more mechanistic understanding of this could be used to examine other tissues or to manipulate the contact angle to gain insight into cell sorting. The underlying mechanisms of cell sorting also need to be explored further. How the changes in cell-cell interactions cause cell sorting to occur are still not completely understood (Ch1). This is because the mechanical properties of cell collectives are complicated and have not been studied in detail. In particular, dynamic and mechanical measurements during cell sorting are still required to develop a detailed understanding of how this process occurs.

5.1.3 Collective cell behavior controls cell proliferation through contact inhibition

Finally, we explored how proliferation is regulated in the context of epithelia and introduced a new phenomenological framework to understand contact inhibition of proliferation. Here we demonstrated that there is a feedback between cell and tissue growth, which can be quantified by the "tissue confinement" (Fig. 5.2A). One consequence of this relationship between confinement and cell growth is that cell size changes in epithelium as the growth rate is reduced, but cell division rates remain high (Fig. 5.2B). The cell size reduces through division until the cell cycle arrests at a specific cell size protecting the cell from DNA damage (Fig. 5.2C).

We tested this in our *in vitro* model of epithelial tissue, but it remains an open question whether such a model can be applied broadly - some existing data suggests it might. For example, we observed a change in cell size between epithelial cells *in vivo* and single cell cultures *in vitro* across many tissues and cell lines ([71]). There is also data in mouse skin which suggests that cells regulate the cell cycle by a G1 sizer mechanism in a confined tissue *in vivo* ([348]). Other studies of tissue growth also show that proliferation responds to changes in cell turnover ([203]), but not growth signaling ([228]). We propose two methods to test the generality of these results. The first would be to collect tissue growth data from

published work in developmental systems and calculate the confinement, cell size and YAP or other growth signaling pathways. These results could then be compared to our *in vitro* results. A second approach would be to continue making more perturbations to the system *in vitro* to find the underlying molecular mechanisms of tissue confinement and then testing a perturbation of these mechanisms on tissues *in vivo*. Several simple experiments would help narrow down the possible mechanisms. First, the geometry of expanding colonies could be altered and different configurations could be used to see if the signal is mechanical. For example, a bridge of cells between two colonies would transmit a mechanical signal but not a diffusable signal. Different epithelial cell lines could be tested to see if this behavior generalizes to different types of epithelium. Non-epithelial cells could be tested to see if cell-cell junctions and epithelial characteristics are required for a response to confinement. Finally, disruption of junctions or contractility could be used to see if junctional tension is important for signal transmission. The YAP pathway is potentially implicated in the response and is thought to be mechanosensitive ([129], [132]). If the model of tissue confinement turns out to be general, it could provide insight into the regulation of cell proliferation across many conditions in tissue homeostasis and disease.

In our experiments, we show that the cell cycle becomes arrested in G1 at small cell size but we did not link this back to a cell size sensing mechanism directly. Further experiments are needed to determine the mechanism by which cyclin D is downregulated and connect this to cell size. However, the question of size sensing has been pursued by other labs and has proven to be challenging ([349]). Our p27 expression system may be useful as it allows for cell size to be easily manipulated from the minimum size to a size 2-3 times larger. This change in cell size is also independent of cell growth, whereas most other ways of perturbing cell size involve changing the growth rate. Different methods of perturbing cell size will have different systematic errors, so combining them will be more likely to yield factors which are truely size dependent. Cyclin D degradation is a top candidate for the regulatory mechanism

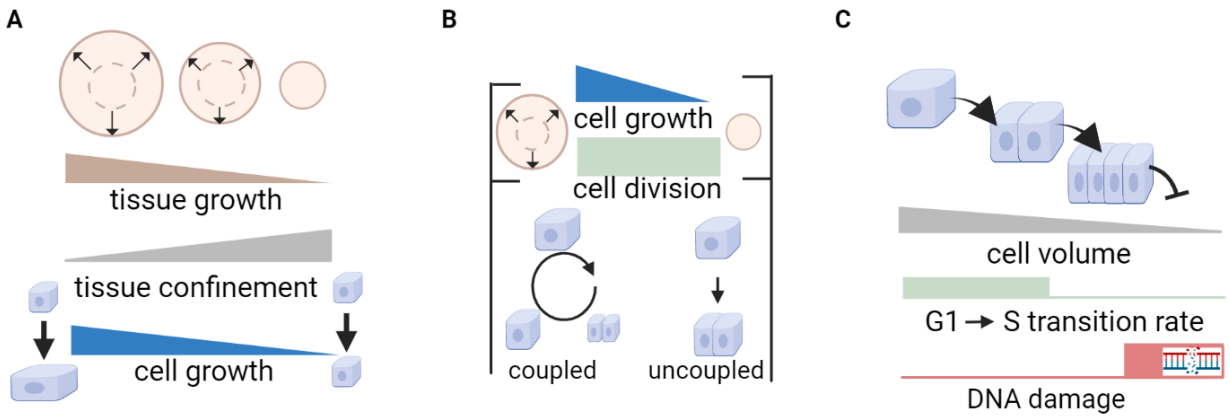

Figure 5.2: Tissue confinement controls cell size and growth in epithelia (A) tissue scale processes regulate how a tissue grows in response to changes in the environement setting the tissue confinement. Cells respond to the tissue confinement by regulating the growth rate. (B) Tissue confinement regulates cell growth but not the cell cycle leading to decoupling and changes in cell size (C) Cell size can decrease to a limit where the G1 to S transition becomes inhibited. This point occurs at a cell size where the cell is protected from DNA damage from low size.

([4]) because the RNA levels do not change but protein levels are very different when cells are small. There are multiple kinases which are known to regulate the degradation of Cyclin D (ERK, p38MAPK, DYRK1, and GSK3B). Using our model system, one could look at how the kinase localization and activity changes with cell size, then continue to look upstream until a mechanism linked directly to cell size is uncovered. However, it is also possible that the Cyclin D is not actively regulated but is related to the overall changes in the proteome with cell size ([167], [51]).

An understanding of cell size regulation could be useful in the context of cancer where size regulation becomes disrupted. Our model provides a means for understanding this loss of size regulation. In most cancers, where cell size is increased, this could occur as cancer cells evade contact inhibition and continue to grow in high confinement where normal cells arrest their growth. In the case of small cell cancers, the mutation of cell cycle regulators may allow cells to overcome the lower limit of cell size while remaining confined, which could lead to DNA damage and drive the transformation of cells to a cancerous state. Future work is

required to understand how cell size regulation is perturbed in cancer and the consequences.

5.2 Outlook

Here we study several collective behaviors of the epithelium using simple phenomenological models. The aim of these studies is to find underlying principles that may apply broadly across epithelial development and homeostasis. However, biological systems display significant diversity and it remains a challenge to determine which properties are conserved at the multicellular scale. While we have demonstrated several mechanisms which may be general, future work is required to test these mechanisms in more detail and in other types of epithelia.

While we chose to focus on the behavior of epithelia in these studies, there are many other collective systems which are of interest to biology and physics (Fig.5.3). These range from more simple physical systems like liquid crystals and glass forming materials where the physical interactions underlie collective phenomena like phase transitions. An interesting area of current research is examining what happens when these systems are driven away from equilibrium by active mechanical stress. Such active materials provide a simplified system for thinking about the physics of living systems. On the other hand, complex biological systems like the nervous or immune system are essential to multicellular organisms and human health. As a result, these systems have been actively studied for the past 50+ years. Epithelia are an interesting system which is somewhere in between these in complexity. In epithelia, collective behavior is determined by physical interactions between cells, but due to the complexity of individual cells, there can also be nonlocal effects, time-varying properties, and feedback. Just as many of the ideas involved in studying epithelia have been borrowed from the study of nonliving systems ([304], [86], [124]), more complex biological systems like the immune system may be inspired by the principles that are found studying epithelia. In some cases, like the electrical signaling between epithelial cells, the analogy between epithelium and

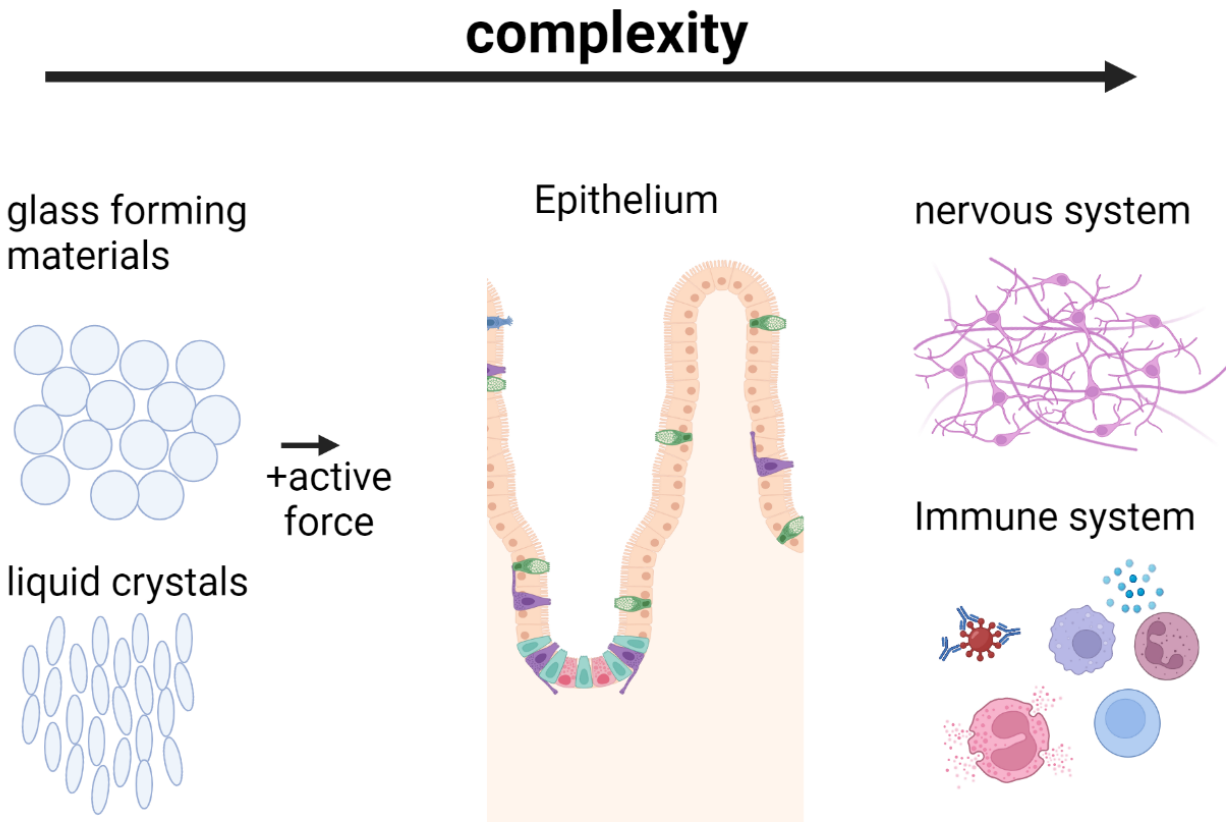

Figure 5.3: Epithelia as a model of collective behavior. Many physical and biological systems show collective behavior. More simple physical systems like glass forming materials and liquid crystals are more well understood and have been used as analogies for understanding more complex systems. These systems can be made active by using particles which exert stress at the microscopic level leading to new collective behavior. Epithelium are of intermediate complexity and analogies from the physical systems have been used to describe them. It is possible that analogies from physical systems and epithelium could be used to learn about more complex biological systems like the nervous system or immune system.

neurons is already an active area of research ([175]).

Interestingly, the models we used to describe the collective behavior of epithelia are naively simple, yet seem to describe many of the phenomena we observe. Individual cells have over 25000 genes which can influence the cell state, simply taking each of these as a binary state would permit 2^{25000} different cell states ([2]). In our models, we consider all cells to have the same behavior or to act as binary populations. The assumption that cells have a fairly uniform mechanical state turns out to be reasonable, but this could not

be predicted from physics directly. Instead, all simplifications must be directed by our experimental observations. Biology may turn out to be simple to model, but understanding which parameters are important and which can be ignored remains an open challenge. Many phenomena of physics are described by a small number of simple equations. Whether such a description of biology is possible has yet to be determined. One possibility is that a description of biology requires a complete understanding of the properties of every molecule in the cell and their quantities. However, as we build and test simple models of biological phenomena, we may find that many of these details are not required to understand how biological systems operate.

Modern biological approaches allow for unprecedented quantification of thousands of RNA and proteins across tissues. Cataloging these interactions is a clear avenue for new biological research. In principle, after many years of research, we may come to know all the molecular details of a cell. But what will we do with a list of billions of interactions? One key area of biology research in the coming years is concerned with putting these facts back together to understand the big picture of how biological systems function. However, the space of phenomenological models is also vast and must be constrained by experiments and biological data. Both molecular and systems level descriptions of biology are required together to describe and understand biology. Moreover, these molecular and theoretical methods can build on and direct one another. We focused our efforts on experimental studies of tissue-scale processes and connected them to corresponding models. We then attempted to connect back to details of the cytoskeleton and cell cycle. We were able to describe new collective phenomena and suggest how they are regulated by cell scale properties. We hopefully set the stage for future studies which reveal these molecular mechanisms in detail and test the generality of tissue phenomena more broadly. I hope that the work presented in this thesis plays a small part in guiding future work to reveal how epithelial tissues function in health and disease.

APPENDIX A

EXPERIMENTAL PROTOCOLS

A.1 Epithelial cultures on collagen gels

Methods for making collagen gels on glass. Makes a gel which is $\approx 200\mu m$ thick. Reduced volumes of collagen can be used to prepare thinner gels, but below 50μl/22x22mm cover glass ($\approx 150\mu m$) it becomes difficult to make without breaking the gel. Glass silane modification quality also controls gel breaking.

Materials

1. Collagen polymerization mix (70μl per 22x22mm coverglass) 2mg/ml Collegen I (BD, rat tail collagen I - brand can affect the polymerization rates and mechanics) 1X PBS (diluted from 10x stock) pH 7 (Just before using add 1μl of 1M NaOH per 90μl of Collagen I added to the mix - check with pH paper for your conditions)

(optional - for visualizing the gel) - 1:20-1:100 labeled collagen I

2. APTMS-Glutaraldahyde modified coverglass

Gel preparation

1. Transfer the modified coverglass to a sterile petri dish

2. Prepare collagen gel mix to specifications above on ice - add NaOH last just before polymerization - perform 3-6 as quickly as possible

3. Vortex the solution for 5 seconds

4. Add 70μl of collagen polymerization mix on to each cover glass - try to avoid bubbles

5. Take two 1ml pipette tips and spread the collagen mix to all parts of the glass using the tip - tilt the dish to help with spreading

6. Put lid on and transfer the petri dish to the 37 degree incubator for 20 minutes

7. As quickly as possible - remove petri dish and add 5-10ml of pbs to the lid - pick up coverglass, invert and submerge the gel in the pbs, then transfer to a 35mm cuture dish with

gel up - repeat with all the gels

8. Add 100μl of 1x PBS to each gel to prevent drying

9. Check that the gel is not broken under tissue culture microscope - turn on illumitation and look at the gel by naked eye - if gel is broken only some of the gel will scatter light and appear white with other parts clear - the gel can also be visualized looking through the microscope as a light gray mesh

Plating cells

1. Prepare cell suspension

2. Tilt gel and aspirate the pbs then add cell suspsension on the gel surface - 50-250ul volume will stay on the gel $\approx 4 \times 10^5$ cells on 22x22mm for monolayer, $\approx 2 \times 10^4$ for small colonies

3. Incubate at 37C for 5-10 minutes to allow for cell adhesion to the gel

4. Add 1.5ml culture medium to the dish

5. Wait for monolayer to form for at least 12 hours

Gel crosslinking

1. Gel stiffness can be modified by changing the concentration and by glutaraldahyde crosslinking ([166])

2. Polymerize gels as described above

3. Apply 1xPBS containing 0.2% glutaraldehyde for 30 minutes

4. Wash gels quickly 3 times in 1xTBS, then wash in 1x TBS at 1 hour intervals 5 times and left in 1x TBS overnight to quench excess crosslinking groups on the gel

A.2 Cell doublet preparation

Cell doublets can be prepared in suspension to allow for quantification of contact angle between pairs of cells.

Materials

1. SYLGARD™ 184 Silicone Elastomer Kit

2. 500μl microcentrifuge tubes

3. 10 cm petri dish

4. Glass coverslips and imaging chamber

5. 1% pluronic F-127 solution

6. Cell culture materials

Making PDMS chambers for cells

1. Mix 0.8g of 1:10 SYLGARD in a 10cm petri dish - this should form a ≈0.3mm layer of pdms

2. Spread this solution as evenly as possible across the surface - it should be difficult to cover the whole dish with this volume

3. Degass the solution in the dessicator to remove bubbles

4. Polymerize for >1 hour at 70C

5. While polymerizing soak ≈20 microcenrifuge tubes in 1% pluronic top down - this will prevent sticking later

6. While polymerizing mix 3g of 1:10 SYLGARD in a weigh boat

7. Degass the solution

8. Pour this on the polymerized PDMS and spread evenly

9. Dry and place the microcentrifuge tubes lid down into the PMDS spaced appart to make the wells

10. Polymerize overnight

11. Pull off the microcentrifuge tubes. This will leave a well to put the cells in.

preparing and passivating the chambers

1. Cut out the chambers and stick them on to coverslips - remove any bubbles between the glass and PDMS

2. UV-ozone the coverslips and PDMS for 15 minutes to sterilize

3. Place in a petri dish and move to the culture room hood

4. Add 200ul of 1% pluronic solution into the PDMS well and wait 1 hour

5. Wash the well with 1X PBS 3 times

6. Add cell suspension to the well approximately 15000 cells in the well

7. Wait 4 hours, mount the coverslip in an imaging chamber, and image - with this protocol the sample is thick enough that a >0.3mm working distance objective should be used

A.3 Expanding colony assay

Method used for preparing expanding monolayers based on the methods of Heinrich et. al. 2020 eLife ([117])

Materials

1. SYLGARD™ 184 Silicone Elastomer Kit

2. Leather hole punch set (Nuhank 0795787181775)

3. 10cm petri dish

4. Collagen I solution - 0.2mg/ml collagen, 0.02M Acetic Acid, 1x PBS

5. Cover slips with imaging chamber

PDMS mask preparation

1. Add 4g 1:10 PDMS to the petridish and mix

2. Degass the solution

3. Polymerize overnight at 70C

4. Cut sqaures out of the PDMS with approximately the same size at the coverslips

5. Use hole punches to make holes for the initial monolayers - space a few mm apart to allow for expansion

6. Wash the masks in 70% ethanol solution followed by milli-Q water

7. Dry the masks completely

Preparation of monolayers

1. Apply collagen solution to coverslips for 1 hour

2. Wash coverslips with 1x PBS then milli-Q water

3. Allow coverslip to fully dry

4. Apply PDMS mask - ensure both are fully dry and adhere without bubbles

5. Add cell suspension into the wells - solution 1.2×10^6 cells/ml - 12ul for 3mm diameter, 4ul for 1.5mm diameter, 2.5ul for 1mm diameter

6. Prepare 2 samples without masks in subconfluent (2×10^4 cells per 22x22mm) and confluent (3×10^5 cells per 22x22mm) states as controls

7. Allow cells to adhere for 10 minutes then add 2ml media to the culture dish so the PDMS is fully submerged

8. Wait overnight for monolayer to form then remove the PDMS mask

A.4 Lentivirus preparation

Method used by John Devany for preparing lentivirus based on the following protocols :
$https://www.hollingscancercenter.org/research/$
$shared-resources/shRNA/Lentivirusproduction-shRNA.pdf$,
$https://www.mdanderson.org/documents/core-facilities/$
$Functional\%20Genomics\%20Core/Homemade\%204fold\%20$
$lentivirus\%20concentrator.pdf$

All materials in contact with the viral material should be bleached and put in separate waste bags for disposal.

Materials

1. 293T cells

2. Plasmids for lentiviral genome, delta 8.2 and VSVG

3. Lipofection reagent - fugene HD, fugene 6, Lipofecatmine etc.

4. Cell culture reagents

5. 4x peg solution (40% peg 8000, 1.2M NaCl, 1xPBS, pH 7) or a 15ml amicon centrifuge

filter

6. 1M NaOH and HEPES for pH (optional)

preparing lentiviral supernatant

1. Determine good transfection conditions for 293T cells ($> 50\%$ transfection is okay but $80-90\%$ is ideal - maximize by trying different reagents or getting cells from different people)

2. Culture 293T cells on a 10cm dish to $30-50\%$ confluence (higher confluence can reduce transfection efficiency but use whatever conditions were determined above)

3. Prepare lipofection solution (for 10cm I use 3ug of target plasmid, 2.7 ug of pHR1-8.2-deltaR and 0.3ug of VSVG and 3:1 ratio with fugene HD)

4. Transfect cells and leave them overnight

5. Replace the medium - dispose of this media and treat cells as if it contains virus (adding HEPES to help buffer the medium might help as the virus is more stable at pH7)

6. Collect virus and replace every 12 or 24 hours. From this point up to 72+ hours expression should continue (12h should give higher titer because the virus half life is 8h in 37C, 24 usually works okay and is more convenient)

7. Store virus in a labled 50ml tube in the 4 degree fridge (adding NaOH to reach ph7 may help with stability)

Concentrating the virus solution - PEG precipitation

1. Spin down at 1.5k for 5 minutes to pelette any cells

2. Add peg solution to the viral supernatant to 1x contentration and adjust pH to around 7 (I just eyeball with the phenol red)

3. Parafilm the falcon tube and put it on the shaker in the cold room for 4 hours to overnight

4. Spin down the solution at 9k for 30 minutes (I've also tried 1k for 90 minutes using the culture centrifuge before but 9k should work better)

5. Pour out the supernatant

6. Resuspend in final volume (I use 1ml) of cold 1x PBS - pipette up and down to fully

disolve the pellet (can also use medium but it is more difficult to disolve)

7. Continue to viral infection or freeze virus for storage in -80 (add to cell freezing vial - flash freeze in liquid nitrogen)

Concentrating the virus solution - amicon

1. Spin down at 1.5k for 5 minutes to pelette any cells

2. Load virus into the amicon filter and spin down according to the protocol

3. continue loading and spinning until all the viral supernatant is filtered

4. Add volume to reach final desired volume (typically 1ml) and pipette up and down on the filters to remove any virus stuck on the filters

5. Continue to viral infection or freeze virus for storage in -80 (add to cell freezing vial - flash freeze in liquid nitrogen)

Viral infection

1. Plate 50,000 cells in a 6cm dish with 2ml medium (this is all for MDCK - might want to adjust the number of cells, polybrene, and virus concentration for other cell lines)

2. Add polybrene at 8μg/ml to the cells

3. Add virus and leave overnight (I typically add 1/3 of the prep and freeze the rest)

4. Change the medium and culture the cells for 2 more days before selection with antibiotic or sorting

APPENDIX B

SUBCELLULAR NANORHEOLOGY REVEALS LYSOSOMAL VISCOSITY AS A REPORTER FOR LYSOSOMAL STORAGE DISEASES

This appendix is repproduced from the publication Subcellular Nanorheology Reveals Lysosomal Viscosity as a Reporter for Lysosomal Storage Diseases by John Devany, Kasturi Chakraborty, and Yamuna Krishnan published in ACS Nanoletters ([70]).

The work is included in full because it was completed mainly by me during my PhD training but it is inculded in the appendix because the topic is different from the main thesis. Kasturi Chakraborty provided data in Figure B.12 . Yamuna krishnan and Kasturi Charkaborty provided guidance on the project and helped with writing the manuscript

B.1 Abstract

Cells have evolved a diverse set of membrane-bound compartments known as organelles that each enclose specialized, nanoscale chemical environments optimized to facilitate specific kinds of biochemical reactions. While we are aware of the chemical composition of many organelles, we know very little about their physical properties and the influence of these properties on the biochemistry therein. Following the discovery and characterization of dozens of biological condensates in cells, it has become apparent that physical characteristics such as viscosity and mesh size are critical factors controlling the chemical reactions that take place in phase-separated compartments ([31], [128]). In some cases, the viscoelastic properties of these condensates can evolve with time, causing compartment, which initially allows free diffusion to form gels in which reaction rates are significantly reduced ([16]). However, no nanoscale technologies exist to probe physicochemical characteristics within organelles to identify whether chemical reactions follow similar or different rules within nanoscale,

membrane-bound compartments.

Previous attempts to study organelle viscosity used small molecule fluorescent probes that, while useful, cannot provide information about material phase or elasticity. Furthermore, successful targeting of those probes relied critically on the high acidity of the lysosome or membrane potential of the mitochondria ([292], [330]). Results are further complicated because the fluorescence of viscosity sensing dyes is intrinsically dependent on environmental composition and may be affected by protein binding ([330], [112]). In diseases or stressed conditions, the chemical composition of the lysosome in particular is known to change, affecting these results and making viscosity measurements in perturbed conditions nontrivial. Here, we describe a generalizable method to measure viscosity in an organelle based on passive particle-tracking nanorheology (PPTN). This new method provides an absolute measure of viscoelastic properties that is independent of solvent composition. Moreover, probe targeting is independent of the ionic composition of the organelle and is generalizable to a variety of endocytic organelles. We demonstrate as a proof of concept, measurement of viscosity in the lysosome under normal conditions and in several disease conditions in which the ionic and solvent composition change substantially.

The lysosome is a subcellular organelle that houses an array of enzymes to degrade material ingested by the cell as well as to degrade and recycle obsolete cellular machinery. Within the lysosome, a specific ionic composition is maintained to allow degradative enzymes to function. If enzymes within the lysosome are unable to function substrates of these proteins, accumulate within dysfunctional lysosomes, disrupting cell function. Lysosomal storage diseases (LSDs) are a group of over 70 different genetic diseases, each of which arises due to a defect in a specific lysosomal protein that causes the lysosomal storage of a specific biological substrate ([95]). In many cases, material storage is accompanied by ionic imbalance that can further amplify lysosomal dysfunction ([183], [278], [45]). This ultimately leads to tissue damage and lethality ([230], [15]). Although substrate accumulation is central

to the pathology of LSDs, LSDs themselves are typically identified by assaying for lysosomal enzymatic activity, because in most cases substrate accumulation is difficult to measure. In some LSDs, lower enzymatic activity shows a correlation with more severe symptoms but in others it does not ([171]). Furthermore, many LSDs are caused by defects in proteins whose function is unrelated to enzymatic cleavage, e.g., transporters, activator proteins, proteins involved in maintenance of lysosomal membrane integrity, etc. These LSDs cannot be detected by standard enzyme activity assays, which detect bond-cleavage events ([88]). Measuring the amount of stored material directly within the lysosome would allow for a more-generalizable, direct monitoring of the disease progression and treatment in all LSDs independent of their cause.

Niemann Pick C disease (NPC) is a well-studied LSD that arises not due to an enzymatic cleavage event but rather due to defective cholesterol transport at the lysosome ([319]). Available tools to directly and indirectly measure cholesterol within cells have formed the basis of diagnosing this disease. Moreover, directly measuring cholesterol has been critical to the discovery and development of the therapeutic hydroxy-propyl β-cyclodextrin (H-βCD), which is currently in clinical trials to treat the disease ([225], [67]). Studies using cholesterol stains, assays for cholesterol esterification, and measurement of cholesterol synthesis have revealed the mechanism of action of H-βCD ([251], [164]). These assays also revealed the tissue specific effects of H-βCD and concentration in the brain required for treatment of neurons and astrocytes ([252], [234]). Overall, the ability to measure storage material in NPC has been critical for these developments, but such methods are lacking for other storage diseases.

We hypothesized that when material accumulates within the lysosome, the viscosity within its lumen could also increase. If so, then lysosomal viscosity could potentially function as a general marker of lysosomal storage. Here, through nanoparticle tracking measurements made in cell culture and fluorescence recovery after photobleaching measurements in C.

elegans models of several LSDs, we report that lysosomal viscosity is indeed increased by substrate accumulation in the lysosome. We show that in a cell culture model of NPC, the levels of cholesterol storage correlate directly with the increase in lysosomal viscosity. We further show that in eight different LSD models in nematodes, lysosomal viscosity is increased, demonstrating the generality of this effect. We verify in several of these models in which storage material accumulates with time that lysosomal viscosity also increased with time. Our findings indicate that measurement of lysosomal viscosity has considerable potential for disease diagnosis, the monitoring of disease progression, and the development of therapeutics for lysosomal storage diseases that cannot otherwise be studied.

B.2 Results and discussion

B.2.1 Measurement of lysosomal viscosity in cell culture

To measure lysosomal viscosity in cell culture, we used passive nanoparticle tracking nanorheology (PPTN), a previously developed method for measuring material properties ([192], [342]). In PPTN, the diffusion of an ensemble of tracer nanoparticles is recorded and trajectories of the nanoparticles can be analyzed to obtain viscoelastic properties of the medium. PPTN has been used extensively to quantify the properties of cellular actin networks in the cytoplasm ([313], [229], [64], [347]). Here, we report what is to our knowledge the first use of PPTN to measure properties of fluid within an organelle. We first studied the uptake of the fluorescent tracer nanoparticles in three different cell culture models previously used to study lysosomal storage diseases: J774A.1 mouse macrophages, HeLa cells, and baby hamster kidney (BHK) fibroblasts ([272], [134], [281]). Cells were first incubated with 100 nm fluorescent polystyrene nanoparticles which are up-taken by the cells through scavenger receptor mediated endocytosis (Figure B.2). After endocytosis, nanoparticles are trafficked from the early endosome (EE) to the late endosome (LE) which subsequently fuses with the

lysosome (LY) (Figure B.1A). To study the time scales for the nanoparticle trafficking to the lysosome, we first labeled lysosomes with Alexafluor-488 labeled 10 kDa dextran (A488 Dextran), a fluorescent molecule previously shown to traverse the endolysosomal pathway and specifically mark lysosomes in each of these cell lines (Figure B.1B) ([344], [151], [19]). We studied the trafficking kinetics of internalized nanoparticles in each cell type by monitoring the co-localization of nanoparticles with labeled lysosomes as a function of time. Lysosomes are the final organelle on the endolysosomal pathway, so we determined the earliest time point at which maximal co-localization was achieved. This occurred at 1 h in J774A.1 and 12 h in both HeLa and BHK cells (Figure B.1C). In all cases, at least 70% co-localization with dextran-labeled lysosomes was achieved by this time point. We subsequently performed all measurements of lysosomal viscosity using PPTN at these times. We also confirmed that only 1 nanoparticle is present in each lysosome because when we incubated cells with fluorescent nanoparticles of two different colors; we found that only 2% of lysosomes contain nanoparticles of both colors (Figure B.3).

After the nanoparticles were trafficked to the lysosome, time lapse images were acquired and in each frame the nanoparticle's position was measured. Positions in subsequent frames were assembled to form trajectories (Figure B.4A, B). Trajectories were analyzed by computing the displacement of each subtrajectory for a given nanoparticle. The mean squared displacement (MSD) as a function of subtrajectory duration (lag time) was then computed for the entire ensemble of nanoparticles (Figure B.4D). An increase in viscosity is expected to reduce diffusion rates, resulting in a downward shift of the MSD curve. For diffusion through purely viscous media, the MSD should scale linearly with lag time according to an equation derived from the Stokes-Einstein relation $MSD = \frac{2kT}{3\pi\eta a}t$, where k is the Boltzmann constant, T is the temperature, η (eq 1) is the shear viscosity, and a is the nanoparticle radius ([342], [79]) However, inside the lysosome, we observed slightly subdiffusive behavior in which MSD scales as a power law of $t^{0.8-0.9}$ depending on conditions. Subdiffusive behavior has been ob-

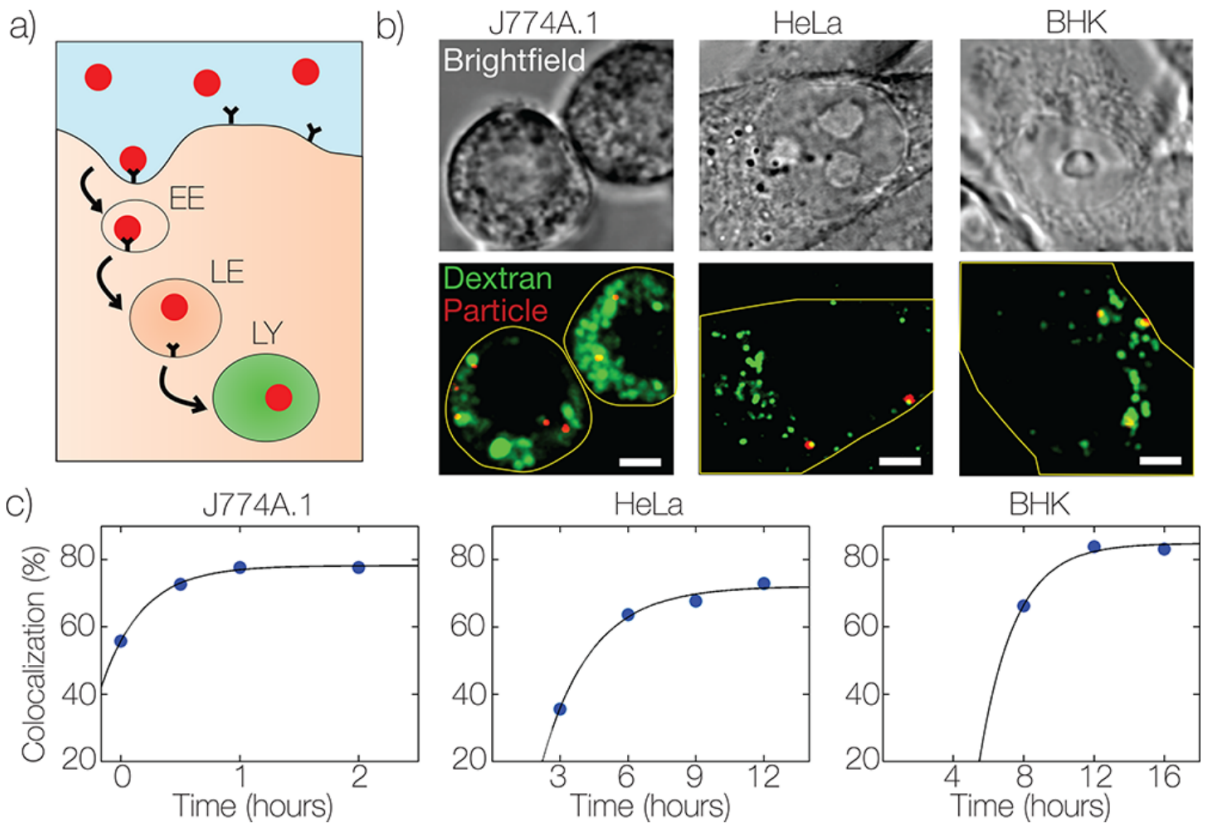

Figure B.1: . Fluorescent nanoparticles tracked to the lysosome in three different cell models. (a) Cells were incubated with 100 nm fluorescent nanoparticles, which enter the cell by endocytosis and are subsequently trafficked from early endosome (EE) to late endosome (LE) and finally to the lysosome (LY). (b) Representative images of co-localization between fluorescent nanoparticles (red) and Alexa 488 dextran labeled lysosomes (green) in several cell types. Cells are outlined in yellow. Scale bar is 5-μm. (c) Percentage of nanoparticles which co-localize with labeled lysosomes as a function of time postincubation for each cell type. The value increases monotonically with time and reaches an asymptotic maximum value that indicates the time scale for nanoparticles to traverse the endocytic pathway and reach the lysosome.

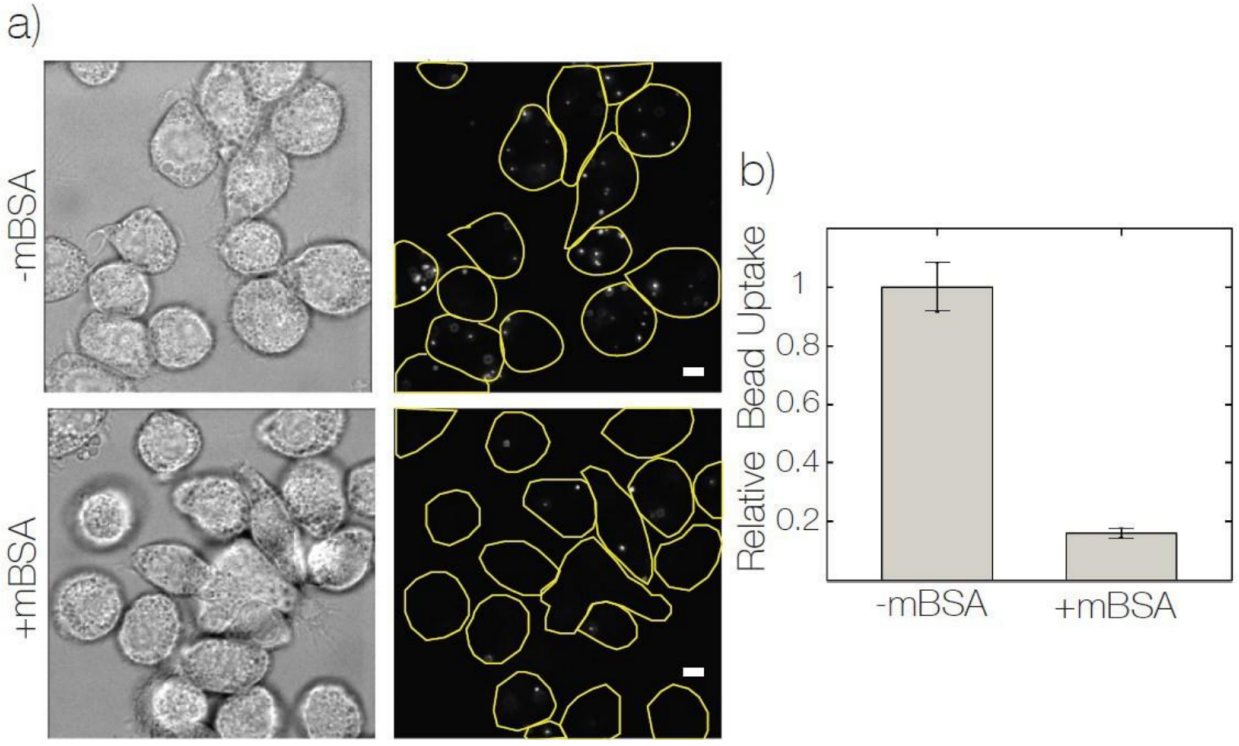

Figure B.2: Competition with ligand for anionic ligand binding receptor (ALBR) reduces nanoparticle uptake (a) Representative images of J774A.1 cells incubated with 0.4 pM fluorescent nanoparticles in the absence (-mBSA) or presence (+mBSA) of 9μM mBSA. (b) Histogram representing quantification of relative nanoparticle uptake in the presence and absence of mBSA. Error bars represent s.e.m for particles per cell in at least 80 cells in each condition. Scale Bar is 5 μm.

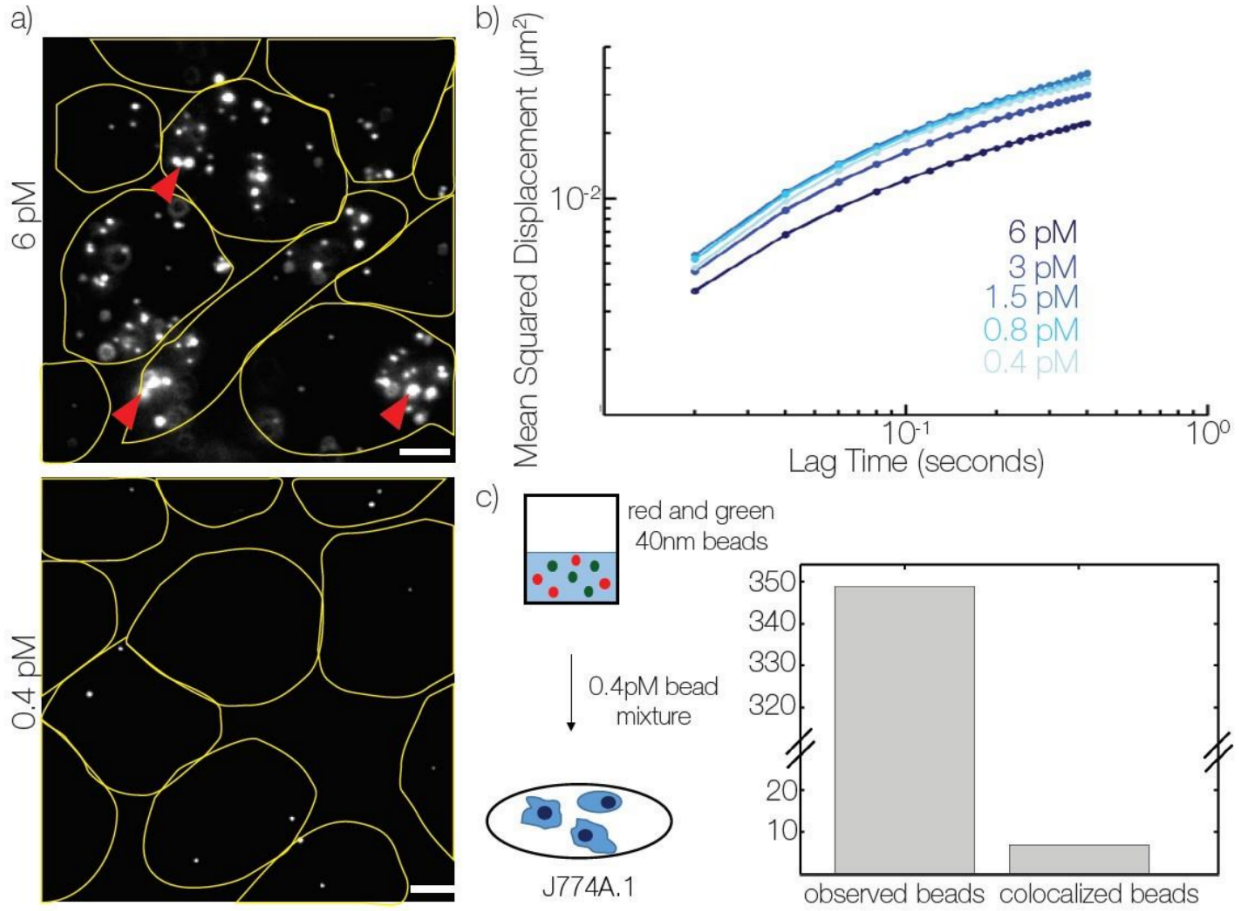

Figure B.3: Single nanoparticles are present in lysosome at working concentration. (a) Representative images of lysosomes of J774A.1 cells labelled at two different concentrations of fluorescent 100 nm nanoparticles. We see objects much larger than the diffraction limit in the 6 pM sample indicating formation of aggregates (red arrow). (b) Mean squared displacement (MSD) as a function of Lag time for each indicated concentration of fluorescent nanoparticles. Aggregates move more slowly in the lysosome and reduce the measured mean squared displacement. At low concentrations, we see asymptotic behavior of the MSD indicating that the aggregates are likely no longer present. (c) To test for the presence of small aggregates we created a mixture of 40 nm nanoparticles of two colors (red and green) each at 20 pM with a final nanoparticle concentration of 40 pM and incubated it overnight. This mixture was then sonicated and cells were incubated with a 100x dilution of the mixture (0.4pM nanoparticles) for 30 minutes in Opti-MEM. Colocalization of green and red nanoparticles in a lysosome would indicate that more than one nanoparticle is in the compartment. Scale Bar is 5 μm.

served in many PPTN measurements within the cytosol of cells, however, its origins are not entirely clear ([73], [336]). In our case, trapping by the lysosomal membrane sets a maximum value of MSD for individual nanoparticles which likely results in the observed subdiffusion. We see less subdiffusion in J774A.1 cells, which have larger lysosomes compared to BHK or HeLa cells (Figure B.1B). We see from the agreement at short lag times that J774A.1 and BHK cells show similar viscosity. HeLa cells have slightly higher viscosity, consistent with a previous report that lysosomal viscosity is higher in cancer cells ([55]). Apart from a change in subdiffusive behavior, we expect that the measurement does not have any dependence on the relative size of the particle to the lysosome. To confirm this, we carried out the same experiments in J774A.1 cells with 40 nm nanoparticles which yielded similar results (Figure B.6). We used 100 nm nanoparticles for all subsequent experiments because they contain more fluorophores resulting in higher signal-to-noise and, therefore, less error in localization of the nanoparticle center.

Neglecting the small elastic component of the nanoparticle displacement and applying eq 1, our results indicate average lysosomal viscosity of 410 ± 40, 510 ± 10, and 730 ± 60 cP in J774A.1, BHK, and HeLa cells, respectively. Previously reported lysosomal viscosity values using fluorescent viscosity probes are 65 and 150 cP in MCF-7 cells ([330], [182]). However, reports using similar fluorescent sensors localized to unidentified punctate structures with lysosomal morphology showed viscosities of 260 and 400 cP in SK-OV-3 cells and 400 and 950 cP in MCF7 cells ([292], [326], [163], [236]). Given the sensitivity to solvent composition intrinsic to fluorescent viscosity probes and contributions from autofluorescence, it is difficult to assess the accuracy of the above measurements ([112]). However, it appears that our measurements are within a reasonable range of other reported values.

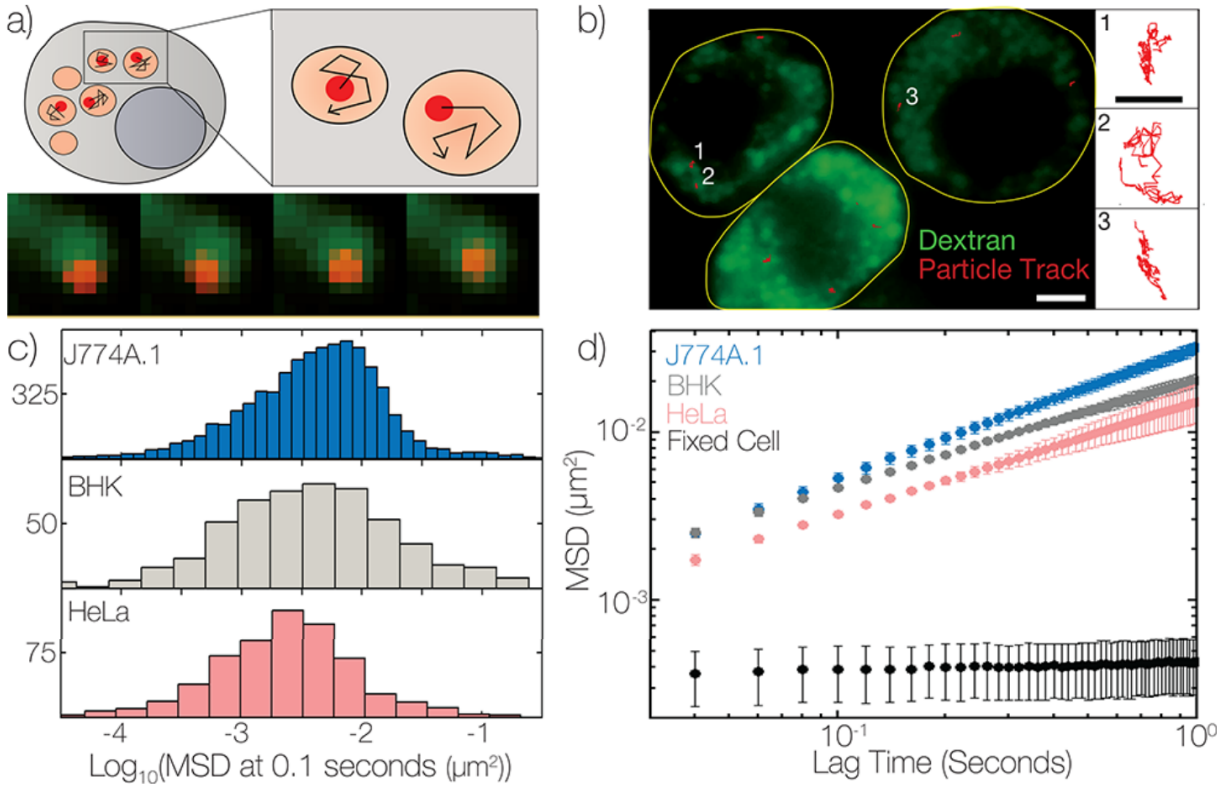

Figure B.4: Particle tracking of fluorescent nanoparticles reveals viscoelastic properties of lysosomes in mammalian cells. (a) To extract viscoelastic properties of the lysosome, particle trajectories of fluorescent nanoparticles in the lysosome are recorded by fluorescence microscopy. Representative time series of nanoparticle images (red) at 2 s intervals show a nanoparticle moving in an A488 dextran (green) labeled lysosomal lumen. (b) Representative image of J774A.1 lysosomes labeled by A488 Dextran (green) and particle trajectories from a time lapse of the same field of view (red). Cells are outlined in yellow. Scale bar is 5 μm. Panels on the right show zoomed-in trajectories of the nanoparticles denoted by numbers specified in the main image. Scale bar is 500 nm. (c) Histogram of mean squared displacement of individual nanoparticles after 0.1 s for three different cell types (J774A.1 $n = 7271$, 10 experiments; BHK $n = 532$, 2; HeLa $n = 599$, 2). (d) MSD as a function of lag time for nanoparticles diffusing in the lysosome of each cell type compared to immobilized nanoparticles in the lysosome of chemically fixed J774A.1 cells. Error bars indicate standard error of the mean from multiple experiments in each condition.

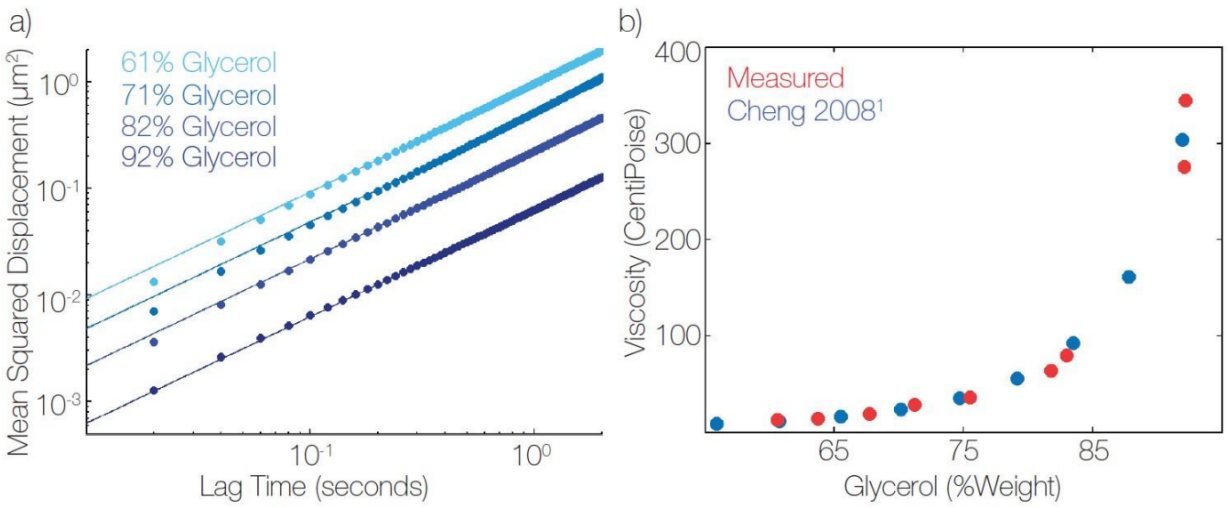

Figure B.5: *in vitro* viscosity measurement with particle tracking nanorheology (a) Mean squared displacement (MSD) as a function of lag time for fluorescent nanoparticles at each indicated weight percentage of glycerol in water. (b) Plot of experimental measurements of viscosity as a function of percentage of glycerol. MSD curves were fit with a linear model and viscosity was computed from the fit parameter using equation 1. Measurements show strong agreement with theoretical model from Cheng et al. ([52]).

B.2.2 Lysosomal Viscosity Increase in a Niemann Pick C Model.

The first model we used to study an LSD was the wellestablished cell culture model of NPC in which J774A.1 cells are treated with U18666a ([276], [44], [142]). U18666a acts as a potent and specific inhibitor of the Niemann Pick C1 protein (NPC1), a key protein involved in export of cholesterol from the late endosome and lysosome. Mutation or knockdown of NPC1 has previously been shown to cause cholesterol accumulation in the lysosome and symptoms of NPC disease.15 U18666a-treated cells phenocopy NPC1 knockout cells, knockout mouse primary cells, and patient samples in a variety of assays ([301], [325], [217], [181]). When cells were treated with the inhibitor U18666a, the PPTN assay revealed a striking change in nanoparticle mobility within the lysosome. The nanoparticles traversed significantly shorter distances, and we observed a large downward shift of the MSD curve indicative of an increase in viscosity (Figure B.7A-C). We then performed colocalization experiments in inhibitor treated cells and confirmed that the change in viscosity was not due to a change in localization

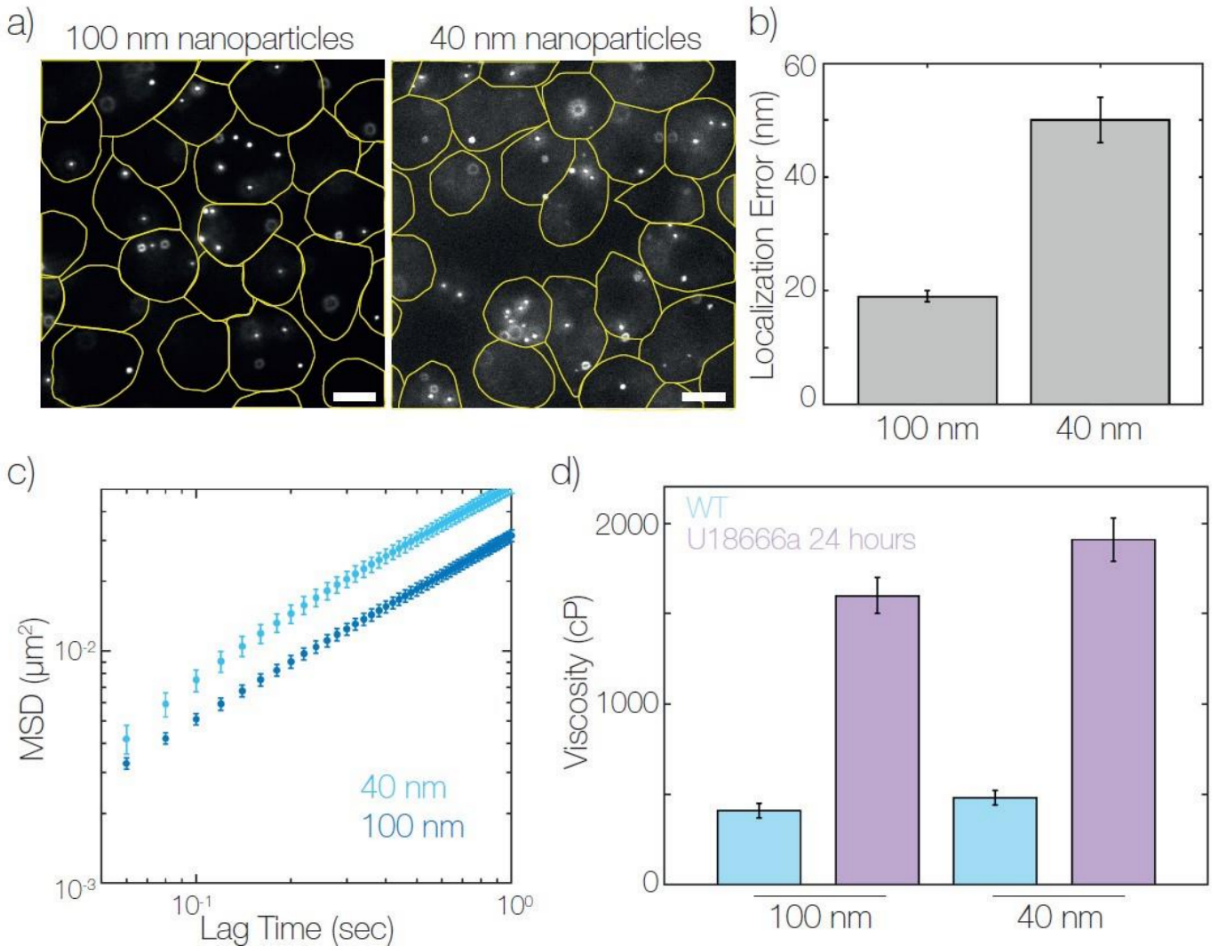

Figure B.6: Effect of particle size on lysosomal viscosity measurement (a) Representative images of fluorescent 40 nm and 100 nm nanoparticles in J774A.1 cells. Image settings were adjusted for 40 nm images such that mean nanoparticle intensity is similar. Cells are outlined in yellow. Scale bar is 10 μm. (b) Localization error assessed by tracking the motion of nanoparticles in fixed J774A.1 cells where particles are completely immobilized. Due to fluctuations in noise particles are perceived to have a small nearly constant MSD with time. This error limits the measurement of displacements below this localization error. Error bars indicate s.e.m from two experiments. (c) MSD as a function of lag time shows similar behavior for 40nm and 100 nm particles. 40 nm particles are more diffusive as expected due to their smaller radius. (d) Quantification of the viscosity for 40 and 100nm

(Figure B.8). We treated the other cell models, BHK and HeLa cells, with the inhibitor for 24 h and observed similar results. Nanoparticles moved nearly 4-fold more slowly in the disease model than wild type for all three cell types (Figure B.9). This observation revealed that viscosity was indeed higher in lysosomes when a storage condition was induced. In NPC, cholesterol storage has been documented in all tissues and cell types in the body, which is also consistent with the observed reduction in diffusion all three cell types ([252]).

B.2.3 Viscosity correlation with cholesterol levels in the lysosome

We next wanted to explicitly test whether the decrease in nanoparticle motion correlated with the amount of accumulated cholesterol in the lysosomes. Cholesterol accumulation in J774A.1 cells was measured by staining with filipin, a fluorescent molecule which binds cholesterol. Filipin is commonly used to diagnose NPC because of the notable difference in the staining pattern of NPC cells ([320]). In untreated cells, filipin uniformly labeled the cell, while cells treated with the inhibitor show distinct enhancement of fluorescence in punctate structures as previously described (Figure B.7A).

We incubated J774A.1 cells with U18666a for various durations to allow cholesterol to accumulate in the lysosome. We measured the viscosity by nanoparticle tracking as a function of time in NPC1 inhibited cells. These same cells were then fixed, stained with filipin, and imaged to visualize cholesterol content. We quantified cholesterol storage by using the ratio of filipin within high and low thresholds of the images, as previously described (see methods) and plotted this as a function of incubation time with U18666a ([260], [242]). We observed that in NPC1 inhibited cells, both lysosomal cholesterol and lysosomal viscosity increased in a highly correlated manner as a function of time (Figure B.7D-i).

To further confirm that cholesterol is responsible for the changing viscosity we then removed the stored cholesterol using H-βCD. H-βCD is a molecule currently in clinical trials for treatment of NPC and likely functions by forming a complex with cholesterol, altering

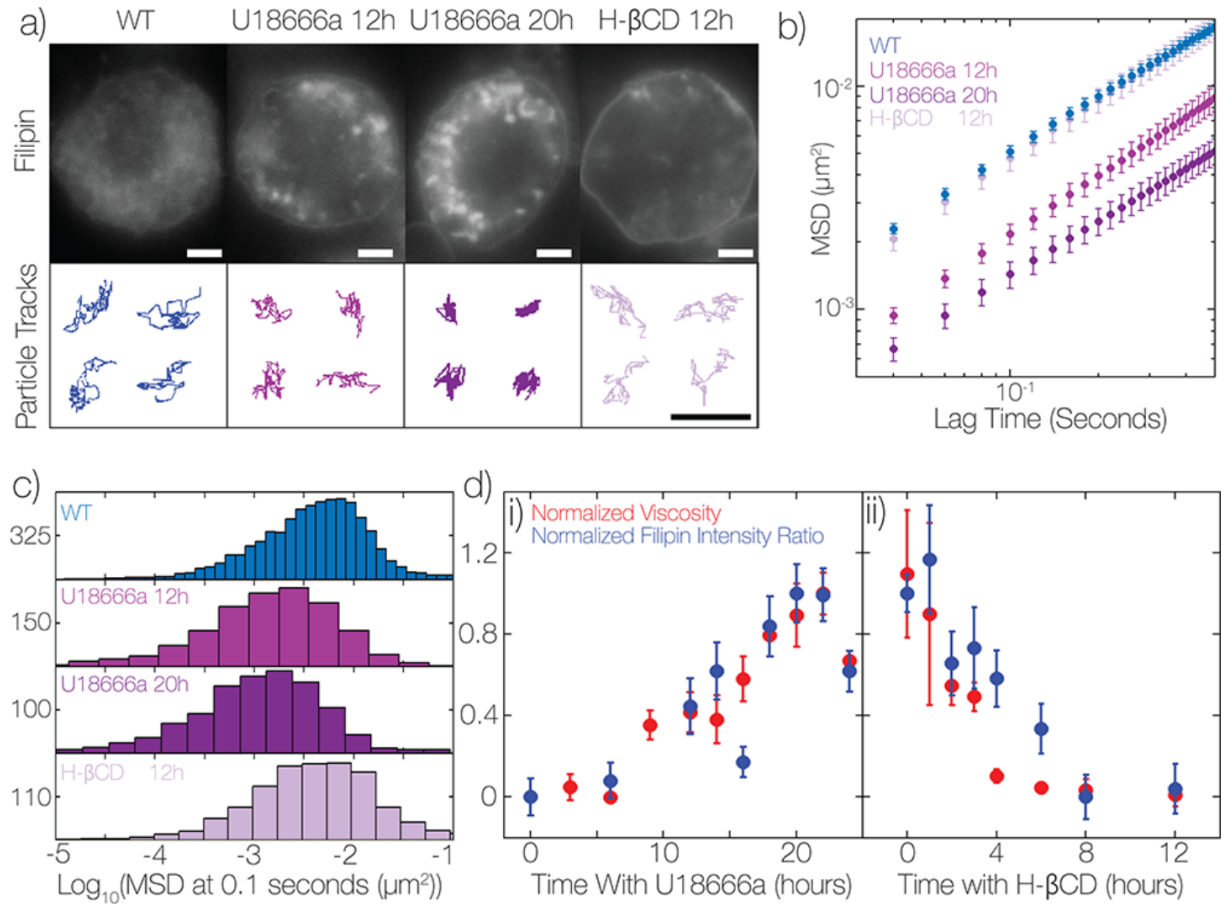

Figure B.7: Lysosomal viscosity increase by accumulation of cholesterol in the lysosome (a) Representative filipin staining images and particle tracks randomly selected near the mean for various indicated conditions in J774A.1 cells. Staining intensity in punctate structures increases and particle displacements decreases after incubation with 5 μM U18666a. These effects are reversed by treating the cells with 500 μM H-βCD. Scale bar for images is 5-μm. Scale bar for particle trajectories is 500 nm. (b) Average MSD values as a function of lag time under the same conditions as in panel a. Error bars represent the standard error of the mean for multiple experiments in each condition. Downward shift in the curve indicates an increase in viscosity. (c) Histograms of MSD at 0.1 s for the data plotted in panel b.(d) Relative viscosity values obtained from fitting MSD curves and the ratio of filipin intensity in punctate structures to whole cell intensity plotted against time. (i) Cells were incubated with 5 μM U18666a until given time point (ii) after a 20 h incubation with 5 μM U18666a cells were treated with 500 μM H-βCD until the indicated time point. Error bars for relative viscosity represent the standard error of the mean of the viscosity measured in multiple experiments for each condition. Error bars for filipin staining represents the standard error of the mean of the ratio measured in greater than 100 cells for each condition.

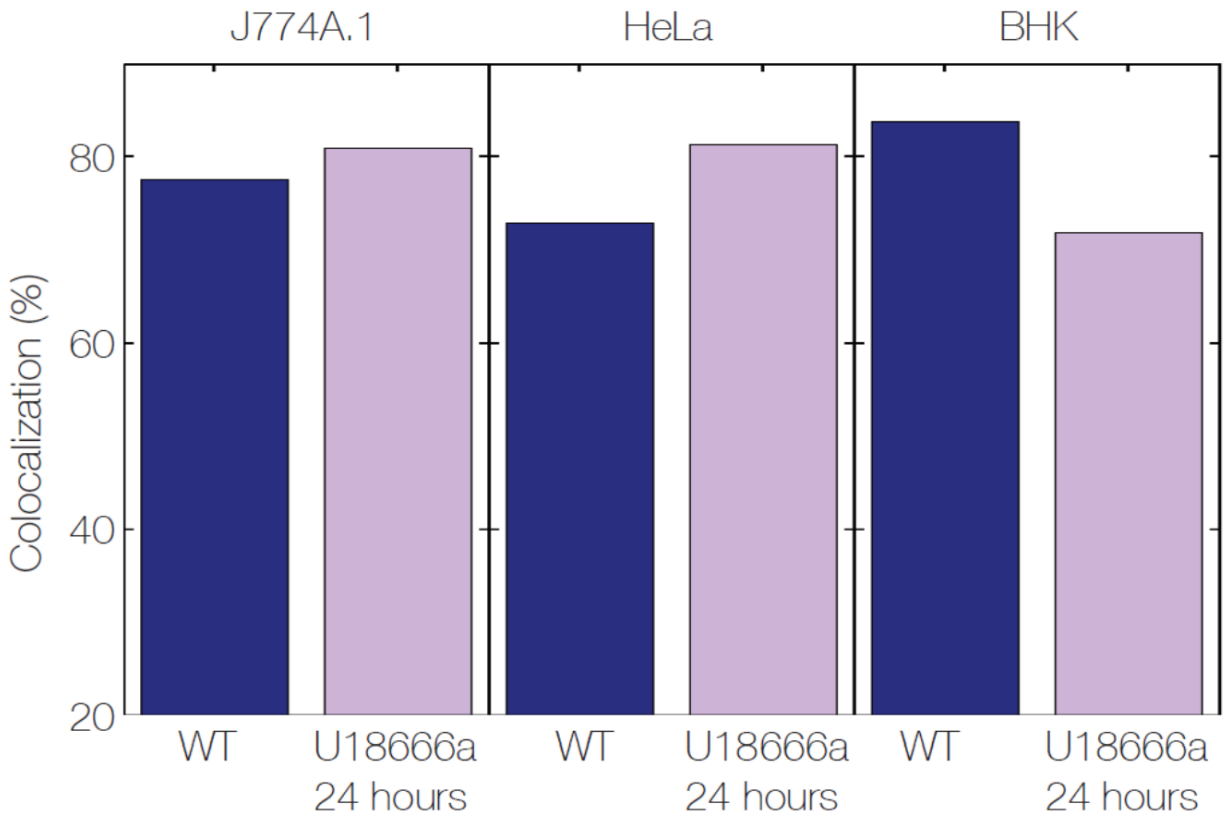

Figure B.8: U18666a treatment does not affect nanoparticle trafficking to the Lysosome. Percentage colocalization of fluorescent nanoparticles with the lysosome labeled with Alexa488 dextran in wild type or post 24 hour incubation in 5 μM U18666a in the indicated cell models. In each case over 200 particles were measured in more than 50 cells.

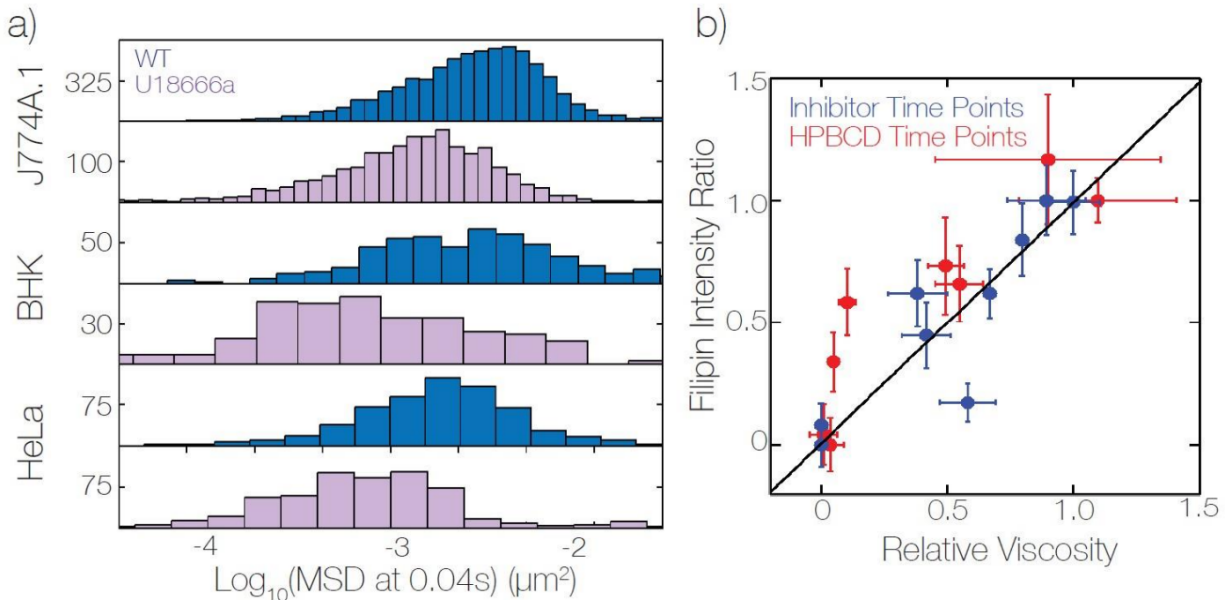

Figure B.9: Particle motion is reduced in other cell lines treated with U18666a and summary of J774A.1 inhibitor experiments (a) Histograms of mean squared displacement of individual particles in wild type cells and cells treated with U18666a for 24 hours for each cell model. We observe nearly a four fold decrease in nanoparticle mobility in each case. For each condition the total number of tracked particles is as follows $J774A.1(n_{WT} = 7271$ (10 experiments) $n_{U18666a} = 2065$ (4)) BHK ($n_{WT} = 532$ (2), $n_{U18666a} = 321$ (2)) $HeLa(n_{WT} = 599(2)$, $n_{U18666a} = 572(2))$ (b) Plot of relative filipin ratio against relative viscosity summarizes the experiments presented in Figure 3d. We observed strong correlation between relative filipin intensity ratio and relative viscosity in all conditions tested.

its export pathway from the lysosome ([251]). We observed that lysosomal viscosity and lysosomal cholesterol both reversibly decreased in a highly correlated manner when U18666a-treated cells were subjected to treatment with H-βCD (Figure B.7D-ii). This coordinated increase and decrease in lysosomal viscosity, upon inducing the accumulation and depletion of stored lysosomal cholesterol, indicates that presence of cholesterol in the lysosomal milieu increases its viscosity.

B.2.4 Increased lysosomal viscosity as a general marker of lysosomal storage

To see if lysosomal viscosity could report more generally on different types of accumulated material in the lysosome, we investigated a selection of LSD models in the model organism

Caenorhabditis elegans. C. elegans homologues of proteins responsible for most human LSDs have been identified and studied ([45], [69]). These models recapitulate many features of mammalian models including changes in lysosomal pH, morphology, degradative capacity, and dysregulated autophagy ([45], [176], [268], [98]). The short lifespan, ease of handling, and compatibility with microfluidic technologies also make C. elegans amenable to high-throughput screening methods ([256]). Furthermore, one can leverage versatile genetics of C. elegans to dissect the mechanisms of action of various therapeutics ([138]).

To measure relative lysosomal viscosity *in vivo* in nematodes, we devised a novel assay based on fluorescence recovery after photobleaching (FRAP). Fluorescein isothiocyanate (FITC)- labeled dextran (70 kDa) (FD70) was injected into the pseudocoelom of nematodes of various genetic backgrounds 2 days after they reached adulthood. Labeled dextran has been previously shown to be taken up by coelomocytes, a set of six phagocytic cells in the pseudocoelom, through fluid-phase endocytosis, where it is trafficked to the lysosome (Figure 4a) ([295], [22]). Dextran nonspecifically labels endosomes in many tissues within the worm; therefore, we co-injected Alexa 647 labeled duplex-DNA (dsDNA), which is a clean endocytic tracer that specifically labels the lysosomes of coelomocytes in diverse genetic backgrounds corresponding to LSDs ([45]). We observed nearly all DNA labeled compartments also contained FD70 (Figure B.10). For FRAP experiments only those compartments containing both DNA and Dextran, corresponding to lysosomes, were investigated.

To measure relative viscosity using FRAP, the central plane of a lysosome larger than 2 μm was photobleached using a confocal scanning laser. It is known that, for $NA > 1.2$, the intensity of a confocal laser is $> 95\%$ attenuated at distances of $> 700nm$ from the focal plane ([121]). Therefore, after a short highintensity laser pulse, fluorophores within 700 nm of the focal plane are selectively photobleached compared to fluorophores outside this region. Using confocal microscopy, we then observe only a thin section centered at the bleaching region. FD70 molecules above and below the bleached region quickly diffuse into

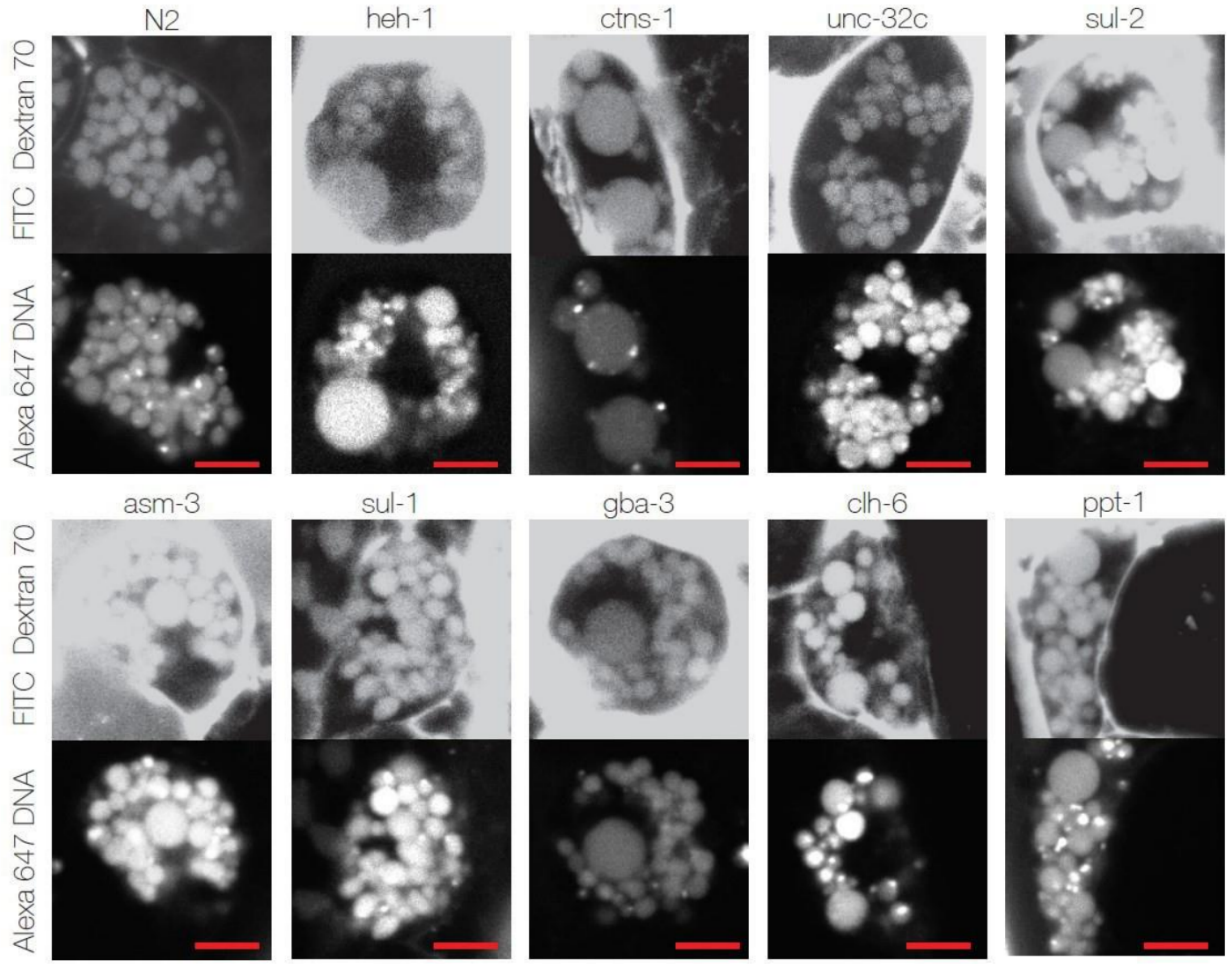

Figure B.10: FITC dextran traffics to the lysosome in storage disease models in C elegans. Representative images of coelomocytes labelled with FD70 (upper) and dsDNAAlexa647 (lower), 8 hours after pseudocoelomic injection of the in 2 day old adult worms of indicated genetic backgrounds. In all genetic backgrounds of C. elegans used for experiments we see a similar but more specific labeling of the lysosomes with DNA. Compartments containing both DNA and FD70 were considered as lysosomes in experiments. Scale bar is 5μm.

the plane of interest. Within a few seconds, the distribution of nonbleached FD70 within the lysosome becomes homogeneous. In wild type nematodes, we observed that the time constant of exponential recovery (τ) for this process was 0.60 $\pm$ 0.04 s. This time scale is similar to FRAP recovery of eYFP in the cytoplasm consistent with the FD70 freely diffusing in the lysosome ([165]).

If lysosomal viscosity is increased by storage of material, then in nematode LSD models we should observe slower FRAP recovery times. We therefore tested our hypothesis in a nematode model of NPC disease. In humans, NPC is caused by mutations in either NPC1 or NPC2, which are lysosomal cholesterol transport proteins. Although only 5% of all NPC cases arise due to defective NPC2, NPC arising from mutations in either protein are phenotypically indistinguishable. In C. elegans, NPC1 has two homologues, while NPC2 has a single homologue, namely HEH-1. We therefore chose heh-1 mutant nematodes as a model of NPC ([69]). We showed that heh-1 mutants phenocopy NPC disease in worms, exhibiting increased cholesterol, decreased lifespan in the absence of cholesterol and lysosomal hypoacidification (Figure B.12). Importantly, FRAP recovery times in lysosomes of heh-1 mutants were significantly higher than in wild type worms, indicating an increase in lysosomal viscosity (Figure B.11B).

Next, we studied a variety of other storage disease mutants using this method. This screen included a set of wellcharacterized LSDs with a wide variety of different storage materials: cholesterol (heh-1), glycolipids (gba-3), sphingolipids (asm-3), heparan sulfate polysaccharides (sul-1), keratan sulfate polysaccharides (sul-2), amino acids, e.g., cysteine (ctns-1), and lipid modified proteins (ppt-1). We assayed disorders arising from both substrate cleaving enzymes (gba-3, asm-3, sul-1, sul-2, and ppt-1) as well as transporters (heh-1, ctns-1, and clh-6). In all cases, we observed an increase in viscosity relative to wild type despite the diverse nature of storage materials. Notably unc-32c, a mutant for a subunit of a lysosomal proton transporter that is not associated with lysosomal storage, showed no such change in

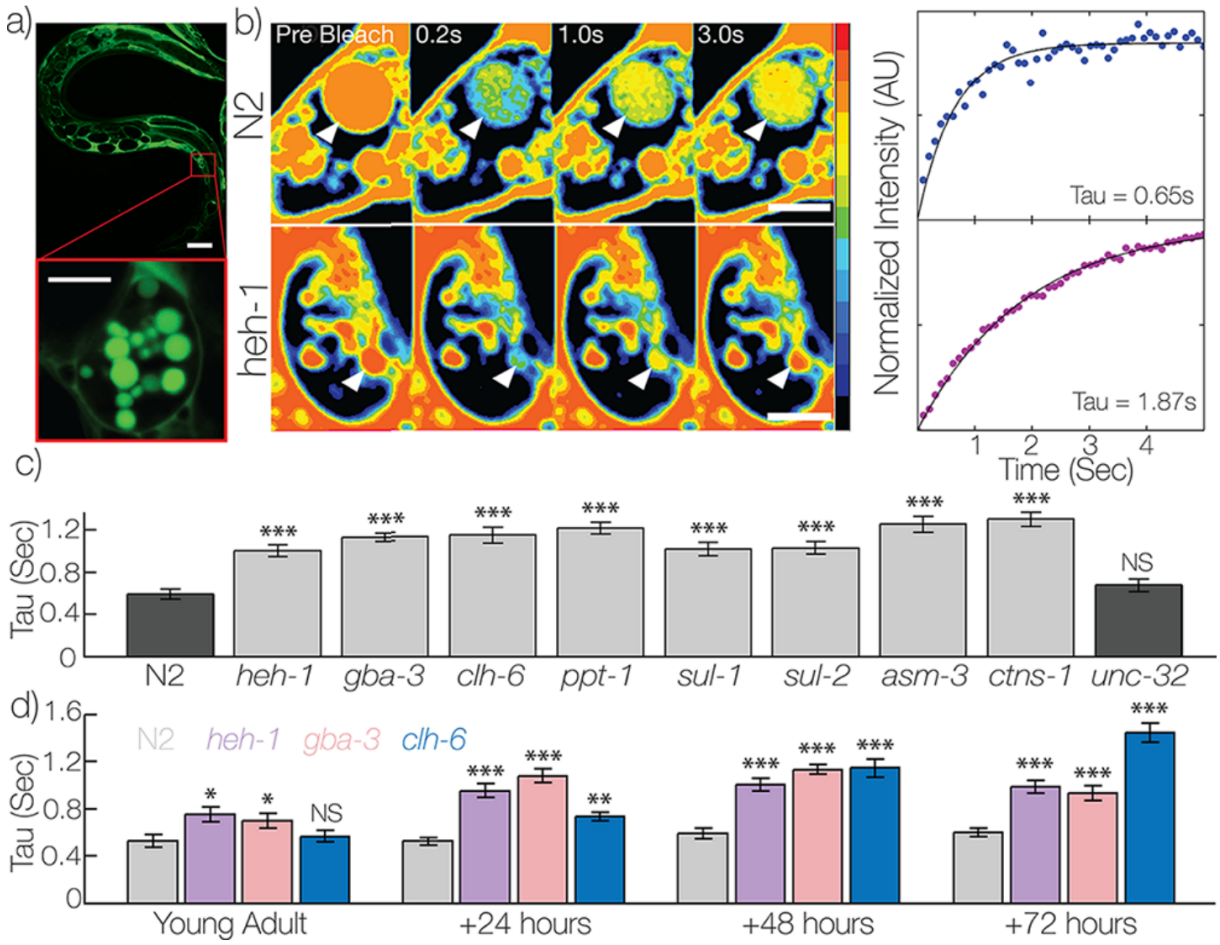

Figure B.11: Increased lysosomal viscosity is observed in a variety of lysosomal storage diseases. (a) Representative image of FITC Dextran labeling of a whole C. elegans nematode and zoomed-in image of a coelomocyte 8 h after pseudocoelomic injection. Scale bar in the whole worm image is 50 μm. Scale bar in the coelomocyte image is 5 μm. (b) Representative time series from fluorescence recovery after photobleaching (FRAP) experiments performed on a lysosome of the coelomocyte for wildtype (N2) and heh-1 nematodes. In heh-1, a C. elegans model of NPC, we observe a significantly increased recovery time indicating a relative increase in lysosomal viscosity. The scale bar is 5 μm. (c) Fluorescence recovery times calculated for a variety of lysosomal storage disease mutants show increased recovery time. The mutation of a lysosomal transporter unrelated to LSD, unc-32, shows no change in viscosity. Error bars represent the standard error of the mean for at least 15 lysosomes from at least 5 different worms in each condition. (d) Measurement of FRAP recovery times in worms of different genetic background as a function of age. Error bars represent s.e.m. for at least 25 lysosomes from at least 5 different worms in each condition. For panels c and d, P values were obtained by a two-sample t test comparing each sample to the N2 control of the same age. Indications (NS, $P > 0.05$; *, $P < 0.05$; **, $P < 0.01$; ***, $P < 0.001$) are given above each sample.

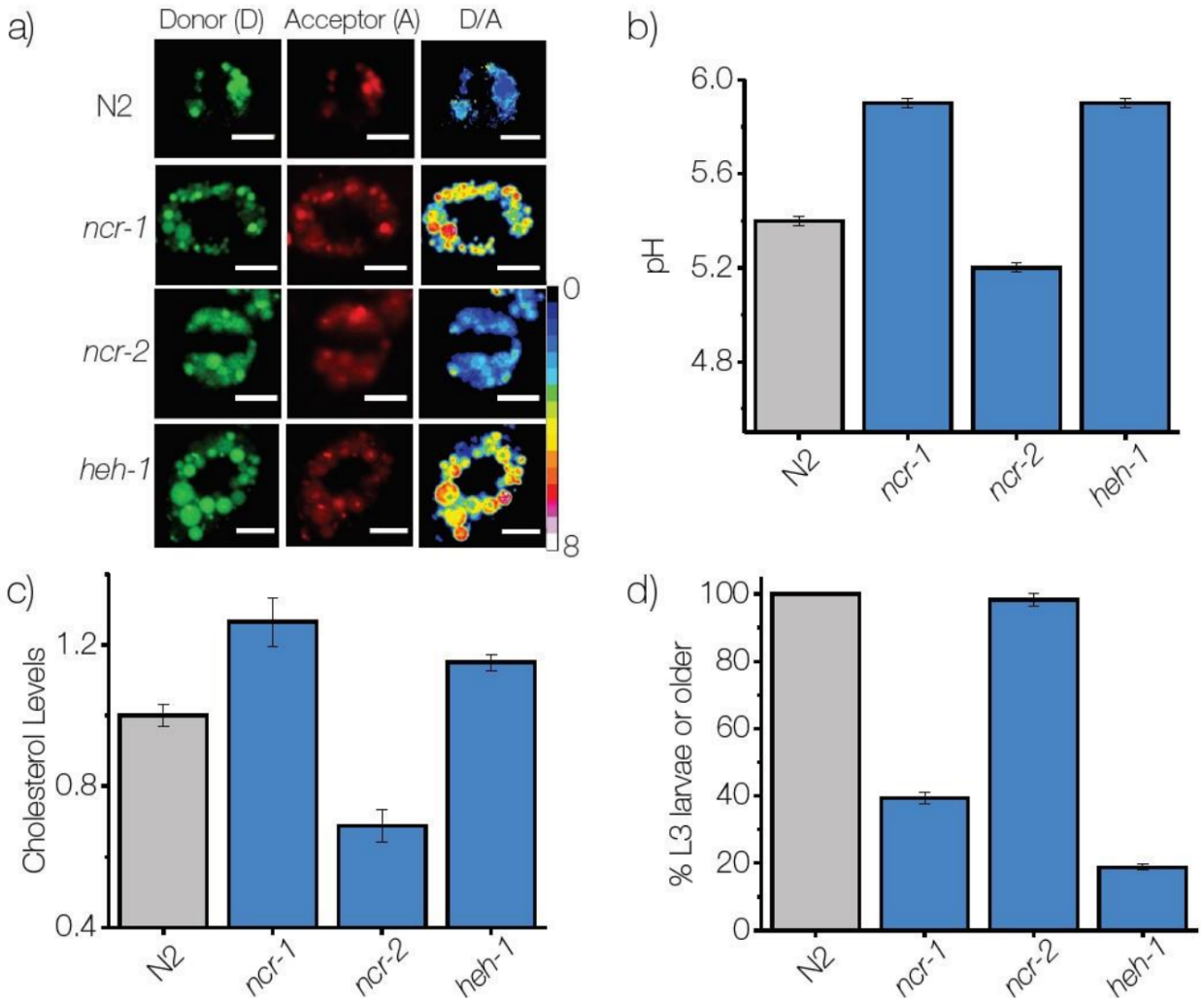

Figure B.12: heh-1 phenocopies NPC disease in worms (a) Representative images acquired in donor channel (D), acceptor channel (A) and corresponding pseudocolored D/A images of lysosomes labelled with $I4c_{LY}$ A488/A647 one hour after injection, in the indicated genetic backgrounds. Scale bar, 5 μm. (b) lysosomal pH under indicated genetic backgrounds. Error bars indicate s.e.m. ($n = 10$ worms, > 100 endosomes). (c) cholesterol levels obtained from TLC analysis of total lipids, extracted from worms of indicated genetic backgrounds, equivalent to 400μg of total protein. Error bars indicate s.e.m. (d) Percentage of progeny grown to larva stage 3 or higher in the absence of cholesterol. Error bars indicate s.e.m. ($n = 3$ plates).

lysosomal viscosity. Therefore, we conclude that lysosomal viscosity is generally increased by material storage in the lysosome (Figure B.11C).

In LSDs, disease severity increases with age due to progressive accumulation of stored material ([171]). C. elegans is an excellent model for aging, and therefore, ideally suited to study substrate accumulation as a function of age. We therefore monitored lysosomal viscosity in nematodes as a function of time for several storage disease models to monitor disease progression (Figure B.11D). For heh-1 and gba-3 mutants, young adults showed only a small increase lysosomal viscosity compared to wild type. However, lysosomal viscosity in these mutants increased substantially 24 h later, beyond which it plateaued. This plateau could arise because cells can invoke mechanisms such as lysosomal exocytosis to clear the lysosome to offset the accumulation ([264]).

We then studied lysosomal viscosity in clh-6 mutants. CLH-6 is a lysosomal chloride channel whose mammalian homologue CLCN7, causes a lysosomal disease called osteopetrosis ([159]). CLCN7 dysfunction strongly phenocopies lysosomal storage disorders, with mice showing neuronal and retinal degeneration, up-regulation of mitophagy, and increased protease expression ([140]). However, there is still no direct evidence of lysosomal storage in any organism. Mutating clh-6 in nematodes dramatically alters resting lysosomal chloride within 1 day of adulthood and impairs the ability of the lysosome to degrade cargo ([45], [98]). Interestingly, we observe normal lysosomal viscosity at these early time points in clh-6, likely indicating that stored material has not yet built up. Importantly, at increasing times of 24 h, 48 and 72 h, lysosomal viscosity also increased steadily, directly reflecting the consequences of accumulated material. We then investigated unc-32c, a subunit of the C. elegans homologue of V-ATPase which, when compromised, is also known to cause osteopetrosis. It was previously shown that while impaired V-ATPase function causes osteopetrosis, this phenotype differs from that of CLCN7 because no symptoms of lysosomal storage disease are observed.64 Consistent with these observations, we do not see any increase in lysosomal

viscosity in unc-32c mutants.

Our results indicate, using two different diffusion-based reporters of lysosomal viscosity, that accumulation of material in the lysosome increases viscosity within the lysosomal lumen. In most LSDs, the storage material cannot be measured directly or even indirectly. In such cases, lysosomal viscosity might provide a generalizable method for monitoring material accumulation in the lysosome which could lead to the identification of new LSDs. For instance, CLCN7, a chloride channel on the lysosome was originally identified because it causes osteopetrosis ([159]). However, CLCN7 dysfunction causes many symptoms similar to neuronal ceroid lipofuscinosis and it was subsequently identified as an LSD even though there was no direct measurement of stored material ([140]). Our measurements of lysosomal viscosity confirm these findings through the direct observation of stored material in the lysosome in situ.

Often storage diseases are diagnosed and characterized by enzyme activity. However, it is unclear in many LSDs exactly how enzyme activity is related to the time scale of material accumulation. Theoretical models and substrate measurements in metachromatic leukodystrophy and Tay-Sachs disease have demonstrated that a critical level of enzyme activity prevents the accumulation of stored material ([171], [61]). A viscosity reporter that could indirectly reveal this critical level of activity could be used to assess minimum therapeutic dosage ([200], [257]). Lysosomal viscosity can also be a useful reporter to track lysosomal storage and dysfunction in neurodegenerative diseases that are linked to LSDs such as Gaucher's disease associated Parkinson's disease ([194]).

Lysosomal viscosity is sensitive to the accumulation of diverse biomolecules, and therefore, it can enable the study of LSDs in which the nature of the stored material remains ambiguous or in which storage is suspected but not yet identified. Our results indicate that lysosomal viscosity may be a novel reporter to develop a new class of diagnostics for LSDs by directly probing for storage in the lysosome.

B.3 Materials and methods

Reagents

U18666a, filipin, amino dextran, levamisole, isopropyl β-D-1-thiogalactopyranoside (IPTG), and FITC dextran were all purchased from SigmaAldrich (Saint Louis, MO). (2-Hydroxypropyl)-β-cyclodextrin (H-βCD) was purchased from Cayman Chemical (Ann Arbor, MI). Alexa-488 NHS ester and all fluorescent nanoparticles (FluoSpheres carboxylate-modified microspheres) were purchased from Molecular Probes (Eugene, OR). All oligonucleotides were high-performance liquid chromatography (HPLC)- purified and purchased from IDT (Coralville, IA). All cell culture reagents and medium (Dulbecco's modified Eagle medium (DMEM), Opti-MEM, and fetal bovine serum) were purchased from Invitrogen Corporation. All other reagents, unless otherwise specified, were purchased from Sigma-Aldrich.

Cell Culture

J774A.1, BHK, and HeLa cells were cultured in DMEM/F-12 (1:1) (DMEM-F12) (Invitrogen Corporation) supplemented with 10% (v/v) heat inactivated fetal bovine serum (Invitrogen Corporation), 100 U/mL penicillin, and 100 μg/mL streptomycin. Cells were grown in a humidified incubator at 37 °C and 5% CO2. J774A.1 macrophages were received as a gift from Prof. Deborah Nelson Department of Pharmacological and Physiological Sciences at the University of Chicago. BHK cells were received as a gift from Prof. Michaela Gack Department of Microbiology and the Committee on Microbiology at the University of Chicago.

For all experiments using U18666a, cells were incubated in DMEM containing 5 μm U18666a until the indicated time points. For experiments with H-βCD, the cells were first incubated in DMEM containing U18666a for 20 h, and then H-βCD was added at 500 μM until the indicated time points. The incubation time included a 30 min pulse of nanoparticles in Opti-MEM, which was supplemented with U18666a or both depending on the condition.

None of the cell lines used in this study were on the list of commonly misidentified cell

lines maintained by the International Cell Line Authentication Committee. The sources of each cell line are as mentioned above and were used directly by us without additional authentication. Cells were regularly checked for mycoplasma contamination by DAPI staining and were found to be negative for contamination.

C. elegans Strains and Maintenance

C. elegans were maintained at 22 °C on nematode growth medium seeded with OP50 bacteria. The wild type stain used in these experiments was the N2 strain isolated from Bristol ([33]). The following strains used in this study were provided by the Caenorhabditis Genetics Center (CGC): RRID: WB-STRAIN:RB920 clh6 (ok791), RRID: WB-STRAIN:CB189 unc-32 (e189), RRID: WB-STRAIN:VC3135 gba-3 (gk3287), RRID: WBSTRAIN:VC183 ppt-1 (gk139), RRID: WB-STRAIN:JT11323 heh-1 (ok603), RRID: WB-STRAIN:VC238 sul-1 (gk151), RRID:WB-STRAIN:VC382 sul-2
(gk187), RRID:WBSTRAIN:RB1487 asm-3 (ok1744), RRID: WB-STRAIN: RB934 C41C4.7 (ok813).

Co-localization Experiments

To measure colocalization of nanoparticles with lysosomes each cell type was first incubated for 45 min with 0.2 mg/mL Alexa488 Dextran 16 h before imaging. Next, cells were washed 3 times with 1x PBS buffer and incubated in DMEM. Thirty minutes prior to various indicated time points the cells were washed and incubated in 0.4 pM fluorescent nanoparticles in Opti-MEM for 30 min. Cells were then washed and incubated in DMEM until the time of imaging. Cells were imaged in 1x PBS for up to 30 min at room temperature. Images were acquired using a Leica TCS SP5 II laser scanning confocal microscope (Leica Microsystems, Inc., Buffalo Grove, IL) with a HCX PlApo 63×/1.4 NA objective. Alexa 488 dextran was excited using a 488 nm argon laser, and the red fluorescent nanoparticles were excited using a 594 nm HeNe laser. Emission wavelengths were set using acousto-optical Beamsplitters (AOBS) such that there was no detected bleed through between the channels.

Images were acquired by a hybrid GaAsP detector (Leica Microsystems, Inc., Buffalo Grove, IL). Images were analyzed by thresholding the image to select lysosomes and nanoparticles in the respective images. Image thresholds were selected on the basis of visual inspection and held constant for all samples in the same experiment. Percentage co-localization was calculated from the ratio of number of nanoparticles overlapping with regions designated as lysosomes to the total number of nanoparticles detected.

Passive Nanoparticle Tracking Nanorheology

In cellulo nanoparticle tracking was performed as previously described ([342], [313]). However, in our case cells would uptake the tracer nanoparticles through endocytosis rather than being injected into the cytoplasm. Cells were first incubated with red fluorescent 100 nm (99 ± 5 nm) or 40 nm (45 ± 9 nm) carboxylate modified PS microspheres at a concentration of 0.4 pM (2×10^8 particles/mL) for 30 min in Opti-MEM buffer. Immediately before adding the nanoparticles a working 100x stock of fluorescent nanoparticles in DI water were sonicated in a bath sonicator for about 30 s to remove any aggregates. Cells were then incubated in DMEM until nanoparticles reached the lysosome as determined by colocalization, then mounted in Opti-MEM for imaging periods up to 30 min at room temperature. Images were acquired using an Olympus IX83 wide-field microscope with a 100× UPLSAPO Super Apochromat objective and Evolve Delta 512 EMCCD camera (Photometrics). Fluorescent nanoparticles were excited using a 572/35 excitation filter, 632/60 emission filter and DAPI/ FITC/TexasRed Dichroic bandpass filter acquired from Chroma (Chroma technology, Bellows Falls, VT). Images of each field were acquired at 50 Hz for 10 s. For each condition 20 fields were taken, each typically containing 20-40 nanoparticles in a field of view of 81.92×81.92 μm. This setup allowed for the localization of 100 nm nanoparticle centers in fixed cells of approximately $19\pm 1nm$ ($3.5 \pm 1.2 \times 10^{-4} \mu m^2$) as determined by tracking nanoparticles in cells fixed at room temperature for 10 min with 4% paraformaldehyde (PFA) (Figure 2d). This localization error was accounted for as previously described ([267]).

Image series were processed by Gaussian smoothing and bandpass filtering to identify regions of interest as previously described ([63]). Regions which were large enough to contain multiple nanoparticles or had maximum intensity less than 10 times the background were excluded from the analysis. Nanoparticles centers were then detected by taking the weighted centroid of each region. Nanoparticle tracks were generated from the position measurements using Simple Tracker, a Matlab-based particle track generation software ([305]). Trajectories were then analyzed to obtain mean squared displacement as a function of lag time for each nanoparticle by first measuring the displacement at every sub trajectory then averaging the squared displacement with all sub trajectories of the same duration. Viscosity values were determined by fitting the first 10 points of the MSD curve to a power law model and applying eq 1.

Measurement of Cholesterol in the Lysosome

Cholesterol was measured by filipin staining similar to previously described methods ([242], [259]). Cells were fixed in 4% PFA for 10 min at room temperature then stained with filipin (50 μg/mL for 1 h) in the dark at room temperature. Images were acquired using Olympus IX83 Wide Field Microscope with a 100X UPLSAPO Super Apochromat objective and Evolve Delta 512 EMCCD camera (Photometrics, USA). Images were acquired using an excitation filter 376/30, emission filter 470/30, and DAPI/FITC/TexasRed bandpass filter acquired from Chroma (Chroma technology, Bellows Falls, VT)

Images were then analyzed by a custom Matlab routine based on the "LSO compartment ratio assay" previously described ([242]). Images were first thresholded at a low level, which selected regions containing cells. The mean intensity outside the cells was subtracted from the whole image as a background noise on the detector. Next, a high threshold that selected the brightly stained lysosomal regions of the image was set based on examining the images. High and low thresholds were set globally for all images in the same experiment. All image settings were held constant and the same diluted filipin stock was used to stain all cells. The

average intensity in the highthresholded region was divided by the average intensity in the low-thresholded region to provide the LSO ratio. This ratio was then normalized by wild type and 20 h U18666a treated cells stained in the same experiment.

Fluorescence Recovery after Photobleaching

FRAP data was taken using a Leica TCS SP5 II laser scanning confocal microscope HCX PlApo 63×/1.4 NA objective. FITC dextran 70 was excited using a 488 nm argon laser, and the Alexa 647 labeled dsDNA was excited using a 633 nm HeNe laser. Emission filters were set by AOBS to minimize bleed through between the different channels. Images were acquired using a chilled PMT fluorescence detector (Leica Microsystems, Inc., Buffalo Grove, IL). For all images, a scan speed of 1400 Hz and image size of 256 × 256 pixels was used to image at a rate of 97 ms per image. Pinhole size of 2 AU was used to minimize required laser power during acquisition. Laser power (2-6%) was used for image acquisition before and after bleaching, and 100% laser power was used for bleaching. A total of 20 images were acquired at 97 ms per image followed by a 194 ms bleaching pulse, and 60 images were acquired at 97 ms per image to monitor recovery. Average intensity in the bleaching region for each post bleach image was measured and the time series was fit with a single exponential. Data that did not show exponential recovery were discarded ($\approx$ 10% of samples). Around 10% of the time series contained sudden jerking movement from the worm. These time series were truncated to the time prior to this motion or discarded if this occurred less than 2 s after the bleach event. The exponential time constant for at least 15 lysosomes from at least 5 worms were averaged to quantify relative viscosity in each sample.

For FRAP experiments, the worm ages were synchronized by placing 10-20 gravid adults on an empty plate for 4 h to lay eggs. Adults were then removed from the plate, and eggs were given 55 h to reach young adulthood. At this time, we observed the initial presence of small numbers of eggs inside the nematodes. Worms were then transferred to new plates each day to ensure enough food was present. Worms (55, 79, 103, or 127 h old) were then

microinjected with FD70 at 1 mg/mL and Alexa647-labeled-DNA at 500 nM in M9 buffer (3.0 mg/ mL KH2PO4, 6.0 mg/mL Na2HPO4, 0.5 mg/mL NaCl, and 1.0 mg/mL NH4Cl). Injected worms were incubated at 22 °C for 8 h, and worms that were determined to be alive by watching for movement were mounted for imaging on $6-10\%$ agarose dissolved in M9. Worms were anesthetized with 500 μM Levamisole in M9. We also added fluorescent red 40 nm nanoparticles (Molecular Probes, Eugene Oregon) to the M9 buffer containing levamisole at 10^{14} nanoparticles/mL to improve immobilization of worms, as previously described ([145]).

APPENDIX C

ADDITIONAL PUBLICATION CONTRIBUTIONS

During my PhD I also contributed to other published works which are listed here along with my contributions:

A pH-correctable, DNA-based fluorescent reporter for organellar calcium ([216])
By Nagarjun Narayanaswamy, Kasturi Chakraborty, Anand Saminathan, Elizabeth Zeichner, KaHo Leung, John Devany, and Yamuna Krishnan

I wrote data analysis code which was used to produce Figure 2C and D, 3J, K, and L, discussed analysis results and proofread the paper

A DNA-based voltmeter for organelles ([265])
By Anand Saminathan, John Devany, Aneesh Tazhe Veetil, Bhavyashree Suresh, Kavya Smitha Pillai, Michael Schwake, and Yamuna Krishnan,

I helped set up a patch clamping apparatus on the microscope, helped perform initial patch clamping experiments, helped collect and analyze data in Figure 1C, D, E, and F, Fig.S4, S8. I also discussed the results during the intial stages and proofread the paper.

Essential role of the Crk family-dosage in DiGeorge-like anomaly and metabolic homeostasis ([130])
By Akira Imamoto, Sewon Ki, Leiming Li, Kazunari Iwamoto, Venkat Maruthamuthu, John Devany, Ocean Lu, Tomomi Kanazawa, Suxiang Zhang, Takuji Yamada, Akiyoshi Hirayama, Shinji Fukuda, Yutaka Suzuki, and Mariko Okada

I wrote analysis code used to produce Figure 6B, Figure S9, Figure 7G, Figure S11 and discussed the analysis results.

REFERENCES

[1] Figures 1.1, 1.2, 1.3, 1.4, 3.5e, 4.2a, c, e, 4.6c, 4.7a, b, c, 4.10c, 4.17f, 5.1, 5.2, and 5.3 were prepared using biorender - biorender.com.

[2] The Origins of Order: Self-organization and Selection in Evolution - Stuart A. Kauffman, Member of the Santa Fe Institute and Professor of Biochemistry Stuart A Kauffman - Google Books.

[3] N. Akhtar and N. A. Hotchin. RAC1 regulates adherens junctions through endocytosis of E-cadherin. *Molecular Biology of the Cell*, 12(4):847–862, April 2001.

[4] John P. Alao. The regulation of cyclin D1 degradation: roles in cancer development and the potential for therapeutic invention. *Molecular Cancer*, 6(1):24, April 2007.

[5] Cristina Albanesi, Stefania Madonna, Paolo Gisondi, and Giampiero Girolomoni. The Interplay Between Keratinocytes and Immune Cells in the Pathogenesis of Psoriasis. *Frontiers in Immunology*, 9:1549, July 2018.

[6] Silvanus Alt, Poulami Ganguly, and Guillaume Salbreux. Vertex models: from cell mechanics to tissue morphogenesis. *Philosophical Transactions of the Royal Society B: Biological Sciences*, 372(1720):20150520, May 2017.

[7] Ariel Amir. Cell Size Regulation in Bacteria. *Physical Review Letters*, 112(20):208102, May 2014. Publisher: American Physical Society.

[8] Thomas E. Angelini, Edouard Hannezo, Xavier Trepat, Manuel Marquez, Jeffrey J. Fredberg, and David A. Weitz. Glass-like dynamics of collective cell migration. *Proceedings of the National Academy of Sciences*, 108(12):4714–4719, March 2011.

[9] Mariaceleste Aragona, Tito Panciera, Andrea Manfrin, Stefano Giulitti, Federica Michielin, Nicola Elvassore, Sirio Dupont, and Stefano Piccolo. A mechanical checkpoint controls multicellular growth through YAP/TAZ regulation by actin-processing factors. *Cell*, 154(5):1047–1059, August 2013.

[10] Mariaceleste Aragona, Alejandro Sifrim, Milan Malfait, Yura Song, Jens Van Herck, Sophie Dekoninck, Souhir Gargouri, Gaëlle Lapouge, Benjamin Swedlund, Christine Dubois, Pieter Baatsen, Katlijn Vints, Seungmin Han, Fadel Tissir, Thierry Voet, Benjamin D. Simons, and Cédric Blanpain. Mechanisms of stretch-mediated skin expansion at single-cell resolution. *Nature*, 584(7820):268–273, August 2020.

[11] Yvonne Aratyn-Schaus and Margaret L. Gardel. Transient frictional slip between integrin and the ECM in focal adhesions under myosin II tension. *Current biology: CB*, 20(13):1145–1153, July 2010.

[12] Mohammad H. Asghari and Bahram Jalali. Edge Detection in Digital Images Using Dispersive Phase Stretch Transform. *International Journal of Biomedical Imaging*, 2015:1–6, 2015.

[13] Lior Atia, Dapeng Bi, Yasha Sharma, Jennifer A. Mitchel, Bomi Gweon, Stephan A. Koehler, Stephen J. DeCamp, Bo Lan, Jae Hun Kim, Rebecca Hirsch, Adrian F. Pegoraro, Kyu Ha Lee, Jacqueline R. Starr, David A. Weitz, Adam C. Martin, Jin-Ah Park, James P. Butler, and Jeffrey J. Fredberg. Geometric constraints during epithelial jamming. *Nature Physics*, 14(6):613–620, June 2018.

[14] Darren J. Baker, Bennett G. Childs, Matej Durik, Melinde E. Wijers, Cynthia J. Sieben, Jian Zhong, Rachel A. Saltness, Karthik B. Jeganathan, Grace Casaclang Verzosa, Abdulmohammad Pezeshki, Khashayarsha Khazaie, Jordan D. Miller, and Jan M. van Deursen. Naturally occurring p16Ink4a-positive cells shorten healthy lifespan. *Nature*, 530(7589):184–189, February 2016. Number: 7589 Publisher: Nature Publishing Group.

[15] Andrea Ballabio and Volkmar Gieselmann. Lysosomal disorders: From storage to cellular damage. *Biochimica et Biophysica Acta (BBA) - Molecular Cell Research*, 1793(4):684–696, April 2009.

[16] Salman F. Banani, Hyun O. Lee, Anthony A. Hyman, and Michael K. Rosen. Biomolecular condensates: organizers of cellular biochemistry. *Nature Reviews Molecular Cell Biology*, 18(5):285–298, May 2017.

[17] Min Bao, Jake Cornwall-Scoones, Estefania Sanchez-Vasquez, Dong-Yuan Chen, Joachim De Jonghe, Shahriar Shadkhoo, Florian Hollfelder, Matt Thomson, David M. Glover, and Magdalena Zernicka-Goetz. Stem cell-derived synthetic embryos self-assemble by exploiting cadherin codes and cortical tension. *Nature Cell Biology*, 24(9):1341–1349, September 2022. Number: 9 Publisher: Nature Publishing Group.

[18] Y Barrandon and H Green. Cell size as a determinant of the clone-forming ability of human keratinocytes. *Proceedings of the National Academy of Sciences*, 82(16):5390–5394, August 1985.

[19] Herve Barriere, Miklos Bagdany, Florian Bossard, Tsukasa Okiyoneda, Gabriella Wojewodka, Dieter Gruenert, Danuta Radzioch, and Gergely L. Lukacs. Revisiting the Role of Cystic Fibrosis Transmembrane Conductance Regulator and Counterion Permeability in the pH Regulation of Endocytic Organelles. *Molecular Biology of the Cell*, 20(13):3125–3141, July 2009.

[20] Ludovic Berthier and Giulio Biroli. Theoretical perspective on the glass transition and amorphous materials. *Reviews of Modern Physics*, 83(2):587–645, June 2011. Publisher: American Physical Society.

[21] Arnaud Besson, Mark Gurian-West, Anja Schmidt, Alan Hall, and James M. Roberts. p27 ^{kip1} modulates cell migration through the regulation of RhoA activation. *Genes & Development*, 18(8):862–876, April 2004.

[22] Dhiraj Bhatia, Sunaina Surana, Saikat Chakraborty, Sandhya P. Koushika, and Yamuna Krishnan. A synthetic icosahedral DNA-based host–cargo complex for functional in vivo imaging. *Nature Communications*, 2(1):339, September 2011.

[23] Dapeng Bi, J. H. Lopez, J. M. Schwarz, and M. Lisa Manning. A density-independent rigidity transition in biological tissues. *Nature Physics*, 11(12):1074–1079, December 2015. Number: 12 Publisher: Nature Publishing Group.

[24] Dapeng Bi, Xingbo Yang, M. Cristina Marchetti, and M. Lisa Manning. Motility-Driven Glass and Jamming Transitions in Biological Tissues. *Physical Review X*, 6(2):021011, April 2016. Publisher: American Physical Society.

[25] M. J. Bissell. The differentiated state of normal and malignant cells or how to define a "normal" cell in culture. *International Review of Cytology*, 70:27–100, 1981.

[26] Mina J Bissell, Aylin Rizki, and I Saira Mian. Tissue architecture: the ultimate regulator of breast epithelial function. *Current Opinion in Cell Biology*, 15(6):753–762, December 2003.

[27] J. Todd Blankenship, Stephanie T. Backovic, Justina S. P. Sanny, Ori Weitz, and Jennifer A. Zallen. Multicellular rosette formation links planar cell polarity to tissue morphogenesis. *Developmental Cell*, 11(4):459–470, October 2006.

[28] Floris Bosveld, Olga Markova, Boris Guirao, Charlotte Martin, Zhimin Wang, Anaëlle Pierre, Maria Balakireva, Isabelle Gaugue, Anna Ainslie, Nicolas Christophorou, David K. Lubensky, Nicolas Minc, and Yohanns Bellaïche. Epithelial tricellular junctions act as interphase cell shape sensors to orient mitosis. *Nature*, 530(7591):495–498, February 2016.

[29] Kimberly Box, Bradley W Joyce, and Danelle Devenport. Epithelial geometry regulates spindle orientation and progenitor fate during formation of the mammalian epidermis. *eLife*, 8:e47102, June 2019.

[30] Cord Brakebusch, Richard Grose, Fabio Quondamatteo, Angel Ramirez, Jose L. Jorcano, Alison Pirro, Marcus Svensson, Rainer Herken, Takako Sasaki, Rupert Timpl, Sabine Werner, and Reinhard Fässler. Skin and hair follicle integrity is crucially dependent on 1 integrin expression on keratinocytes. *The EMBO Journal*, 19(15):3990–4003, August 2000.

[31] Clifford P. Brangwynne, Christian R. Eckmann, David S. Courson, Agata Rybarska, Carsten Hoege, Jöbin Gharakhani, Frank Jülicher, and Anthony A. Hyman. Germline P Granules Are Liquid Droplets That Localize by Controlled Dissolution/Condensation. *Science*, 324(5935):1729–1732, June 2009.

[32] Nicolas L. Bray, Harold Pimentel, Páll Melsted, and Lior Pachter. Near-optimal probabilistic RNA-seq quantification. *Nature Biotechnology*, 34(5):525–527, May 2016. Number: 5 Publisher: Nature Publishing Group.

[33] S Brenner. THE GENETICS OF CAENORHABDITIS ELEGANS. *Genetics*, 77(1):71–94, May 1974.

[34] James R Broach. Nutritional Control of Growth and Development in Yeast. *Genetics*, 192(1):73–105, September 2012.

[35] Courtney K. Brock, Stephen T. Wallin, Oscar E. Ruiz, Krystin M. Samms, Amrita Mandal, Elizabeth A. Sumner, and George T. Eisenhoffer. Stem cell proliferation is induced by apoptotic bodies from dying cells during epithelial tissue maintenance. *Nature Communications*, 10(1):1044, March 2019. Number: 1 Publisher: Nature Publishing Group.

[36] Samara Brown, Cristiana M. Pineda, Tianchi Xin, Jonathan Boucher, Kathleen C. Suozzi, Sangbum Park, Catherine Matte-Martone, David G. Gonzalez, Julie Rytlewski, Slobodan Beronja, and Valentina Greco. Correction of aberrant growth preserves tissue homeostasis. *Nature*, 548(7667):334–337, August 2017. Bandiera_abtest: a Cg_type: Nature Research Journals Number: 7667 Primary_atype: Research Publisher: Nature Publishing Group Subject_term: Adult stem cells;Regeneration;Skin stem cells Subject_term_id: adult-stem-cells;regeneration;skin-stem-cells.

[37] David M. Bryant, Julie Roignot, Anirban Datta, Arend W. Overeem, Minji Kim, Wei Yu, Xiao Peng, Dennis J. Eastburn, Andrew J. Ewald, Zena Werb, and Keith E. Mostov. A molecular switch for the orientation of epithelial cell polarization. *Developmental Cell*, 31(2):171–187, October 2014.

[38] Clotilde Cadart, Sylvain Monnier, Jacopo Grilli, Pablo J. Sáez, Nishit Srivastava, Rafaele Attia, Emmanuel Terriac, Buzz Baum, Marco Cosentino-Lagomarsino, and Matthieu Piel. Size control in mammalian cells involves modulation of both growth rate and cell cycle duration. *Nature Communications*, 9(1):3275, August 2018.

[39] C. Elizabeth Caldon, Robert L. Sutherland, and Elizabeth A. Musgrove. Cell cycle proteins in epithelial cell differentiation: Implications for breast cancer. *Cell Cycle*, 9(10):1918–1928, May 2010. Publisher: Taylor & Francis _eprint: https://doi.org/10.4161/cc.9.10.11474.

[40] Laura Canty, Eleyine Zarour, Leily Kashkooli, Paul François, and François Fagotto. Sorting at embryonic boundaries requires high heterotypic interfacial tension. *Nature Communications*, 8(1):157, July 2017. Number: 1 Publisher: Nature Publishing Group.

[41] Kate E. Cavanaugh, Michael F. Staddon, Theresa A. Chmiel, Robert Harmon, Srikanth Budnar, Alpha S. Yap, Shiladitya Banerjee, and Margaret L. Gardel. Force-dependent intercellular adhesion strengthening underlies asymmetric adherens junction contraction. *Current Biology*, 32(9):1986–2000.e5, May 2022.

[42] Kate E. Cavanaugh, Michael F. Staddon, Edwin Munro, Shiladitya Banerjee, and Margaret L. Gardel. RhoA Mediates Epithelial Cell Shape Changes via Mechanosensitive Endocytosis. *Developmental Cell*, 52(2):152–166.e5, January 2020.

[43] Jordi Cayuso, Qiling Xu, Megan Addison, and David G Wilkinson. Actomyosin regulation by Eph receptor signaling couples boundary cell formation to border sharpness. *eLife*, 8:e49696, 2019.

[44] Richard J. Cenedella, Robert Jacob, Douglas Borchman, Daxin Tang, Amanda R. Neely, Abbas Samadi, R. Preston Mason, and Patricia Sexton. Direct perturbation of lens membrane structure may contribute to cataracts caused by U18666A, an oxidosqualene cyclase inhibitor. *Journal of Lipid Research*, 45(7):1232–1241, July 2004.

[45] Kasturi Chakraborty, KaHo Leung, and Yamuna Krishnan. High lumenal chloride in the lysosome is critical for lysosome function. *eLife*, 6:e28862, July 2017.

[46] Sanjukta Chakraborty, M. N. Nagashri, S. M. Azeem Mohiyuddin, K. S. Gopinath, and Arun Kumar. Gene expression profiling of oral squamous cell carcinoma by differential display rt-PCR and identification of tumor biomarkers. *Indian Journal of Surgical Oncology*, 1(4):284–293, December 2010.

[47] Guillaume Charras and Alpha S. Yap. Tensile Forces and Mechanotransduction at Cell–Cell Junctions. *Current Biology*, 28(8):R445–R457, April 2018.

[48] Anne-Amandine Chassot, Gerald Lossaint, Laurent Turchi, Guerrino Meneguzzi, Daniel Fisher, Gilles Ponzio, and Vjekoslav Dulic. Confluence-induced cell cycle exit involves pre-mitotic CDK inhibition by p27Kip1 and cyclin D1 downregulation. *Cell Cycle*, 7(13):2038–2046, July 2008.

[49] Bor-Huah Chen, Jason T. C. Tzen, Anne R. Bresnick, and Hong-Chen Chen. Roles of Rho-associated kinase and myosin light chain kinase in morphological and migratory defects of focal adhesion kinase-null cells. *The Journal of Biological Chemistry*, 277(37):33857–33863, September 2002.

[50] Christopher S. Chen, Milan Mrksich, Sui Huang, George M. Whitesides, and Donald E. Ingber. Geometric Control of Cell Life and Death. *Science*, 276(5317):1425–1428, May 1997. Publisher: American Association for the Advancement of Science.

[51] Ling Cheng, Jingyuan Chen, Yidi Kong, Ceryl Tan, Ran Kafri, and Mikael Björklund. Size-scaling promotes senescence-like changes in proteome and organelle content. Technical report, bioRxiv, August 2021. Section: New Results Type: article.

[52] Nian-Sheng Cheng. Formula for the Viscosity of a GlycerolWater Mixture. *Industrial & Engineering Chemistry Research*, 47(9):3285–3288, May 2008. Publisher: American Chemical Society.

[53] Oleksandr Chepizhko, Costanza Giampietro, Eleonora Mastrapasqua, Mehdi Nourazar, Miriam Ascagni, Michela Sugni, Umberto Fascio, Livio Leggio, Chiara Malinverno, Giorgio Scita, Stéphane Santucci, Mikko J. Alava, Stefano Zapperi, and Caterina A. M. La Porta. Bursts of activity in collective cell migration. *Proceedings of the National Academy of Sciences*, 113(41):11408–11413, October 2016.

[54] Kevin K. Chiou, Lars Hufnagel, and Boris I. Shraiman. Mechanical Stress Inference for Two Dimensional Cell Arrays. *PLoS Computational Biology*, 8(5):e1002512, May 2012.

[55] Rajdeep Chowdhury, Abhijit Saha, Amit Kumar Mandal, Batakrishna Jana, Surajit Ghosh, and Kankan Bhattacharyya. Excited State Proton Transfer in the Lysosome of Live Lung Cells: Normal and Cancer Cells. *The Journal of Physical Chemistry B*, 119(6):2149–2156, February 2015.

[56] Priyamvada Chugh, Andrew G. Clark, Matthew B. Smith, Davide A. D. Cassani, Kai Dierkes, Anan Ragab, Philippe P. Roux, Guillaume Charras, Guillaume Salbreux, and Ewa K. Paluch. Actin cortex architecture regulates cell surface tension. *Nature Cell Biology*, 19(6):689–697, June 2017.

[57] Andrew G. Clark and Ewa Paluch. Mechanics and Regulation of Cell Shape During the Cell Cycle. In Jacek Z. Kubiak, editor, *Cell Cycle in Development*, Results and Problems in Cell Differentiation, pages 31–73. Springer, Berlin, Heidelberg, 2011.

[58] Jonathan Cohen, Shaul Raviv, Orit Adir, Krishnanand Padmanabhan, Arad Soffer, and Chen Luxenburg. The Wave complex controls epidermal morphogenesis and proliferation by suppressing Wnt–Sox9 signaling. *Journal of Cell Biology*, 218(4):1390–1406, April 2019.

[59] Claudio Collinet, Matteo Rauzi, Pierre-François Lenne, and Thomas Lecuit. Local and tissue-scale forces drive oriented junction growth during tissue extension. *Nature Cell Biology*, 17(10):1247–1258, October 2015.

[60] John T. Connelly, Julien E. Gautrot, Britta Trappmann, David Wei-Min Tan, Giacomo Donati, Wilhelm T.S. Huck, and Fiona M. Watt. Actin and serum response factor transduce physical cues from the microenvironment to regulate epidermal stem cell fate decisions. *Nature Cell Biology*, 12(7):711–718, July 2010.

[61] E. Conzelmann and K. Sandhoff. Partial Enzyme Deficiencies: Residual Activities and the Development of Neurological Disorders. *Developmental Neuroscience*, 6(1):58–71, 1983.

[62] Stephen C. Cowin. Tissue Growth and Remodeling. *Annual Review of Biomedical Engineering*, 6(1):77–107, 2004. _eprint: https://doi.org/10.1146/annurev.bioeng.6.040803.140250.

[63] John C. Crocker and David G. Grier. Methods of Digital Video Microscopy for Colloidal Studies. *Journal of Colloid and Interface Science*, 179(1):298–310, April 1996.

[64] John C. Crocker and Brenton D. Hoffman. Multiple-Particle Tracking and Two-Point Microrheology in Cells. In *Methods in Cell Biology*, volume 83 of *Cell Mechanics*, pages 141–178. Academic Press, January 2007.

[65] Michael Czajkowski, Daniel M. Sussman, M. Cristina Marchetti, and M. Lisa Manning. Glassy dynamics in models of confluent tissue with mitosis and apoptosis. *Soft Matter*, 15(44):9133–9149, 2019.

[66] Robert David, Olivia Luu, Erich W. Damm, Jason W. H. Wen, Martina Nagel, and Rudolf Winklbauer. Tissue cohesion and the mechanics of cell rearrangement. *Development*, 141(19):3672–3682, October 2014.

[67] Cristin D. Davidson, Nafeeza F. Ali, Matthew C. Micsenyi, Gloria Stephney, Sophie Renault, Kostantin Dobrenis, Daniel S. Ory, Marie T. Vanier, and Steven U. Walkley. Chronic Cyclodextrin Treatment of Murine Niemann-Pick C Disease Ameliorates Neuronal Cholesterol and Glycosphingolipid Storage and Disease Progression. *PLoS ONE*, 4(9):e6951, September 2009.

[68] Chiara De Pascalis, Carlos Pérez-González, Shailaja Seetharaman, Batiste Boëda, Benoit Vianay, Mithila Burute, Cécile Leduc, Nicolas Borghi, Xavier Trepat, and Sandrine Etienne-Manneville. Intermediate filaments control collective migration by restricting traction forces and sustaining cell–cell contacts. *Journal of Cell Biology*, 217(9):3031–3044, September 2018.

[69] Gert de Voer, Dorien Peters, and Peter E.M. Taschner. Caenorhabditis elegans as a model for lysosomal storage disorders. *Biochimica et Biophysica Acta (BBA) - Molecular Basis of Disease*, 1782(7-8):433–446, July 2008.

[70] John Devany, Kasturi Chakraborty, and Yamuna Krishnan. Subcellular Nanorheology Reveals Lysosomal Viscosity as a Reporter for Lysosomal Storage Diseases. *Nano Letters*, 18(2):1351–1359, February 2018. Publisher: American Chemical Society.

[71] John Devany, Martin J. Falk, Liam J. Holt, Arvind Murugan, and Margaret L. Gardel. Tissue confinement regulates cell growth and size in epithelia, September 2022. Pages: 2022.07.04.498508 Section: New Results.

[72] John Devany, Daniel M. Sussman, Takaki Yamamoto, M. Lisa Manning, and Margaret L. Gardel. Cell cycle–dependent active stress drives epithelia remodeling. *Proceedings of the National Academy of Sciences*, 118(10), March 2021. Publisher: National Academy of Sciences Section: Physical Sciences.

[73] James A. Dix and A.S. Verkman. Crowding Effects on Diffusion in Solutions and Cells. *Annual Review of Biophysics*, 37(1):247–263, June 2008.

[74] Amin Doostmohammadi, Sumesh P. Thampi, Thuan B. Saw, Chwee T. Lim, Benoit Ladoux, and Julia M. Yeomans. Celebrating Soft Matter's 10th Anniversary: Cell division: a source of active stress in cellular monolayers. *Soft Matter*, 11(37):7328–7336, 2015.

[75] Dormer. *Fundamental Tissue Geometry for Biologists*.

[76] Wiebke Drenckhan and Stefan Hutzler. Structure and energy of liquid foams. *Advances in Colloid and Interface Science*, 224:1–16, October 2015.

[77] B. Dubertret and N. Rivier. The renewal of the epidermis: a topological mechanism. *Biophysical Journal*, 73(1):38–44, July 1997.

[78] Eran Eden, Naama Geva-Zatorsky, Irina Issaeva, Ariel Cohen, Erez Dekel, Tamar Danon, Lydia Cohen, Avi Mayo, and Uri Alon. Proteome Half-Life Dynamics in Living Human Cells. *Science*, 331(6018):764–768, February 2011. Publisher: American Association for the Advancement of Science.

[79] A. Einstein. Über die von der molekularkinetischen Theorie der Wärme geforderte Bewegung von in ruhenden Flüssigkeiten suspendierten Teilchen. *Annalen der Physik*, 322(8):549–560, 1905.

[80] Elhaseen Elamin, Daisy Jonkers, Kati Juuti-Uusitalo, Sven van IJzendoorn, Freddy Troost, Hans Duimel, Jos Broers, Fons Verheyen, Jan Dekker, and Ad Masclee. Effects of Ethanol and Acetaldehyde on Tight Junction Integrity: In Vitro Study in a Three Dimensional Intestinal Epithelial Cell Culture Model. *PLoS ONE*, 7(4):e35008, April 2012.

[81] T. Elsdale and J. Bard. Collagen substrata for studies on cell behavior. *The Journal of Cell Biology*, 54(3):626–637, September 1972.

[82] Jesse A. Engelberg, Anirban Datta, Keith E. Mostov, and C. Anthony Hunt. MDCK cystogenesis driven by cell stabilization within computational analogues. *PLoS computational biology*, 7(4):e1002030, April 2011.

[83] François Fagotto. The cellular basis of tissue separation. *Development*, 141(17):3303–3318, September 2014.

[84] François Fagotto, Nazanin Rohani, Anne-Sophie Touret, and Rui Li. A Molecular Base for Cell Sorting at Embryonic Boundaries: Contact Inhibition of Cadherin Adhesion by Ephrin/Eph-Dependent Contractility. *Developmental Cell*, 27(1):72–87, October 2013.

[85] Yilin Fan and Tobias Meyer. Molecular control of cell density-mediated exit to quiescence. *Cell Reports*, 36(4):109436, July 2021.

[86] Reza Farhadifar, Jens-Christian Röper, Benoit Aigouy, Suzanne Eaton, and Frank Jülicher. The Influence of Cell Mechanics, Cell-Cell Interactions, and Proliferation on Epithelial Packing. *Current Biology*, 17(24):2095–2104, December 2007.

[87] Aliya Fatehullah, Si Hui Tan, and Nick Barker. Organoids as an in vitro model of human development and disease. *Nature Cell Biology*, 18(3):246–254, March 2016.

[88] Mirella Filocamo and Amelia Morrone. Lysosomal storage disorders: Molecular basis and laboratory testing. *Human Genomics*, 5(3):156, 2011.

[89] Vincent F. Fiore, Matej Krajnc, Felipe Garcia Quiroz, John Levorse, H. Amalia Pasolli, Stanislav Y. Shvartsman, and Elaine Fuchs. Mechanics of a multilayer epithelium instruct tumour architecture and function. *Nature*, 585(7825):433–439, September 2020.

[90] Joao Firmino, Didier Rocancourt, Mehdi Saadaoui, Chloe Moreau, and Jerome Gros. Cell Division Drives Epithelial Cell Rearrangements during Gastrulation in Chick. *Developmental Cell*, 36(3):249–261, February 2016.

[91] Daniel A. Fletcher and R. Dyche Mullins. Cell mechanics and the cytoskeleton. *Nature*, 463(7280):485–492, January 2010. Number: 7280 Publisher: Nature Publishing Group.

[92] Maria Fomicheva and Ian G Macara. Genome-wide CRISPR screen identifies non-canonical NF-B signaling as a regulator of density-dependent proliferation. *eLife*, 9:e63603, November 2020. Publisher: eLife Sciences Publications, Ltd.

[93] null Foty, null Forgacs, null Pfleger, and null Steinberg. Liquid properties of embryonic tissues: Measurement of interfacial tensions. *Physical Review Letters*, 72(14):2298–2301, April 1994.

[94] W. Fritzsche and E. Henderson. Volume determination of human metaphase chromosomes by scanning force microscopy. *Scanning Microscopy*, 10(1):103–108; discussion 108–110, 1996.

[95] Anthony H. Futerman and Gerrit van Meer. The cell biology of lysosomal storage disorders. *Nature Reviews Molecular Cell Biology*, 5(7):554–565, July 2004.

[96] Simon Garcia, Edouard Hannezo, Jens Elgeti, Jean-François Joanny, Pascal Silberzan, and Nir S. Gov. Physics of active jamming during collective cellular motion in a monolayer. *Proceedings of the National Academy of Sciences*, 112(50):15314–15319, December 2015.

[97] Steven Xijin Ge, Eun Wo Son, and Runan Yao. iDEP: an integrated web application for differential expression and pathway analysis of RNA-Seq data. *BMC Bioinformatics*, 19(1):534, December 2018.

[98] Kevin Gee, Danniel Zamora, Teresa Horm, Laeth George, Cameron Upchurch, Justin Randall, Colby Weaver, Caitlin Sanford, Austin Miller, Sebastian Hernandez, Hope Dang, and Hanna Fares. Regulators of Lysosome Function and Dynamics in *Caenorhabditis elegans*. *G3 Genes/Genomes/Genetics*, 7(3):991–1000, March 2017.

[99] Steve N. Georas and Fariba Rezaee. Epithelial barrier function: At the front line of asthma immunology and allergic airway inflammation. *Journal of Allergy and Clinical Immunology*, 134(3):509–520, September 2014. Number: 3.

[100] Fabio Giavazzi, Matteo Paoluzzi, Marta Macchi, Dapeng Bi, Giorgio Scita, M. Lisa Manning, Roberto Cerbino, and M. Cristina Marchetti. Flocking transitions in confluent tissues. *Soft Matter*, 14(18):3471–3477, May 2018.

[101] Matthew C. Gibson, Ankit B. Patel, Radhika Nagpal, and Norbert Perrimon. The emergence of geometric order in proliferating metazoan epithelia. *Nature*, 442(7106):1038–1041, August 2006.

[102] Giovanni Giudice. Restitution of whole larvae from disaggregated cells of sea urchin embryos. *Developmental Biology*, 5(3):402–411, December 1962.

[103] Benoit G Godard and Carl-Philipp Heisenberg. Cell division and tissue mechanics. *Current Opinion in Cell Biology*, 60:114–120, October 2019.

[104] Deborah A. Goldspink, Chris Rookyard, Benjamin J. Tyrrell, Jonathan Gadsby, James Perkins, Elizabeth K. Lund, Niels Galjart, Paul Thomas, Tom Wileman, and Mette M. Mogensen. Ninein is essential for apico-basal microtubule formation and CLIP-170 facilitates its redeployment to non-centrosomal microtubule organizing centres. *Open Biology*, 7(2):160274, February 2017. Publisher: Royal Society.

[105] Guillermo A. Gomez, Robert W. McLachlan, and Alpha S. Yap. Productive tension: force-sensing and homeostasis of cell–cell junctions. *Trends in Cell Biology*, 21(9):499–505, September 2011.

[106] Rosemarie E. Gough, Matthew C. Jones, Thomas Zacharchenko, Shimin Le, Miao Yu, Guillaume Jacquemet, Ste P. Muench, Jie Yan, Jonathan D. Humphries, Claus Jørgensen, Martin J. Humphries, and Benjamin T. Goult. Talin mechanosensitivity is modulated by a direct interaction with cyclin-dependent kinase-1. *Journal of Biological Chemistry*, 297(1), July 2021. Publisher: Elsevier.

[107] Gavin D. Grant, Katarzyna M. Kedziora, Juanita C. Limas, Jeanette Gowen Cook, and Jeremy E. Purvis. Accurate delineation of cell cycle phase transitions in living cells with PIP-FUCCI. *Cell Cycle*, 17(21-22):2496–2516, November 2018.

[108] S. A. Gudipaty, J. Lindblom, P. D. Loftus, M. J. Redd, K. Edes, C. F. Davey, V. Krishnegowda, and J. Rosenblatt. Mechanical stretch triggers rapid epithelial cell division through Piezo1. *Nature*, 543(7643):118–121, March 2017.

[109] Charlène Guillot and Thomas Lecuit. Mechanics of Epithelial Tissue Homeostasis and Morphogenesis. *Science*, 340(6137):1185–1189, June 2013. Publisher: American Association for the Advancement of Science.

[110] Ming Guo, Adrian F. Pegoraro, Angelo Mao, Enhua H. Zhou, Praveen R. Arany, Yulong Han, Dylan T. Burnette, Mikkel H. Jensen, Karen E. Kasza, Jeffrey R. Moore, Frederick C. Mackintosh, Jeffrey J. Fredberg, David J. Mooney, Jennifer Lippincott-Schwartz, and David A. Weitz. Cell volume change through water efflux impacts cell stiffness and stem cell fate. *Proceedings of the National Academy of Sciences*, 114(41):E8618–E8627, October 2017. Publisher: National Academy of Sciences Section: PNAS Plus.

[111] Anna Haeger, Marina Krause, Katarina Wolf, and Peter Friedl. Cell jamming: Collective invasion of mesenchymal tumor cells imposed by tissue confinement. *Biochimica et Biophysica Acta (BBA) - General Subjects*, 1840(8):2386–2395, August 2014.

[112] M.A. Haidekker, T.P. Brady, D. Lichlyter, and E.A. Theodorakis. Effects of solvent polarity and solvent viscosity on the fluorescent properties of molecular rotors and related probes. *Bioorganic Chemistry*, 33(6):415–425, December 2005.

[113] Robert M. Harmon, John Devany, and Margaret L. Gardel. Dia1 coordinates differentiation and cell sorting in a stratified epithelium. *Journal of Cell Biology*, 221(5):e202101008, March 2022.

[114] Albert K. Harris. Is cell sorting caused by differences in the work of intercellular adhesion? A critique of the steinberg hypothesis. *Journal of Theoretical Biology*, 61(2):267–285, September 1976.

[115] Albert K. Harris. The need for a concept of shape homeostasis. *Biosystems*, 173:65–72, November 2018.

[116] Hidehiko Hashimoto and Edwin Munro. Differential expression and homotypic enrichment of a classic Cadherin directs tissue-level contractile asymmetry during neural tube closure. *Developmental cell*, 51(2):158–172.e4, October 2019.

[117] Matthew A. Heinrich, Ricard Alert, Julienne M. LaChance, Tom J. Zajdel, Andrej Košmrlj, and Daniel J. Cohen. Size-dependent patterns of cell proliferation and migration in freely-expanding epithelia. *eLife*, 9:e58945, August 2020.

[118] Frank S. Heldt, Reece Lunstone, John J. Tyson, and Béla Novák. Dilution and titration of cell-cycle regulators may control cell size in budding yeast. *PLOS Computational Biology*, 14(10):e1006548, October 2018. Publisher: Public Library of Science.

[119] Silke Henkes, Yaouen Fily, and M. Cristina Marchetti. Active jamming: Self-propelled soft particles at high density. *Physical Review E*, 84(4):040301, October 2011.

[120] J. S. Heslop-Harrison, A. R. Leitch, T. Schwarzacher, J. B. Smith, M. D. Atkinson, and M. D. Bennett. The volumes and morphology of human chromosomes in mitotic reconstructions. *Human Genetics*, 84(1):27–34, December 1989.

[121] Samuel T. Hess and Watt W. Webb. Focal Volume Optics and Experimental Artifacts in Confocal Fluorescence Correlation Spectroscopy. *Biophysical Journal*, 83(4):2300–2317, October 2002.

[122] Johannes Holtfreter. Properties and functions of the surface coat in amphibian embryos. *Journal of Experimental Zoology*, 93(2):251–323, 1943. _eprint: https://onlinelibrary.wiley.com/doi/pdf/10.1002/jez.1400930205.

[123] H. Honda, Y. Ogita, S. Higuchi, and K. Kani. Cell movements in a living mammalian tissue: Long-term observation of individual cells in wounded corneal endothelia of cats. *Journal of Morphology*, 174(1):25–39, October 1982.

[124] Hisao Honda and Goro Eguchi. How much does the cell boundary contract in a monolayered cell sheet? *Journal of Theoretical Biology*, 84(3):575–588, June 1980.

[125] C. E. Stevens Hooper. CELL TURNOVER IN EPITHELIAL POPULATIONS. *Journal of Histochemistry & Cytochemistry*, 4(6):531–540, November 1956.

[126] Robert J Huebner, Abdul Naseer Malmi-Kakkada, Sena Sarıkaya, Shinuo Weng, D Thirumalai, and John B Wallingford. Mechanical heterogeneity along single cell-cell junctions is driven by lateral clustering of cadherins during vertebrate axis elongation. *eLife*, 10:e65390, May 2021.

[127] Jeremy M. Hugh and Jeffrey M. Weinberg. Update on the pathophysiology of psoriasis. *Cutis*, 102(5S):6–12, November 2018.

[128] Anthony A. Hyman, Christoph A. Weber, and Frank Jülicher. Liquid-Liquid Phase Separation in Biology. *Annual Review of Cell and Developmental Biology*, 30(1):39–58, October 2014.

[129] Consuelo Ibar, Elmira Kirichenko, Benjamin Keepers, Edward Enners, Katelyn Fleisch, and Kenneth D. Irvine. Tension-dependent regulation of mammalian Hippo signaling through LIMD1. *Journal of Cell Science*, 131(5):jcs214700, March 2018.

[130] Akira Imamoto, Sewon Ki, Leiming Li, Kazunari Iwamoto, Venkat Maruthamuthu, John Devany, Ocean Lu, Tomomi Kanazawa, Suxiang Zhang, Takuji Yamada, Akiyoshi Hirayama, Shinji Fukuda, Yutaka Suzuki, and Mariko Okada. Essential role of the Crk family-dosage in DiGeorge-like anomaly and metabolic homeostasis. *Life Science Alliance*, 3(2), February 2020. Publisher: Life Science Alliance Section: Research Articles.

[131] K. Inoue and K. Kimura. A method for calculating the perimeter of objects for automatic recognition of circular defects. *NDT International*, 20(4):225–230, August 1987.

[132] Kenneth D. Irvine and Boris I. Shraiman. Mechanical control of growth: ideas, facts and challenges. *Development (Cambridge, England)*, 144(23):4238–4248, December 2017.

[133] Akanksha Jain, Vladimir Ulman, Arghyadip Mukherjee, Mangal Prakash, Marina B. Cuenca, Lokesh G. Pimpale, Stefan Münster, Robert Haase, Kristen A. Panfilio, Florian Jug, Stephan W. Grill, Pavel Tomancak, and Anastasios Pavlopoulos. Regionalized tissue fluidization is required for epithelial gap closure during insect gastrulation. *Nature Communications*, 11(1):5604, November 2020. Number: 1 Publisher: Nature Publishing Group.

[134] I. Jarvela, M. Sainio, T. Rantamaki, V. M. Olkkonen, O. Carpen, L. Peltonen, and A. Jalanko. Biosynthesis and Intracellular Targeting of the CLN3 Protein Defective in Batten Disease. *Human Molecular Genetics*, 7(1):85–90, January 1998.

[135] Matthew C. Jones, Janet A. Askari, Jonathan D. Humphries, and Martin J. Humphries. Cell adhesion is regulated by CDK1 during the cell cycle. *Journal of Cell Biology*, 217(9):3203–3218, September 2018.

[136] LEO P. KADANOFF, WOLFGANG GÖTZE, DAVID HAMBLEN, ROBERT HECHT, E. A. S. LEWIS, V. V. PALCIAUSKAS, MARTIN RAYL, J. SWIFT, DAVID ASPNES, and JOSEPH KANE. Static Phenomena Near Critical Points: Theory and Experiment. *Reviews of Modern Physics*, 39(2):395–431, April 1967. Publisher: American Physical Society.

[137] Girish R. Kale, Xingbo Yang, Jean-Marc Philippe, Madhav Mani, Pierre-François Lenne, and Thomas Lecuit. Distinct contributions of tensile and shear stress on E-cadherin levels during morphogenesis. *Nature Communications*, 9(1):5021, November 2018. Number: 1 Publisher: Nature Publishing Group.

[138] Titus Kaletta and Michael O. Hengartner. Finding function in novel targets: C. elegans as a model organism. *Nature Reviews Drug Discovery*, 5(5):387–399, May 2006.

[139] Sayali S. Karve, Suman Pradhan, Doyle V. Ward, and Alison A. Weiss. Intestinal organoids model human responses to infection by commensal and Shiga toxin producing Escherichia coli. *PLOS ONE*, 12(6):e0178966, June 2017. Publisher: Public Library of Science.

[140] Dagmar Kasper, Rosa Planells-Cases, Jens C Fuhrmann, Olaf Scheel, Oliver Zeitz, Klaus Ruether, Anja Schmitt, Mallorie Poët, Robert Steinfeld, Michaela Schweizer, Uwe Kornak, and Thomas J Jentsch. Loss of the chloride channel ClC-7 leads to lysosomal storage disease and neurodegeneration. *The EMBO Journal*, 24(5):1079–1091, March 2005.

[141] Ganesan Keerthivasan, Yang Mei, Baobing Zhao, Ling Zhang, Chad E. Harris, Juehua Gao, Ashley A. Basiorka, Matthew J. Schipma, James McElherne, Jing Yang, Amit K. Verma, Andrea Pellagatti, Jacqueline Boultwood, Alan F. List, David A. Williams, and Peng Ji. Aberrant overexpression of CD14 on granulocytes sensitizes the innate immune response in mDia1 heterozygous del(5q) MDS. *Blood*, 124(5):780–790, July 2014.

[142] G. Kellner-Weibel, W. G. Jerome, D. M. Small, G. J. Warner, J. K. Stoltenborg, M. A. Kearney, M. H. Corjay, M. C. Phillips, and G. H. Rothblat. Effects of Intracellular Free Cholesterol Accumulation on Macrophage Viability: A Model for Foam Cell Death. *Arteriosclerosis, Thrombosis, and Vascular Biology*, 18(3):423–431, March 1998.

[143] Paraic A. Kenny and Mina J. Bissell. Tumor reversion: correction of malignant behavior by microenvironmental cues. *International Journal of Cancer*, 107(5):688–695, December 2003.

[144] Nargess Khalilgharibi, Jonathan Fouchard, Nina Asadipour, Ricardo Barrientos, Maria Duda, Alessandra Bonfanti, Amina Yonis, Andrew Harris, Payman Mosaffa, Yasuyuki Fujita, Alexandre Kabla, Yanlan Mao, Buzz Baum, José J. Muñoz, Mark Miodownik, and Guillaume Charras. Stress relaxation in epithelial monolayers is controlled by the actomyosin cortex. *Nature Physics*, 15(8):839–847, August 2019. Number: 8 Publisher: Nature Publishing Group.

[145] Eric Kim, Lin Sun, Christopher V. Gabel, and Christopher Fang-Yen. Long-Term Imaging of Caenorhabditis elegans Using Nanoparticle-Mediated Immobilization. *PLoS ONE*, 8(1):e53419, January 2013.

[146] Hye Young Kim, Timothy R. Jackson, Carsten Stuckenholz, and Lance A. Davidson. Tissue mechanics drives regeneration of a mucociliated epidermis on the surface of Xenopus embryonic aggregates. *Nature Communications*, 11(1):665, January 2020. Number: 1 Publisher: Nature Publishing Group.

[147] Nam-Gyun Kim, Eunjin Koh, Xiao Chen, and Barry M. Gumbiner. E-cadherin mediates contact inhibition of proliferation through Hippo signaling-pathway components. *Proceedings of the National Academy of Sciences*, 108(29):11930–11935, July 2011. Publisher: National Academy of Sciences Section: Biological Sciences.

[148] Sangwoo Kim, Muyun Cai, and Sascha Hilgenfeldt. Lewis' law revisited: the role of anisotropy in size-topology correlations. *New Journal of Physics*, 16(January):015024, January 2014.

[149] Sangwoo Kim and Sascha Hilgenfeldt. Cell shapes and patterns as quantitative indicators of tissue stress in the plant epidermis. *Soft Matter*, 11(37):7270–7275, 2015.

[150] Sangwoo Kim, Marie Pochitaloff, Georgina A. Stooke-Vaughan, and Otger Campàs. Embryonic tissues as active foams. *Nature Physics*, 17(7):859–866, July 2021. Number: 7 Publisher: Nature Publishing Group.

[151] Shunsuke Kimura, Takeshi Noda, and Tamotsu Yoshimori. Dissection of the Autophagosome Maturation Process by a Novel Reporter Protein, Tandem Fluorescent-Tagged LC3. *Autophagy*, 3(5):452–460, September 2007.

[152] Abigail A. Kindberg, Vasudha Srivastava, Jonathon M. Muncie, Valerie M. Weaver, Zev J. Gartner, and Jeffrey O. Bush. EPH/EPHRIN regulates cellular organization by actomyosin contractility effects on cell contacts. *Journal of Cell Biology*, 220(6):e202005216, April 2021.

[153] Anna Klabunde and Frans Willekens. Decision-Making in Agent-Based Models of Migration: State of the Art and Challenges. *European Journal of Population*, 32(1):73–97, February 2016.

[154] Agnieszka Kobielak, H. Amalia Pasolli, and Elaine Fuchs. Mammalian formin-1 participates in adherens junctions and polymerization of linear actin cables. *Nature Cell Biology*, 6(1):21–30, January 2004.

[155] M. J. Koehler, S. Zimmermann, S. Springer, P. Elsner, K. König, and M. Kaatz. Keratinocyte morphology of human skin evaluated by in vivo multiphoton laser tomography: Keratinocyte morphology of human skin by in vivo MPT. *Skin Research and Technology*, 17(4):479–486, November 2011.

[156] Marco Kokic, Antonella Iannini, Gema Villa-Fombuena, Fernando Casares, and Dagmar Iber. Minimisation of surface energy drives apical epithelial organisation and gives rise to Lewis' law, March 2019. Pages: 590729 Section: New Results.

[157] Shunsuke Kon, Kojiro Ishibashi, Hiroto Katoh, Sho Kitamoto, Takanobu Shirai, Shinya Tanaka, Mihoko Kajita, Susumu Ishikawa, Hajime Yamauchi, Yuta Yako, Tomoko Kamasaki, Tomohiro Matsumoto, Hirotaka Watanabe, Riku Egami, Ayana Sasaki, Atsuko Nishikawa, Ikumi Kameda, Takeshi Maruyama, Rika Narumi, Tomoko Morita, Yoshiteru Sasaki, Ryosuke Enoki, Sato Honma, Hiromi Imamura, Masanobu Oshima, Tomoyoshi Soga, Jun-ichi Miyazaki, Michael R. Duchen, Jin-Min Nam, Yasuhito Onodera, Shingo Yoshioka, Junichi Kikuta, Masaru Ishii, Masamichi Imajo, Eisuke Nishida, Yoichiro Fujioka, Yusuke Ohba, Toshiro Sato, and Yasuyuki Fujita. Cell competition with normal epithelial cells promotes apical extrusion of transformed cells through metabolic changes. *Nature Cell Biology*, 19(5):530–541, May 2017. Bandiera_abtest: a Cg_type: Nature Research Journals Number: 5 Primary_atype: Research Publisher: Nature Publishing Group Subject_term: Cancer metabolism;Cell signalling;Oncogenes Subject_term_id: cancer-metabolism;cell-signalling;oncogenes.

[158] Weiyuan Kong, Olivier Loison, Pruthvi Chavadimane Shivakumar, Eunice HoYee Chan, Mehdi Saadaoui, Claudio Collinet, Pierre-François Lenne, and Raphaël Clément. Experimental validation of force inference in epithelia from cell to tissue scale. *Scientific Reports*, 9(1):14647, October 2019. Number: 1 Publisher: Nature Publishing Group.

[159] Uwe Kornak, Dagmar Kasper, Michael R Bösl, Edelgard Kaiser, Michaela Schweizer, Ansgar Schulz, Wilhelm Friedrich, Günter Delling, and Thomas J Jentsch. Loss of the ClC-7 Chloride Channel Leads to Osteopetrosis in Mice and Man. *Cell*, 104(2):205–215, January 2001.

[160] S. F. Gabby Krens and Carl-Philipp Heisenberg. Chapter six - Cell Sorting in Development. In Michel Labouesse, editor, *Current Topics in Developmental Biology*, volume 95 of *Forces and Tension in Development*, pages 189–213. Academic Press, January 2011.

[161] M. Krieg, Y. Arboleda-Estudillo, P.-H. Puech, J. Käfer, F. Graner, D. J. Müller, and C.-P. Heisenberg. Tensile forces govern germ-layer organization in zebrafish. *Nature*

Cell Biology, 10(4):429–436, April 2008. Number: 4 Publisher: Nature Publishing Group.

[162] Denis Krndija, Fatima El Marjou, Boris Guirao, Sophie Richon, Olivier Leroy, Yohanns Bellaiche, Edouard Hannezo, and Danijela Matic Vignjevic. Active cell migration is critical for steady-state epithelial turnover in the gut. *Science*, 365(6454):705–710, August 2019. Publisher: American Association for the Advancement of Science.

[163] Marina K. Kuimova, Gokhan Yahioglu, James A. Levitt, and Klaus Suhling. Molecular Rotor Measures Viscosity of Live Cells via Fluorescence Lifetime Imaging. *Journal of the American Chemical Society*, 130(21):6672–6673, May 2008.

[164] Hyock Joo Kwon, Lina Abi-Mosleh, Michael L. Wang, Johann Deisenhofer, Joseph L. Goldstein, Michael S. Brown, and Rodney E. Infante. Structure of N-Terminal Domain of NPC1 Reveals Distinct Subdomains for Binding and Transfer of Cholesterol. *Cell*, 137(7):1213–1224, June 2009.

[165] Thomas Kühn, Teemu O. Ihalainen, Jari Hyväluoma, Nicolas Dross, Sami F. Willman, Jörg Langowski, Maija Vihinen-Ranta, and Jussi Timonen. Protein Diffusion in Mammalian Cell Cytoplasm. *PLoS ONE*, 6(8):e22962, August 2011.

[166] Nadine R. Lang, Kai Skodzek, Sebastian Hurst, Astrid Mainka, Julian Steinwachs, Julia Schneider, Katerina E. Aifantis, and Ben Fabry. Biphasic response of cell invasion to matrix stiffness in three-dimensional biopolymer networks. *Acta Biomaterialia*, 13:61–67, February 2015.

[167] Michael C. Lanz, Evgeny Zatulovskiy, Matthew P. Swaffer, Lichao Zhang, Ilayda Ilerten, Shuyuan Zhang, Dong Shin You, Georgi Marinov, Patrick McAlpine, Josh E. Elias, and Jan M. Skotheim. Increasing cell size remodels the proteome and promotes senescence. Technical report, bioRxiv, November 2021. Section: New Results Type: article.

[168] Thomas Lecuit and Pierre-François Lenne. Cell surface mechanics and the control of cell shape, tissue patterns and morphogenesis. *Nature Reviews Molecular Cell Biology*, 8(8):633–644, August 2007. Number: 8 Publisher: Nature Publishing Group.

[169] Thomas Lecuit, Pierre-François Lenne, and Edwin Munro. Force Generation, Transmission, and Integration during Cell and Tissue Morphogenesis. *Annual Review of Cell and Developmental Biology*, 27(1):157–184, November 2011.

[170] Sung Haeng Lee and Roberto Dominguez. Regulation of actin cytoskeleton dynamics in cells. *Molecules and Cells*, 29(4):311–325, April 2010.

[171] P. Leinekugel, S. Michel, E. Conzelmann, and K. Sandhoff. Quantitative correlation between the residual activity of -hexosaminidase A and arylsulfatase A and the severity of the resulting lysosomal storage disease. *Human Genetics*, 88(5):513–523, March 1992.

[172] Olga V. Leontieva, Zoya N. Demidenko, and Mikhail V. Blagosklonny. Contact inhibition and high cell density deactivate the mammalian target of rapamycin pathway, thus suppressing the senescence program. *Proceedings of the National Academy of Sciences of the United States of America*, 111(24):8832–8837, June 2014.

[173] Clémence Lepelletier, Jean-David Bouaziz, Michel Rybojad, Martine Bagot, Sophie Georgin-Lavialle, and Marie-Dominique Vignon-Pennamen. Neutrophilic Dermatoses Associated with Myeloid Malignancies. *American Journal of Clinical Dermatology*, 20(3):325–333, June 2019.

[174] Euphemia Leung, Ji Eun Kim, Marjan Askarian-Amiri, Graeme J. Finlay, and Bruce C. Baguley. Evidence for the Existence of Triple-Negative Variants in the MCF-7 Breast Cancer Cell Population. *BioMed Research International*, 2014:e836769, March 2014. Publisher: Hindawi.

[175] Michael Levin. Bioelectric signaling: Reprogrammable circuits underlying embryogenesis, regeneration, and cancer. *Cell*, 184(8):1971–1989, April 2021.

[176] Jie Li, Gemma Brown, Michael Ailion, Samuel Lee, and James H. Thomas. NCR-1 and NCR-2, the *C. elegans* homologs of the human Niemann-Pick type C1 disease protein, function upstream of DAF-9 in the dauer formation pathways. *Development*, 131(22):5741–5752, November 2004.

[177] Yubing Li, Dianyi Liu, Cristina López-Paz, Bradley JSC Olson, and James G Umen. A new class of cyclin dependent kinase in Chlamydomonas is required for coupling cell size to cell division. *eLife*, 5:e10767, March 2016. Publisher: eLife Sciences Publications, Ltd.

[178] Jackson Liang, Shruthi Balachandra, Sang Ngo, and Lucy Erin O'Brien. Feedback regulation of steady-state epithelial turnover and organ size. *Nature*, 548(7669):588–591, August 2017.

[179] Yi Liao and Michael J. Rust. The circadian clock ensures successful DNA replication in cyanobacteria. *Proceedings of the National Academy of Sciences*, 118(20):e2022516118, May 2021. Publisher: Proceedings of the National Academy of Sciences.

[180] Andrew M. Lin, Cory J. Rubin, Ritika Khandpur, Jennifer Y. Wang, MaryBeth Riblett, Srilakshmi Yalavarthi, Eneida C. Villanueva, Parth Shah, Mariana J. Kaplan, and Allen T. Bruce. Mast Cells and Neutrophils Release IL-17 through Extracellular Trap Formation in Psoriasis. *The Journal of Immunology*, 187(1):490–500, July 2011.

[181] Laura Liscum and Stephen L. Sturley. Intracellular trafficking of Niemann–Pick C proteins 1 and 2: obligate components of subcellular lipid transport. *Biochimica et Biophysica Acta (BBA) - Molecular and Cell Biology of Lipids*, 1685(1-3):22–27, October 2004.

[182] Tianyu Liu, Xiaogang Liu, David R. Spring, Xuhong Qian, Jingnan Cui, and Zhaochao Xu. Quantitatively Mapping Cellular Viscosity with Detailed Organelle Information via a Designed PET Fluorescent Probe. *Scientific Reports*, 4(1):5418, May 2015.

[183] Emyr Lloyd-Evans, Anthony J Morgan, Xingxuan He, David A Smith, Elena Elliot-Smith, Daniel J Sillence, Grant C Churchill, Edward H Schuchman, Antony Galione, and Frances M Platt. Niemann-Pick disease type C1 is a sphingosine storage disease that causes deregulation of lysosomal calcium. *Nature Medicine*, 14(11):1247–1255, November 2008.

[184] Marine Luciano, Shi-Lei Xue, Winnok H. De Vos, Lorena Redondo-Morata, Mathieu Surin, Frank Lafont, Edouard Hannezo, and Sylvain Gabriele. Cell monolayers sense curvature by exploiting active mechanics and nuclear mechanoadaptation. *Nature Physics*, 17(12):1382–1390, December 2021. Number: 12 Publisher: Nature Publishing Group.

[185] Chen Luxenburg, Evan Heller, H. Amalia Pasolli, Sophia Chai, Maria Nikolova, Nicole Stokes, and Elaine Fuchs. Wdr1-mediated cell shape dynamics and cortical tension are essential for epidermal planar cell polarity. *Nature Cell Biology*, 17(5):592–604, May 2015.

[186] Chen Luxenburg and Ronen Zaidel-Bar. From cell shape to cell fate via the cytoskeleton — Insights from the epidermis. *Experimental Cell Research*, 378(2):232–237, May 2019.

[187] Chiara Malinverno, Salvatore Corallino, Fabio Giavazzi, Martin Bergert, Qingsen Li, Marco Leoni, Andrea Disanza, Emanuela Frittoli, Amanda Oldani, Emanuele Martini, Tobias Lendenmann, Gianluca Deflorian, Galina V. Beznoussenko, Dimos Poulikakos, Kok Haur Ong, Marina Uroz, Xavier Trepat, Dario Parazzoli, Paolo Maiuri, Weimiao Yu, Aldo Ferrari, Roberto Cerbino, and Giorgio Scita. Endocytic reawakening of motility in jammed epithelia. *Nature Materials*, 16(5):587–596, May 2017.

[188] M. Lisa Manning, Ramsey A. Foty, Malcolm S. Steinberg, and Eva-Maria Schoetz. Coaction of intercellular adhesion and cortical tension specifies tissue surface tension. *Proceedings of the National Academy of Sciences*, 107(28):12517–12522, July 2010.

[189] Eliana Marinari, Aida Mehonic, Scott Curran, Jonathan Gale, Thomas Duke, and Buzz Baum. Live-cell delamination counterbalances epithelial growth to limit tissue overcrowding. *Nature*, 484(7395):542–545, April 2012.

[190] Michael P. Marino, Milson J. Luce, and Jakob Reiser. Small- to Large-Scale Production of Lentivirus Vectors. In Maurizio Federico, editor, *Lentivirus Gene Engineering Protocols*, Methods in Molecular Biology™, pages 43–55. Humana Press, Totowa, NJ, 2003.

[191] Chioniso Patience Masamha and Doris Mangiaracina Benbrook. Cyclin D1 Degradation Is Sufficient to Induce G1 Cell Cycle Arrest despite Constitutive Expression of Cyclin E2 in Ovarian Cancer Cells. *Cancer Research*, 69(16):6565–6572, August 2009.

[192] T. G. Mason, K. Ganesan, J. H. van Zanten, D. Wirtz, and S. C. Kuo. Particle Tracking Microrheology of Complex Fluids. *Physical Review Letters*, 79(17):3282–3285, October 1997.

[193] D. A. Matoz-Fernandez, Kirsten Martens, Rastko Sknepnek, J. L. Barrat, and Silke Henkes. Cell division and death inhibit glassy behaviour of confluent tissues. *Soft Matter*, 13(17):3205–3212, 2017.

[194] Joseph R. Mazzulli, You-Hai Xu, Ying Sun, Adam L. Knight, Pamela J. McLean, Guy A. Caldwell, Ellen Sidransky, Gregory A. Grabowski, and Dimitri Krainc. Gaucher Disease Glucocerebrosidase and -Synuclein Form a Bidirectional Pathogenic Loop in Synucleinopathies. *Cell*, 146(1):37–52, July 2011.

[195] Jean-Léon Maître, Hélène Berthoumieux, Simon Frederik Gabriel Krens, Guillaume Salbreux, Frank Jülicher, Ewa Paluch, and Carl-Philipp Heisenberg. Adhesion functions in cell sorting by mechanically coupling the cortices of adhering cells. *Science (New York, N.Y.)*, 338(6104):253–256, October 2012.

[196] Andrea I McClatchey and Alpha S Yap. Contact inhibition (of proliferation) redux. *Current Opinion in Cell Biology*, 24(5):685–694, October 2012.

[197] Jamie McGinn, Adrien Hallou, Seungmin Han, Kata Krizic, Svetlana Ulyanchenko, Ramiro Iglesias-Bartolome, Frances J. England, Christophe Verstreken, Kevin J. Chalut, Kim B. Jensen, Benjamin D. Simons, and Maria P. Alcolea. A biomechanical switch regulates the transition towards homeostasis in oesophageal epithelium. *Nature Cell Biology*, 23(5):511–525, May 2021. Number: 5 Publisher: Nature Publishing Group.

[198] Donella H. Meadows. *Thinking in Systems: A Primer*. Chelsea Green Publishing, 2008. Google-Books-ID: CpbLAgAAQBAJ.

[199] Gustavo de Medeiros, Raphael Ortiz, Petr Strnad, Andrea Boni, Francisca Maurer, and Prisca Liberali. Multiscale light-sheet organoid imaging framework. Technical report, May 2021. Company: Cold Spring Harbor Laboratory Distributor: Cold Spring Harbor Laboratory Label: Cold Spring Harbor Laboratory Section: New Results Type: article.

[200] Peter J. Meikle. Prevalence of Lysosomal Storage Disorders. *JAMA*, 281(3):249, January 1999.

[201] Alisha M. Mendonsa, Tae-Young Na, and Barry M. Gumbiner. E-cadherin in contact inhibition and cancer. *Oncogene*, 37(35):4769–4780, August 2018. Bandiera_abtest: a Cg_type: Nature Research Journals Number: 35 Primary_atype: Reviews Publisher: Nature Publishing Group Subject_term: Cadherins;Metastasis Subject_term_id: cadherins;metastases.

[202] Marisa M. Merino, Romain Levayer, and Eduardo Moreno. Survival of the Fittest: Essential Roles of Cell Competition in Development, Aging, and Cancer. *Trends in Cell Biology*, 26(10):776–788, October 2016. Publisher: Elsevier.

[203] Kailin R. Mesa, Kyogo Kawaguchi, Katie Cockburn, David Gonzalez, Jonathan Boucher, Tianchi Xin, Allon M. Klein, and Valentina Greco. Homeostatic Epidermal Stem Cell Self-Renewal Is Driven by Local Differentiation. *Cell Stem Cell*, 23(5):677–686.e4, November 2018.

[204] Staddon Mf, Cavanaugh Ke, Munro Em, Gardel Ml, and Banerjee S. Mechanosensitive Junction Remodeling Promotes Robust Epithelial Morphogenesis. *Biophysical journal*, 117(9), November 2019. Publisher: Biophys J.

[205] Ron Milo and Rob Phillips. *Cell Biology by the numbers*. Garland Science, New York, December 2015.

[206] Yekaterina A. Miroshnikova, Huy Q. Le, David Schneider, Torsten Thalheim, Matthias Rübsam, Nadine Bremicker, Julien Polleux, Nadine Kamprad, Marco Tarantola, Irène Wang, Martial Balland, Carien M. Niessen, Joerg Galle, and Sara A. Wickström. Adhesion forces and cortical tension couple cell proliferation and differentiation to drive epidermal stratification. *Nature Cell Biology*, 20(1):69–80, January 2018. Number: 1 Publisher: Nature Publishing Group.

[207] Melanie Mitchell. *Complexity: A Guided Tour*. Oxford University Press, April 2009.

[208] Alessandro Mongera, Payam Rowghanian, Hannah J. Gustafson, Elijah Shelton, David A. Kealhofer, Emmet K. Carn, Friedhelm Serwane, Adam A. Lucio, James Giammona, and Otger Campàs. A fluid-to-solid jamming transition underlies vertebrate body axis elongation. *Nature*, 561(7723):401–405, September 2018.

[209] Bruno Monier, Anne Pélissier-Monier, Andrea H. Brand, and Bénédicte Sanson. An actomyosin-based barrier inhibits cell mixing at compartmental boundaries in Drosophila embryos. *Nature Cell Biology*, 12(1):60–65, January 2010. Number: 1 Publisher: Nature Publishing Group.

[210] R. Montesano, G. Schaller, and L. Orci. Induction of epithelial tubular morphogenesis in vitro by fibroblast-derived soluble factors. *Cell*, 66(4):697–711, August 1991.

[211] Cary A. Moody and Laimonis A. Laimins. Human papillomavirus oncoproteins: pathways to transformation. *Nature Reviews Cancer*, 10(8):550–560, August 2010.

[212] Thierry Mora and William Bialek. Are Biological Systems Poised at Criticality? *Journal of Statistical Physics*, 144(2):268–302, July 2011.

[213] Ryuji Morizane, Albert Q. Lam, Benjamin S. Freedman, Seiji Kishi, M. Todd Valerius, and Joseph V. Bonventre. Nephron organoids derived from human pluripotent stem cells model kidney development and injury. *Nature Biotechnology*, 33(11):1193–1200, November 2015. Bandiera_abtest: a Cg_type: Nature Research Journals Number: 11 Primary_atype: Research Publisher: Nature Publishing Group Subject_term: Disease model;Embryonic stem cells;Induced pluripotent stem cells;Stem-cell differentiation Subject_term_id: disease-model;embryonic-stem-cells;induced-pluripotent-stem-cells;stem-cell-differentiation.

[214] Akankshi Munjal, Jean-Marc Philippe, Edwin Munro, and Thomas Lecuit. A self-organized biomechanical network drives shape changes during tissue morphogenesis. *Nature*, 524(7565):351–355, August 2015.

[215] Andrew Wood Murray and Tim Hunt. *The Cell Cycle: An Introduction*. Oxford University Press, 1993. Google-Books-ID: 4nmOovzIc0IC.

[216] Nagarjun Narayanaswamy, Kasturi Chakraborty, Anand Saminathan, Elizabeth Zeichner, KaHo Leung, John Devany, and Yamuna Krishnan. A pH-correctable, DNA-based fluorescent reporter for organellar calcium. *Nature Methods*, 16(1):95–102, January 2019. Number: 1 Publisher: Nature Publishing Group.

[217] Edward B. Neufeld, Meryl Wastney, Shutish Patel, Sundar Suresh, Adele M. Cooney, Nancy K. Dwyer, Calvin F. Roff, Kousaku Ohno, Jill A. Morris, Eugene D. Carstea, John P. Incardona, Jerome F. Strauss, Marie T. Vanier, Marc C. Patterson, Roscoe O. Brady, Peter G. Pentchev, and E. Joan Blanchette-Mackie. The Niemann-Pick C1 Protein Resides in a Vesicular Compartment Linked to Retrograde Transport of Multiple Lysosomal Cargo. *Journal of Biological Chemistry*, 274(14):9627–9635, April 1999.

[218] Gabriel E. Neurohr, Rachel L. Terry, Jette Lengefeld, Megan Bonney, Gregory P. Brittingham, Fabien Moretto, Teemu P. Miettinen, Laura Pontano Vaites, Luis M. Soares, Joao A. Paulo, J. Wade Harper, Stephen Buratowski, Scott Manalis, Folkert J. van Werven, Liam J. Holt, and Angelika Amon. Excessive Cell Growth Causes Cytoplasm Dilution And Contributes to Senescence. *Cell*, 176(5):1083–1097.e18, February 2019.

[219] Mei Rosa Ng, Achim Besser, Gaudenz Danuser, and Joan S. Brugge. Substrate stiffness regulates cadherin-dependent collective migration through myosin-II contractility. *Journal of Cell Biology*, 199(3):545–563, October 2012.

[220] Nicholas Noll, Sebastian J. Streichan, and Boris I. Shraiman. Variational Method for Image-Based Inference of Internal Stress in Epithelial Tissues. *Physical Review X*, 10(1):011072, March 2020. Publisher: American Physical Society.

[221] Paul Nurse. A Long Twentieth Century of the Cell Cycle and Beyond. *Cell*, 100(1):71–78, January 2000. Publisher: Elsevier.

[222] L. E. O'Brien, T. S. Jou, A. L. Pollack, Q. Zhang, S. H. Hansen, P. Yurchenco, and K. E. Mostov. Rac1 orientates epithelial apical polarity through effects on basolateral laminin assembly. *Nature Cell Biology*, 3(9):831–838, September 2001.

[223] L. H. H. Olde Damink, P. J. Dijkstra, M. J. A. Van Luyn, P. B. Van Wachem, P. Nieuwenhuis, and J. Feijen. Glutaraldehyde as a crosslinking agent for collagen-based biomaterials. *Journal of Materials Science: Materials in Medicine*, 6(8):460–472, August 1995.

[224] Linda Oswald, Steffen Grosser, David M Smith, and Josef A Käs. Jamming transitions in cancer. *Journal of Physics D: Applied Physics*, 50(48):483001, December 2017.

[225] Elizabeth Ottinger, Mark Kao, Nuria Carrillo-Carrasco, Nicole Yanjanin, Roopa Shankar, Marjo Janssen, Marcus Brewster, Ilona Scott, Xin Xu, Jim Cradock, Pramod Terse, Seameen Dehdashti, Juan Marugan, Wei Zheng, Lili Portilla, Alan Hubbs, William Pavan, John Heiss, Charles H.Vite, Steven Walkley, Daniel Ory, Steven Silber, Forbes Porter, Christopher Austin, and John McKew. Collaborative Development of 2-Hydroxypropyl-β-Cyclodextrin for the Treatment of Niemann-Pick Type C1 Disease. *Current Topics in Medicinal Chemistry*, 14(3):330–339, January 2014.

[226] Horng D. Ou, Sébastien Phan, Thomas J. Deerinck, Andrea Thor, Mark H. Ellisman, and Clodagh C. O'Shea. ChromEMT: Visualizing 3D chromatin structure and compaction n interphase and mitotic cells. *Science (New York, N.Y.)*, 357(6349):eaag0025, July 2017.

[227] Olivia Padovan-Merhar, Gautham P. Nair, Andrew G. Biaesch, Andreas Mayer, Steven Scarfone, Shawn W. Foley, Angela R. Wu, L. Stirling Churchman, Abhyudai Singh, and Arjun Raj. Single Mammalian Cells Compensate for Differences in Cellular Volume and DNA Copy Number through Independent Global Transcriptional Mechanisms. *Molecular Cell*, 58(2):339–352, April 2015.

[228] Yuanwang Pan, Idse Heemskerk, Consuelo Ibar, Boris I. Shraiman, and Kenneth D. Irvine. Differential growth triggers mechanical feedback that elevates Hippo signaling. *Proceedings of the National Academy of Sciences*, 113(45):E6974–E6983, November 2016. Publisher: National Academy of Sciences Section: PNAS Plus.

[229] Porntula Panorchan, Jerry S.H. Lee, Thomas P. Kole, Yiider Tseng, and Denis Wirtz. Microrheology and ROCK Signaling of Human Endothelial Cells Embedded in a 3D Matrix. *Biophysical Journal*, 91(9):3499–3507, November 2006.

[230] Giancarlo Parenti, Generoso Andria, and Andrea Ballabio. Lysosomal Storage Diseases: From Pathophysiology to Therapy. *Annual Review of Medicine*, 66(1):471–486, January 2015.

[231] Jin-Ah Park, Jae Hun Kim, Dapeng Bi, Jennifer A. Mitchel, Nader Taheri Qazvini, Kelan Tantisira, Chan Young Park, Maureen McGill, Sae-Hoon Kim, Bomi Gweon, Jacob Notbohm, Robert Steward Jr, Stephanie Burger, Scott H. Randell, Alvin T. Kho, Dhananjay T. Tambe, Corey Hardin, Stephanie A. Shore, Elliot Israel, David A. Weitz, Daniel J. Tschumperlin, Elizabeth P. Henske, Scott T. Weiss, M. Lisa Manning, James P. Butler, Jeffrey M. Drazen, and Jeffrey J. Fredberg. Unjamming and cell shape in the asthmatic airway epithelium. *Nature Materials*, 14(10):1040–1048, October 2015.

[232] Kidong Park, Larry J. Millet, Namjung Kim, Huan Li, Xiaozhong Jin, Gabriel Popescu, N. R. Aluru, K. Jimmy Hsia, and Rashid Bashir. Measurement of adherent cell mass and growth. *Proceedings of the National Academy of Sciences of the United States of America*, 107(48):20691–20696, November 2010.

[233] Steve Pawlizak, Anatol W. Fritsch, Steffen Grosser, Dave Ahrens, Tobias Thalheim, Stefanie Riedel, Tobias R. Kießling, Linda Oswald, Mareike Zink, M. Lisa Manning, and Josef A. Käs. Testing the differential adhesion hypothesis across the epithelial-mesenchymal transition. *New Journal of Physics*, 17(8):083049, August 2015. Publisher: IOP Publishing.

[234] Kyle B. Peake and Jean E. Vance. Normalization of Cholesterol Homeostasis by 2-Hydroxypropyl--cyclodextrin in Neurons and Glia from Niemann-Pick C1 (NPC1)-deficient Mice. *Journal of Biological Chemistry*, 287(12):9290–9298, March 2012.

[235] Jun Peng, Susan M. Kitchen, Richard A. West, Robert Sigler, Kathryn M. Eisenmann, and Arthur S. Alberts. Myeloproliferative defects following targeting of the Drf1 gene encoding the mammalian diaphanous related formin mDia1. *Cancer Research*, 67(16):7565–7571, August 2007.

[236] Xiaojun Peng, Zhigang Yang, Jingyun Wang, Jiangli Fan, Yanxia He, Fengling Song, Bingshuai Wang, Shiguo Sun, Junle Qu, Jing Qi, and Meng Yan. Fluorescence Ratiometry and Fluorescence Lifetime Imaging: Using a Single Molecular Sensor for Dual Mode Imaging of Cellular Viscosity. *Journal of the American Chemical Society*, 133(17):6626–6635, May 2011.

[237] Nicolas A. Perez-Gonzalez, Nash D. Rochman, Kai Yao, Jiaxiang Tao, Minh-Tam Tran Le, Shannon Flanary, Lucia Sablich, Ben Toler, Eliana Crentsil, Felipe Takaesu, Bram Lambrus, Jessie Huang, Vivian Fu, Pragati Chengappa, Tia M. Jones, Andrew J. Holland, Steven An, Denis Wirtz, Ryan J. Petrie, Kun-Liang Guan, and Sean X. Sun. YAP and TAZ regulate cell volume. *Journal of Cell Biology*, 218(10):3472–3488, September 2019.

[238] Nicoletta I. Petridou, Bernat Corominas-Murtra, Carl-Philipp Heisenberg, and Edouard Hannezo. Rigidity percolation uncovers a structural basis for embryonic tissue phase transitions. *Cell*, 184(7):1914–1928.e19, April 2021.

[239] Nicoletta I. Petridou, Silvia Grigolon, Guillaume Salbreux, Edouard Hannezo, and Carl-Philipp Heisenberg. Fluidization-mediated tissue spreading by mitotic cell rounding and non-canonical Wnt signalling. *Nature Cell Biology*, 21(2):169–178, February 2019.

[240] Nicoletta I. Petridou, Zoltán Spiró, and Carl-Philipp Heisenberg. Multiscale force sensing in development. *Nature Cell Biology*, 19(6):581–588, June 2017. Number: 6 Publisher: Nature Publishing Group.

[241] Hermann Pinkus. Examination of the Epidermis by the Strip Method of Removing Horny Layers. *Journal of Investigative Dermatology*, 16(6):383–386, June 1951.

[242] Nina H. Pipalia, Amy Huang, Harold Ralph, Madalina Rujoi, and Frederick R. Maxfield. Automated microscopy screening for compounds that partially revert cholesterol

accumulation in Niemann-Pick C cells. *Journal of Lipid Research*, 47(2):284–301, February 2006.

[243] Martin P. Playford, Kavita Vadali, Xinming Cai, Keith Burridge, and Michael D. Schaller. Focal adhesion kinase regulates cell-cell contact formation in epithelial cells via modulation of Rho. *Experimental Cell Research*, 314(17):3187–3197, October 2008.

[244] S R Podmirseg, H Jäkel, G D Ranches, M K Kullmann, B Sohm, A Villunger, H Lindner, and L Hengst. Caspases uncouple p27Kip1 from cell cycle regulated degradation and abolish its ability to stimulate cell migration and invasion. *Oncogene*, 35(35):4580–4590, September 2016.

[245] Alberto Puliafito, Lars Hufnagel, Pierre Neveu, Sebastian Streichan, Alex Sigal, D. Kuchnir Fygenson, and Boris I. Shraiman. Collective and single cell behavior in epithelial contact inhibition. *Proceedings of the National Academy of Sciences*, 109(3):739–744, January 2012. Publisher: National Academy of Sciences Section: Physical Sciences.

[246] Alberto Puliafito, Luca Primo, and Antonio Celani. Cell-size distribution in epithelial tissue formation and homeostasis. *Journal of the Royal Society, Interface*, 14(128):20170032, March 2017.

[247] Carlos Pérez-González, Ricard Alert, Carles Blanch-Mercader, Manuel Gómez-González, Tomasz Kolodziej, Elsa Bazellieres, Jaume Casademunt, and Xavier Trepat. Active wetting of epithelial tissues. *Nature Physics*, 15(1):79–88, January 2019. Number: 1 Publisher: Nature Publishing Group.

[248] Srikala Raghavan, Christoph Bauer, Gina Mundschau, Qingqin Li, and Elaine Fuchs. Conditional Ablation of 1 Integrin in Skin. *Journal of Cell Biology*, 150(5):1149–1160, September 2000.

[249] Subramanian P. Ramanathan, Jonne Helenius, Martin P. Stewart, Cedric J. Cattin, Anthony A. Hyman, and Daniel J. Muller. Cdk1-dependent mitotic enrichment of cortical myosin II promotes cell rounding against confinement. *Nature Cell Biology*, 17(2):148–159, February 2015.

[250] Subramanian P. Ramanathan, Matej Krajnc, and Matthew C. Gibson. Cell-Size Pleomorphism Drives Aberrant Clone Dispersal in Proliferating Epithelia. *Developmental Cell*, 51(1):49–61.e4, October 2019.

[251] Charina M. Ramirez, Benny Liu, Amal Aqul, Anna M. Taylor, Joyce J. Repa, Stephen D. Turley, and John M. Dietschy. Quantitative role of LAL, NPC2, and NPC1 in lysosomal cholesterol processing defined by genetic and pharmacological manipulations. *Journal of Lipid Research*, 52(4):688–698, April 2011.

[252] Charina M Ramirez, Benny Liu, Anna M Taylor, Joyce J Repa, Dennis K Burns, Arthur G Weinberg, Stephen D Turley, and John M Dietschy. Weekly Cyclodextrin Administration Normalizes Cholesterol Metabolism in Nearly Every Organ of the Niemann-Pick Type C1 Mouse and Markedly Prolongs Life. *Pediatric Research*, 68(4):309–315, October 2010.

[253] Jonas Ranft, Markus Basan, Jens Elgeti, Jean-François Joanny, Jacques Prost, and Frank Jülicher. Fluidization of tissues by cell division and apoptosis. *Proceedings of the National Academy of Sciences*, 107(49):20863–20868, December 2010.

[254] Aparna Ratheesh, Guillermo A. Gomez, Rashmi Priya, Suzie Verma, Eva M. Kovacs, Kai Jiang, Nicholas H. Brown, Anna Akhmanova, Samantha J. Stehbens, and Alpha S. Yap. Centralspindlin and -catenin regulate Rho signalling at the epithelial zonula adherens. *Nature cell biology*, 14(8):818–828, August 2012.

[255] Maria Rescigno. The intestinal epithelial barrier in the control of homeostasis and immunity. *Trends in Immunology*, 32(6):256–264, June 2011.

[256] Christopher B. Rohde, Fei Zeng, Ricardo Gonzalez-Rubio, Matthew Angel, and Mehmet Fatih Yanik. Microfluidic system for on-chip high-throughput whole-animal sorting and screening at subcellular resolution. *Proceedings of the National Academy of Sciences*, 104(35):13891–13895, August 2007.

[257] Marianne Rohrbach and Joe T R Clarke. Treatment of Lysosomal Storage Disorders: Progress with Enzyme Replacement Therapy. *Drugs*, 67(18):2697–2716, 2007.

[258] E A Rorke, G Adhikary, C A Young, R H Rice, P M Elias, D Crumrine, J Meyer, M Blumenberg, and R L Eckert. Structural and biochemical changes underlying a keratoderma-like phenotype in mice lacking suprabasal AP1 transcription factor function. *Cell Death & Disease*, 6(2):e1647–e1647, February 2015.

[259] Anton I. Rosenbaum, Madalina Rujoi, Amy Y. Huang, Hong Du, Gregory A. Grabowski, and Frederick R. Maxfield. Chemical screen to reduce sterol accumulation in Niemann–Pick C disease cells identifies novel lysosomal acid lipase inhibitors. *Biochimica et Biophysica Acta (BBA) - Molecular and Cell Biology of Lipids*, 1791(12):1155–1165, December 2009.

[260] Anton I. Rosenbaum, Guangtao Zhang, J. David Warren, and Frederick R. Maxfield. Endocytosis of beta-cyclodextrins is responsible for cholesterol reduction in Niemann-Pick type C mutant cells. *Proceedings of the National Academy of Sciences*, 107(12):5477–5482, March 2010.

[261] Michael H. Ross and Wojciech Pawlina. *Histology*. Lippincott Williams & Wilkins, 2006. Google-Books-ID: FoSiGTXn6BUC.

[262] Ninna S. Rossen, Jens M. Tarp, Joachim Mathiesen, Mogens H. Jensen, and Lene B. Oddershede. Long-range ordered vorticity patterns in living tissue induced by cell division. *Nature Communications*, 5(1):5720, December 2014.

[263] Mehdi Saadaoui, Didier Rocancourt, Julian Roussel, Francis Corson, and Jerome Gros. A tensile ring drives tissue flows to shape the gastrulating amniote embryo. *Science*, 367(6476):453–458, January 2020.

[264] Mohammad Ali Samie and Haoxing Xu. Lysosomal exocytosis and lipid storage disorders. *Journal of Lipid Research*, 55(6):995–1009, June 2014.

[265] Anand Saminathan, John Devany, Aneesh Tazhe Veetil, Bhavyashree Suresh, Kavya Smitha Pillai, Michael Schwake, and Yamuna Krishnan. A DNA-based voltmeter for organelles. *Nature Nanotechnology*, 16(1):96–103, January 2021. Number: 1 Publisher: Nature Publishing Group.

[266] Toshiro Sato, Robert G. Vries, Hugo J. Snippert, Marc van de Wetering, Nick Barker, Daniel E. Stange, Johan H. van Es, Arie Abo, Pekka Kujala, Peter J. Peters, and Hans Clevers. Single Lgr5 stem cells build crypt-villus structures in vitro without a mesenchymal niche. *Nature*, 459(7244):262–265, May 2009.

[267] Thierry Savin and Patrick S. Doyle. Static and Dynamic Errors in Particle Tracking Microrheology. *Biophysical Journal*, 88(1):623–638, January 2005.

[268] Lara Schaheen, Greg Patton, and Hanna Fares. Suppression of the *cup-5* mucolipidosis type IV-related lysosomal dysfunction by the inactivation of an ABC transporter in *C. elegans*. *Development*, 133(19):3939–3948, October 2006.

[269] Robert P. Schleimer and Sergejs Berdnikovs. Etiology of epithelial barrier dysfunction in patients with type 2 inflammatory diseases. *Journal of Allergy and Clinical Immunology*, 139(6):1752–1761, June 2017. Number: 6.

[270] J. Schlessinger and A. Ullrich. Growth factor signaling by receptor tyrosine kinases. *Neuron*, 9(3):383–391, September 1992.

[271] Veronika M. Schoop, Norbert E. Fusenig, and Nicolae Mirancea. Epidermal Organization and Differentiation of HaCaT Keratinocytes in Organotypic Coculture with Human Dermal Fibroblasts. *Journal of Investigative Dermatology*, 112(3):343–353, March 1999.

[272] U. H. Schueler, T. Kolter, C. R. Kaneski, G. C. Zirzow, K. Sandhoff, and R. O. Brady. Correlation between enzyme activity and substrate storage in a cell culture model system for Gaucher disease. *Journal of Inherited Metabolic Disease*, 27(5):649–658, September 2004.

[273] Frans Schutgens, Maarten B. Rookmaaker, Thanasis Margaritis, Anne Rios, Carola Ammerlaan, Jitske Jansen, Linda Gijzen, Marianne Vormann, Annelotte Vonk, Marco Viveen, Fjodor Yousef Yengej, Sepide Derakhshan, Karin M. de Winter-de Groot, Benedetta Artegiani, Ruben van Boxtel, Edwin Cuppen, Antoni P. A. Hendrickx, Marry M. van den Heuvel-Eibrink, Ellen Heitzer, Henriette Lanz, Jeffrey Beekman, Jean-Luc Murk, Rosalinde Masereeuw, Frank Holstege, Jarno Drost, Marianne C.

Verhaar, and Hans Clevers. Tubuloids derived from human adult kidney and urine for personalized disease modeling. *Nature Biotechnology*, 37(3):303–313, March 2019. Bandiera_abtest: a Cg_type: Nature Research Journals Number: 3 Primary_atype: Research Publisher: Nature Publishing Group Subject_term: Biological models;Stem-cell biotechnology Subject_term_id: biological-models;stem-cell-biotechnology.

[274] Matthew Scott and Terence Hwa. Bacterial growth laws and their applications. *Current Opinion in Biotechnology*, 22(4):559–565, August 2011.

[275] Ron Sender and Ron Milo. The distribution of cellular turnover in the human body. *Nature Medicine*, 27(1):45–48, January 2021. Bandiera_abtest: a Cg_type: Nature Research Journals Number: 1 Primary_atype: Research Publisher: Nature Publishing Group Subject_term: Metabolism;Systems biology Subject_term_id: metabolism;systems-biology.

[276] Toru Seo, Wanda Velez-Carrasco, Kemin Qi, Marni Hall, Tilla S. Worgall, Rebecca A. Johnson, and Richard J. Deckelbaum. Selective Uptake from LDL Is Stimulated by Unsaturated Fatty Acids and Modulated by Cholesterol Content in the Plasma Membrane: Role of Plasma Membrane Composition in Regulating Non-SR-BI-Mediated Selective Lipid Transfer. *Biochemistry*, 41(25):7885–7894, June 2002.

[277] Indra A. Shaltiel, Lenno Krenning, Wytse Bruinsma, and René H. Medema. The same, only different – DNA damage checkpoints and their reversal throughout the cell cycle. *Journal of Cell Science*, 128(4):607–620, February 2015.

[278] Dongbiao Shen, Xiang Wang, Xinran Li, Xiaoli Zhang, Zepeng Yao, Shannon Dibble, Xian-ping Dong, Ting Yu, Andrew P. Lieberman, Hollis D. Showalter, and Haoxing Xu. Lipid storage disorders block lysosomal trafficking by inhibiting a TRP channel and lysosomal calcium release. *Nature Communications*, 3(1):731, January 2012.

[279] Charles J. Sherr and James M. Roberts. CDK inhibitors: positive and negative regulators of G1-phase progression. *Genes & Development*, 13(12):1501–1512, June 1999. Company: Cold Spring Harbor Laboratory Press Distributor: Cold Spring Harbor Laboratory Press Institution: Cold Spring Harbor Laboratory Press Label: Cold Spring Harbor Laboratory Press Publisher: Cold Spring Harbor Lab.

[280] Boris I. Shraiman. Mechanical feedback as a possible regulator of tissue growth. *Proceedings of the National Academy of Sciences*, 102(9):3318–3323, March 2005. Publisher: National Academy of Sciences Section: Biological Sciences.

[281] E. Siintola. Cathepsin D deficiency underlies congenital human neuronal ceroid-lipofuscinosis. *Brain*, 129(6):1438–1445, April 2006.

[282] K. Simons and S. D. Fuller. Cell surface polarity in epithelia. *Annual Review of Cell Biology*, 1:243–288, 1985.

[283] Cory L. Simpson, Shin-ichiro Kojima, and Spiro Getsios. RNA Interference in Keratinocytes and an Organotypic Model of Human Epidermis. In Kursad Turksen, editor, *Epidermal Cells: Methods and Protocols*, Methods in Molecular Biology, pages 127–146. Humana Press, Totowa, NJ, 2010.

[284] Cory L. Simpson, Dipal M. Patel, and Kathleen J. Green. Deconstructing the skin: cytoarchitectural determinants of epidermal morphogenesis. *Nature Reviews Molecular Cell Biology*, 12(9):565–580, September 2011.

[285] Jana Slováková, Mateusz Sikora, Feyza Nur Arslan, Silvia Caballero-Mancebo, S. F. Gabriel Krens, Walter A. Kaufmann, Jack Merrin, and Carl-Philipp Heisenberg. Tension-dependent stabilization of E-cadherin limits cell–cell contact expansion in zebrafish germ-layer progenitor cells. *Proceedings of the National Academy of Sciences*, 119(8):e2122030119, February 2022. Publisher: Proceedings of the National Academy of Sciences.

[286] D. B. Staple, R. Farhadifar, J. C. Röper, B. Aigouy, S. Eaton, and F. Jülicher. Mechanics and remodelling of cell packings in epithelia. *The European Physical Journal E*, 33(2):117–127, October 2010.

[287] M. S. Steinberg. Reconstruction of tissues by dissociated cells. Some morphogenetic tissue movements and the sorting out of embryonic cells may have a common explanation. *Science (New York, N.Y.)*, 141(3579):401–408, August 1963.

[288] M S Steinberg and M Takeichi. Experimental specification of cell sorting, tissue spreading, and specific spatial patterning by quantitative differences in cadherin expression. *Proceedings of the National Academy of Sciences*, 91(1):206–209, January 1994. Publisher: Proceedings of the National Academy of Sciences.

[289] M. Stoker, E. Gherardi, M. Perryman, and J. Gray. Scatter factor is a fibroblast-derived modulator of epithelial cell mobility. *Nature*, 327(6119):239–242, May 1987.

[290] Sebastian J. Streichan, Christian R. Hoerner, Tatjana Schneidt, Daniela Holzer, and Lars Hufnagel. Spatial constraints control cell proliferation in tissues. *Proceedings of the National Academy of Sciences*, 111(15):5586–5591, April 2014. Publisher: National Academy of Sciences Section: Biological Sciences.

[291] Sebastian J Streichan, Matthew F Lefebvre, Nicholas Noll, Eric F Wieschaus, and Boris I Shraiman. Global morphogenetic flow is accurately predicted by the spatial distribution of myosin motors. *eLife*, 7:e27454.

[292] Dongdong Su, Chai Teoh, Nengyue Gao, Qing-Hua Xu, and Young-Tae Chang. A Simple BODIPY-Based Viscosity Probe for Imaging of Cellular Viscosity in Live Cells. *Sensors*, 16(9):1397, August 2016.

[293] Gopinath M. Sundaram, John E. A. Common, Felicia E. Gopal, Satyanarayana Srikanta, Krishnaswamy Lakshman, Declan P. Lunny, Thiam C. Lim, Vivek Tanavde,

E. Birgitte Lane, and Prabha Sampath. 'See-saw' expression of microRNA-198 and FSTL1 from a single transcript in wound healing. *Nature*, 495(7439):103–106, March 2013.

[294] Gopinath M. Sundaram, Hisyam M. Ismail, Mohsin Bashir, Manish Muhuri, Candida Vaz, Srikanth Nama, Ghim Siong Ow, Ivshina Anna Vladimirovna, Rajkumar Ramalingam, Brian Burke, Vivek Tanavde, Vladimir Kuznetsov, E. Birgitte Lane, and Prabha Sampath. EGF hijacks miR-198/FSTL1 wound-healing switch and steers a two-pronged pathway toward metastasis. *Journal of Experimental Medicine*, 214(10):2889–2900, October 2017.

[295] Sunaina Surana, Jaffar M. Bhat, Sandhya P. Koushika, and Yamuna Krishnan. An autonomous DNA nanomachine maps spatiotemporal pH changes in a multicellular living organism. *Nature Communications*, 2(1):340, September 2011.

[296] Daniel M. Sussman. cellGPU: Massively parallel simulations of dynamic vertex models. *Computer Physics Communications*, 219:400–406, October 2017.

[297] Daniel M. Sussman, M. Paoluzzi, M. Cristina Marchetti, and M. Lisa Manning. Anomalous glassy dynamics in simple models of dense biological tissue. *EPL (Europhysics Letters)*, 121(3):36001, February 2018.

[298] Daniel M. Sussman, J.M. Schwarz, M. Cristina Marchetti, and M. Lisa Manning. Soft yet Sharp Interfaces in a Vertex Model of Confluent Tissue. *Physical Review Letters*, 120(5):058001, January 2018. Publisher: American Physical Society.

[299] Masatoshi Takeichi. Dynamic contacts: rearranging adherens junctions to drive epithelial remodelling. *Nature Reviews Molecular Cell Biology*, 15(6):397–410, June 2014.

[300] Ceryl Tan, Miriam B. Ginzberg, Rachel Webster, Seshu Iyengar, Shixuan Liu, David Papadopoli, John Concannon, Yuan Wang, Douglas S. Auld, Jeremy L. Jenkins, Hannes Rost, Ivan Topisirovic, Andreas Hilfinger, W. Brent Derry, Nish Patel, and Ran Kafri. Cell size homeostasis is maintained by CDK4-dependent activation of p38 MAPK. *Developmental Cell*, 56(12):1756–1769.e7, June 2021.

[301] Yuyang Tang, Ihid Carneiro Leao, Ebony M. Coleman, Robin Shepard Broughton, and James E. K. Hildreth. Deficiency of Niemann-Pick Type C-1 Protein Impairs Release of Human Immunodeficiency Virus Type 1 and Results in Gag Accumulation in Late Endosomal/Lysosomal Compartments. *Journal of Virology*, 83(16):7982–7995, August 2009.

[302] Zan Tang, Yucheng Hu, Zheng Wang, Kewu Jiang, Cheng Zhan, Wallace F. Marshall, and Nan Tang. Mechanical Forces Program the Orientation of Cell Division during Airway Tube Morphogenesis. *Developmental Cell*, 44(3):313–325.e5, February 2018.

[303] Harriet B. Taylor, Anaïs Khuong, Zhonglin Wu, Qiling Xu, Rosalind Morley, Lauren Gregory, Alexei Poliakov, William R. Taylor, and David G. Wilkinson. Cell segregation and border sharpening by Eph receptor–ephrin-mediated heterotypic repulsion. *Journal of the Royal Society Interface*, 14(132):20170338, July 2017.

[304] D'Arcy Wentworth Thompson. *On growth and form*. Cambridge University Press, Cambridge, Eng, 2nd ed edition, 1942.

[305] Jean-Yves Tinevez. simpletracker.

[306] Jean-Yves Tinevez, Ulrike Schulze, Guillaume Salbreux, Julia Roensch, Jean-François Joanny, and Ewa Paluch. Role of cortical tension in bleb growth. *Proceedings of the National Academy of Sciences*, 106(44):18581–18586, November 2009. Publisher: Proceedings of the National Academy of Sciences.

[307] Christopher L. Tinkle, H. Amalia Pasolli, Nicole Stokes, and Elaine Fuchs. New insights into cadherin function in epidermal sheet formation and maintenance of tissue integrity. *Proceedings of the National Academy of Sciences*, 105(40):15405–15410, October 2008.

[308] Cristian Tomasetti and Bert Vogelstein. Variation in cancer risk among tissues can be explained by the number of stem cell divisions. *Science*, 347(6217):78–81, January 2015. Publisher: American Association for the Advancement of Science.

[309] Antonio Totaro, Martina Castellan, Giusy Battilana, Francesca Zanconato, Luca Azzolin, Stefano Giulitti, Michelangelo Cordenonsi, and Stefano Piccolo. YAP/TAZ link cell mechanics to Notch signalling to control epidermal stem cell fate. *Nature Communications*, 8(1):15206, August 2017.

[310] Philip L. Townes and Johannes Holtfreter. Directed movements and selective adhesion of embryonic amphibian cells. *Journal of Experimental Zoology*, 128(1):53–120, 1955. _eprint: https://onlinelibrary.wiley.com/doi/pdf/10.1002/jez.1401280105.

[311] Xavier Trepat, Michael R. Wasserman, Thomas E. Angelini, Emil Millet, David A. Weitz, James P. Butler, and Jeffrey J. Fredberg. Physical forces during collective cell migration. *Nature Physics*, 5(6):426–430, June 2009.

[312] Tony Y.-C. Tsai, Mateusz Sikora, Peng Xia, Tugba Colak-Champollion, Holger Knaut, Carl-Philipp Heisenberg, and Sean G. Megason. An adhesion code ensures robust pattern formation during tissue morphogenesis. *Science*, 370(6512):113–116, October 2020. Publisher: American Association for the Advancement of Science.

[313] Yiider Tseng, Thomas P. Kole, and Denis Wirtz. Micromechanical Mapping of Live Cells by Multiple-Particle-Tracking Microrheology. *Biophysical Journal*, 83(6):3162–3176, December 2002.

[314] Jerrold R. Turner. Molecular Basis of Epithelial Barrier Regulation: From Basic Mechanisms to Clinical Application. *The American Journal of Pathology*, 169(6):1901–1909, December 2006.

[315] Mathias Uhlén, Linn Fagerberg, Björn M. Hallström, Cecilia Lindskog, Per Oksvold, Adil Mardinoglu, Åsa Sivertsson, Caroline Kampf, Evelina Sjöstedt, Anna Asplund, IngMarie Olsson, Karolina Edlund, Emma Lundberg, Sanjay Navani, Cristina Al-Khalili Szigyarto, Jacob Odeberg, Dijana Djureinovic, Jenny Ottosson Takanen, Sophia Hober, Tove Alm, Per-Henrik Edqvist, Holger Berling, Hanna Tegel, Jan Mulder, Johan Rockberg, Peter Nilsson, Jochen M. Schwenk, Marica Hamsten, Kalle von Feilitzen, Mattias Forsberg, Lukas Persson, Fredric Johansson, Martin Zwahlen, Gunnar von Heijne, Jens Nielsen, and Fredrik Pontén. Tissue-based map of the human proteome. *Science*, 347(6220):1260419, January 2015. Publisher: American Association for the Advancement of Science.

[316] Léo Valon, Anđela Davidović, Florence Levillayer, Alexis Villars, Mathilde Chouly, Fabiana Cerqueira-Campos, and Romain Levayer. Robustness of epithelial sealing is an emerging property of local ERK feedback driven by cell elimination. *Developmental Cell*, 56(12):1700–1711.e8, June 2021.

[317] Rob van der Kammen, Ji-Ying Song, Iris de Rink, Hans Janssen, Stefania Madonna, Claudia Scarponi, Cristina Albanesi, Wim Brugman, and Metello Innocenti. Knockout of the Arp2/3 complex in epidermis causes a psoriasis-like disease hallmarked by hyperactivation of transcription factor Nrf2. *Development*, page dev.156323, January 2017.

[318] Sjoerd van Helvert, Cornelis Storm, and Peter Friedl. Mechanoreciprocity in cell migration. *Nature Cell Biology*, 20(1):8–20, January 2018.

[319] Marie T Vanier. Niemann-Pick disease type C. *Orphanet Journal of Rare Diseases*, 5(1):16, December 2010.

[320] Marie T. Vanier and Philippe Latour. Laboratory diagnosis of Niemann–Pick disease type C: The filipin staining test. In *Methods in Cell Biology*, volume 126, pages 357–375. Elsevier, 2015.

[321] Valeri Vasioukhin, Christoph Bauer, Linda Degenstein, Bart Wise, and Elaine Fuchs. Hyperproliferation and Defects in Epithelial Polarity upon Conditional Ablation of -Catenin in Skin. *Cell*, 104(4):605–617, February 2001.

[322] Matheus P. Viana, Jianxu Chen, Theo A. Knijnenburg, Ritvik Vasan, Calysta Yan, Joy E. Arakaki, Matte Bailey, Ben Berry, Antoine Borensztejn, Jackson M. Brown, Sara Carlson, Julie A. Cass, Basudev Chaudhuri, Kimberly R. Cordes Metzler, Mackenzie E. Coston, Zach J. Crabtree, Steve Davidson, Colette M. DeLizo, Shailja Dhaka, Stephanie Q. Dinh, Thao P. Do, Justin Domingus, Rory M. Donovan-Maiye, Tyler J. Foster, Christopher L. Frick, Griffin Fujioka, Margaret A. Fuqua, Jamie L. Gehring, Kaytlyn A. Gerbin, Tanya Grancharova, Benjamin W. Gregor, Lisa J. Harrylock, Amanda Haupt, Melissa C. Hendershott, Caroline Hookway, Alan R. Horwitz, Chris

Hughes, Eric J. Isaac, Gregory R. Johnson, Brian Kim, Andrew N. Leonard, Winnie W. Leung, Jordan J. Lucas, Susan A. Ludmann, Blair M. Lyons, Haseeb Malik, Ryan McGregor, Gabe E. Medrash, Sean L. Meharry, Kevin Mitcham, Irina A. Mueller, Timothy L. Murphy-Stevens, Aditya Nath, Angelique M. Nelson, Luana Paleologu, T. Alexander Popiel, Megan M. Riel-Mehan, Brock Roberts, Lisa M. Schaefbauer, Magdalena Schwarzl, Jamie Sherman, Sylvain Slaton, M. Filip Sluzewski, Jacqueline E. Smith, Youngmee Sul, Madison J. Swain-Bowden, W. Joyce Tang, Derek J. Thirstrup, Daniel M. Toloudis, Andrew P. Tucker, Veronica Valencia, Winfried Wiegraebe, Thushara Wijeratna, Ruian Yang, Rebecca J. Zaunbrecher, Allen Institute for Cell Science, Graham T. Johnson, Ruwanthi N. Gunawardane, Nathalie Gaudreault, Julie A. Theriot, and Susanne M. Rafelski. Robust integrated intracellular organization of the human iPS cell: where, how much, and how variable. Technical report, bioRxiv, January 2021. Section: New Results Type: article.

[323] Benoit Vianay, Fabrice Senger, Simon Alamos, Maya Anjur-Dietrich, Elizabeth Bearce, Bevan Cheeseman, Lisa Lee, and Manuel Théry. Variation in traction forces during cell cycle progression: Traction forces during cycle progression. *Biology of the Cell*, 110(4):91–96, April 2018.

[324] Jaromir Vlach. Phosphorylation-dependent degradation of the cyclin-dependent kinase inhibitor p27Kip1. *The EMBO Journal*, 16(17):5334–5344, September 1997. Publisher: John Wiley & Sons, Ltd.

[325] Danielle te Vruchte, Emyr Lloyd-Evans, Robert Jan Veldman, David C.A. Neville, Raymond A. Dwek, Frances M. Platt, Wim J. van Blitterswijk, and Dan J. Sillence. Accumulation of Glycosphingolipids in Niemann-Pick C Disease Disrupts Endosomal Transport. *Journal of Biological Chemistry*, 279(25):26167–26175, June 2004.

[326] Aurimas Vyšniauskas, Ismael López-Duarte, Nicolas Duchemin, Thanh-Truc Vu, Yilei Wu, Ekaterina M. Budynina, Yulia A. Volkova, Eduardo Peña Cabrera, Diana E. Ramírez-Ornelas, and Marina K. Kuimova. Exploring viscosity, polarity and temperature sensitivity of BODIPY-based molecular rotors. *Physical Chemistry Chemical Physics*, 19(37):25252–25259, 2017.

[327] John B Wallingford, Scott E Fraser, and Richard M Harland. Convergent Extension: The Molecular Control of Polarized Cell Movement during Embryonic Development. *Developmental Cell*, 2(6):695–706, June 2002.

[328] Deepika Walpita and Elizabeth Hay. Studying actin-dependent processes in tissue culture. *Nature Reviews. Molecular Cell Biology*, 3(2):137–141, February 2002.

[329] G-Q Wang. Histological precursors of oesophageal squamous cell carcinoma: results from a 13 year prospective follow up study in a high risk population. *Gut*, 54(2):187–192, February 2005.

[330] Lu Wang, Yi Xiao, Wenming Tian, and Liezheng Deng. Activatable Rotor for Quantifying Lysosomal Viscosity in Living Cells. *Journal of the American Chemical Society*, 135(8):2903–2906, February 2013.

[331] Xun Wang, Matthias Merkel, Leo B. Sutter, Gonca Erdemci-Tandogan, M. Lisa Manning, and Karen E. Kasza. Anisotropy links cell shapes to tissue flow during convergent extension. *Proceedings of the National Academy of Sciences*, 117(24):13541–13551, June 2020.

[332] Zhihui Wang, Joseph D. Butner, Romica Kerketta, Vittorio Cristini, and Thomas S. Deisboeck. Simulating cancer growth with multiscale agent-based modeling. *Seminars in Cancer Biology*, 30:70–78, February 2015.

[333] F M Watt. Selective migration of terminally differentiating cells from the basal layer of cultured human epidermis. *Journal of Cell Biology*, 98(1):16–21, January 1984.

[334] F. M. Watt. Influence of cell shape and adhesiveness on stratification and terminal differentiation of human keratinocytes in culture. *Journal of Cell Science. Supplement*, 8:313–326, 1987.

[335] F M Watt, P W Jordan, and C H O'Neill. Cell shape controls terminal differentiation of human epidermal keratinocytes. *Proceedings of the National Academy of Sciences*, 85(15):5576–5580, August 1988. Publisher: Proceedings of the National Academy of Sciences.

[336] Matthias Weiss, Markus Elsner, Fredrik Kartberg, and Tommy Nilsson. Anomalous Subdiffusion Is a Measure for Cytoplasmic Crowding in Living Cells. *Biophysical Journal*, 87(5):3518–3524, November 2004.

[337] Ramon J Whitson, Alex Lee, Nicole M Urman, Amar Mirza, Catherine Y Yao, Alexander S Brown, Jiang R Li, Gautam Shankar, Micah A Fry, Scott X Atwood, Eunice Y Lee, S Tyler Hollmig, Sumaira Z Aasi, Kavita Y Sarin, Matthew P Scott, Ervin H Epstein, Jean Y Tang, and Anthony E Oro. Noncanonical hedgehog pathway activation through SRF–MKL1 promotes drug resistance in basal cell carcinomas. *Nature Medicine*, 24(3):271–281, March 2018.

[338] Peter Whyte, Nicola M. Williamson, and Ed Harlow. Cellular targets for transformation by the adenovirus E1A proteins. *Cell*, 56(1):67–75, January 1989.

[339] R. A. Willis. Pathology of tumours. *Pathology of tumours.*, 1948. Publisher: London: Butterworth & Co.

[340] Rudolf Winklbauer. Cell adhesion strength from cortical tension – an integration of concepts. *Journal of Cell Science*, 128(20):3687–3693, October 2015.

[341] Rudolf Winklbauer and Serge E. Parent. Forces driving cell sorting in the amphibian embryo. *Mechanisms of Development*, 144(Pt A):81–91, April 2017.

[342] Denis Wirtz. Particle-Tracking Microrheology of Living Cells: Principles and Applications. *Annual Review of Biophysics*, 38(1):301–326, June 2009.

[343] Stephen Wolfram. Cellular automata as models of complexity. *Nature*, 311(5985):419–424, October 1984. Number: 5985 Publisher: Nature Publishing Group.

[344] Je-Tae Woo, Chikara Shinohara, Kaoru Sakai, Keiji Hasumi, and Akira Endo. Inhibition of the acidification of endosomes and lysosomes by the antibiotic concanamycin B in macrophage J774. *European Journal of Biochemistry*, 207(1):383–389, July 1992.

[345] Tom P. J. Wyatt, Jonathan Fouchard, Ana Lisica, Nargess Khalilgharibi, Buzz Baum, Pierre Recho, Alexandre J. Kabla, and Guillaume T. Charras. Actomyosin controls planarity and folding of epithelia in response to compression. *Nature Materials*, 19(1):109–117, January 2020. Number: 1 Publisher: Nature Publishing Group.

[346] Tom P. J. Wyatt, Andrew R. Harris, Maxine Lam, Qian Cheng, Julien Bellis, Andrea Dimitracopoulos, Alexandre J. Kabla, Guillaume T. Charras, and Buzz Baum. Emergence of homeostatic epithelial packing and stress dissipation through divisions oriented along the long cell axis. *Proceedings of the National Academy of Sciences*, 112(18):5726–5731, May 2015.

[347] Matthias P. Wymann and Roger Schneiter. Lipid signalling in disease. *Nature Reviews Molecular Cell Biology*, 9(2):162–176, February 2008.

[348] Shicong Xie and Jan M. Skotheim. A G1 Sizer Coordinates Growth and Division in the Mouse Epidermis. *Current biology: CB*, 30(5):916–924.e2, March 2020.

[349] Shicong Xie, Matthew Swaffer, and Jan M. Skotheim. Eukaryotic Cell Size Control and Its Relation to Biosynthesis and Senescence. *Annual Review of Cell and Developmental Biology*, 38(1):null, 2022. _eprint: https://doi.org/10.1146/annurev-cellbio-120219-040142.

[350] Jiaqiang Xing and Cuicui Liu. Identification of genes associated with histologic tumor grade of esophageal squamous cell carcinoma. *FEBS Open Bio*, 7(9):1246–1257, September 2017.

[351] Takaki Yamamoto, Daniel M. Sussman, Tatsuo Shibata, and M. Lisa Manning. Nonmonotonic fluidization generated by fluctuating edge tensions in confluent tissues. *Soft Matter*, 18(11):2168–2175, March 2022. Publisher: The Royal Society of Chemistry.

[352] Le Yan and Dapeng Bi. Multicellular Rosettes Drive Fluid-solid Transition in Epithelial Tissues. *Physical Review X*, 9(1):011029, February 2019. Publisher: American Physical Society.

[353] Ayaka Yanagida, Elena Corujo-Simon, Christopher K. Revell, Preeti Sahu, Giuliano G. Stirparo, Irene M. Aspalter, Alex K. Winkel, Ruby Peters, Henry De Belly, Davide

A. D. Cassani, Sarra Achouri, Raphael Blumenfeld, Kristian Franze, Edouard Hannezo, Ewa K. Paluch, Jennifer Nichols, and Kevin J. Chalut. Cell surface fluctuations regulate early embryonic lineage sorting. *Cell*, 185(5):777–793.e20, March 2022.

[354] Jiechao Yang, Liang Zhou, Yanping Zhang, Juan Zheng, Jian Zhou, Zheqiang Wei, and Jiaping Zou. DIAPH1 Is Upregulated and Inhibits Cell Apoptosis through ATR/p53/Caspase-3 Signaling Pathway in Laryngeal Squamous Cell Carcinoma. *Disease Markers*, 2019:1–10, January 2019.

[355] Qiutan Yang, Shi-Lei Xue, Chii Jou Chan, Markus Rempfler, Dario Vischi, Francisca Maurer-Gutierrez, Takashi Hiiragi, Edouard Hannezo, and Prisca Liberali. Cell fate coordinates mechano-osmotic forces in intestinal crypt formation. *Nature Cell Biology*, 23(7):733–744, July 2021. Number: 7 Publisher: Nature Publishing Group.

[356] Xingbo Yang, Dapeng Bi, Michael Czajkowski, Matthias Merkel, M. Lisa Manning, and M. Cristina Marchetti. Correlating cell shape and cellular stress in motile confluent tissues. *Proceedings of the National Academy of Sciences*, 114(48):12663–12668, November 2017.

[357] Kai Yao, Nash D. Rochman, and Sean X. Sun. CTRL – a label-free artificial intelligence method for dynamic measurement of single-cell volume. *Journal of Cell Science*, 133(7), April 2020.

[358] Huapeng H. Yu, Michael R. Dohn, Nicholas O. Markham, Robert J. Coffey, and Albert B. Reynolds. p120-catenin controls contractility along the vertical axis of epithelial lateral membranes. *Journal of Cell Science*, 129(1):80–94, January 2016.

[359] Wei Yu, Lucy E. O'Brien, Fei Wang, Henry Bourne, Keith E. Mostov, and Mirjam M. P. Zegers. Hepatocyte growth factor switches orientation of polarity and mode of movement during morphogenesis of multicellular epithelial structures. *Molecular Biology of the Cell*, 14(2):748–763, February 2003.

[360] Evgeny Zatulovskiy and Jan M. Skotheim. On the Molecular Mechanisms Regulating Animal Cell Size Homeostasis. *Trends in Genetics*, 36(5):360–372, May 2020.

[361] Evgeny Zatulovskiy, Shuyuan Zhang, Daniel F. Berenson, Benjamin R. Topacio, and Jan M. Skotheim. Cell growth dilutes the cell cycle inhibitor Rb to trigger cell division. *Science (New York, N.Y.)*, 369(6502):466–471, July 2020.

[362] L. Zhao, C. D. Kroenke, J. Song, D. Piwnica-Worms, J. J. H. Ackerman, and J. J. Neil. Intracellular Water Specific MR of Microbead-adherent Cells: The HeLa Cell Intracellular Water Exchange Lifetime. *NMR in biomedicine*, 21(2):159–164, February 2008.

[363] Yonggang Zheng and Duojia Pan. The Hippo Signaling Pathway in Development and Disease. *Developmental Cell*, 50(3):264–282, August 2019.

[364] Kang Zhou, Andrew Muroyama, Julie Underwood, Rebecca Leylek, Samriddha Ray, Scott H. Soderling, and Terry Lechler. Actin-related protein2/3 complex regulates tight junctions and terminal differentiation to promote epidermal barrier formation. *Proceedings of the National Academy of Sciences of the United States of America*, 110(40):E3820–E3829, October 2013.

[365] Mojun Zhu, Maria Z. Lerum, and Wei Chen. How To Prepare Reproducible, Homogeneous, and Hydrolytically Stable Aminosilane-Derived Layers on Silica. *Langmuir*, 28(1):416–423, January 2012. Publisher: American Chemical Society.

[366] Jacob Zhurinsky, Klaus Leonhard, Stephen Watt, Samuel Marguerat, Jürg Bähler, and Paul Nurse. A Coordinated Global Control over Cellular Transcription. *Current Biology*, 20(22):2010–2015, November 2010.

[367] Romain Zufferey, Dea Nagy, Ron J. Mandel, Luigi Naldini, and Didier Trono. Multiply attenuated lentiviral vector achieves efficient gene delivery in vivo. *Nature Biotechnology*, 15(9):871–875, September 1997. Number: 9 Publisher: Nature Publishing Group.